ABSTRACT

Title of dissertation: DEVELOPMENT OF A LAGRANGIAN-LAGRANGIAN METHODOLOGY TO PREDICT BROWNOUT DUST CLOUDS

Monica Syal, Doctor of Philosophy, 2012

Dissertation directed by: Minta Martin Professor J. Gordon Leishman
Department of Aerospace Engineering

A Lagrangian-Lagrangian dust cloud simulation methodology has been developed to help better understand the complicated two-phase nature of the rotorcraft brownout problem. Brownout conditions occur when rotorcraft land or take off from ground surfaces covered with loose sediment such as sand and dust, which decreases the pilot's visibility of the ground and poses a serious safety of flight risk. The present work involved the development of a comprehensive, computationally efficient three-dimensional sediment tracking method for dilute, low Reynolds number Stokes-type flows. The flow field generated by a helicopter rotor in ground effect operations over a mobile sediment bed was modeled by using an inviscid, incompressible, Lagrangian free-vortex method, coupled to a viscous semi-empirical approximation for the boundary layer flow near the ground. A new threshold model for the onset of sediment mobility was developed by including the effects of unsteady pressure forces that are induced in vortically dominated rotor flows, which can significantly alter the threshold conditions for particle motion. Other important aspects of particle mobility and uplift in such vortically driven dust flows were also modeled, including bombardment effects when previously suspended particles

impact the bed and eject new particles. Bombardment effects were shown to be a particularly significant contributor to the mobilization and eventual suspension of large quantities of smaller-sized dust particles, which tend to remain suspended. A numerically efficient Lagrangian particle tracking methodology was developed where individual particle or clusters of particles were tracked in the flow. To this end, a multi-step, second-order accurate time-marching scheme was developed to solve the numerically stiff equations that govern the dynamics of particle motion. The stability and accuracy of this scheme was examined and matched to the characteristics of free-vortex method. One-way coupling of the flow and the particle motion was assumed. Particle collisions were not considered. To help reduce numerical costs, the methodology was implemented on graphic processing units, which gave over an order of magnitude reduction in simulation time without any loss in accuracy. Validation of the methodology was performed against available measurements, including flow field measurements that have been made with laboratory-scale and full-scale rotors in ground effect operations. The predicted dust clouds were also compared against measurements of developing dust clouds produced by a helicopter during taxi-pass and approach-to-touchdown flight maneuvers. The results showed that the problem of brownout is mostly driven by the local action of the rotor wake vortices and the grouping or bundling of vortex filaments near the sediment bed. The possibilities of mitigating the intensity of brownout conditions by diffusing the blade tip vortices was also explored. While other means of brownout mitigation may be possible, enhancing the diffusion of the tip vortices was shown to drastically reduce the quantity of mobilized particles and the overall severity of the brownout dust cloud.

DEVELOPMENT OF A LAGRANGIAN-LAGRANGIAN METHODOLOGY TO PREDICT BROWNOUT DUST CLOUDS

by

Monica Syal

Dissertation submitted to the Faculty of the Graduate School of the
University of Maryland, College Park in partial fulfillment
of the requirements for the degree of
Doctor of Philosophy
2012

Advisory Committee:

Minta Martin Professor J. Gordon Leishman, Chairman/Advisor
Gessow Professor Inderjit Chopra
Professor Roberto Celi
Associate Professor James D. Baeder
Associate Professor Ramani Duraiswami, Dean's representative

Dedication

To my parents for giving me this wonderful life

And, to my husband, my best friend, for making it better everyday

Acknowledgments

During the course of these six years, I have met so many wonderful people, who have made this journey memorable for me. I want to take this opportunity to thank all of them from the bottom of my heart. First of all, I express my deepest gratitude to my advisor, Dr. J. Gordon Leishman for providing me an opportunity to work with him, and constantly guiding me through this process. His enthusiasm toward work has always motivated me. His critical evaluation of my work has honed my analyzing, writing and presentation skills. I can proudly say that, thanks to him, today I stand as a much more confident person than I was six years ago.

I would also like to express my sincere thanks to my committee, Professors Inderjit Chopra, James Baeder, Roberto Celi and Ramani Duraiswami, for the insightful discussions on different aspects related of my research. I am especially thankful to Dr. James Baeder for his constant help toward the development of numerical integration schemes, and Dr. Ramani Duraiwsami and Dr. Nail Gumerov for sharing their ideas on the computational aspects of my research problem.

I have made many good friends in these years, who made this journey a very comfortable one. I want to thank Bharath Govindarajan, Arun Issac Jose and John Tritschler for being such special friends, and for always being there for me. I would like to thank everyone in "Team Leishman" for the fun and energy that they add to work. David, Jaime, Anish, Joe, Juergen, Nate, Conor, Ben: you all have been a constant source of inspiration for me. I will miss the workout sessions that we enjoyed so much. I also want to thank Vikram, Moble, Asitav and Vinod for being good friends over these years.

They say that a good work life requires a good personal life, and I regard myself very lucky to have lived with many good housemates, who have become my friends for life. I want to thank Neha, Ruchika, Ria, Deepa, Savita and Ritaja, who I have always considered my family in this distant place.

Words cannot express how much love and respect I feel for my parents who have always been my pillars of strength. I want to thank them for giving me such a beautiful life, making me an independent person to explore it on my own, and supporting me in all my decisions. I cannot be thankful enough to them for making so many sacrifices in their life to provide us with good education and making us good human beings. I love my younger siblings, Gaurav and Rashmi, for always making me feel very special. The values of compassion, honesty, and humbleness that I have learnt from my family will always remain the central part of my life.

Last but not the least, I want to thank my husband, Satinder Singh, who has been my greatest strength through this journey. He is the one person, who has always been with me through all the thicks and thins for the past six years. Thanks to him for making me a more optimistic, patient, understanding and balanced person. Marrying him was the best decision I have made. His support, even from 6000 miles away, made me ride smoothly through the last year of my Ph.D. I am so looking forward to submitting this dissertation and moving to California to spend my life with him.

Finally, I want to thank God for giving me a happy and healthy life.

Table of Contents

List of Tables

List of Figures

NOMENCLATURE

A	Cross-sectional (frontal) area of suspended particle
A_B	Non-dimensional threshold friction velocity parameter
A_s	Frontal area of stationary particle on the sediment bed
c	Blade chord
C_d	Drag coefficient of suspended particle
C_d	Sectional drag coefficient
C_{d_s}	Drag coefficient of a stationary particle on the bed
C_l	Sectional lift coefficient
C_{l_α}	Sectional lift-curve slope
C_P	Rotor power coefficient, $= P/\rho A\Omega^3 R^3$
C_{P_i}	Rotor induced power coefficient, $= P_i/\rho A\Omega^3 R^3$
C_{P_0}	Rotor profile power coefficient, $= P_0/\rho A\Omega^3 R^3$
C_Q	Rotor torque coefficient, $= Q/\rho A\Omega^2 R^3$
C_T	Rotor thrust coefficient, $= T/\rho A\Omega^2 R^2$
$C_{T_{\text{req}}}$	Target thrust coefficient, $= T_{\text{req}}/\rho A\Omega^2 R^2$
d_p	Particle diameter
D	Rotor diameter
e	Coefficient of restitution
e	Flapping hinge offset as a fraction of rotor radius
E_c	Kinetic energy of a cluster
E_R	Kinetic energy of a rebounding particle

$\mathbf{f}$	Forcing function in the particle equations of motion
$\mathbf{F}$	Total force acting on a particle
$\mathbf{F}_{\text{am}}$	Apparent mass force
$\mathbf{F}_b$	Buoyancy force
$\mathbf{F}_{\text{Basset}}$	Basset force
$\mathbf{F}_d$	Drag force from viscous shear effects on a stationary particle
$\mathbf{F}_D$	Fluid drag force on a suspended particle
$\mathbf{F}_g$	Gravitational force
$\mathbf{F}_i$	Inter-particle force
$\mathbf{F}_l$	Lift force from viscous shear effects on a stationary particle
$\mathbf{F}_L$	Lift force on a suspended particle
$\mathbf{F}_m$	Force produced by moments
$\mathbf{F}_{\Delta P}$	Lift force from unsteady pressure on a stationary particle
g	Acceleration under gravity
h	Perpendicular distance between a vortex element and an evaluation point
h	Rotor height (of the rotor plane) above the ground
h	Time step size
$\hat{i}$, $\hat{k}$	Unit vectors along x and z directions, repectively
I	Influence coefficient matrix
I_B	Influence coefficient matrix for the bound circulation
I_{NW}	Influence coefficient matrix for the near-wake circulation

$\mathbf{J}$	Jacobian matrix
k	Von Kármán's constant (= 0.4)
k_r	Roughness height
m	Mass of a particle
m_n	Mass of the nth ejected particle
m_R	Mass of a rebounding particle
m_0	Mass of an impacting particle
M	Aerodynamic moment
M_A	Aerodynamic moment about the flapping hinge
M_I'	Inertial moment about the flapping hinge
n	Index used for time steps
n	Index of particles ejected by bombardment
N	Total number of particles in the brownout simulation
N_b	Number of blades
N_b	Number of particles ejected from the bed by bombardment
N_d	Number of particles mobilized by the direct entrainment mechanism
N_I	Initial number of particles on the bed
N_s	Number of spanwise blade segments
N_r	Number of rotors
N_v	Total number of vortex elements in the flow field
N_2	Particles associated with a cluster in the Gaussian clustering method
P_s	Plastic pressure

P_∞	Free-stream static pressure
P	Rotor power
P_i	Rotor induced power
P_0	Rotor profile power
Q	Rotor torque
r	Non-dimensional blade spanwise distance
r	Radial distance of a point on the ground measured from rotor shaft axis
$\mathbf{r}$	Position vector of an evaluation point relative to a vortex filament
r_c	Core radius of a vortex filament
r_{c_0}	Initial core radius of a vortex filament
r_d	Moment arm of drag force F_d about the point of particle mobility
r_i	Moment arm of interparticle force F_i about the point of particle mobility
r_l	Moment arm of lift force F_l about the point of particle mobility
R	Rotor radius
R_{exact}	Radius of the exact path traversed by a particle around a vortex
Re_p	Particle Reynolds number, $= \dfrac{\left\lvert \mathbf{V}_p - \mathbf{V} \right\rvert d_p}{\nu}$
Re_ν	Vortex Reynolds number, $= \Gamma_\nu / \nu$
S	Cross-sectional area of a vortex filament
t	Time
T	Rotor thrust
T_{req}	Target rotor thrust

$u_\star$	Friction velocity, $= \sqrt{\tau/\rho}$
$u_{\star_t}$	Threshold friction velocity
U_s	Characteristic flow velocity
v_h	Hover inflow velocity, $= \sqrt{T/2\rho A}$
v_i	Inflow velocity
V_{px}, V_{py}, V_{pz}	Components of particle velocity along the x, y and z directions, respectively
V_{tip}	Rotor hover tip speed, $= \Omega R$
V_x, V_y, V_z	Components of flow velocity along the x, y and z directions, respectively
V_θ	Tangential or swirl velocity
$\mathbf{V}$	Flow velocity
$\mathbf{V}_{\text{B}}$	Velocity induced by the bound vortices
$\mathbf{V}_{\text{FW}}$	Velocity induced by the free-wake trailers
$\mathbf{V}_i$	Total velocity at a control point
$\mathbf{V}_{\text{ind}}$	Total induced velocity at a Lagrangian marker
$\mathbf{V}_{\text{man}}$	Velocity induced by maneuvering effects
$\mathbf{V}_n$	Velocity of the nth ejected particle
$\mathbf{V}_{\text{NW}}$	Velocity induced by the near-wake vortices
$\mathbf{V}_p$	Particle velocity
$\mathbf{V}_R$	Velocity of a rebounding particle
$\mathbf{V}_v$	Convection velocity of a vortex filament
$\mathbf{V}_0$	Velocity of an impacting particle

$\mathbf{V}_\infty$	Free-stream velocity
x, y, z	Cartesian coordinates along longitudinal, lateral and vertical directions, respectively
x_v, y_v	Coordinates of a two-dimensional vortex along the x and y directions, respectively
$\mathbf{X}_p$	Particle position
$\bar{\mathbf{X}}_p$	Particle position at the predictor step

Greek Symbols

α	Lamb-Oseen's constant, $= 1.25643$
α	Angle of attack
α_0	Incident angle of an impacting particle
β	Blade flapping angle
β_c	Constant of proportionality in the interparticle force equations
β_p	Blade precone angle
β_{1c}	Longitudinal flapping angle
β_{1s}	Lateral flapping angle
Γ	Strength of a vortex filament
Γ_b	Strength of a bound vortex
Γ_t	Strength of a near-wake trailer
Γ_v	Strength of a finite length filament
δ	Boundary layer thickness
δ	Turbulent or eddy viscosity parameter

Δl	Change in the length of a vortex filament
ΔP	Unsteady pressure difference relative to ambient, $= P - P_\infty$
ΔP_t	Threshold pressure difference
Δr_c	Change in the core radius of a vortex filament
Δt	Time step size
$\Delta\zeta$	Discretization along the spatial direction
$\Delta\psi$	Discretization along the azimuthal or temporal direction
ε	Strain rate, $= \Delta l / l$
$\varepsilon_{\mathbf{v}_{\max}}$	Maximum absolute error in induced velocity
$\varepsilon_{\mathbf{x}_{\max}}$	Maximum absolute error in particle position
ζ	Wake age
θ, ϕ, ρ	Elevation, eccentricity, and distance in a spherical coordinate system, respectively
θ_0	Collective pitch angle
θ_{1c}	Lateral cyclic pitch angle
θ_{1s}	Longitudinal cyclic pitch angle
θ_{tw}	Linear blade twist rate
ϑ	Volume of crater formed on the sediment bed
λ	Eigenvalue of an ODE
λ	Non-dimensional inflow velocity, $= v_i / \Omega R$
μ	Rotor advance ratio
μ_B	Mean vector for the Gaussian distribution

μ_c	Mean vector for clustering
$\mu^\star$	Normalized advance ratio, $= \dfrac{\mu}{\sqrt{C_T/2}}$
ν	Kinematic viscosity coefficient
ν_β	Non-dimensional rotating blade flap frequency, $= \omega_\beta/\Omega$
ρ	Flow density
ρ_p	Particle density
σ	Rotor solidity, $= N_b c/\pi R$
σ	Root of the characteristic equation
Σ_B	Covariance matrix for the Gaussian distribution
Σ_c	Covariance matrix for clustering
τ	Shear stress
τ_{s_t}	Threshold shear stress
τ_p	Particle response time
τ_{p_s}	Particle response time in Stokes' flow
ϕ	Sectional inflow angle
ϕ	Threshold friction parameter, $= \sqrt{\dfrac{\rho_p}{\rho} g d_p}$
ϕ	Velocity potential
ψ	Azimuth angle
$\vec{\omega}$	Vorticity vector
ω_β	Rotating blade flapping frequency
Ω	Rotational angular speed of the rotor

Superscripts

$\overset{\star}{()}$	Azimuthal derivative, $= \partial()/\partial\psi = \Omega\partial()/\partial t$

Subscripts

x, y, z	Components of vectors along the longitudinal, lateral and vertical directions, respectively

List of Abbreviations

AB2	2^{nd}-order Adams-Bashforth
BBO	Basset-Boussinesq-Oseen
BDF2	Two-point backward difference
BDF3	Three-point backward difference
CFD	Computational Fluid Dynamics
CVC	Constant Vorticity Contour
DNS	Direct Numerical Simulation
EI	Euler Implicit
EOM	Equations of Motion
EI-BDF2	Multi-step EI and BDF2 scheme
EI-BDF2-E	Multi-step EI and BDF2 scheme with particle position extrapolation
EI-BDF3-E	Multi-step EI and BDF3 scheme with particle position extrapolation
FMM	Fast Multipole Methods

FOV	Field of View
FVM	Free-Vortex Method
GPU	Graphic Processing Units
HDD	Head-Down Display
HMD	Helmet-Mounted Display
HUD	Head-Up display
IGE	In-Ground-Effect
MTF	Modulation Transfer Function
ODE	Ordinary Differential Equation
OGE	Out-of-Ground-Effect
OΔE	Ordinary Difference Equation
PC2B	Predictor-Corrector 2^{nd}-order Backward difference
PED	Particle Entrainment and Dispersion
PIV	Particle Image Velocimetry
PTV	Particle Tracking Velocimetry
RANS	Reynolds Averaged Navier–Stokes
ROI	Region of Interest
TPP	Tip-Path-Plane
TR	Trapezoidal
TR-BDF2-E	Multi-step TR and BDF2 scheme with particle position extrapolation
TR-BDF3-E	Multi-step TR and BDF3 scheme with particle position extrapolation
VTM	Vorticity Transport Method

WAF	Weighted Average Flux

Chapter 1

Introduction

1.1 The Problem of Brownout

Brownout is a phenomenon that occurs when a rotorcraft lands on or takes off from ground surfaces covered with loose material such as sand or dust. By means of a series of complex fluid dynamic uplift and mobilization mechanisms, the rotor wake stirs up an intense dust cloud that can quickly engulf the helicopter. A photograph illustrating an example of a helicopter encountering brownout conditions during a landing in the desert is shown in Fig. 1.1, where the dust cloud has started to from below the helicopter. The corresponding phenomenon under snowy conditions is often known as whiteout.

Under brownout conditions, the developing dust cloud can build into sufficient concentrations such that it can degrade pilot's visibility of the landing or takeoff zone. Pilots usually use visual cues from the ground such as the horizon, a nearby structure (e.g., a building), blades of grass, etc., to help determine the spatial orientation and motion of the aircraft. The developing dust cloud can degrade or completely eliminate these optical cues. The relative motion between the developing dust clouds and the decelerating helicopter (while landing) can also produce apparent motion effects (i.e., vection illusions), which can lead to the pilot experiencing spatial disorientation. These spurious sensory cues, combined with pilot's loss of visual reference of the landing zone, can lead to serious safety of flight issues. In some cases, pilots may lose control of the helicopter, or

Figure 1.1: A helicopter encountering brownout conditions during a landing in the desert. (Photo courtesy of Optical Air Data Systems LLC.)

may drift into other obstacles, which can lead to serious mishaps. In fact, encounters with brownout conditions are the leading cause of human factor-related mishaps during military rotorcraft operations (Ref. 1), and civilian helicopters have also suffered from the problem (Ref. 2), especially during MEDEVAC operations.

The suspended sediment particles in a brownout cloud can also lead to other serious consequences, such as rapid abrasion of rotor blades, engine wear, and various mechanical problems and maintenance issues. Typically, the leading edges of the rotor blades are covered with metallic strips (composed of stainless steel or alloys of titanium) to prevent abrasion. These metallic strips can, however, become quickly eroded by the impact of the dust particles (Ref. 3); see Fig. 1.2. The erosion of the metallic material may even lead to visible sparks (Ref. 3). The consequences are significant shortening of the life of the rotor blades. Such sparks can also be caused by a triboluminescent phenomenon as the

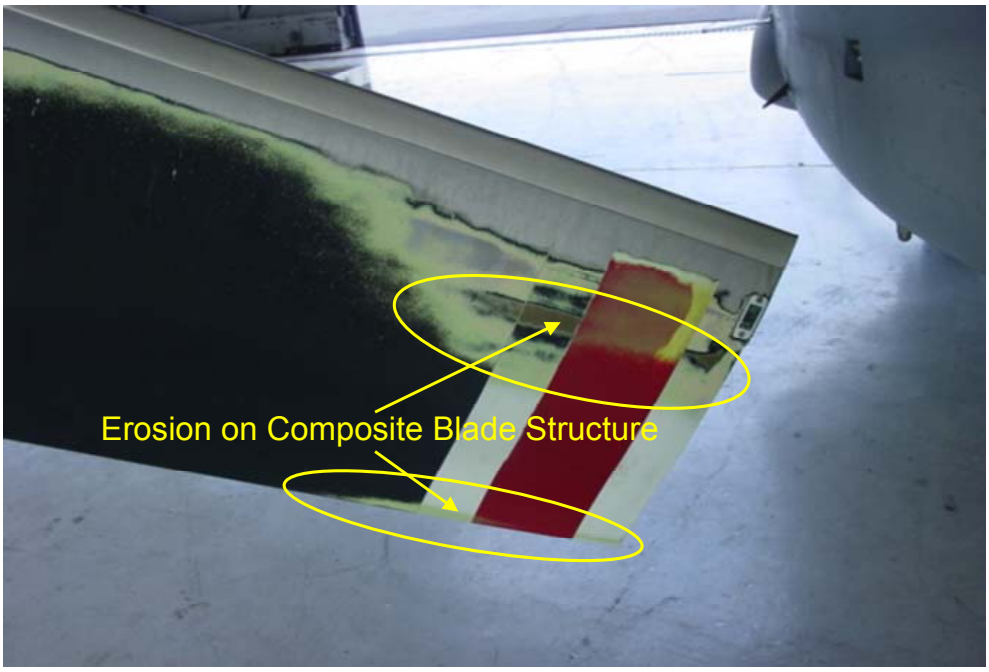

Figure 1.2: Erosion damage on a rotor blade from encounters with brownout (Ref. 3).

crystalline structure of certain minerals become deformed and sheared by impacts with the rotating blades.

An improved understanding of the factors that influence the occurrence of brownout, and an informed exploration of strategies to mitigate it, are of great practical importance for safe and cost-effective rotorcraft operations. However, a permanent solution to the mitigation of brownout poses many challenges. Technical efforts are underway to develop sensor technology to help the pilot to "see-through" the dust clouds (e.g., Refs. 4–6). Most of these efforts focus on projecting either flight parameter values or sensory displays on either a Head-Up display (HUD), Head-Down Display (HDD) or Helmet-Mounted Display (HMD). The most recent work on the development of tactical displays (Ref. 4) focuses on providing pilots with visual references of the landing zone, as well as the crucial "feeling"

of the speed and altitude of the helicopter. Such systems have been reasonably effective in improving safety of flight when they are combined with certain operational tactics involving flight path management. However, the number of operational mishaps with rotorcraft remains unacceptably high, and brownout related maintenance issues continue to reduce mission readiness rates and drive up operational costs.

Another operational tactic widely adopted by pilots is the use of specialized strategies during landing and takeoff maneuvers to minimize the effects of brownout (Ref. 7). One such example is flying faster near the ground to outpace the evolving dust cloud. Another possible option is to minimize the time in flare during landing, thereby potentially stirring up less dust. Such landing strategies have served to operationally mitigate brownout, but only to a limited extent because they depend upon the weight of the vehicle, density altitude, particle characteristics, and they may be very risky with potentially serious implications on flight operations.

The root cause of the brownout problem is the dual-phase dusty flow field created by a rotorcraft operating close to the sediment bed. It is known through videographic observations and preliminary calculations (Ref. 8) that different rotorcraft (i.e., in terms of number of rotors that they use, the disk loading, number of blades, etc.) can produce different types of brownout clouds. These differences in the dust clouds encompass their spatial extent, concentration, and rapidity of development. For example, some landing helicopters appear to produce radially expanding toroidal-type brownout clouds with little in the way of vertical entrainment, leaving zones of good visibility for the pilot within the cloud. Other helicopters can produce large, dome-shaped brownout clouds that engulf the entire helicopter, often with significant recirculation of the dust back through

the rotor disk. The tendency to form recirculating flows can be accompanied by vertical bombardment of the sediment particles back onto the ground at relatively high velocity, stirring up more dust through a cascading series of bombardment ejections. Even with the same rotorcraft performing substantially the same landing or takeoff maneuvers, different brownout conditions can be expected based on the characteristics of surface sediment, such as the type and size of the particles, their compactness, moisture content, etc. Such observations show that understanding the processes involved in the formation of brownout clouds is critical to attempt to mitigate this problem. In this respect, computational modeling of brownout clouds can offer a very effective and practical tool to study the problem, as well as to understand the most effective strategies for its mitigation.

1.2 Physics of Brownout

Clearly, a fundamental understanding of the factors affecting the formation of a brownout dust cloud is a prerequisite for its mitigation. This understanding can be achieved by addressing the root causes of brownout, which (as will be shown) have their source in phenomena associated with the multiphase fluid dynamics. Two phases of matter contribute to the problem of brownout: (a) *The carrier phase*, which in this case is the three-dimensional, unsteady flow field produced by a rotorcraft operating in ground effect (IGE), and (b) *The dispersed phase*, which comprises the nonuniform concentration of sediment particles that are lofted into the flow by the action of the rotor wake on the ground. This multiphase aspect of the problem drastically increases the complexity of measuring, understanding, and modeling brownout because the sediment and carrier fluid

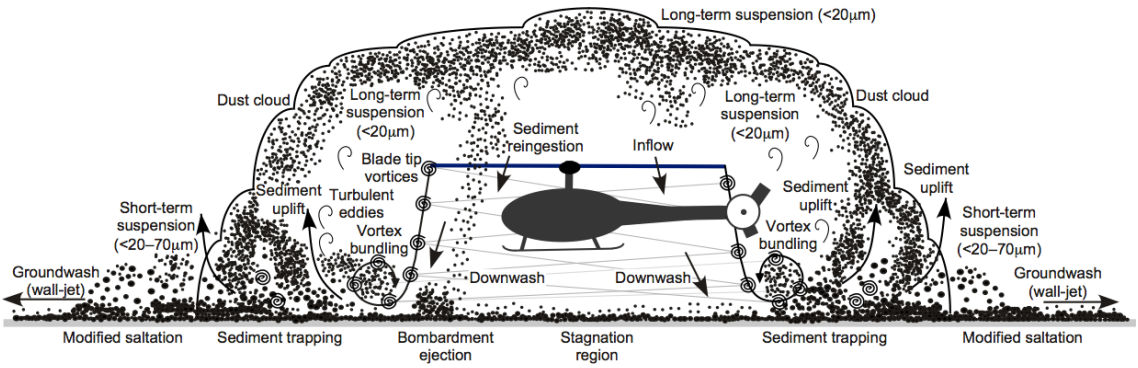

Figure 1.3: Schematic showing different modes of particle motion in the dust field generated by a rotor hovering IGE.

are intrinsically coupled, and will transfer momentum and energy to and from each other to a lesser or greater degree

A schematic of the general problem of brownout is shown in Fig. 1.3, which identifies some of the fluid mechanics and sedimentology processes that are involved. The combined downwash flow from the rotor and the proximity of the vortical rotor wake to the sediment bed induces an unsteady velocity field that, when sufficiently intense, causes the incipient motion of loose sediment particles from the bed. Depending on the vertical velocities near the bed, the sediment can settle back on to it, or it can be picked up and carried off into the flow around the rotor. Once entrained, these sediment particles move under the influence of the rotor flow field, and can interact with each other or with the bed, which results in the formation of a dynamically evolving brownout dust cloud.

1.2.1 Rotor Flows In Ground Effect

The flow field created by a rotor is greatly influenced by the presence of the ground below it. From a performance perspective, this problem has already been extensively

studied; see Refs. 9–15. It is known that the thrust of a hovering rotor IGE increases for a given power. Similarly, lower power is required for a rotor hovering IGE at the same thrust. This reduction in power is primarily induced in nature because the induced velocity of a rotor hovering IGE decrease significantly compared to that for a rotor hovering out of ground effect (OGE) at the same thrust. Profile power also reduces for IGE operations because rotor blades operate at reduced angles of attack to produce the same rotor thrust (Ref. 16).

From a brownout perspective, an understanding of the flow below the rotor in regions close to the ground is very important because this region directly affects the motion of the sediment and its entrainment into the overall flow near the rotor. The flow below a rotor hovering IGE is clearly very different from that found under OGE conditions, as shown in Figs. 1.4 and 1.5. In these flow visualization images, the flow is being seeded with smoke and is illuminated by a laser sheet in a radial plane. As the rotor blades pass through the imaging plane, helicoidal vortex filaments are trailed from the blade tips, which can be identified by seed voids in Figs. 1.4 and 1.5. Under OGE conditions (see Fig. 1.4), the vortex filaments undergo radial contraction closer to the plane of the rotor disk. Coherent seed voids close to the rotor plane show that these vortices have primarily laminar cores, devoid of small eddies and turbulence that are present in the surrounding area of the rotor flow. After about 2–3 rotor revolutions, the tip vortices start to diffuse under the influence of turbulence and viscosity, and instabilities in the wake further downstream become more apparent, in part because of pairing of adjacent turns of the helical vortices as they reach older wake ages.

Under IGE conditions (see Fig. 1.5), the wake below the hovering rotor initially

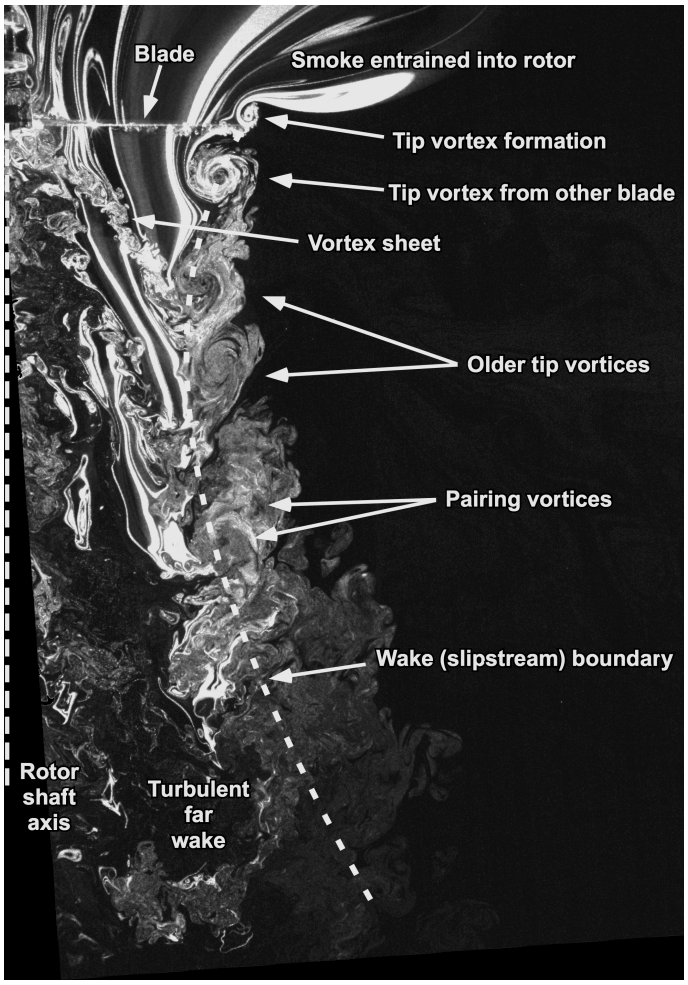

Figure 1.4: Flow visualization image of a 2-bladed rotor operating under out of ground effect conditions (Ref. 17).

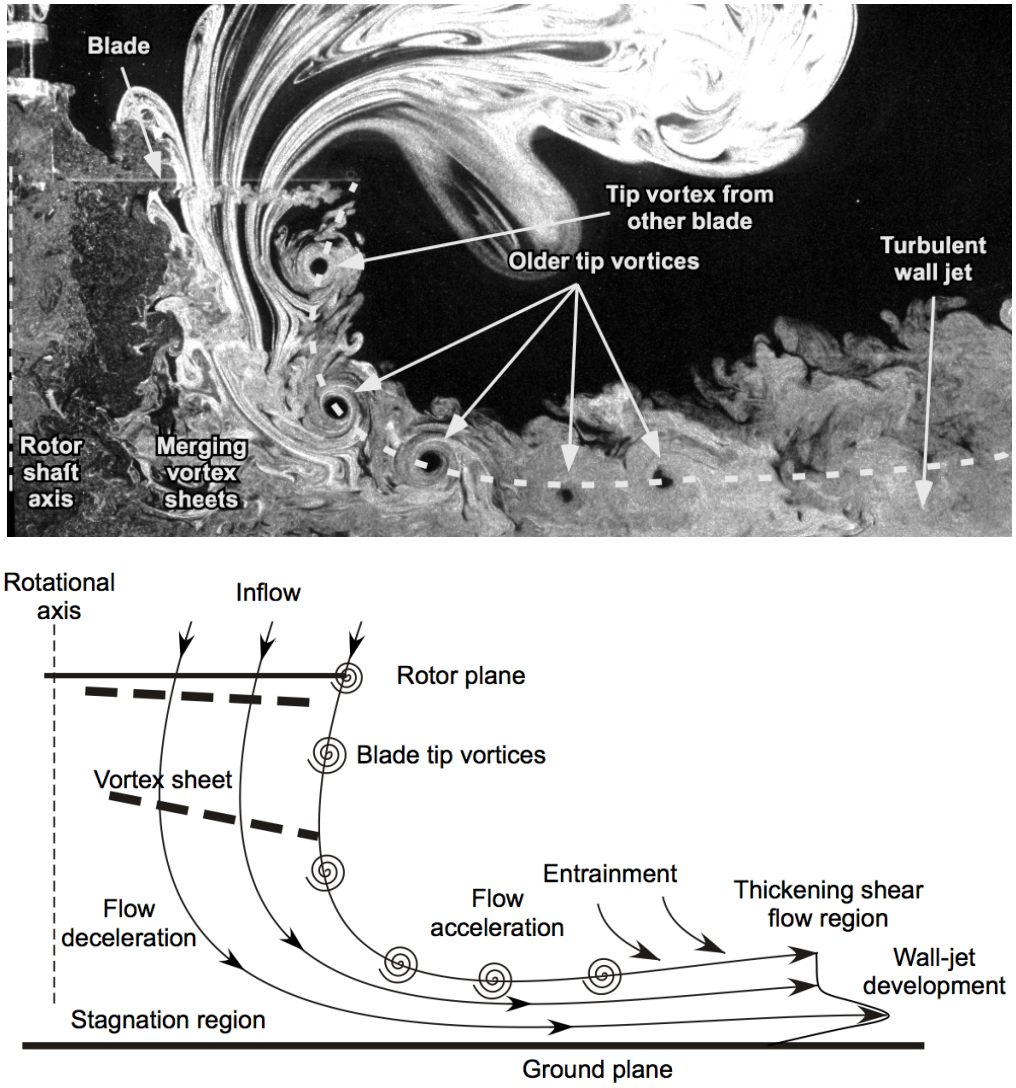

Figure 1.5: Flow visualization image of a 2-bladed rotor operating IGE near a ground plane (Ref. 17).

contracts below the rotor as for the OGE case, but then turns predominantly into a radial flow close to the ground, expanding outward almost parallel to the ground plane. The physics of the rotor flow IGE are explained in more detail in Refs. 17–20. In particular, the radial expansion of the rotor wake close to the ground results in the lengthwise stretching of the vortex filaments. This important mechanism reintensifies their vorticity and increases the swirl velocities, in effect countering their normal diffusive action and causing them to persist in the flow to much older wake ages (Ref. 19). This stretching phenomenon clearly must participate in the mobilization and uplift of sediment particles from the bed (Ref. 18).

A helicopter usually encounters brownout conditions during landing and takeoff operations, for which the flow field is even more complex when compared to that found under hover conditions. The transient changes in rotor height and velocity close to the ground can produce localized regions of the flow that affect sediment mobilization and uplift from the ground. Two such distinct regimes are "recirculation" at very low advance ratios, and the "ground vortex" region at higher advance ratios (Refs. 13 and 21). The advance ratios that define the extent of these regions can be expressed in terms of a normalized rotor advance ratio $\mu^\star = \frac{\mu}{\sqrt{C_T/2}}$. A helicopter approaching the ground in a landing maneuver first encounters the formation of a ground vortex, which is then followed by the recirculation region as the helicopter further decelerates (Ref. 22). Therefore, understanding and modeling of these flow regimes will be very important in the study of the formation of brownout clouds.

The recirculation regime is usually observed at low advance ratios, i.e., for $0.4 < \mu^\star < 0.7$. In this case, the wake recirculates through the upstream of the rotor disk with

significant unsteadiness and aperiodicity. This operating condition is particularly bad from the brownout perspective because it can result in the reingestion of many sediment particles through the front of the rotor disk, which can obstruct pilot's field of view (FOV). As the advance ratio of the helicopter increases further, the recirculation region weakens and the flow passes under the leading edge of the rotor disk, forming a distinct vortex called the "ground vortex." Curtiss et al. (Ref. 13) observed that the flow field in this region was relatively steady. As advance ratio increases further, the ground vortex becomes weaker and passes rearwards under the rotor, and ultimately disappears at higher advance ratios (Ref. 13). Experiments conducted by Nathan & Green (Ref. 21) also showed that the regions where the ground vortex and recirculation form will affect particle uplift.

1.2.2 Behavior of Sediment Particles

The rotor induced flow field is clearly the root cause of the mobilization and uplift of particles that form a brownout dust cloud. Therefore, a good understanding of the characteristics of the rotor wake is needed, as well as a knowledge of sediment transport physics. Sediment transport is a large research topic in itself, with two main activities being wind-driven particle transport (i.e., sediment motion by the wind or so-called aeolian flows) and hydrodynamic particle transport (i.e., sediment motion in coastal environments) or riverine flows. Sediment dynamics by the action of air is of the primary interest in the present problem, and has been discussed in detail in some of the classical works published on sedimentology, such as by Bagnold (Ref. 23) and Greeley and Iversen (Ref. 24).

Particle motion in the rotorcraft brownout problem can be influenced by various

factors that include rotor parameters (e.g., disk loading, blade loading, rotor design and tip shapes), helicopter configuration and interference from the fuselage, the flight path followed by the helicopter, the soil properties (e.g., soil texture, composition and strength), the atmospheric conditions (e.g., temperature), and land-surface characteristics (e.g., topology, moisture and aerodynamic roughness height). All of these factors may potentially contribute to the formation and intensity of the brownout dust clouds.

Typically, brownout dust clouds are comprised of a very large number of uplifted particles. Figure 1.6(a) shows characterization of brownout dust clouds in terms of concentrations of particles with sizes ranging from 1 μm to 1,000 μm. It is significant to note the very high concentrations of small-sized dust particles (diameters of the order of 1–10 μm), which if uplifted are those that tend to remain in suspension for extended periods, and are responsible for much of the visual obscuration effects produced inside the brownout cloud. Also of significance here, is the equivalent mass fraction of the dispersed phase (i.e., the particles present in the rotor flow) to the carrier phase (i.e., the rotor flow), as shown in Fig. 1.6(b). This figure shows that on an average, the mass fraction of the dispersed phase to the carrier phase in a brownout dust cloud is $<0.1\%$. This means that the brownout problem can probably be modeled as one-way coupled, at least away from the immediate area close to the ground. Such a simplification, if suitably justified, can reduce significantly the computational cost of modeling dust clouds.

It is important to characterize particles of different sizes using their more commonly referred-to names, which will also be used in the present work. Figure 1.7 shows the characterization of soil particles as given by the International Society of Soil Science. According to such classifications, the soil particles can be divided into four categories:

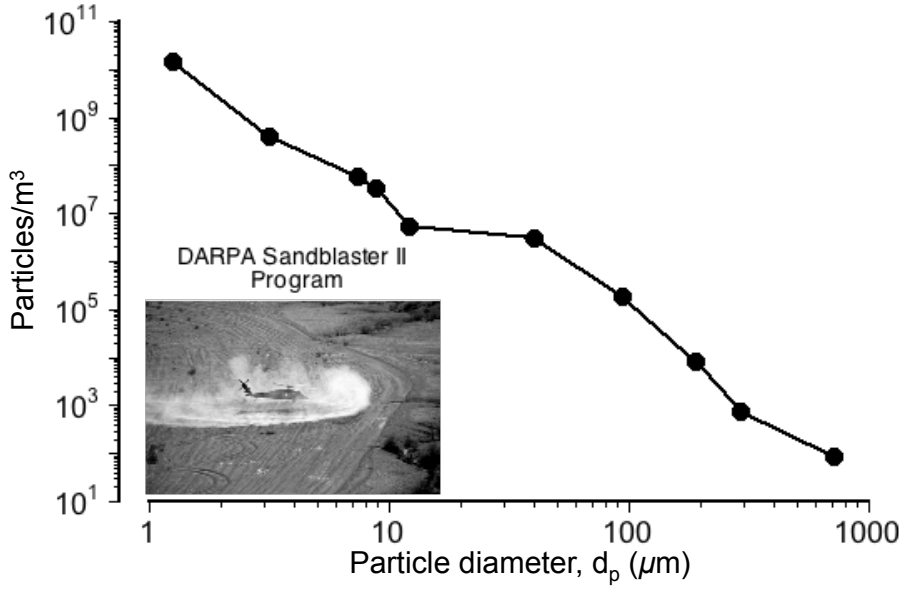

(a) Average particle concentration

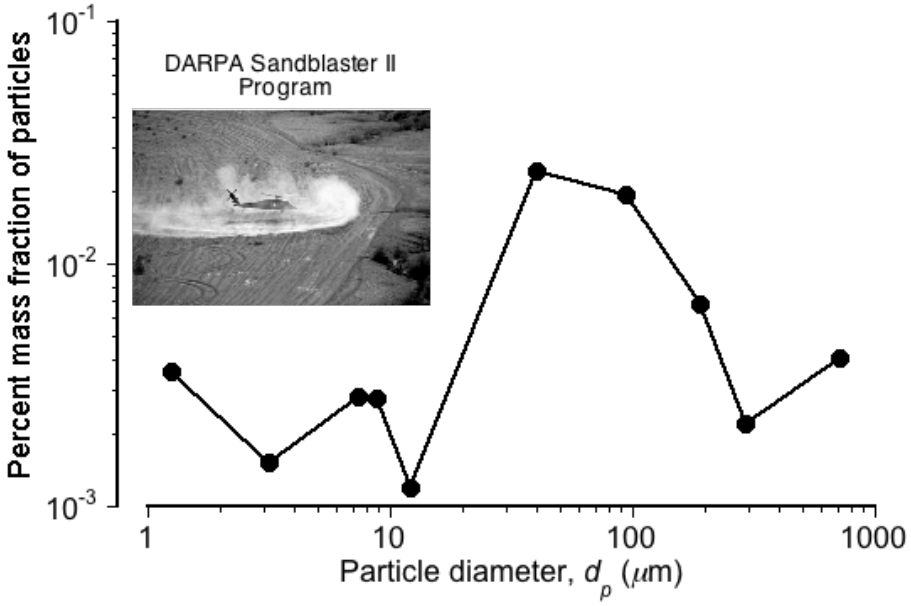

(b) Percentage of the mass density of particles to air

Figure 1.6: Concentration and percent mass density of particles of different diameters in a dust cloud (Refs. 5 and 6): (a) average particle concentration, i.e., number of particles per cubic meter, and (b) percentage of the mass fraction of the dispersed phase to the carrier phase.

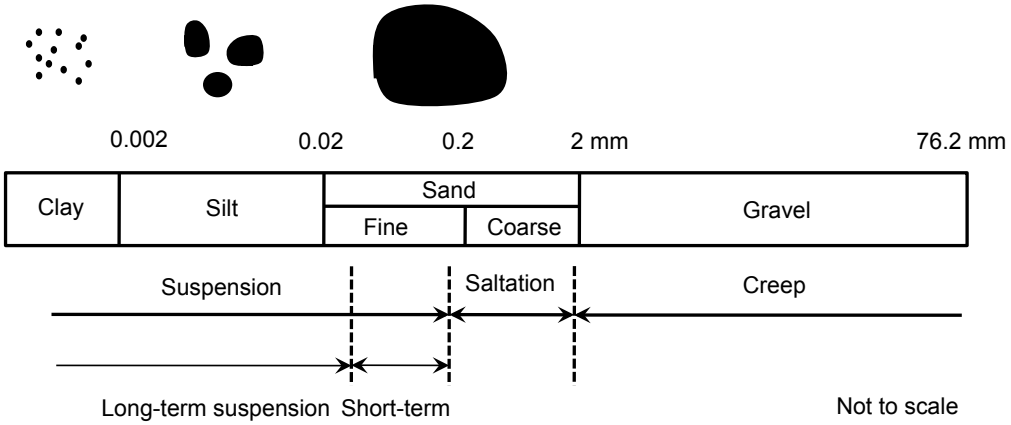

Figure 1.7: Characterization of particle size according to the International Society of Soil Science (Ref. 25).

(a) Gravel (2,000 μm $\leq d_p \leq$ 2 m), (b) Sand (63 μm $\leq d_p \leq$ 2,000 μm), (c) Silt (4 μm $\leq d_p \leq$ 63 μm), and (d) Clay ($d_p \leq$ 4 μm). Usually, silt and clay are referred to as dust, i.e., for $d_p \leq 63$ μm. This type of characterization shows that brownout clouds are usually comprised of sand and dust particles; see Fig. 1.6(a). However, because of the preponderance of small dust-like particles in brownout clouds, they are usually referred to as brownout dust clouds.

It is known that particle motion under the action of an external or carrier flow comprises three main processes: (a) *Mobilization*, which is where the particles just start to become mobilized by the external flow, (b) *Entrainment*, which involves processes responsible for pickup of particles from the bed under the influence of the flow, and (c) *Transport*, which governs the trajectory followed by a particle after it is entrained into the flow field. These processes have been studied in rotor flows as reported in Refs. 17 and 18. Figure 1.8 shows a more detailed schematic of the primary mobilization and transport mechanisms of particles found below a rotor.

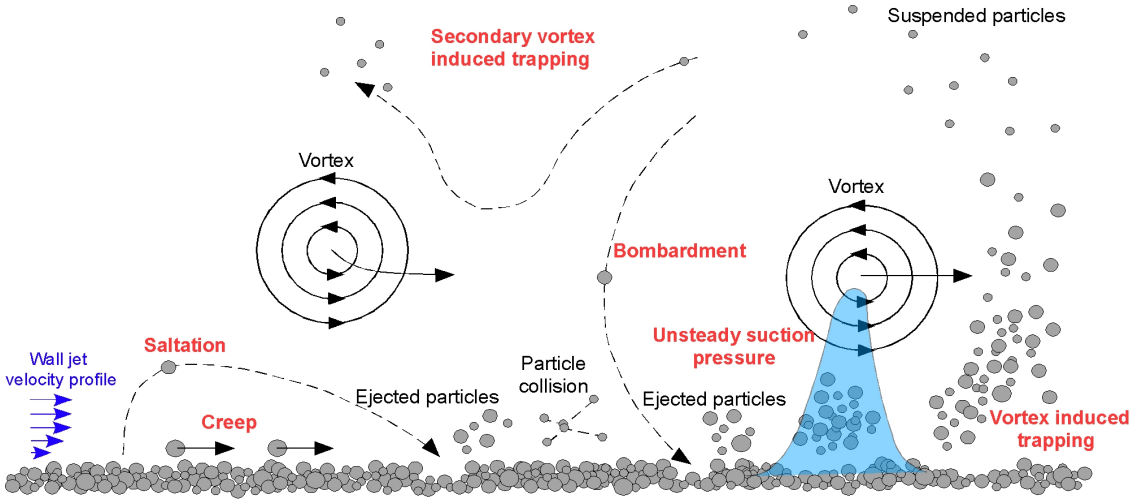

Figure 1.8: A schematic showing important particle mobilization and transport processes in rotor flows (Ref. 17).

The initial mobilization and entrainment of the particles from the bed is governed by the forces acting on them when they are stationary. These forces include aerodynamic (from the shearing action of the boundary layer and possibly also from unsteady pressure effects), gravitational effects, and inter-particle forces. Particles can be mobilized (and eventually entrained) when these aerodynamic forces exceed the gravitational and inter-particle forces; this form of entrainment is usually known as direct aerodynamic entrainment. In rotor flows, the vortical flow structures on the ground can also significantly affect the velocity and pressure fields, as well as the shear stress distributions at the ground, which can produce significant sediment mobilization and uplift (Refs. 26 and 27).

Another mechanism of sediment entrainment is through bombardment ejections (Refs. 17 and 25), in which previously suspended sediment particles in the regions of strong vortical flows can impact the bed with higher momentum, and so eject many more

particles into the flow. The dust mobilization studies conducted in Refs. 28–30 have shown that the process of bombardment ejection is one of the important mechanisms responsible for the formation of aeolian dust clouds. In fact, this mechanism has also been observed in the development of actual brownout dust clouds (e.g., Fig. 1.9), and has also been measured and quantified in laboratory experiments (Refs. 17 and 18). In this case, suspended particles can be recirculated in the rotor wake flow and bombarded back onto the underlying sediment bed, ejecting copious quantities of more particles into the flow from the resulting impacts (Refs. 17 and 28).

For example, the sediment particles that are initially mobilized by the action of the wake below the rotor, as shown in Fig. 1.9(a) and 1.9(b), become suspended, uplifted, and then recirculated. The resulting bombardment of these suspended particles back onto the bed below the rotor at relatively high velocities, quickly mobilizing large volumes of more particles, as shown in Figs. 1.9(b) to 1.9(e). In this regard, it is mostly the strong vortical flows generated by the rotor that create the significant upwash and downwash regions that trap and recirculate the particles, but recirculation of flow through the rotor disk can also occur and is a major contributor to the brownout problem; see also Fig. 1.3.

Once a particle is mobilized by the flow, the resulting forces acting on the particle govern its motion. In detail, the initial motion of the particles can be categorized as: (a) creep, (b) saltation, and (c) suspension; see Figs. 1.3 and 1.8. "Creep" is the rolling motion of particles along the sediment bed and occurs because the forces acting in the vertical direction are not large enough to uplift them (e.g., Ref. 17). Either large-sized particles, or particles in the regions of the bed where vertical velocities are small usually experience this type of particle motion. "Saltation" is the bouncing and jumping motion

Figure 1.9: Snapshots showing the development of a brownout dust cloud (Source: Optical Air Data Systems).

of particles across a surface, the word saltation coming from the Latin root "salto". Typically, saltation is the principal mechanism of transport of sand particles in unidirectional flows. However, for rotor flows a modified form of saltation is usually observed, in which the presence of vortical flows modify the trajectories followed by these particles compared to that obtained with unidirectional flows. Finally, "suspension" is the motion of dust particles, in which these particles remain in the air for longer durations because of their very small terminal velocities.

Based on observations of particle motion in unidirectional flows, Shao (Ref. 25) mentioned that "suspension" can be further be divided into long- and short-term suspension. In long-term suspension, dust particles of very small sizes (usually, $d_p \leq 20\,\mu$m) can remain suspended for very long durations (usually many hours or days), and in short-term suspension, particles of size $20\,\mu\text{m} \leq d_p \leq 70\,\mu$m, can remain suspended for hours (see Fig. 1.7). Notice, that these definitions were developed for simpler, unidirectional aeolian flows, and the particle size range for each mode of motion may ultimately be different for rotor flows.

1.3 Survey of Related Previous Work

Brownout is a multidisciplinary problem, which involves at a minimum, fluid dynamics (i.e., rotor flow IGE), particle dynamics (i.e., particle mobilization and transport), and flight mechanics (i.e., handling qualities and visual perception). From the perspective of the present work, the two primary areas of interest are the fluid dynamics and sedimentology aspects of brownout. The present section discusses the previous work performed

in these areas that have attempted to better understand aspects of the brownout problem.

The characteristics of rotor IGE (without dust) has been extensively studied, but mainly from a standpoint of rotor performance. Recently, several laboratory experiments (Refs. 17–19, 21) have been undertaken to study the rotor flow field close to the ground by using small-scale rotor systems. A series of computational techniques, ranging from RANS solutions of the Navier-Stokes equations (Refs. 31 and 32) to free-vortex methods (FVM) (Refs. 33 and 34), have also been used to model the flow IGE. While reasonably good results have been obtained, quantitative validation of these methods has met with mixed levels of success.

The dual-phase aspect of the brownout problem has been studied much less. Work conducted in the field of sedimentology (Refs. 23 and 24) to study sediment particle dynamics is based on simpler flows, e.g., simple jet-type flows or channel flows, which are very different from the more complex vorticity-laden rotor flows. Recently, field tests (Refs. 5, 6, 35) have been conducted to characterize the dust clouds produced by different helicopters. Recent laboratory studies of rotors operating over mobile sediment beds using dual-phase particle image velocimetry (PIV) techniques have also started to expose the more intricate details of the dual-phase flows below and around a rotor (Refs. 17 and 18). Using the insight gained from these experiments, several computational models (Refs. 22, 36–40) have been developed in an attempt to predict brownout clouds under more general conditions, and also to explore strategies for brownout mitigation.

The main focus of the present work was to develop a much more comprehensive and complete brownout dust cloud simulation methodology, using findings from field tests, experiments, and classical sedimentology. All of these different aspects of the brownout

problem are discussed in thefollowing section, which is classified into: (a) brownout field tests, (b) laboratory experiments (to study the single- and dual-phase aspects of the problem), (c) computational methods to study the single- and dual-phase aspects of the problem, (d) related work from the classical field of sedimentology, and (e) brownout mitigation studies.

1.3.1 Measurements of Brownout in Field Tests

Observations and measurements of brownout dust clouds that are generated by actual rotorcraft operating in desert-like conditions are important so as to better characterize and understand their formation, as well as to explore potential sensitivities to different rotorcraft configurations and rotor parameters. Such measurements, if they can be successfully made, can be very useful for validating brownout simulation methodologies.

Rodgers (Ref. 41) conducted field tests to measure the concentration of particles in the dust clouds generated by single rotor and tandem rotor helicopters (and at different disk loadings) as a function of the type of soil and hover height above the ground. The concentrations of sediment particles were recorded using 25 samplers, which were attached to the fuselage of the helicopter. The data were sampled every 4 minutes. It was found that the concentration of dust was the lowest below the rotor hub, and for the tandem helicopter it was the highest in the regions of rotor overlap. Also, the maximum size of the particles decreased with an increase in the rotor height above the ground. It was further found that the dust concentration increased significantly (by a factor of three) during landing and takeoff maneuvers versus that obtained in a steady hover.

Brownout field tests have been conducted under DARPA's "Sandblaster" program at Yuma Proving Grounds (Refs. 5 and 6). The goal of these field tests was to characterize the brownout dust clouds generated by various helicopters during a hover-taxi maneuver when flown at different heights above the ground; one helicopter was also tested during landing and takeoff maneuvers. The primary measurements were particle concentrations and particle size distributions in the brownout clouds. The data obtained in these tests were sampled in containers (bins) over a time period of 2 minutes. Again, the results obtained showed that a brownout dust cloud is primarily comprised of small-sized dust particles (see Fig. 1.6(a)), the larger particles quickly falling back to the ground. It was found that higher dust cloud densities are associated with helicopters that operate at higher disk loadings, and so create higher average flow velocities closer to the ground. Furthermore, the measurements showed that the concentration of sand-sized particles (i.e., the larger particles) in a brownout cloud was affected by the size of the airframe of the helicopter.

Another field test was conducted by Gillies et al. (Ref. 35) to measure the dust emissions generated by a low flying helicopter at different operating conditions above undisturbed and previously disturbed desert surfaces. These measurements showed that the dust emissions decreased with an increase in the forward airspeed of the aircraft for two reasons: (a) the shear stresses on the ground from the wake flow decreases with an increase in airspeed, and (b) the residence time of the aircraft over any region decreases with an increase in its airspeed, which reduces the time of interaction of helicopter downwash with the surface. The measurements made over different surfaces also showed that disturbed surfaces produced approximately an order of magnitude greater dust emissions than the undisturbed surfaces.

While the field tests (Refs. 5, 6, 35, 41) measured the average dust concentration of the sediment particles at different locations around the helicopters, such data cannot be used for validating the mathematical models that are being developed to simulate brownout clouds. Although the needed measurements are not yet available, the first attempt to better quantify the detailed structure of the brownout dust clouds was made by Wong and Tanner (Ref. 42) and then by Tanner (Ref. 43). A photogrammetry technique was used in which photographs of the dust clouds were taken using several synchronous cameras, and then analyzed using triangulation methods to find the coordinates of different features on the cloud. Wong & Tanner (Ref. 42) measured the location, size and average convective velocity of the dust cloud, along with the characteristics of defined structures within the cloud. These measurements have been used to compare the dust clouds predicted by the present methodology. The challenge here, however, was that insufficient data was measured to fully validate the approach. For example, the actual weight of the helicopter during the tests, the blade control angles, and the instantaneous wind velocities, were not measured.

1.3.2 Single-Phase and Dual-Phase Laboratory Experiments

While controlled tests with rotorcraft operating in desert environments have given some insight into the brownout problem, it remains difficult from field tests alone to identify all underlying mechanisms that are responsible for the development of such dust clouds. Challenges in better understanding the physics of brownout include the need to expose the detailed fluid dynamic processes of sediment lift-off from the underlying

bed. Such aspects of the brownout problem have been recently studied in laboratory experiments.

The earliest efforts to understand rotor aerodynamics IGE operations quantified the effects of the ground on rotor performance (Refs. 9–15). The changes to the rotor wake geometry in the presence of the ground were studied by using different flow visualization techniques. Taylor (Ref. 44) conducted flow visualization experiments using the balsa-dust technique to qualitatively study the flow patterns IGE produced by both single and coaxial rotor systems. Curtiss et al. (Ref. 13) conducted an experimental study to investigate the aerodynamic characteristics of an isolated rotor IGE at low advance ratios. This study included flow visualization of "recirculation" and "ground vortex" regimes at low advance ratios at different rotor heights above the ground. It was found that the flow field associated with the recirculation regime was unsteady, and that associated with the ground vortex regime was steady. It was further shown that the strength of the ground vortex was about an order of magnitude larger than the individual tip vortices. Later, Light (Ref. 14) conducted flow visualization by using wide-field shadowgraph method of rotor tip vortices produced by a hovering rotor IGE.

Nathan and Green (Ref. 21) studied the single- and dual- phase flow fields created by a small-scale rotor IGE for a range of rotor heights above the ground and at low advance ratios. The single-phase experiments were conducted using both two-dimensional PIV (allows for measurement of two velocity components), and stereoscopic PIV (allows for measurements of all the three velocity components). Investigation of the flow field ahead of the rotor at different flow speeds confirmed the formation of recirculation region at low forward speeds, and the formation of the ground vortex at somewhat higher for-

ward speeds. This work, however, did not examine the flow field in the boundary layer region. The dual-phase flow visualization study was conducted using fine talcum powder, and it was observed that the dust particles could accumulate in the regions of high vorticity ahead of the rotor disk near the ground.

Lee et al. (Ref. 19) conducted flow visualization and phase-resolved particle image velocimetry (PIV) experiments on a small-scale rotor hovering at various heights above a ground plane. Time-averaged and phase-averaged measurements of the velocity profile in the boundary layer region were made. The significance of the processes of vortex diffusion, vortex straining, and turbulence generation was studied. Filament strain was shown to increase the swirl velocities in the vortex flow, which resulted in a reintensification of vorticity within their cores. When the rotor was higher above the ground, the effects of diffusion dominated over filament straining effects. However, further into ground effect, the effects of straining dominated over diffusion. It was found that straining effects reached a maximum when the rotor hovered at an intermediate height above the ground.

The first more detailed study of the time varying single-phase and dual-phase flows generated by a rotor hovering IGE was conducted by Johnson et al. (Ref. 18). These experiments were conducted on a small-scale rotor using time-resolved flow visualization and PIV. The single-phase results showed the unsteady and aperiodic nature of the flow field on the ground, which was primarily a result of pairing and merging of adjacent turns of the blade tip vortices. These processes increased the induced velocities (and shear stresses) on the ground, and played a significant role in the initial mobilization and uplift of particles from the bed. Measurements of the flow velocity were made in the boundary layer region, which showed the presence of a separation bubble just downstream of the

vortex flow on the ground. The processes of saltation, saltation bombardment, reingestion bombardment, and vortex induced trapping (because of high vertical velocities induced on the particles in the vicinity of a vortex) were observed.

Milluzzo et al. (Ref. 20) measured the evolution of a rotor wake IGE for rotors with different blade tip shapes (rectangular, swept, BERP-like, and slotted-tip). The goal was to quantify the local flow near the ground as it could potentially affect the mobilization of sediment and, ultimately, lead to the creation of brownout conditions. The core size and velocity profile of the tip vortices for each blade tip shape were measured, as well as the resultant velocities in the near-wall region. Also examined was the effect that each tip shape had on the velocity profiles along the ground, and how this affected the local boundary layer profile at progressively further downstream locations. One interesting outcome of this study was that the slotted-tip blade geometry was the most effective in diffusing the tip vortices, including when they approached the ground plane.

Extending the work of Johnson et al. (Ref. 18), Sydney et al. (Ref. 17) conducted further time-resolved flow visualization, PIV, and particle tracking velocimetry (PTV) experiments to study the flow fields produced by 1- and 2-bladed rotors operating IGE. A comparison of the rotor flow fields was conducted at the same rotor blade loading coefficient, C_T/σ. The analysis of the results from the 1- and 2-bladed rotor systems showed that the latter was more susceptible to the creation of aperiodicity in the flow, which was caused by vortex merging and pairing. This aperiodicity was also shown to be a significant factor influencing sediment uplift. The 2-bladed rotor system also changed significantly the bed topology by erosion effects, which altered the trajectories followed by the older tip vortices, and increased the susceptibility to producing vortex-vortex interactions,

thereby further increasing the aperiodicity in the flow. Several fundamental processes of sediment uplift and mobilization were identified: (a) creep, (b) modified saltation and saltation bombardment, (c) vortex induced trapping, (d) reingestion bombardment (local and global), and (e) secondary suspension. Although these mechanisms were shown to play an important role in the entrainment of sediment particles from the bed, modeling their effects still remains a significant challenge.

Haehnel & Dade (Ref. 45) conducted high-speed videography experiments to understand sediment dynamics near the ground under the action of an axisymmetric jet flow. Measurements of sediment bed profile were made to quantify the rate of erosion of the bed. It was found that the turbulent shear stresses on the surface can drive the mobilization of sediment particles.

Mulinti & Kiger (Ref. 46) and Geiser & Kiger (Ref. 47) studied sediment dynamics under the action of an impinging jet flow, a vortex ring, and a combination of both flows. These studies allowed a simplified analysis of the rotor flow by decomposing it into its constituent parts, i.e., vortical flow superimposed upon an axial jet-like flow. These studies used PIV and high-speed videography to characterize these flows as well as the resulting motion of the sediment particles. It was found that the interaction of the vortex ring with the ground can produce strong secondary vortical flows that can also influence particle motion.

1.3.3 Computational Modeling of Rotorcraft Brownout

The number of interdependent factors involved in the brownout problem suggests that computational modeling of the dust clouds can offer new physical insight into the fundamental parameters that influence the severity of the dust clouds. Such models have much value for the brownout problem not only for their potential predictive capability, but also for their ability to help understand the individual contributing mechanisms of sediment mobility and their overall significance to the brownout problem as a whole.

1.3.3.1 Models of Rotor Flows

The simulation of brownout clouds involves two main parts: (a) the simulation of the rotor flow IGE, and (b) the simulation of particle mobilization, uplift, and convection. A prerequisite for a brownout simulation is obviously to predict the rotor flow close to the ground.

Earlier modeling efforts have focused on developing theoretical and computational approaches for rotor performance IGE operation. Betz (Ref. 48) developed an analytical method to study the effect of ground on the performance of a lifting propeller, showing that the power required by the propeller decreased at heights lower than the propeller radius when its thrust was kept constant. Knight & Hefner (Ref. 11) developed a vortex-cylinder model to predict rotor performance IGE. This model was based on the method of images (Ref. 49). Experiments were also conducted with sub-scale rotor models to validate the theoretical analysis. Cheeseman and Bennett (Ref. 9) developed a theoretical method to relate thrust and power of rotors in and out of ground effect at different

operating heights and rotor tip speeds.

Several other methodologies have been developed to model the complex, unsteady, three-dimensional flow field produced by a rotor IGE operation. Kalra (Refs. 31 and 32) used a compressible, structured, overset Reynolds Averaged Navier-Stokes (RANS) solver, which was developed by Lakshminarayan and Baeder (Refs. 50 and 51). This formulation solves the compressible RANS equations using a pre-conditioned dual-time scheme in the diagonalized approximate factorization framework, as described by Buelow et al. (Ref. 52) and Pandya et al. (Ref. 53). The inviscid terms are computed using a third order MUSCL scheme utilizing Koren's limiter with Roe's flux differences splitting, and the viscous terms are computed using second order central differencing. The Spalart-Allmaras (Ref. 54) turbulence model was employed for closure. The rotor flow field generated using this method was validated against the experimental results of Lee et al. (Ref. 19), and showed good potential for modeling rotor flows IGE. Although this methodology can provide good results, the large computational expense with all RANS approaches makes it mostly impractical for modeling the two-phase brownout problem.

Another method, based on the solution of incompressible RANS equations, was developed by Rajagopalan (Ref. 55). This method uses a momentum-source representation of the rotor blades and modeled the time-averaged effects of the rotor flow field on structured meshes. A limitation of this approach is that it does not model the localized effects of the blade tip wake vortices, which are now known to play a critical role in the brownout problem.

Phillips & Brown (Refs. 22, 56, 57) used the Vorticity Transport Method (VTM) (Refs. 58 and 59) to solve for the rotor flow IGE. VTM is a finite-volume method that pre-

dicts the evolution of vorticity on structured grids by solving the incompressible Navier-Stokes equations in vorticity-velocity form. Because of this particular formulation, it addresses the primary deficiency of Eulerian approaches, i.e., numerical diffusion of vorticity in the computational domain. Time marching of the solution was performed using Toro's Weighted Average Flux (WAF) algorithm (Ref. 60). This algorithm allows for a tight control on the rate of dissipation of vorticity, allowing the method to retain the vortical structures in the flow field over many rotor revolutions.

Another approach for modeling rotors IGE operation is to use Lagrangian-based flow field solvers. One such method is the free-vortex analysis, which has been used extensively over many decades; see Leishman (Ref. 16) for a review. A constant vorticity contour formulation of the free-vortex wake model has been developed (Refs. 33, 40, 61), in which the vortex elements track the regions in the flow field with same circulation strengths. This method represents the rotor wake using full-span curved vortex filaments, which allows for coarser step resolutions without significant loss in accuracy. The rotor blades were modeled using a vortex lattice lifting surface model, and the airframe and the ground plane were modeled using a lifting surface/source-doublet panel model.

Bagai and Leishman (Refs. 62 and 63) developed a relaxation-based FVM for steady flight conditions. This is an iterative method, which assumed periodicity of the wake solution and, therefore, cannot be used for non-steady flight conditions. This methodology was later extended to a time-accurate approach by Bhagwat and Leishman (Refs. 64–68). In each case, a Weissinger-L blade model was used to obtain the strengths of the bound circulation on the rotor blades. The strength of the tip vortices was then obtained from the bound circulation on the blades. The wake was solved by using vortex

filaments, which were discretized using straight-line segments (Ref. 67). These straight-line segments were convected at the local flow velocities that were calculated using the Biot-Savart law. The convection of the free-vortex markers was conducted using a second-order, two-step backward, predictor-corrector, time-marching algorithm (Ref. 66), which used a 5-point central differencing in space, and a 2-point backward differencing in time. The effects of the viscous diffusion, turbulence, scaling, and stretching (Ref. 69) on the vortex core growth were considered for the evolution of the tip vortices by using a model based on the value of vortex Reynolds number (Ref. 70). This method was later used by Griffiths et al. (Ref. 34) to study the rotor wake in ground effect operation.

1.3.3.2 Models for Particle Motion

Ryerson et al. (Ref. 36) developed an Eulerian-based particle entrainment and dispersion (PED) model. In this methodology, the advection-diffusion equations were used to solve for the particle concentrations in space and time. Gravitational effects were modeled by using a terminal velocity approach. The changes in particle concentration were computed as a function of the velocity gradients in three-dimensions. An equilibrium boundary flux, as given by Pomeroy and Gray (Ref. 71) was used, which is based on the threshold friction velocity. The flow field in the ground effect was solved by using an Eulerian based inviscid, incompressible solver developed by Rajagopalan (Ref. 55), which as discussed previously, solves the RANS equations with momentum-source representation for the rotor blades. The friction velocity was computed by assuming a logarithmic profile close to the ground plane. However, this methodology (as previously

explained) cannot model the localized effects of the blade tip vortices that are now known to entrain dust particles into the rotor flow.

Haehnel et al. (Ref. 38) developed a brownout cloud simulation methodology by coupling the PED developed by Ryerson et al. (Ref. 36) with an unsteady incompressible flow solver (Refs. 37, 72, 73). A surface vorticity confinement method was used to preserve vorticity in the tip vortices. The friction velocity was calculated by assuming a logarithmic boundary layer profile close to the ground. Although modeling of the effects of the blade tip vortices was an improvement over Ryerson's approach (Ref. 36), the key assumptions remained the same. In this work, the important mechanism of bombardment ejections and particle-ground interactions were not modeled.

Phillips and Brown (Ref. 56) developed an Eulerian particle transport method, which was similar to that developed by Ryerson et al. (Ref. 36). In this formulation, the mass transport equations were used to analyze the dust convection problem in an Eulerian reference frame. This model was also based on the assumption that away from the ground the suspended particles remain in near-equilibrium under the action of the aerodynamic forces. Near the ground, a sublayer type of source model was used in which particles were entrained by the mechanism of saltation. The initiation of particle mobility was modeled by using an empirical flux model, as developed by White (Ref. 74), which uses the threshold friction velocity expression developed by Shao & Lu (Ref. 75). The resulting particle transport equations were mathematically similar to the vorticity transport equation, and the evolution of vorticity in the VTM (Refs. 58 and 59) was generalized to convect vorticity, as well as the particle density field.

A Lagrangian-based methodology to simulate the brownout problem was developed

by Wachspress et al. (Ref. 40). This methodology solved for the particle equations of motion in the Lagrangian frame, and was coupled with the constant vorticity contour (CVC) based FVM (Refs. 33, 40, 61) that was outlined previously. The entrainment of particles was based on a threshold friction velocity model, which was developed from Shao & Lu's model (Ref. 75). It was determined that the threshold velocity predicted by this model was too high for particles of smaller size, which are those that are predominantly present in a brownout cloud. Wachspress et al. (Ref. 40) made ad hoc modifications to the empirical constants in the model developed by Shao & Lu (Ref. 75) such that the threshold velocity required for smaller particles was commensurately reduced. The threshold friction velocity was compared to the friction velocity obtained from a logarithmic boundary layer assumption. In this model, particles were also convected in the form of clusters (Ref. 40) to save on computational time.

D'Andrea (Refs. 39, 76–78) also developed a Lagrangian based brownout simulation methodology, similar in structure to the one developed by Wachspress et al. (Ref. 40). The rotor flow was modeled using a full-unstructured panel method coupled with a time-accurate free-vortex wake model based on the CVC approach. The ground surface was modeled by using the method of images (Ref. 49). The entrainment of particles in this model was also based on satisfying a threshold friction velocity criterion (Ref. 75).

Although dual-phase rotor experiments (Refs. 17 and 18) have exposed the significant sediment uplift mechanisms that are likely to be involved in brownout, all the existing brownout simulations methodologies (Refs. 36, 38–40, 56) are based on threshold models that consider only boundary layer shear effects. Clearly, there is a need to update these models such that other mobilization mechanisms can be more thoroughly modeled. Most

of the existing brownout simulation methodologies are also based on inviscid rotor wake solutions and, therefore, cannot model the details of fluid and sediment particle interactions in the near-wall regions. Several other simplifications have also been made in their development, e.g., particle-particle collisions were ignored and the transfer of momentum from the particles to the fluid was not modeled. These approximations can, however, be justified (or not) by examining this problem in a small region of interest (ROI) close to the ground.

Such a study has been conducted by Morales & Squires (Ref. 79) by examining the detailed particle dynamics in a turbulent boundary layer under the action of vortices. The effects of the vortices, particle-particle collisions, and gravity on the particle-fluid dynamics were examined. One-way coupling was considered, in which particles were influenced by flow velocities, but not vice-versa. The flow field in the near-wall region was modeled by using Direct Numerical Simulation (DNS) with the fractional-step method to compute the velocities on the particles in a Lagrangian frame of reference. The results showed that the presence of the vortices affects the boundary layer flow, and also suggested that the effects of particle collisions may be more significant in the near-wall region.

1.3.4 Related Research from the Field of Sedimentology

The physics of the sediment dynamics produced by rotor flows is very complex because of the presence of discrete vortical flow structures and large turbulent eddies close to the ground. Although a few experiments have now been performed to understand the dual-phase nature of the brownout problem (e.g., Refs. 17 and 18), this work is still in

its initial stages. In this respect, the work performed in the field of sedimentology to study the sediment dynamics in wind-blown sands, riverine sediment flows, and canonical jet-type flows, can be very useful for gaining a fundamental understanding of the formation of brownout clouds. This work has also provided models that can be used to help model sediment dynamics in the brownout problem. In the present section, related research from the field of sedimentology that was used in the present work is discussed.

Bagnold (Ref. 23) provides a very detailed understanding of the fundamental processes related to the mobilization and convection of sediment particles in aeolian desert flows. Several wind-tunnel experiments were also conducted to understand the initiation of sediment movement. As an outcome of these studies, Bagnold introduced the concept of threshold friction velocity, which is the minimum friction velocity required to entrain particles of different sizes and densities. Bagnold then introduced a model that was based on the consideration of a balance of aerodynamic drag and gravitational forces acting on stationary particles that comprised a bed.

Sutherland (Ref. 26) studied the entrainment of sediment particles in turbulent flows, and developed an entrainment hypothesis based on the concept of turbulent eddies disrupting viscous sublayer and impinging onto the sediment bed. It was hypothesized that sediment motion initiates when turbulent eddies disrupt the viscous sublayer, which increases the local shear stress beyond the critical values. Also, at high rates of sediment transport, the swirling motion of eddies exerts a drag force on the particles that accelerates them, and these particles then roll over the neighboring particles if the vertical velocities are sufficient to lift them from the bed.

Another classical work is the compilation of theoretical and experimental studies

of sediment motion by Greeley & Iversen (Ref. 24) and Iversen et al. (Ref. 80). In this work, the model of the threshold friction velocity developed by Bagnold was revisited by accounting for the effects of inter-particle forces. This threshold friction velocity model was later simplified by Marticona & Bregmetti (Ref. 81) and Shao & Lu (Ref. 75). The present work has used the latter model because it provides a physical representation of the effects of different forces associated with sediment motion.

A series of laboratory simulations (Refs. 82–85) have also been performed to understand dust entrainment by tornados or "dust devils." Dust devils basically comprise a very strong vortex with its axis of rotation perpendicular to the ground, which is in contrast to rotor flows where the vorticity vector is more parallel to the ground. Laboratory experiments were performed by Greeley et al. (Ref. 83) to simulate tornados by using a vortex generator, the goal being to understand the threshold conditions for the entrainment of sand and dust particles. The measurements showed that the low pressure created by the vortices near the ground can provide extra lift forces to overcome inter-particle forces and so affect the threshold conditions for sediment mobilization.

Shao et al. (Ref. 28) conducted wind tunnel experiments to understand the uplift and entrainment of very small-sized dust particles by the action of saltating sand particles over wind-blown surfaces. In these experiments, two beds of different materials were placed in a wind tunnel, the upstream bed comprising of sand particles to start the saltation process, and the downstream bed comprising of dust particles to examine saltation bombardment. The results showed that the principle mechanism responsible for entrainment of dust is by saltation bombardment, not through the direct (shearing) action of the aerodynamic forces. The significance of saltation impacts of mobilized particles was also observed by

Greeley (Ref. 82).

While it seems that modeling bombardment ejection mechanisms in brownout dust cloud simulations will be important, the challenge lies in the mathematical formulation of rather complex physical processes that are involved. To this end, Shao (Ref. 28) developed a dust flux emission model that was based on balance of particle binding energy and kinetic energy of the saltating particles. The dust flux determined by this model was a function of the threshold friction velocity. However, a limitation of this formulation was the difficulties in predicting the binding energy, which cannot be easily measured or calculated from first principles.

Another empirical dust emission model was developed by Marticorena & Bregametti (Ref. 81), which was obtained by correlating the data from the dust emission experiments of Gillette (Ref. 86). These dust flux emission models, however, are not very useful for the present work, which is based on the Lagrangian convection of individual particles, and not particle concentrations or fluxes.

Lu & Shao (Ref. 29) proposed a dust emission model that was based on a volume removal method. In this approach, a saltating particle impacts the bed, forms a crater, and so removes a finite volume of dust from the bed. This model provides an estimate of the volume of dust removed after each impact, and estimates the microphysics of the process where the bombardment ejections from each saltation impact can be estimated.

However, there are several limitations with this model. In particular, it is based partly on a quantity called plastic pressure, which is based on soil properties and is very difficult to measure. However, the strength of this model is that it provides an analytical expression for the volume of dust removed from a crater, and so, can be used to help

model the problem of bombardment ejections at relatively low computational cost. Shao (Ref. 30) later developed a more generic model of the proves, which is also based on the volume of dust removed from the bed during impacts. In this model, the plastic pressure exerted by the bed varies with particle velocity as the particle ploughs though it. This method requires the solution of the separate equations of motion for each particle as they describe the impact with the bed and the removal of dust particles.

1.3.5 Brownout Mitigation Studies

The severity of brownout potentially depends upon many parameters, such as rotor disk loading, blade loading, rotor tip speed, number of blades, blade tip shape, and flight profile of the aircraft near the ground. These parameters may have interdependent influences. Milluzzo and Leishman (Ref. 8) analyzed photographs and videography of rotorcraft landing in brownout conditions, and used a parsimonious model to characterize brownout severity for different rotorcraft based on their geometric and aerodynamic operating conditions. It was shown that brownout severity depends not only on the rotor downwash velocities, but also on the strengths of tip vortices and the frequency at which they are convected toward the ground. A tentative ranking of brownout severity for different rotorcraft was proposed.

The potential sensitivity of severity of brownout to the rotor design parameters, i.e., blade radius, chord and twist rate, was further confirmed by means of a formal optimization study conducted by Tritschler et al. (Ref. 87). The objective function used in this study was a metric that was derived from a simplified representation of the Modula-

tion Transfer Function (MTF) (Refs. 88 and 89), which is based on the optical properties of dust clouds. This metric allowed for a comparison of different brownout clouds for different rotor blade designs, as "good" (i.e., allows "perfect" visibility) or "bad" (i.e., completely cancels visual cues) from the pilot's perspective.

In parallel, Milluzzo et al. (Ref. 20) conducted experiments to study the effects of four different blade tip shapes on the formation and evolution of rotor wakes as they interacted with a ground plane. The tip shapes examined were a standard rectangular tip, a simple swept tip with a constant sweep angle, a BERP-like tip (Ref. 90), and a slotted-tip (Ref. 91). The measurements concluded that the blade tip shape could likely be an important aspect of the blade design for altering the flow velocities near the ground and, therefore, having the potential for mitigating the development of brownout conditions.

D'Andrea (Refs. 77 and 78) has utilized a brownout model to illustrate the effect of rotorcraft configuration on brownout signatures. Whitehouse et al. (Refs. 92 and 93) have utilized simulations and experiments to examine the potential for aerodynamic mitigation of brownout using retrofittable concepts to more rapidly diffuse the tip vortex. Phillips et al. (Refs. 22 and 94) have also examined the potential for aerodynamic mitigation using simulations, examining configurational effects as well as the sensitivity of brownout to rotor design parameters such as blade twist and tip shape. Each of these approaches has contributed much to developing a better understanding of the problem of rotorcraft brownout, and the growing body of research lends confidence to the premise that aerodynamic methods for brownout mitigation may be feasible.

1.4 Limitations of Existing Brownout Methods

The various brownout simulation methodologies that have been outlined in the previous section have been based on Eulerian-Eulerian, Lagrangian-Lagrangian, or Eulerian-Lagrangian approaches, depending on the formulations used to model the rotor wake solution and particle tracking processes, respectively. These formulations all have relative advantages and disadvantages. A prerequisite for any brownout simulation is to model the rotor wake. To this end, the modeling of the rotor flow field IGE requires the use of methodologies that can preserve vorticity to relatively old wake ages. A variety of tools have been described previously, ranging from CFD solvers to free-vortex methods.

The CFD solvers (Refs. 31 and 32) have been based on solutions to the RANS equations, which have been shown to give good predictions of the rotor flow fields IGE. The major limitation with such CFD approaches, however, is the high computational expense. The Eulerian CFD based methods also have inherent issues in preserving vorticity in the flow field, requiring very fine meshes that further increase the computational expense.

One approach that is frequently used to contain the computational cost of a CFD solution, is to refine the meshes only in the regions containing high vorticity (Ref. 32). However, this approach requires an a priori knowledge of the flow field, i.e., about the regions where the mesh actually needs to be refined. This information is not known, except if measurements are available or by running the CFD method many times. A good demonstration of the time required for a state-of-the-art CFD solution is given in Ref. 31, the flow field being computed for a small-scale rotor hovering IGE at a height of one rotor radius above the ground. It was estimated that about 32,000 CPU hours were required to

obtain this solution over 18 rotor revolutions with a time step of 0.25° and with about 17 million mesh points on a cluster of processors. Because of these limitations, CFD is yet to emerge as a feasible tool for brownout simulations, especially not for mitigation studies. Other Eulerian solvers, e.g., Brown's VTM (Refs. 56, 58, 59, 95), solve for the evolution of vorticity over Eulerian meshes. Although this particular method addresses the primary deficiency of RANS solvers (i.e., numerical dissipation of vorticity), very fine meshes are required to obtain an accurate solution and, therefore, the computational costs can still be very high.

Lagrangian based free-vortex methods also provide a very practical and flexible tool to compute rotor flow fields IGE operation. Such methods have been used by Wachspress (Refs. 33 and 40), Whitehouse (Ref. 92), D'Andrea (Refs. 39, 76, 77), and Griffiths (Ref. 34). These methods solve the vorticity transport equations in the Lagrangian frame of reference, and are free from any artificial vorticity dissipation issues that would otherwise be associated with grid discretization. Such methods are at least two orders of magnitude faster than RANS approaches.

The main limitation of these Lagrangian methods is that, being inviscid, they cannot solve for the boundary layer region very close to the ground. Therefore, they either have to be coupled to a CFD solution closer to the ground, or require an empirical or semi-empirical realization of the boundary layer flow. In other words, these Lagrangian methods offer a computationally more efficient solution, with good levels of overall accuracy (except in the viscous flow region very close to the ground), which is critical from a practical standpoint for brownout predictions and mitigation studies.

Another significant drawback of modeling brownout using Eulerian formulations

is at the dust particle level. This includes the inability to model brownout-relevant phenomena such as modified saltation, particle trapping by discrete vortices, particle-ground interactions, and bombardment ejections. For modeling particle motion, a Lagrangian formulation is a more natural and pleasing approach, and allows for modeling of the details of particle level interactions that are needed to make quantitative predictions of the evolving dust clouds.

For these reasons, the present formulation of the brownout simulation methodology was based on the use of a Lagrangian-Lagrangian approach. However, for a good quality brownout simulation, a very large number of individual particles, $O(10^{14})$–$O(10^{16})$, must be tracked over time, which also makes the use of Lagrangian based methods computationally challenging. Computational costs must be contained if practical simulations of brownout dust clouds are ever to be performed. One approach, first adopted by Wachspress (Ref. 40), was to convect particles in the form of "clusters" or groups of particles, instead of convecting them individually. Although significant reductions in cost were obtained, the errors caused by such approximations were not evaluated, and the results were not validated.

Govindarajan & Leishman (Ref. 96) also studied various clustering techniques, and found that their accuracy depends upon the total number of clusters considered as well as the number of particles within each cluster. It was also found that these methods can become less suitable in regions of high velocity gradients, where a very large number of clusters can be required to obtain an acceptable solution and the overhead costs of declustering and reclustering become expensive. Therefore, a thorough analysis of such techniques must always be made in terms of the accuracy of the resulting solution versus

the reductions in computational costs before they can be used for brownout simulations.

Other methods to reduce the computational costs of brownout cloud simulations can be through hardware level accelerations and/or by using faster solution algorithms. In the first approach, the simulation can be implemented in parallel on multiple processors and/or on multithreaded or multicore CPUs. In advanced scientific computing studies, multi-parallel, multi-threaded, multi-core graphic processing units (GPUs) have been shown to be very effective in containing cost of such simulations (Ref. 97). Algorithmic level speedups can also be achieved by using Fast Multipole Methods (FMM) (Refs. 98 and 97). In fact, Hu et al. (Ref. 97) has recently shown that the implementation of FMM on GPUs for N-body problems such as brownout simulations, can offer at least two orders of magnitude speedups on a single CPU processor with one GPU, without compromising on the accuracy of the solution.

Brownout cloud simulation methodologies (Refs. 22, 36, 38–40, 56, 57, 76, 77) are also based on certain other assumptions and simplifications, some of which have been adopted from the field of sedimentology. First, all of these methodologies assume that sediment is mobilized and entrained by the shearing action of the flow field at the ground, i.e., by the use of a threshold friction velocity criterion. The expressions for sediment threshold friction velocity were obtained for much simpler dusty flows, so their validity has not been established for rotor flows. However, these expressions do not explain the mobilization and entrainment of the very small-sized, cohesive dust particles that are known to be present in copious quantities in a typical brownout cloud.

Wachspress et al. (Ref. 40) modeled the entrainment of particles by arbitrarily modifying the empirical coefficients in the threshold friction velocity expression. However,

this approach excludes the possibility that shear may not be the only mechanism through which small dust particles can become entrained. In fact, the mechanism of bombardment ejection turns out to be responsible for the initial mobilization and entrainment of many particles (Refs. 17 and 28). In this case, saltating particles impact the sediment bed, lose a part of their kinetic energy during the impact, break the inter-particle bonds between dust particles (on the bed), and so facilitate particle ejections through bombardment. Furthermore, these dust-sized particles may also become entrained through the action of unsteady pressure forces (Refs. 17 and 83). Therefore, modeling simultaneously of all these potentially important mechanisms is critical if better predictions of brownout clouds is to be obtained.

Another limitation of existing brownout methodologies is their low predictive confidence because of the lack of validation against actual measurements, both of the flow fields and of the dust clouds. In this respect, a major challenge in validation is the relative dearth of really useful measurements. The photogrammetric measurements of Wong and Tanner (Ref. 42), which have been previously described, are the only quantitative measurements available that document the evolutionary shapes of brownout dust clouds. However, even then these results are insufficient to fully validate predictions because many of the important parameters (e.g., the exact weight of the helicopter during the tests, the exact flight path, and the blade control angles and the trim state) were not measured.

1.5 Objectives of this Dissertation

The main objectives of the present work were to develop a comprehensive methodology that can be used to help better understand and predict the development of brownout dust clouds generated by rotorcraft operating over dusty ground surfaces. To this end, the methodology must represent most, if not all, aspects of sediment motion and uplift that have been exposed in the dual-phase flow experiments conducted in the laboratory (e.g., experiments with small-scale rotors operating over mobile sediment beds) and at full-scale (e.g., landing helicopters encountering actual brownout conditions). The computational modeling of such dust clouds can provide a very useful approach to help better understand the brownout problem, as well as to help support and interpret experimental measurements. The developed methodology must also be computationally efficient such that high quality simulations of the evolving brownout dust clouds can be undertaken in practical wall clock times, e.g., of the order of a few hours rather than days.

Of course, fundamental to any brownout simulation is the prediction of the three-dimensional, unsteady wake dynamics produced by a rotor when it operates near the ground. The formation of brownout conditions occurs when a rotorcraft lands or takes off, so that the wake modeling must be capable of representing the additional temporal effects caused by the motion of the rotor system relative to the ground, i.e., the model must be capable of representing the effects associated with maneuvering flight conditions. Any rotor wake methodology must also be capable of conserving the vorticity in the rotor tip vortices at the older wake ages where they actually interact with the ground, which can be when they are six or more rotor revolutions old. Adequate representations of the tip

vortex structure (i.e., the velocity profile and core size) is also a necessary prerequisite for any brownout simulations.

As was previously discussed, Eulerian-based flow solvers require very fine grids to avoid the numerical dissipation of vortices and still cannot predict the rotor wake with any practical level of computational cost. To this end, the well-used Lagrangian free-vortex wake model emerges as a good modeling candidate in terms of conserving vorticity (it does so indefinitely), as well as providing good fidelity at relatively low computational cost. However, the suitability and accuracy of the rotor wake solution using the FVM must first be fully established, especially as it applies to modeling ground effect, i.e., the approach must satisfy flow tangency conditions on the ground plane amongst other things. The numerical schemes used to convect the rotor wake must also be at least second-order accurate, i.e., the schemes used to convect the rotor wake and also provide the induced velocity calculations must both be able to demonstrate second-order accuracy. The effects associated with the intensification of the vorticity in the vortices is also known to be very important in ground effect problems, and such effects can be modeled semi-empirically using core growth models. Ultimately, the rotor flow predicted using the FVM in ground effect operations must be validated against experiments, which was another objective of the present work.

One of the shortcomings of the FVM, which is an inviscid methodology, is that it cannot satisfy the no-slip boundary condition at the ground, i.e., the boundary layer on the ground below the rotor cannot be modeled in an inviscid construct. Therefore, this fundamentally inviscid method must be coupled with another model that can represent the near-wall flow that forms as the rotor wake reaches the ground and then convects

radially outward, in effect forming a wall-jet type of flow. Coupling the FVM with a Navier-Stokes method or a boundary layer method in this near-wall region is one option, however, as previously described such approaches could make the brownout simulations computationally very expensive and most likely prohibitive. Therefore, another objective of the present work was to develop an approximation for the flow near the ground that provides not only good modeling capability, but is much more computationally feasible within the framework of an overall brownout simulation, especially when flight maneuvers are involved.

Notable deficiencies in existing brownout simulation models are with the models that are used to predict sediment mobilization and uplift in a rotor-induced flow environment. As previously described, models currently being used to predict the onset of sediment mobility are based on the attainment of threshold conditions (e.g., a threshold friction velocity), which have been developed from measurements of sediment motion made in steady one-dimensional uniform flows. However, these semi-empirical models may not be entirely applicable to the three-dimensional, unsteady, vortical flow environment found at the ground below rotors. More importantly, the existing models clearly do not represent all of the physical processes of sediment mobility and uplift found in the rotor environment, e.g., particle ejections from reingestion bombardment and particle uplift from unsteady pressure effects. Therefore, it is clear that new models must be developed that can represent all of the primary sediment mobilization and uplift processes that are applicable to rotor flows. Again, any such new models must also still be computationally efficient such that they can be practically included within the overall brownout calculation.

Very significant computational challenges are involved in accurately tracking particles in rotor flows for longer durations. Efficient numerical time-integration algorithms must be developed to solve for the particle motion. One objective of the present work was to seek the best numerical integration scheme that balances both accuracy and cost. To solve the particle equations a double integration must be performed; the first integration is used to find the particle velocities, and the second integration to find the particle displacements. The stability and accuracy of the selected scheme must also be rigorously analyzed, and at least second-order accuracy will be needed for particle displacement calculations and also to be consistent with the overall accuracy of the rotor flow solution.

A typical brownout dust cloud may contain many billions of particles, all of which must be tracked in time, and for the long durations associated with the flight maneuver. For the most part, tracking many separate particles throughout the flow can be cost prohibitive. Therefore, another objective of the present work was to exploit recent advancements in scientific computing to accelerate brownout simulations and bring them to a more practical range of tractability. To this end, an objective was to explore techniques of parallel computing, including methods of porting the computations to make use of graphic processor units. The use of particle clustering methods was also considered, in that convecting clusters or groups of particles should be more cost effective than by convecting all of the particles individually. However, the use of clustering techniques also requires some trade between accuracy and cost.

Another significant challenge in any brownout simulation is to validate the various elements of the modeling. To this end, both laboratory measurements and flight test measurements can be used, although not all of the measurements that might be desired

for validation are currently available. In fact, some types of measurements are clearly difficult or impossible to make. First, results from the FVM must be validated for a rotor operating IGE, for which a variety of measurements are available. There are, however, still relatively few flow measurements near the ground below rotors, even in hover. Validation of brownout dust clouds is obviously much more challenging, not least because of the relative dearth of measurements in this case. It was mentioned previously that the existing dust cloud measurements also fall short of what is needed for validation because various parameters documenting the flight conditions are not available.

After confidence has been established in the modeling, then the underlying physical reasons as to why such dust clouds form can be better understood. Only then can the methodology be used to explore techniques for brownout mitigation. To this end, understanding the mechanisms responsible for the mobilization and uplift of dust may lead to the evaluation of techniques that could reduce the intensity of the dust clouds that would otherwise be generated by the rotor. A final objective in the present work was to begin to consider possible methods of brownout mitigation.

1.6 Organization of the Dissertation

The rotorcraft brownout problem has been introduced in the present chapter. A general discussion of the different aspects of this problem was presented, i.e., of the rotor flow in ground effect operation and of dust particle motion under the action of an external flow. A detailed survey of previous work performed on the brownout problem was also discussed. The limitations of the other brownout simulation methodologies that have been

previous developed have been discussed. The need to rectify these deficiencies, and to develop brownout simulation methodology of higher fidelity, was the primary motivation for the present work.

The remainder of the dissertation is organized into three chapters. The mathematical and algorithmic details of the methodology that was developed to simulate brownout dust clouds are discussed in Chapter 2. This chapter first explains the modeling of the rotor flow field in ground effect using the free-vortex method, followed by the viscous flow approximation used to model the flow near the ground. The methods that were developed to simulate the mobilization, uplift, and convection of the dust particles in the flow is then discussed. The numerical methods developed to solve the particle equations of motion are also described in detail, along with the application of clustering methods.

Chapter 3 discusses in detail the results obtained using the various modeling approaches that were developed, in the present research including the free-vortex wake model, the near-ground flow model, and the sediment mobility model. First, the outcomes from the validation study are presented, where available measurements were used to establish the credibility of the various modeling approaches being used. Then, an analysis of the development of the rotor wake and the corresponding dust clouds produced during hover, landing, and takeoff flight maneuvers is discussed. It is here that the underlying fluid dynamic mechanisms that contribute most to the development of the dust clouds have been exposed, including the tendency of the wake to bundle below the rotor and initiate bombardment ejections of increasing quantities of dust. The possibilities of brownout mitigation by artificially diffusing tip vortices are also explored in this chapter.

Finally, Chapter 4 presents the detailed conclusions obtained from the present work,

and also provides recommendations for future work. It is clear, however, that much further work is needed before simulations can reach the high confidence levels needed for mitigation studies.

Chapter 2

Methodology

This chapter discusses the mathematical models that were developed to help better understand the problem of brownout produced by a rotorcraft in ground effect operation over a mobile sediment bed. The various aspects of the problem, i.e., the aerodynamic flow produced by a rotor in ground effect, the uplift and entrainment of sediment particles from the bed, the subsequent particle motion, and various particle interactions with the ground (i.e., bombardment) are all considered. The development of a comprehensive brownout dust cloud model is particularly difficult in that it must: (a) be capable of representing multiple modes of particle uplift and entrainment; (b) contain enough dust particles to represent the essential features and physical characteristics of the brownout cloud; (c) not contain so many particles that it would be infeasible to compute all of their positions in space and time.

A prerequisite for modeling brownout is to model accurately the time-dependent rotor flow generated by a rotorcraft maneuvering near the ground. In the present work, the rotor flow in ground effect operation was modeled using a free-vortex method (FVM), which is discussed first. An inviscid-viscous method was then used to predict the flow field arising from a combination of the rotor flow (modeled as an inviscid potential flow using the FVM) and the resulting (viscous) flow in the boundary layer region at the ground. The particle mobility mechanisms are then explained. A new particle entrain-

ment model is proposed to simulate the initiation of sediment motion under the action of vorticity-laden flow fields. After that, the solution of the particle equations of motion are discussed, along with a detailed analysis of the stability and accuracy of the different time-marching schemes that were examined to convect the particles. Suspended particles can also bombard the sediment bed and eject new particles from the bed in a process called bombardment ejection. A new model for this latter process has been developed to help represent the physics of the brownout problem. Finally, techniques that were used to expedite the computational solution of the particle equations of motion are discussed.

2.1 Modeling of the Rotor Flow in Ground Effect

This section discusses the free-vortex method (Refs. 64, 65, 99), which was configured to predict the flow produced by a rotor in ground effect operations under arbitrary maneuvering flight conditions. The free-vortex method or FVM is a Lagrangian-based methodology, which solves for the evolution of the rotor wake geometry under the influence of the velocity induced by all the elements in the flow field. The strengths of these elements are determined from the blade aerodynamic solution when it is coupled also with articulated blade motion. The vortical elements in the flow comprise of the rotor blades and the wake filaments. It is assumed that all of the vorticity in the flow field is confined to these elements, and the flow outside is inviscid, incompressible, and irrotational. The velocity induced by all the vortical elements is calculated by using the Biot-Savart law (discussed later). The rotor flow in ground effect operation can be modeled in the FVM formulation by using either an image rotor system or by means of a surface singularity

method (Ref. 34).

2.1.1 Computation of the Induced Velocity using the Biot-Savart Law

The velocity induced at any point in the flow field from the vortical elements can be computed by the application of the Biot-Savart law (see Ref. 49, pp. 226, 227, and Ref. 100, pp. 93, 94), and by numerically integrating the velocity induced by each vortical element. Figure 2.1(a) shows how the application of the Biot-Savart law can be used to compute the induced velocity, $\mathbf{V}$, at a point 'P' from a vortex filament of strength Γ; this velocity is given in analytical form by

$$\mathbf{V} = \frac{\Gamma}{4\pi} \int \frac{d\mathbf{l} \times \mathbf{r}}{|\mathbf{r}|^3} \tag{2.1}$$

where $\mathbf{r}$ is the position vector of the point 'P' with respect to the vortex element $d\mathbf{l}$.

In the present formulation of the FVM, the general curved vortex filaments are discretized into straight-line segments, which give a second-order reconstruction of the induced velocity field (Refs. 67 and 101). For a line vortex with constant circulation Γ (see Fig. 2.1(b)), an exact form of Eq. 2.1 is

$$\mathbf{V} = \frac{\Gamma}{4\pi h} (\cos\theta_1 - \cos\theta_2) \frac{\mathbf{a} \times \mathbf{r}}{|\mathbf{a} \times \mathbf{r}|} \tag{2.2}$$

The numerical solution of the expression given by Eq. 2.2 requires the calculation of trigonometric functions, which requires considerable processor cycles. A better implementation is by using

$$\mathbf{V} = \frac{\Gamma}{4\pi} \left\{ \mathbf{a} \cdot \left(\frac{\mathbf{r}_1}{|\mathbf{r}_1|} - \frac{\mathbf{r}_2}{|\mathbf{r}_2|} \right) \frac{d\mathbf{l} \times \mathbf{r}_1}{|d\mathbf{l} \times \mathbf{r}_1|^2} \right\} \tag{2.3}$$

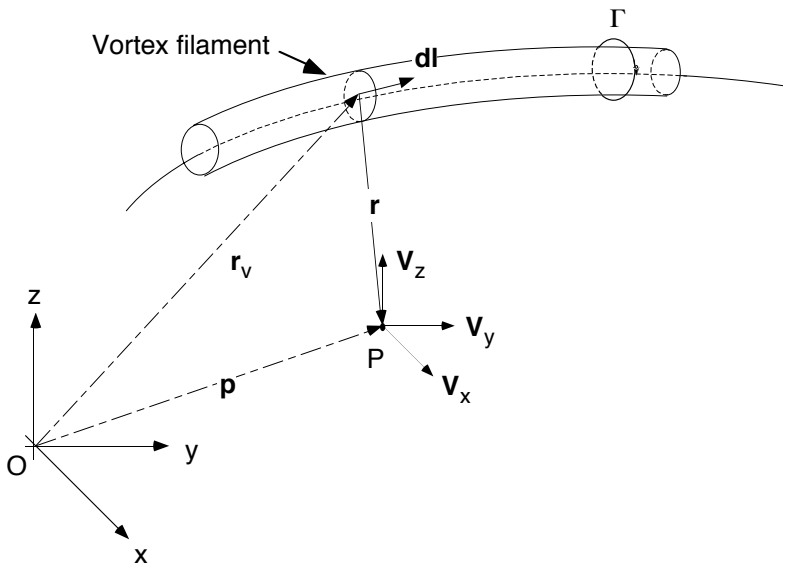

(a) Velocity induced by a curved vortex filament. (Source: Ref. 62)

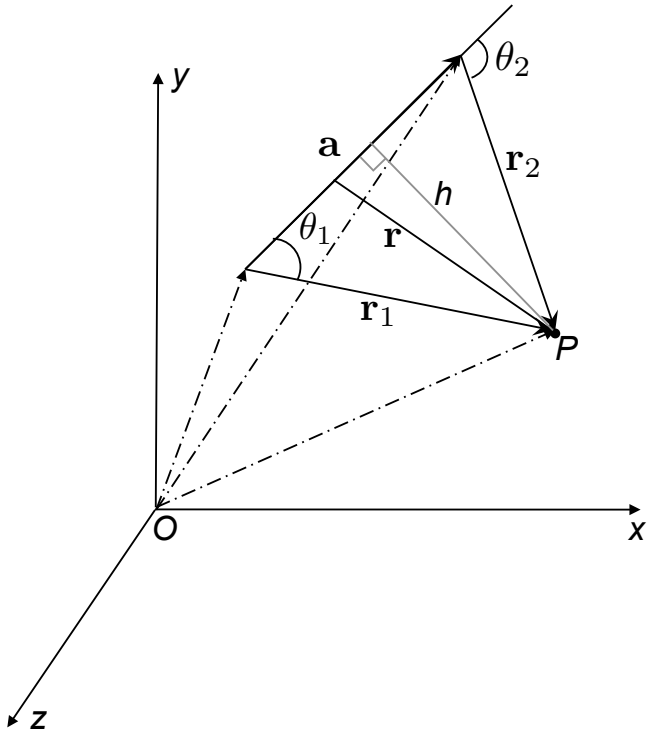

(b) Velocity induced by a straight vortex filament

Figure 2.1: Velocity induced at a point '*P*' from: (a) a curved vortex filament, and (b) a straight vortex segment.

which is based on the vector algebra of floating point numbers and is a very fast vector manipulation on modern computers. This latter implementation is also more efficient on graphical processing units (GPUs), as discussed in Appendix B.

The velocity induced by a curved vortex filament is, therefore, approximated using straight-line segmentation and numerical integration along the length of the vortex filament. This process is equivalent to the use of the trapezoidal method of integration. The errors associated with the approximation can be assessed using a Taylor series analysis. It has been shown in Ref. 66 that the leading error term becomes

$$\mathbf{V}_{\text{discrete}} = \mathbf{V}_{\text{exact}} + \frac{1}{12}\frac{d^2\mathbf{V}}{d\zeta^2}\Delta\zeta^2 + \cdots \text{ higher order terms} \tag{2.4}$$

which is $O(\Delta\zeta^2)$, i.e., the numerical approximation is second-order accurate.

2.1.2 Blade Aerodynamic Solution

The rotor was modeled using N_b rigid, articulated blades, which can execute fully independent, flapping motion. Each blade was modeled as a distribution of vortex singularities (bound vortices) in the flow field by using a lifting surface model. In the present formulation, the Weissinger-L lifting surface model (Ref. 102) was used, where the blades are divided into N_s spanwise segments and one chordwise segment, each segment basically being represented by a horseshoe vortex. The bound vortices were located at $1/4$-chord, and the flow tangency condition was satisfied at the $3/4$-chord; see Fig. 2.2. The bound vortex strength was constant along each blade segment and varied from one segment to another. Therefore, as given by the Helmholtz laws of conservation of vorticity (Ref. 103), circulation must be trailed at the ends of each segment. The strengths of the

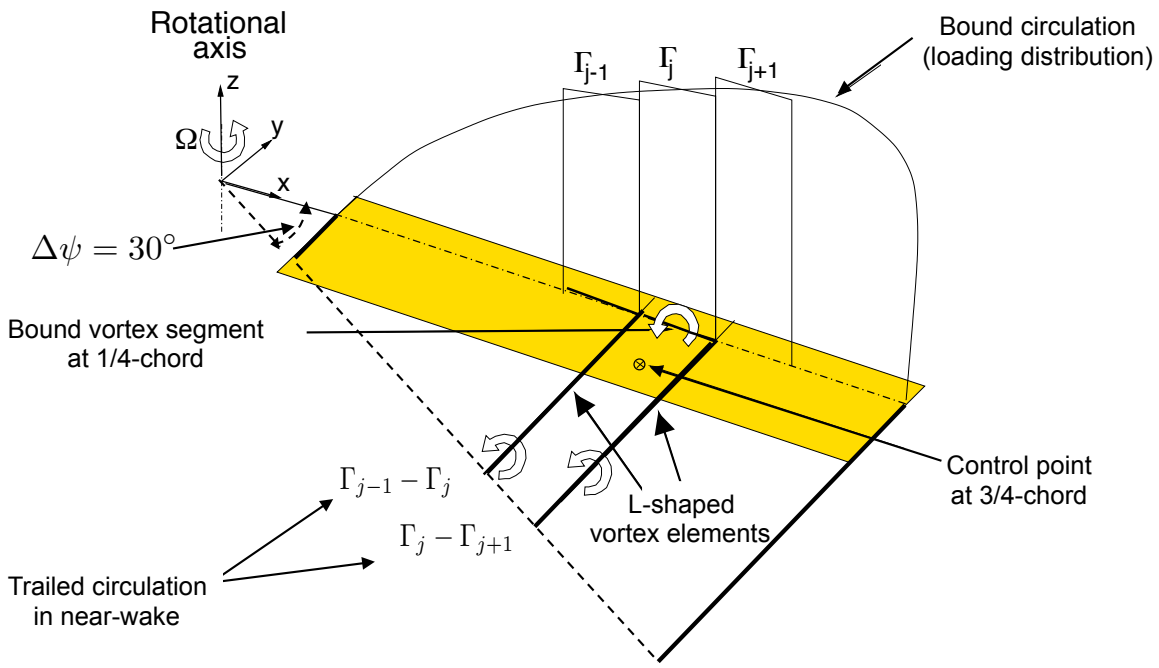

Figure 2.2: Schematic of the Weissinger-L model used to represent the rotor blades. (Source: Ref. 99)

trailers at the end of the j^{th} blade segment (see Fig. 2.2) are

$$\Gamma_t|_j = \Gamma_b|_j - \Gamma_b|_{j+1} \tag{2.5}$$

In general, the wake from a rotor blade comprises of a vortex sheet and a concentrated vortex trailed from the blade tip. The vortex sheet comprises of vorticity with components normal and parallel to the trailing edge of the blade, which are known as the trailed and shed vortices, respectively. The trailed vorticity behind each blade (given by Eq. 2.5) is also known as the near-wake. In the present work, the near-wake was assumed to be rigid and fixed to the blade and was truncated 30° behind each blade; see Fig. 2.2. Further downstream, it was assumed that the near-wake rolls up into the far-wake, which consists of a single tip vortex. The tip vortex was discretized using Lagrangian markers as shown in Fig. 2.3; see Section 2.1.3 for details. The strength of the tip vortex was

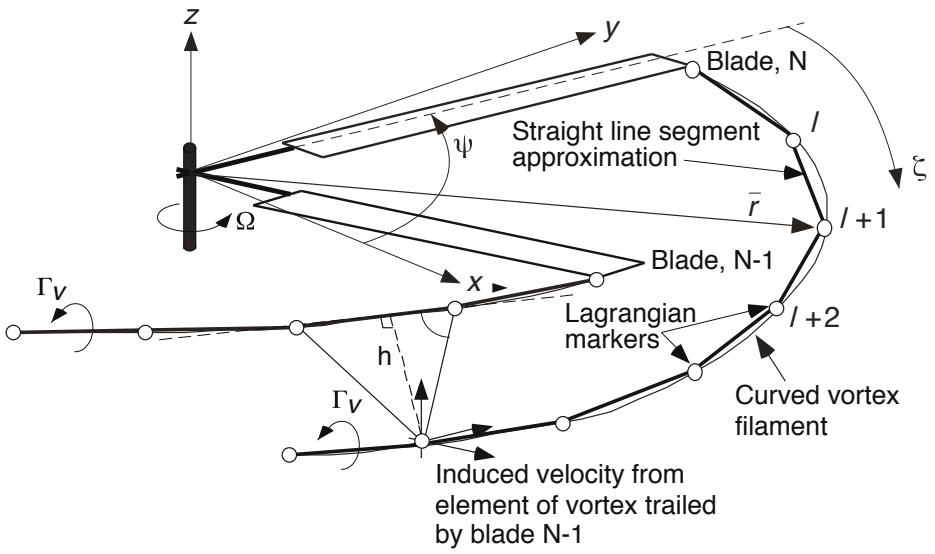

Figure 2.3: Schematic showing representation of the rotor wake using tip vortex filaments, which are discretized using the Lagrangian markers. (Source: Ref. 64)

assumed to be equal to the maximum bound circulation along the blade span (Ref. 62).

2.1.2.1 Calculation of the Bound Circulation Strength

The strength of the bound circulation along the blade span was calculated by satisfying the flow tangency at the blade control points (located at the $3/4$-chord position). This means that the component of the local incident velocity, which was perpendicular to the i^{th} blade segment at the blade control points, was exactly zero, i.e.,

$$\mathbf{V}_i \cdot \mathbf{n}_i \quad = \quad 0 \qquad i = 1, 2, ..., i_{\max} \tag{2.6}$$

where $\mathbf{V}_i$ is the total velocity at the control point. Notice that $\mathbf{V}_i$ comprises the contributions from the free-stream velocity $\mathbf{V}_\infty$, the velocities induced by the near-wake $\mathbf{V}_{\mathrm{NW}}$, the bound vortices $\mathbf{V}_B$, the far-wake $\mathbf{V}_{\mathrm{FW}}$, and by the effects of maneuvers $\mathbf{V}_{\mathrm{man}}$. Therefore,

Eq. 2.6 can be written as

$$(\mathbf{V}_\infty + \mathbf{V}_B + \mathbf{V}_{\mathrm{NW}} + \mathbf{V}_{\mathrm{FW}} + \mathbf{V}_{\mathrm{man}}) \cdot \mathbf{n}_i = 0 \qquad i = 1, 2, ..., i_{max} \tag{2.7}$$

Notice that all the induced velocity contributions, i.e., $\mathbf{V}_B$, $\mathbf{V}_{\mathrm{NW}}$, $\mathbf{V}_{\mathrm{FW}}$, and $\mathbf{V}_{\mathrm{man}}$, can be calculated by means of the application of the Biot-Savart law (i.e., Eq. 2.3). Because the blade and its immediate near-wake are both assumed to be rigid, then $\mathbf{V}_B$ and $\mathbf{V}_{\mathrm{NW}}$ can be expressed as

$$V_{B_i} = \sum_{j=1}^{N_s} I_{B_{ij}} \Gamma_j \tag{2.8}$$

$$V_{\mathrm{NW}_i} = \sum_{j=1}^{N_s} I_{\mathrm{NW}_{ij}} \Gamma_j \tag{2.9}$$

where I_B and I_{NW} are the influence coefficient matrices that depend upon the blade and near-wake geometry, and are computed only once in the entire free-vortex solution; see Ref. 62 for details. The indices i and j in Eqs. 2.8 and 2.9 correspond to the blade control points and bound vortex segments, respectively.

Substituting Eqs. 2.8 and 2.9 into Eq. 2.6 gives

$$[I]\{\Gamma_j\} = \{(\mathbf{V}_\infty + \mathbf{V}_{\mathrm{man}} + \mathbf{V}_{\mathrm{FW}}) \cdot n\}_i \tag{2.10}$$

where $I = I_B + I_{\mathrm{NW}}$, and the bound circulation is obtained by the inversion of the influence coefficient matrix I, i.e., by solving

$$\{\Gamma_j\} = [I]^{-1}\{(\mathbf{V}_\infty + \mathbf{V}_{\mathrm{man}} + \mathbf{V}_{\mathrm{FW}}) \cdot n\}_i \tag{2.11}$$

Because the blade and its near-wake is assumed to be rigid, the inversion of $[I]$ needs to be performed just once, hence saving considerably on computational time.

2.1.2.2 Calculation of the Blade Loads

The strength of the bound vortices, Γ_j, as calculated using Eq. 2.11, varies along the spanwise as well as the azimuthal direction around the rotor disk. As mentioned earlier, the strength of the blade tip vortex is the maximum value of Γ_j along the blade span. The tip vortex attachment point on the blade is determined through the blade flapping response, which is discussed later in Section 2.1.4. The positions of the Lagrangian markers are obtained by solving the vorticity transport equation, which will be discussed next in detail in Section 2.1.3.

Once the strengths and positions of all the vortex elements are known, the velocities induced at the blade control points can be calculated by using the Biot-Savart law. These velocities can then be used to calculate the sectional angles of attack. The effects of unsteady aerodynamics on the blade angles of attack are then calculated using the indicial response method, as proposed by Leishman & Beddoes (Ref. 104). The nonlinear lift and drag characteristics are calculated based on the Beddoes two-dimensional, nonlinear airfoil model for the NACA 0012 airfoil; see Ref. 105. Alternatively, airfoil look-up tables can also be integrated with the FVM to calculate the spanwise loads on rotor blades.

Finally, the sectional airloads can then be integrated to obtain rotor thrust, C_T, and torque, C_Q, by using

$$C_T = \frac{1}{2\pi}\int_0^{2\pi}\int_e^1 \frac{\sigma}{2}\left(\frac{U}{\Omega R}\right)^2 (C_l\cos\phi - C_d\sin\phi)\, dr\, d\psi \tag{2.12}$$

$$C_Q = \frac{1}{2\pi}\int_0^{2\pi}\int_e^1 \frac{\sigma}{2}\left(\frac{U}{\Omega R}\right)^2 (C_l\sin\phi + C_d\cos\phi)\, r dr\, d\psi \tag{2.13}$$

where σ is the rotor solidity, e is the non-dimensional flapping hinge offset, C_l and C_d are the sectional lift and drag coefficients, respectively, ψ is the azimuthal location of the

reference rotor blade, r is the non-dimensional radial distance, U is the total velocity at the blade cross-section, and ϕ is the inflow angle.

2.1.3 Free-Vortex Wake Modeling

The crux of a FVM is to model the convection of vorticity in the rotor wake as physically accurately as possible. This goal is achieved by tracking the Lagrangian markers in a time-accurate manner. Fundamentally, the movement of these Lagrangian markers is governed by the three-dimensional, incompressible Navier-Stokes equations, which can be written in the form of the vorticity transport equation, i.e.,

$$\frac{D}{Dt}\left(\vec{\Omega}\right) = \left(\vec{\Omega}\cdot\vec{\nabla}\right)\mathbf{V} + \nu\Delta\cdot\vec{\Omega} \tag{2.14}$$

This foregoing equation determines the change of vorticity of a fluid element in terms of the instantaneous values of vorticity $\vec{\Omega}$ and velocity field $\mathbf{V}$. The left-hand-side (LHS) of this equation gives the substantive derivative of vorticity, which provides both the time rate of change of vorticity and its convection rate. The first term on the RHS of Eq. 2.14 is the strain term, which accounts for the changes in the length of a vortex filament as it is convected in the flow. The second term on the RHS of Eq. 2.14 represents the diffusion of vorticity under the action of the viscosity and turbulence in the flow.

In the free-wake modeling, vorticity is confined to the vortices themselves and the flow outside is assumed to be inviscid. Under the conditions of inviscid, incompressible and irrotational flow, Helmholtz's law (Ref. 103) states that the vortex lines move as material lines at the local flow velocities, the convection of points on these vortex lines

being governed by

$$\frac{d}{dt}(\mathbf{r}) = \mathbf{V}(\mathbf{r}) \tag{2.15}$$

The vector $\mathbf{r}$ in Eq. 2.15 gives the position of the Lagrangian markers in the vortical wake. In a blade fixed coordinate system, the LHS of Eq. 2.15 can be expressed in terms of the rate of change of $\mathbf{r}$ with blade azimuth ψ (temporal) and wake age ζ (spatial). Therefore, Eq. 2.15 can be written in the form of a partial differential equation as

$$\frac{\partial \mathbf{r}}{\partial \psi} + \frac{\partial \mathbf{r}}{\partial \zeta} = \frac{\mathbf{V}}{\Omega} \tag{2.16}$$

2.1.3.1 Numerical Solution of the Wake Equation

Equation 2.16 can be solved by using finite difference approximations. To this end, the vortex field is discretized in space and time with step sizes of $\Delta\zeta$ and $\Delta\psi$, respectively (see Ref. 106). The RHS of Eq. 2.16 comprises of the local velocity vector at any point in the flow field, which includes the free-stream (i.e., $\mathbf{V}_\infty$) and the induced effects (i.e., $\mathbf{V}_{\text{ind}}$), the bound circulation on the blades, the near-wake, and the effects induced by any flight maneuvers. The finite difference equation can be written in the form

$$D_\psi(\mathbf{r}) + D_\zeta(\mathbf{r}) = \frac{\mathbf{V}_\infty}{\Omega} + \frac{1}{\Omega}\sum_{j=1}^{j=N_v} \Delta\mathbf{V}_{\text{ind}_j} \tag{2.17}$$

Equation 2.17 was solved in the present analysis by using a time-accurate, predictor-corrector (PC2B) scheme developed by Bhagwat & Leishman (Refs. 64 and 66). The numerical solution of Eq. 2.17 is evaluated at the mid-point of each grid cell (i.e., at $\psi + \Delta\psi/2$, $\zeta + \Delta\zeta/2$), as shown in Fig. 2.4. This algorithm uses five-point central discretization in space and two-point backwards discretization in time, i.e.,

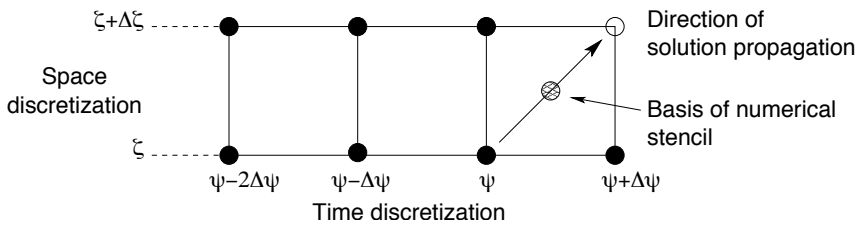

Figure 2.4: Schematic showing the stencil for PC2B finite difference approximation. (Source: Ref. 99)

$$D_\zeta(\mathbf{r}) = \frac{\mathbf{r}(\psi+\Delta\psi,\zeta+\Delta\zeta)+\mathbf{r}(\psi,\zeta+\Delta\zeta)-\mathbf{r}(\psi+\Delta\psi,\zeta)-\mathbf{r}(\psi,\zeta)}{2\Delta\zeta} \tag{2.18}$$

$$D_\psi(\mathbf{r}) = \frac{3\mathbf{r}(\psi+\Delta\psi,\zeta)-\mathbf{r}(\psi,\zeta)-3\mathbf{r}(\psi-\Delta\psi,\zeta)+\mathbf{r}(\psi-2\Delta\psi,\zeta)}{4\Delta\psi} \tag{2.19}$$

The LHS of the governing equation can be obtained from Eqs. 2.18 and 2.19 as

$$D_\psi + D_\zeta = \frac{\partial r}{\partial\psi} + \frac{\partial r}{\partial\zeta} + \left(-\frac{5}{24}\frac{\partial^3 r}{\partial\psi^3} + \frac{1}{8}\frac{\partial^3 r}{\partial\psi^2\partial\zeta}\right)\Delta\psi^2 + \left(\frac{1}{24}\frac{\partial^3 r}{\partial\zeta^3} + \frac{1}{8}\frac{\partial^3 r}{\partial\psi\zeta^2}\right)\Delta\zeta^2 + \frac{1}{4}\frac{\partial^4 r}{\partial\psi^4}\Delta\psi^3 + \ldots \tag{2.20}$$

The leading error terms in Eq. 2.20 are second-order accurate in both space and time, which confirms the overall second-order accuracy of the finite difference approximations to the derivatives.

The self-induced and mutually induced velocities on the RHS of Eq. 2.17 from the N_v vortex filaments are approximated by using the Biot-Savart law; see Section 2.1.1. This type of induced velocity computation using straight-line vortex segments is second-order accurate (Refs. 67 and 101). Furthermore, the approximation at the mid-point of each grid cell (i.e., at $\psi+\Delta\psi/2$, $\zeta+\Delta\zeta/2$) can be obtained by averaging the velocity at the four surrounding grid points; see Fig. 2.4. The leading error terms from velocity

averaging can be written as

$$\mathbf{V}_{\text{discrete}} = \mathbf{V}_{\text{exact}} + \frac{5}{24}\left(\frac{\partial^2 \mathbf{V}}{\partial \zeta^2}\right)\Delta\zeta^2 + \frac{1}{8}\left(\frac{\partial^2 \mathbf{V}}{\partial \psi^2}\right)\Delta\psi^2 + O\left(\Delta\zeta^4\right) \tag{2.21}$$

which are also second-order accurate, so providing the overall second-order accuracy for the induced velocity computations at the mid-point of each grid cell. The modified equation can then be obtained by combining Eqs. 2.20 and 2.21 and using $\Delta\zeta = \Delta\psi$, which can be written as

$$\frac{\partial r}{\partial \psi} + \frac{\partial r}{\partial \zeta} = \mathbf{V} + \Delta\zeta^2\left[\frac{5}{24}\frac{\partial^2 \mathbf{V}}{\partial \zeta^2} + \frac{1}{8}\frac{\partial^2 \mathbf{V}}{\partial \psi^2} - \left(-\frac{5}{24}\frac{\partial^3 r}{\partial \psi^3} + \frac{1}{8}\frac{\partial^3 r}{\partial \psi^2 \partial \zeta}\right) - \left(\frac{1}{24}\frac{\partial^3 r}{\partial \zeta^3} + \frac{1}{8}\frac{\partial^3 r}{\partial \psi \zeta^2}\right) - \frac{1}{4}\frac{\partial^4 r}{\partial \psi^4}\Delta\zeta\right] + O\left(\Delta\zeta^4\right) \tag{2.22}$$

2.1.3.2 Diffusion and Filament Straining

The effects of diffusion and filament strain were neglected in the development of Eq. 2.16 because they are active over a much smaller scale, i.e., within the scales of the vortex cores. However, for several flight conditions, e.g., rotor flow in ground effect and during maneuvering flight, the vortex wake undergoes significant deformations, including stretching. Such effects play an important role in determining the flow near the rotor as well as at the ground (Ref. 18).

In the FVM, these effects are modeled by using a sequential sub-step approach in which the vortex filaments are first convected to new positions under the influence of the local flow velocity. Then, the effects associated with diffusion are applied based on the age of the filaments. Finally, filament strain or stretching effects are applied based on the changes in the vortex core radius.

The effects of diffusion are modeled by using a vortex model. In the present work, the Vatistas (Ref. 107) vortex model was used in which the swirl or tangential component of velocity can be written as

$$V_\theta(r) = \frac{\Gamma_v}{2\pi}\left(\frac{r}{(r^{2n} + r_c^{2n})^{1/n}}\right) \tag{2.23}$$

where r_c is the vortex core radius. The value of $n = 1$ gives the so-called "Scully" vortex profile (Ref. 16). The present work uses the value of $n = 2$ because it generally provides a better correlation with velocity profile measurements for rotor-generated tip vortices (Ref. 108).

A simple model of the growth in vortex core radius, r_c, with time, t, can be obtained starting from the Lamb-Oseen laminar result, as given by

$$r_c(t) = \sqrt{4\alpha\nu t} \tag{2.24}$$

where $\alpha = 1.25643$. Because of the laminar flow assumptions, the vortex core size predicted by Eq. 2.24 gives a much slower diffusion of the tip vortex than has been measured in experiments. The tip vortex exhibits laminar behavior initially, but then becomes turbulent because of the roll up of the vortex sheet and the presence of small-scale eddies in the flow (Ref. 16). To account for these turbulence effects on vortex diffusion, Squire (Ref. 109) proposed the inclusion of an eddy viscosity parameter δ, which depends upon vortex Reynolds number Γ_v/ν. However, the vortex core growth model given by Eq. 2.24 is still singular at $t = t_0$, and produces high induced velocities when compared to measurements.

Bhagwat & Leishman (Ref. 64, 70) proposed another semi-empirical model for a

rotor tip vortex, which was based on Squire's basic approach, i.e.,

$$r_c(\zeta) = \sqrt{4\alpha\delta\nu\left(\frac{\zeta+\zeta_0}{\Omega}\right)} \tag{2.25}$$

where ζ is the wake age, r_{c_0} is the initial core radius of the vortex, and δ is the eddy viscosity coefficient that accounts for the turbulence effects on the vortex core growth. The coefficients in this model, ζ_0 and δ, were defined empirically using tip vortex core growth measurements (Ref. 110). Following Squire, the effective eddy viscosity coefficient δ is a function of the vortex Reynolds number Γ_v/ν, and was given by

$$\delta = 1 + a_1\left(\frac{\Gamma_v}{\nu}\right) = 1 + a_1 Re_\nu \tag{2.26}$$

Based on experimental correlations of full-scale and model-scale rotors, the average value of a_1 was found to be 2×10^{-4}, whereas for a fixed-wing this value was about 2×10^{-5}.

The filament strain or "stretching" effects were modeled by using the method developed by Ananthan and Leishman (Ref. 69). Because the flow field was assumed to be incompressible (except for within the vortices), using Helmholtz's law (Ref. 103) the net circulation, $\Gamma = \int \vec{\Omega} d\mathbf{S}$, of a vortex filament should remain constant. Any change in the length of a vortex filament will result in a change in the vorticity confined within the vortex core.

This latter effect can be modeled by changing the core size with filament strain. Assuming that the net vorticity is confined within a cylinder of core size r_c (see Fig. 2.5), an increase in the length of the cylinder will result in an increase in vorticity in r_c. Using

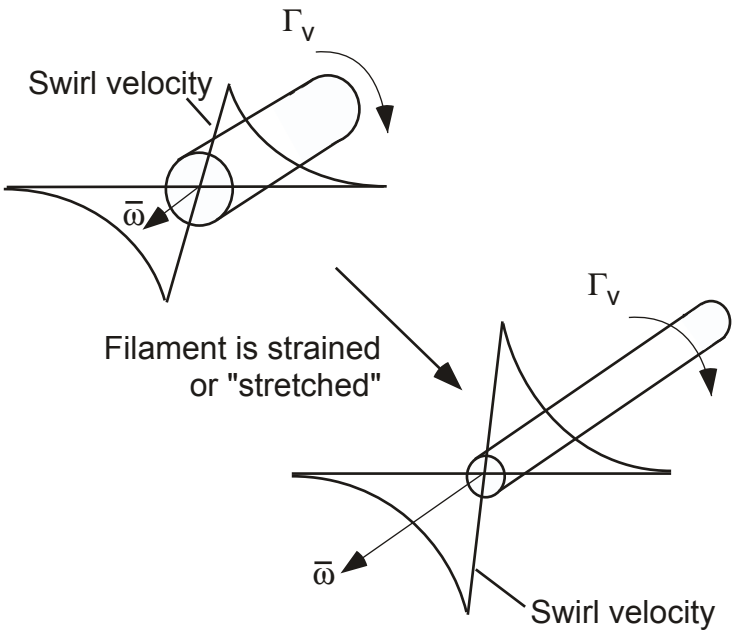

Figure 2.5: Schematic showing the stretching of a vortex filament and the intensification of vorticity within the vortex core. (Source: Ref. 20)

mass conservation for incompressible flows, this process can be expressed as

$$\pi r_c^2 l = \pi(r_c - \Delta r_c)^2 (l + \Delta l) \tag{2.27}$$

$$\Delta r_c = r_c \left(1 - \frac{1}{\sqrt{1+\varepsilon}}\right) \tag{2.28}$$

where $\varepsilon = \Delta l / l$ is the filament strain rate. Using Eq. 2.28 with Eq. 3.4, the resulting expression of the vortex core size is

$$r_c(\zeta, \varepsilon) = \sqrt{r_{c_0}^2 + \frac{4\alpha\delta(Re_v)\nu}{\Omega} \int_0^{\zeta} (1+\varepsilon)^{-1} d\zeta} \tag{2.29}$$

where the net strain effects are accounted for integration from the point of the origin of the vortex as it is convected in the flow field to a wake age ζ.

2.1.4 Blade Flapping Dynamics

Blade flapping dynamics play an important role in determining the airloads on a helicopter rotor blade, and especially so during maneuvering flight. The flapping response of a blade is also coupled to its aerodynamics, which depends upon the velocities induced by the rotor wake. Furthermore, the wake-blade attachment boundary condition also depends upon the blade flapping response, which necessitates the tight coupling of the blade flapping to the wake solution.

The blade flapping response can be determined by solving the governing equation for blade flapping, which can be formulated by considering moments from the aerodynamic and the inertial forces about the blade flapping hinge. In maneuvering flight, the contributions of vehicle dynamics to the aerodynamic and inertial forces must also be accounted for in the derivation of the flapping equation.

A general form of the flapping equation can be written as

$$\overset{\star\star}{\beta} + \beta = \frac{M_A}{I_b \Omega^2} + M_I' \tag{2.30}$$

where M_A is the aerodynamic moment about the flap hinge, I_b is the moment of inertia of the blade, and M_I' is the total inertial moment acting at the flap hinge. For a helicopter undergoing pitching and rolling motion about its center of gravity, the flapping equation of motion can be written as

$$\overset{\star\star}{\beta} + \beta = \frac{M_A}{I_b \Omega^2} - 2\left(\frac{q}{\Omega}\right)\sin\psi + 2\left(\frac{p}{\Omega}\right)\cos\psi + \left(\frac{\overset{\star}{q}}{\Omega}\right)\cos\psi + \left(\frac{\overset{\star}{p}}{\Omega}\right)\sin\psi \tag{2.31}$$

where p and q are pitch and roll rates, respectively. A detailed derivation of this equation is given in Ref. 99.

The flapping equation of motion can also be written as a set of two first-order ordinary differential equations (ODEs) in $\overset{\star}{\beta}$ and β, as

$$\frac{d}{d\psi}\left\{\begin{array}{c}\overset{\star}{\beta}\\ \beta\end{array}\right\}+\left[\begin{array}{cc}0 & \nu_\beta^2\\ -1 & 0\end{array}\right]\left\{\begin{array}{c}\overset{\star}{\beta}\\ \beta\end{array}\right\}=\left\{\begin{array}{c}\dfrac{M_A}{I_b\Omega^2}+M_I'\\ 0\end{array}\right\} \tag{2.32}$$

Notice that the structure of Eq. 2.32 is similar to the rotor wake equation, i.e., Eq. 2.16 and, therefore, it can also be solved by using the PC2B scheme to give a consistent second-order level of accuracy.

2.1.5 Ground Effect Modeling Using the Method of Images

Ground effect problems can be modeled in the FVM by using either an image rotor system or a surface singularity method; see Ref. 34. In the present work, the image system approach was used because of its relatively low computational cost. In this method, an image of the "real" rotor system and its wake (above the ground) are used to simulate the ground plane; see Fig. 2.6. The strength of the vortex filaments from the image and the "real" rotor system are equal and opposite to each other. The Lagrangian markers of the "real" rotor system are convected under the influence of all the vortical elements present in the flow field, including those from the image rotor system. Consequently, the total normal component of velocity at $z/R = 0$ becomes zero, which implicitly satisfies the flow tangency condition at all points over the ground plane. With the singularity method, many panels must be used to explicitly satisfy flow tangency conditions over the ground plane, which can incur very high computational overheads. Nevertheless, the panel method approach lends itself more readily to the modeling of non-planar surfaces.

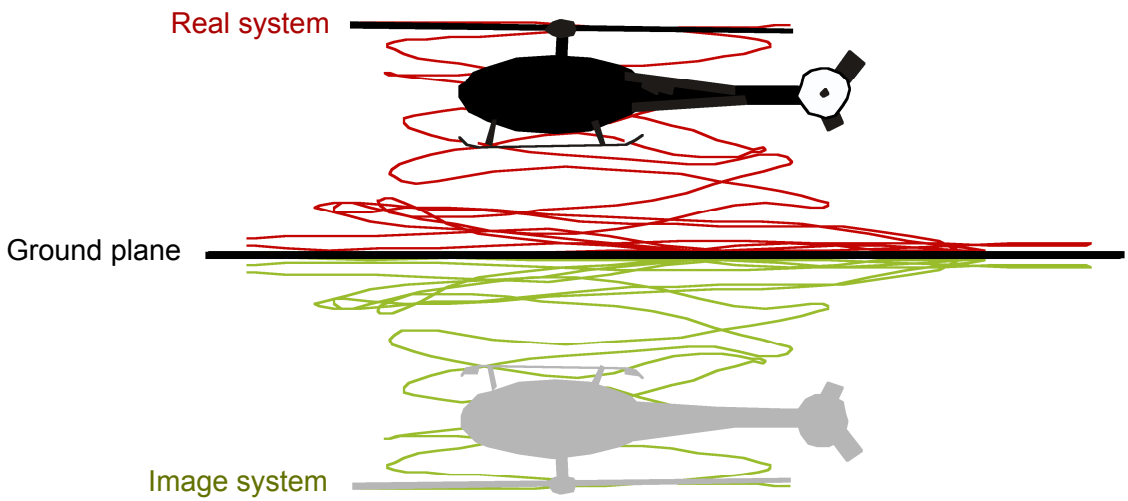

Figure 2.6: A representative free-vortex wake solution obtained using the "method of images" for a rotor operating IGE.

Because the total number of Lagrangian markers for modeling ground effect problems become twice that of those in out of ground effect, the cost of Biot-Savart computations increase by a factor of four because cost is $\sim O(N_v^2)$ where N_v is the total number of vortices from the "real" rotor system. To save the computational cost of updating the marker positions of the image system, these positions can also be obtained as the mirror images of the real rotor marker positions about the ground plane at each time step. This approach also saves on the computer memory requirements because no extra arrays are required to save the positions and strengths of vortex filaments of the image rotor system.

2.1.6 Rotor Trim Methodology

The aerodynamic response of a rotor is a coupled function of the blade control angles and the resulting aerodynamic environment. The positions and strengths of the tip vortex filaments depend upon the rotor operating conditions. Therefore, to obtain the

aerodynamic response for a given flight condition, the rotor must be trimmed to obtain the necessary control angles to produce the required thrust and orientation of the rotor disk plane.

In the present work, the control angles of the rotor blades are calculated to maintain a required thrust such that the rotor tip-path-plane (TPP) is perpendicular to the axis of rotation of the rotor, i.e., the cyclic flapping angles were set so as to be zero during the trimming process. The procedure used to implement trim is based on the Newton-Raphson method, and is the same as that discussed in Ref. 99. For the case of the rotor in ground effect operation, the trimming process is the same as that for the isolated "real" rotor system. The only difference is that the aerodynamic response of the real rotor system is calculated by considering the influence of all the vortical elements of the image rotor system.

The rotor control input vector, $\mathbf{x}$, comprising of blade collective θ_0 lateral cyclic θ_{1c} and longitudinal cyclic θ_{1s} angles (i.e., $\mathbf{x} = \{\theta_0, \theta_{1c}, \theta_{1s}\}^T$), is updated in the trim procedure using a Newton-Raphson approach such that the desired response response vector, $\mathbf{y}$, comprising of thrust and orientation of the TPP (i.e., $\mathbf{y} = \{C_T, \beta_{1c}, \beta_{1s}\}^T$), is obtained. The change in the response vector $\mathbf{y}(\mathbf{x}+\Delta\mathbf{x})$ is approximated using a Taylor series expansion, as given by

$$\mathbf{y}(\mathbf{x}+\Delta\mathbf{x}) = \mathbf{y} + [\mathbf{J}]\Delta\mathbf{x} + \ldots \tag{2.33}$$

The trim Jacobian matrix, **J** is expressed as

$$\mathbf{J} = \frac{\partial \mathbf{y}}{\partial \mathbf{x}} = \begin{bmatrix} \frac{\partial C_T}{\partial \theta_0} & \frac{\partial C_T}{\partial \theta_{1c}} & \frac{\partial C_T}{\partial \theta_{1s}} \\ \frac{\partial \beta_{1c}}{\partial \theta_0} & \frac{\partial \beta_{1c}}{\partial \theta_{1c}} & \frac{\partial \beta_{1c}}{\partial \theta_{1s}} \\ \frac{\partial \beta_{1s}}{\partial \theta_0} & \frac{\partial \beta_{1s}}{\partial \theta_{1c}} & \frac{\partial C_T \beta_{1s}}{\partial \theta_{1s}} \end{bmatrix} \tag{2.34}$$

The updated perturbation is then obtained by rearranging Eq. 2.33 to give

$$\Delta \mathbf{x} = [\mathbf{J}]^{-1} \begin{Bmatrix} C_T - C_{T_{req}} \\ \beta_{1c} \\ \beta_{1s} \end{Bmatrix} \longrightarrow 0 \tag{2.35}$$

where $C_{T_{\text{req}}}$ is the target total thrust coefficient of the rotor system.

The trim is performed by using an initial guess of the input control vector, which is then updated by solving Eq. 2.35. The Jacobian matrix is calculated using a first-order forward difference approximation. This approximation is performed by first calculating the initial response vector based on the initial guess at the input vector. The input vector is then perturbed, and the response vector is recalculated to find the Jacobian matrix.

2.2 Modeling of the Flow Near the Ground

The presence of an impervious ground plane below the rotor significantly affects its developing wake structure. Representative flow velocity measurements (Ref. 20) on the ground below a rotor at several downstream distances are shown in Fig. 2.7, where the developing wall-jet and boundary layer region are evident. The flow in this near-wall region obviously affects the entrainment of sediment particles from the ground. The threshold entrainment models (discussed next) are based on the calculation of the friction velocities

in this region, which means that the details of the flow here must be well represented if brownout conditions are to be predicted. The challenge is to perform such a calculation with results equivalent to those of a full viscous solution.

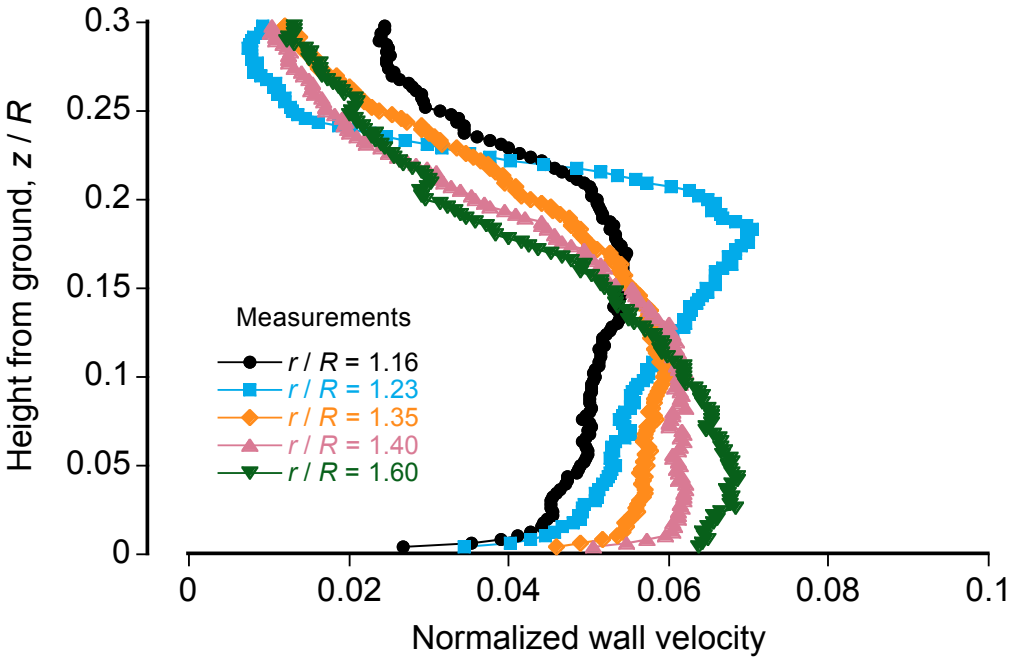

Figure 2.7: Representative measurements of the flow on the ground below a hovering rotor at several downstream distances from a point below the rotational axis of the rotor r. The distance is normalized with the rotor radius R and the wall velocity is normalized with rotor tip speed ΩR. (Source: Ref. 20)

The flow field predicted using the FVM is fundamentally inviscid, so it does not satisfy the physical no-slip condition at the ground plane. An example of this behavior is shown in Fig. 2.8 in terms of the components of velocity parallel to the wall at several downstream distances, which is obtained for similar conditions to that shown previously in Fig. 2.7. Therefore, another type of model must be used to represent the region very near the ground.

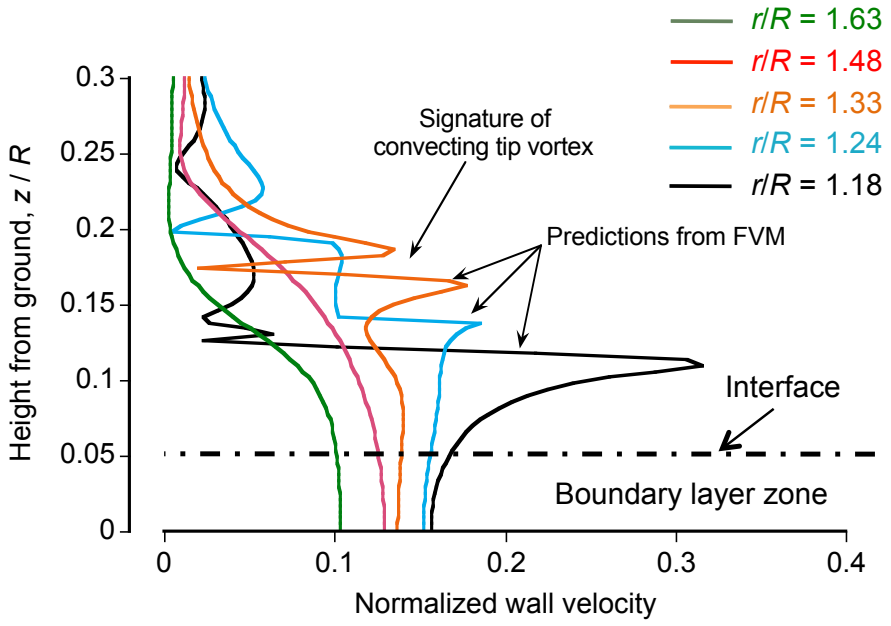

Figure 2.8: Representative computed velocity profiles made from the free-vortex method (FVM) at several radial locations, r/R, from the rotational axis.

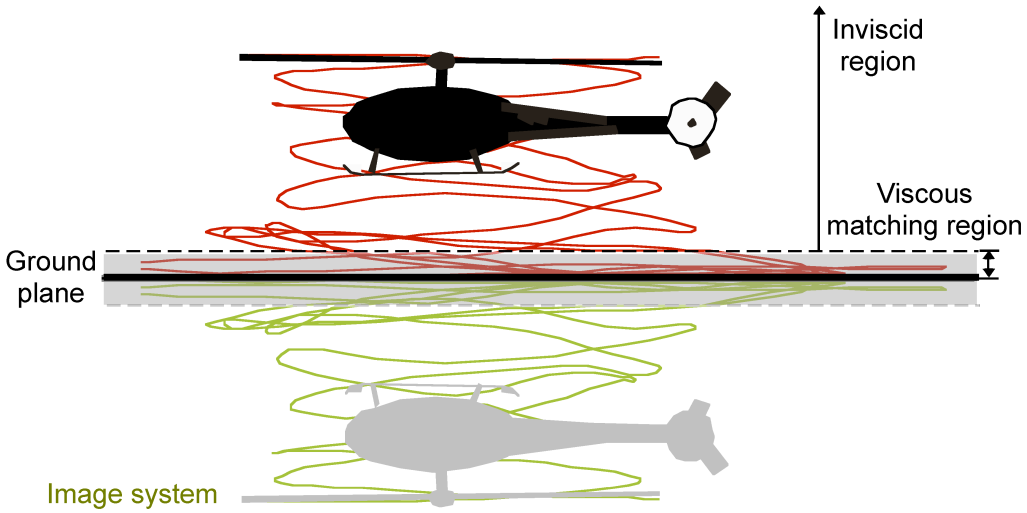

Figure 2.9: Free-vortex wake solution and matching viscous interface for the particle mobility calculations.

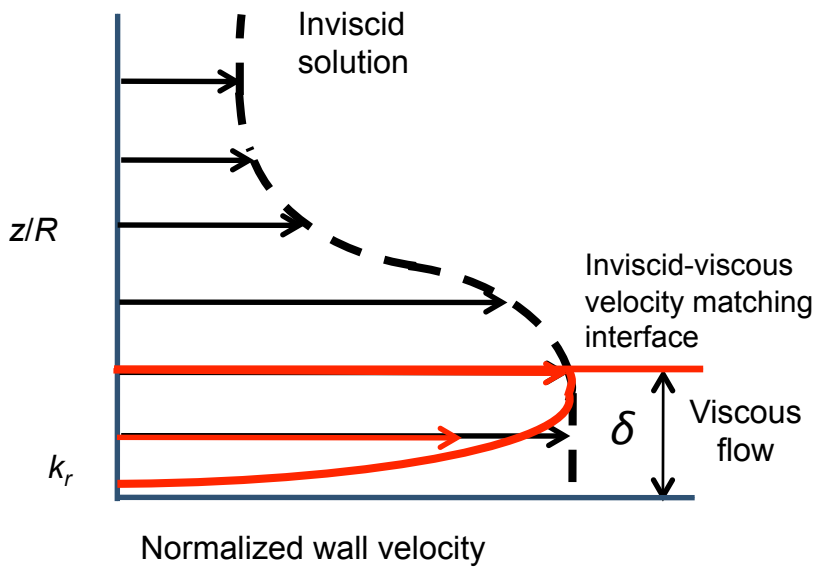

Figure 2.10: Schematic showing the inviscid-viscous matching of the velocity field over an interface in the near-wall region.

In the present work, an inviscid-viscous method was developed to predict the flow field arising from a combination of the rotor flow (modeled as an inviscid potential flow) and the resulting (viscous) flow in the boundary layer region at the ground; see Figs. 2.8 and 2.9. A schematic of the approach used is shown in Fig. 2.10. In this model, the effect of the rotor wake solution (obtained from the FVM) provides the induced velocity field at a computational interface that is located at a small distance above the ground (of the order of the boundary layer thickness, δ). The induced velocity field at the edge of the interface is determined from the vortex wake positions and strengths using the Biot-Savart law; see Section 2.1.1. The flow parameters in the viscous region are then matched to the inviscid solution at the interface by using a semi-empirical boundary layer profile. In the present work, a self-similar logarithmic boundary profile was assumed, which can be written in

the form

$$u(z) = \frac{u_\star}{k} \log\left(\frac{z}{k_r}\right) \tag{2.36}$$

where k_r is the assumed equivalent roughness height of the ground surface, $k = 0.4$ is Von Kármán's constant, z is the height above the ground within the boundary layer region, and $u_\star$ is the friction velocity. The velocity field $u(z)$ within the boundary layer region can be obtained from Eq. 2.36, if the values of k_r and $u_\star$ are known.

The value of k_r can be approximated as 0.0333 d_p, as given by Bagnold (Ref. 23), when the particles are at rest, although the value of k_r may also be affected by several other parameters. In general, however, k_r increases as particles are uplifted and so this effect also changes the value of $u_\star$ (Ref. 25).

The friction velocity, $u_\star$, is a representation of the shear stresses on the ground, and can be expressed as

$$u_\star = \sqrt{\tau/\rho} \tag{2.37}$$

The quantity $u_\star$ is often used in particle entrainment studies, where the onset of particle motion is based on the attainment of a critical threshold friction velocity, $u_{\star t}$. The values of $u_{\star t}$ as obtained from particle mobility observations in canonical (mostly uniform) flows passing over sediment beds of certain known (or estimated) characteristics (Ref. 23). An increase in the velocity induced by the surface flows increases the friction velocity, and when the friction velocity reaches a certain threshold, i.e., $u_\star > u_{\star t}$, particles that are initially in static equilibrium are mobilized and move downstream under the action of the flow.

The value of $u_\star$ in the logarithmic boundary layer can be approximated by matching

the flow parameters in the viscous region to the inviscid solution at the interface; see Fig. 2.10. Notice that the value of $u_\star$ is constant in a logarithmic boundary layer, as given by

$$u_\star = \frac{u(\delta)}{k \log(\delta/k_r)} \tag{2.38}$$

where δ is representative boundary layer thickness, which can be estimated from experiments. Recent experiments (Refs. 18–20) have shown that the thickness of the boundary layer in the fully developed wall-jet flow on the ground below a rotor is of the order of 5% of the rotor radius. The velocity induced by the rotor wake solution at the interface $u(\delta)$ is then calculated from the FVM. Therefore, the value of $u_\star$ can be calculated by using Eq. 2.38. The value of $u_\star$ obtained from this procedure can then be compared to the threshold friction velocity, as discussed in Section 2.3.3.

After calculating $u_\star$ from Eq. 2.38, the value of $u(z)$ in the near-wall region can be approximated by using Eq. 2.36, as discussed previously. Validation of the assumed logarithmic velocity profile in the near-wall region was obtained by using the near-wall velocity measurements of Milluzzo et al. (Ref. 20) and calculating $u(z)$ near the ground by using Eqs. 2.38 and 2.36. The results are shown in Fig. 2.11, which confirms the validity of the logarithmic approximation of the boundary layer flow.

2.3 Entrainment of Sediment from a Bed

As previously discussed, a fundamental aspect of modeling brownout is to model the particle mobility conditions under the action of unsteady, turbulent, vorticity-laden rotor flow field. Existing particle entrainment models (Refs. 23, 24, 75, 81), which are based

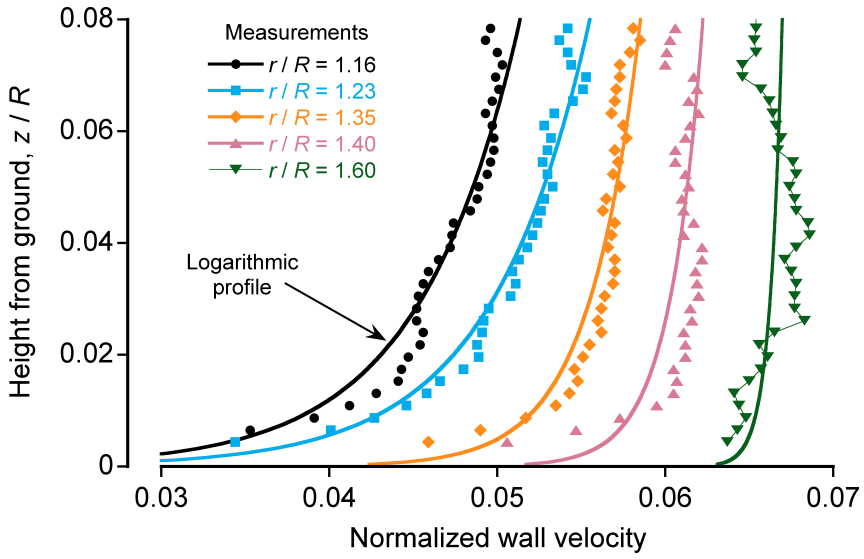

Figure 2.11: Near-wall boundary layer measurements in the flow below the rotor showing that a logarithmic boundary layer profile is a reasonable approximation. (Source of experiments: Ref. 20)

on the determination of $u_{\star_t}$, were originally developed for simpler, one-dimensional, canonical flows. All of the existing brownout simulation methodologies (Refs. 22, 39, 40) use these threshold models to determine particle mobility conditions. Therefore, an assessment of the applicability of these models to the brownout problem is clearly required.

The following section discusses the threshold entrainment mechanisms relevant to rotor-generated flow fields. It discusses the assumptions that were used to develop the threshold friction velocity based models, and analyzes how relevant these assumptions are for the vorticity-laden flow fields typical of rotor flows. In this regard, the significance of unsteady pressure forces in the entrainment of sediment from the bed is also discussed. A new threshold entrainment model is then proposed, which is more appropriate for vortex dominated flow fields.

2.3.1 Forces Acting on Stationary Particles on a Bed

Stationary particles on a bed below the rotor can experience several types of forces such as shear, pressure, inter-particle, and gravitational; see Fig. 2.12. Shear forces on the stationary particles arise because of the high velocity gradients produced by the boundary layer on the sediment bed. The components of the shear force along and perpendicular to the wind direction are referred to as the drag force $\mathbf{F}_d$, and the lift force $\mathbf{F}_l$, respectively; see Fig. 2.12. Significant unsteady pressures may also be produced in the vorticity-laden flow field below the rotor. In fact, the low-pressure zones produced by vortices may have the potential to produce forces, $\mathbf{F}_{\Delta P}$, that can affect the onset of sediment motion (Ref. 83). These aerodynamic forces on the particle (i.e., shear and pressure) will vary as d_p^2. Besides these forces, a particle on the bed also experiences gravitational forces $\mathbf{F}_g$ (which vary as d_p^3) and inter-particle forces $\mathbf{F}_i$. Inter-particle forces comprise of Van der Waals's forces, electrostatic forces, cohesive forces, etc. (Ref. 25). These forces are the most difficult to measure or calculate, and can only be approximated in the development of mathematical models.

In general, a particle subjected to these forces will eventually be mobilized about a point 'P,' as shown in Fig. 2.12, if the moments created by the forces in the flow about this point exceed those of the gravitational and inter-particle forces. This process can be referred to as direct aerodynamic entrainment. The effects of shear forces on sediment entrainment have been studied previously (Refs. 23–25) in steady, unidirectional flow fields. However, the effects of unsteady flows and external pressure forces are not well understood. Greeley et al. (Ref. 83) showed that the contributions of pressure forces

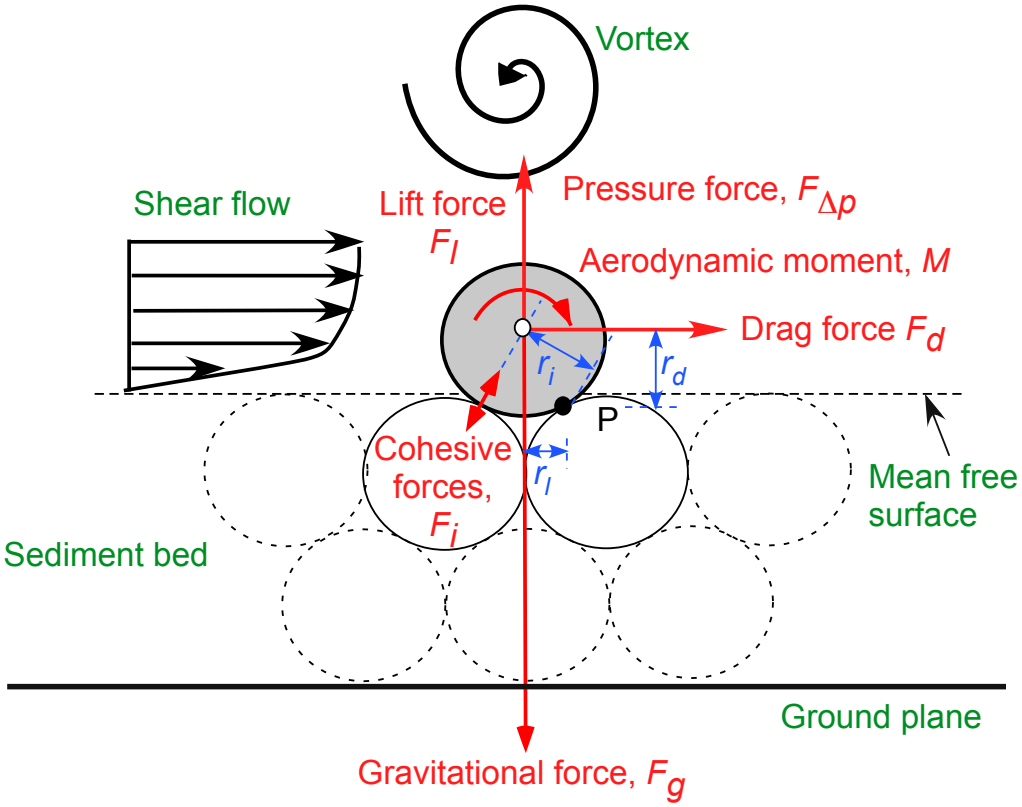

Figure 2.12: Forces acting on sediment particles at the surface of a mobile bed.

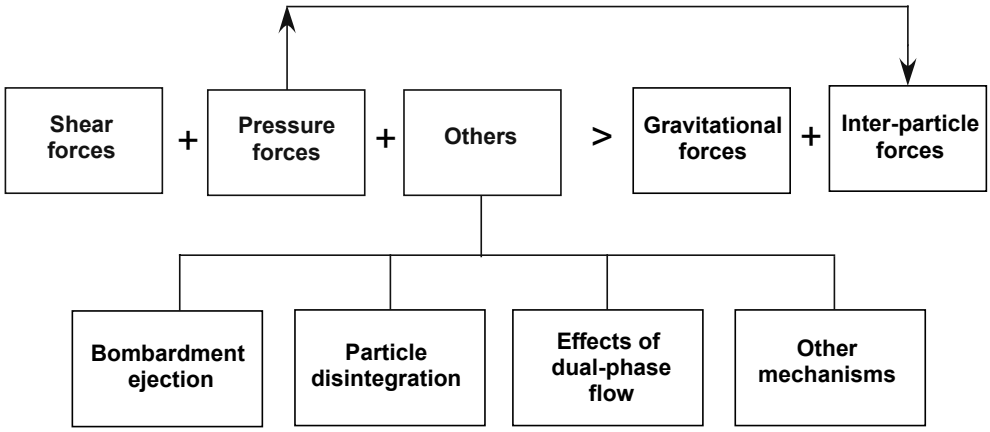

Figure 2.13: A schematic showing the potential sediment mobilization and entrainment processes in the brownout problem.

in vortical flows can be significant for the entrainment of smaller sized or dust particles. These particles are usually very cohesive and are generally difficult to entrain by the action of shear stresses alone. Studies conducted to understand the fluidization of packed beds have shown that the pressure differences on the bed can also affect the inter-particle forces and, therefore, can affect the entrainment of smaller dust particles (sometimes known as Geldart-C particles); see Ref. 111. These processes are discussed later in Section 2.3.3.

Another significant mobilization mechanism in a rotor-induced flow field is by bombardment ejections. This process occurs when previously suspended sediment particles in the flow impact the sediment bed with significant downward velocity and momentum, plough through the bed, and then eject more particles. Research in aeolian sciences (Ref. 28) has shown that this particular mechanism can be a major contributor to the mobilization and ejection of small-sized dust particles. The modeling of this mechanism is discussed in Section 2.5.

Other mechanisms affecting sediment mobility can be attributed to factors that include the effects of dual-phase flow fields. Studies with packed bed fluidization show that the upward flow through the bed can create pressure difference, which can affect the inter-particle forces (Refs. 111 and 112). It is also known that a packed bed is subject to vibrations can affect the inter-particle forces (Ref. 111). In the case of a rotor, the presence of the blade tip vortices, vortex sheets, and secondary vortical structures near the bed can produce eddies and turbulence on the bed that may affect the behavior of the inter-particle forces. Such complex processes need much further understanding, which can be achieved by means of well posed experiments.

Other sediment entrainment mechanisms can arise because of the effects of differ-

ently sized particles, which occurs because of the relative submergence of smaller particles within the boundary immediately adjacent to bigger particles. Disintegration of larger particles, such as after colliding with the bed or other particles, may be another contributor to the ejection of smaller particles. However, these latter mechanisms are obviously much more difficult to model, and are not considered in the present work.

The schematic shown in Fig. 2.13 summarizes most of the sediment entrainment mechanisms that are known to occur on a mobile bed below a rotor. Although it is not possible, at present, to model all of these mechanisms, what is clear is that sediment entrainment in the brownout dust clouds is a very complex behavior and the level of understanding at this point is not sufficient to devise first-principles based mathematical models that can include representations of all the various (and interdependent) effects. However, the present work attempts to provide better understanding of the mobilization mechanisms, and ultimately proposes a new model to determine mobility conditions.

2.3.2 Calculation of the Unsteady Pressures in the Flow

The rotor flow field in ground effect is overall irrotational, except within the core of the vortex and in the boundary layer region. In an unsteady and irrotational flow field (i.e., outside of the vortex core and above the boundary layer), the unsteady pressure can be calculated by the spatial integration of Euler's equation (Ref. 49), which results in the so-called unsteady Bernoulli's equation (or Kelvin's equation), which can be written as

$$\frac{|\mathbf{V}|^2}{2} + \frac{p}{\rho} + \frac{\partial \phi}{\partial t} = \text{constant} \tag{2.39}$$

where $\mathbf{V}$ is the flow velocity at any point in the rotor flow, p is the pressure at that point, and ϕ is the velocity potential, i.e., $\mathbf{V} = \nabla\phi$. The velocity, $\mathbf{V}$, is calculated by considering the induced effects of all the vortical elements present in the rotor flow, i.e., the bound, the near-wake and all of the free-vortex segments. These effects are calculated by invoking the Biot-Savart law; see Section 2.1.1.

The term $\frac{\partial\phi}{\partial t}$ in Eq. 2.39 represents the time rate of change of the velocity potential because of the motion of the vortex elements in the rotor flow field. Therefore, the contributions from the movement of the near-wake, the bound vortices, and the free-vortex markers at any point in the flow field must be considered. The value of $\frac{\partial\phi}{\partial t}$ at any point in the flow, as induced by a vortex filament of strength Γ, moving with velocity $\mathbf{V}$, is given by

$$\frac{\partial\phi}{\partial t} = -\mathbf{V}_v \cdot \mathbf{V} + \phi\frac{\partial(\ln\Gamma)}{\partial t} \tag{2.40}$$

This method was also used by Lorber & Egolf (Ref. 113). Notice that for a free-vortex filament, the strength is constant and, therefore, the second term of Eq. 2.40 is zero.

Using Eq. 2.39, then the unsteady pressure, P, can be written as

$$P = P_\infty + \frac{1}{2}\rho(V_\infty^2 - |\mathbf{V}|^2) - \rho\frac{\partial\phi}{\partial t} \tag{2.41}$$

If there are N_v vortex elements in the flow field, then the value of P at any j^{th} point in the flow field is

$$P_j = P_\infty - \frac{1}{2}\rho|\mathbf{V}_j|^2 + \rho\sum_{i=1}^{N_v}\mathbf{V}_{v_i}\cdot\mathbf{V}_{ij} \tag{2.42}$$

where $\mathbf{V}_{v_i}$ is the velocity of i^{th} vortex element, and $\mathbf{V}_{ij}$ is the velocity induced by the i^{th} vortex element at the j^{th} point in the flow field.

2.3.3 Modeling of Direct Aerodynamic Entrainment of Particles

Numerical modeling of the direct entrainment of each particle is a complex process because of several reasons. First, an actual brownout cloud comprises particles of different shapes and sizes. Second, solving for the moment equilibrium condition at each sediment particle to determine the onset of mobility requires a knowledge of its immediate neighbors, which significantly increases the computational expense of the problem. Third, the entrainment of very small particles is determined mainly by inter-particle forces. However, modeling of these forces is difficult because of the unavailability of general mathematical expressions to describe such physical effects.

Several assumptions and empirical results have to be used to determine the onset of sediment mobility and the initiation of particle entrainment by direct mechanisms. In the present work, direct entrainment was modeled at the mesoscale, i.e., semi-empirical models of the particle effects were used to represent these mechanisms. To this end, the particles were assumed to be equivalent spheres of uniform density.

As mentioned earlier, the process of direct entrainment has been studied extensively for various canonical flows. Several models have been developed, based on the empirical determination of $u_{\star t}$, by considering the balance of forces acting on a particle in these fully turbulent flows, e.g., Bagnold (Ref. 23) and Greeley & Iversen (Ref. 24). However, the flow field generated by a rotor is laden with vorticity, and is more complex than the canonical flows that have been considered previously (Ref. 17). Ultimately, a new entrainment model is required that includes the primary entrainment mechanisms observed in vortex-dominated flows.

The only known experimental measurements of the threshold velocity in vortical flows have been obtained by Greeley et al. (Ref. 83). These experiments were conducted to understand the mobilization of particles of different sizes and densities in dust devils, which are "tornado" types of vortices. These vortices have their axis of rotation (and so their vorticity vector) aligned perpendicular to the ground plane, which is in contrast to the more parallel axis of rotation seen with rotor wake vortices. In the absence of the needed measurements of particle mobilization in rotor flows, Greeley's results were used in the present work to help understand the fundamental mechanisms of particle mobilization as they may ultimately affect the brownout problem.

In the present work, an entrainment model has been developed based on previous research by Bagnold (Ref. 23), Greeley & Iversen (Ref. 24), and Shao (Ref. 25). The forces acting on a stationary particle on the sediment bed are shown in the schematic of Fig. 2.12. These forces include lift from viscous effects $\mathbf{F}_l$, lift from unsteady suction pressure $\mathbf{F}_{\Delta P}$, gravitational force $\mathbf{F}_g$, drag force $\mathbf{F}_d$, inter-particle force $\mathbf{F}_i$, and moment force $\mathbf{F}_m$. The magnitude of these forces can be written as $F_d = |\mathbf{F}_d|$, etc., and the moment arm lengths can be represented as r_l, r_d, r_m, and r_i; see Fig. 2.12. The moment balance on the particle about point 'P' can be expressed as

$$(F_l + F_{\Delta P} - F_g)\, r_l + F_d r_d + F_m r_m - F_i r_i = 0 \tag{2.43}$$

In reality, the moment arms depend upon the distribution of particles on the bed, but for simplicity they can be assumed to be proportional to the particle diameter, d_p, (Refs. 23 and 24). Therefore, they can be written as: $r_l = a_l d_p$, $r_d = a_d d_p$, $r_m = a_m d_p$, and $r_i = a_i d_p$,

and so Eq. 2.43 becomes

$$\left(F_l + F_{\Delta P} - F_g\right) a_l + F_d a_d + F_m a_m - F_i a_i = 0 \tag{2.44}$$

The drag force, F_d, was approximated using

$$F_d = \frac{1}{2} \rho A_s C_{d_s} U_s^2 \tag{2.45}$$

where C_{d_s} is the drag coefficient of the particle when it is stationary on the bed, A_s is the frontal area of the particle that is exposed to the flow, and U_s is the characteristic flow velocity. The calculation of F_d is difficult because the behavior of C_{d_s} is not well understood (Refs. 23 and 25). Also, the choice of U_s is a difficult one because the drag force at the threshold condition may be determined from a momentary increase in the flow velocity from turbulence. However, the mean value of the drag force depends upon the velocity in the boundary layer region and, therefore, it depends upon the shear.

Based on these considerations, Bagnold expressed Eq. 2.45 as

$$F_d = K_d \rho d_p^2 u_\star^2 \tag{2.46}$$

where $u_\star = \sqrt{\tau/\rho}$ is the friction velocity and K_d is a non-dimensional coefficient. Based on this representation of the drag force, Greeley & Iversen (Ref. 24) represented the other aerodynamic forces, which are viscous in nature, as

$$F_l = K_l \rho d_p^2 u_\star^2 \tag{2.47}$$

$$F_m = K_m \rho d_p^2 u_\star^2 \tag{2.48}$$

where K_l, and K_m are the non-dimensional lift and moment coefficients, respectively.

Greeley's experiments (Ref. 83) also suggested that there is a lift force $F_{\Delta P}$, which acts on the particles because of the low pressure created by vortices on the bed. This

force acts in addition to the lift force F_l that is generated by viscous effects. It is easier to quantify the effects of F_l because it depends upon the shear stresses. However, it is more difficult to quantify the effects of $F_{\Delta P}$ on the particles lying on the bed. The challenge lies in determining the extent to which the pressure difference, ΔP, affects the mobility of the particles on the bed.

In the present work, the pressure force, $F_{\Delta P}$, was modeled by using certain assumptions. Firstly, it was assumed that the top half surface of the stationary particle on the bed is acted upon by uniform pressure, which is created by the presence of vortices in the flow field. Secondly, it was assumed that the bottom half surface of the particle is acted upon by the ambient pressure, P_∞. Using these assumptions, the pressure difference, ΔP, acting at the stationary particle can be calculated using Eq. 2.42 as

$$\Delta P_j = -\frac{1}{2}\rho|\mathbf{V}_j|^2 + \rho\sum_{i=1}^{N_v}\mathbf{V}_{v_i}\cdot\mathbf{V}_{ij} \tag{2.49}$$

The resulting force acing on the particle due to the pressure difference, ΔP, can then be written as

$$F_{\Delta P} = -K_p \Delta P d_p^2 \tag{2.50}$$

where K_p is the non-dimensional constant that depends upon the fraction of the particle cross-sectional area affected by the pressure forces; the value of K_p in the present work was $\pi/4$. This force can be approximated to act along the vertical direction, as shown in Fig. 2.12.

The gravitational force F_g with buoyancy effects (i.e., using the effective weight of the particle) can be written as

$$F_g = \frac{\pi}{6}(\rho_p - \rho) g d_p^3 \tag{2.51}$$

Substituting the forces given by Eqs. 2.46, 2.47, 2.48, and 2.51 into Eq. 2.44 gives

$$a_t K_t \rho u_{\star_t}^2 d_p^2 - a_l K_p \Delta P d_p^2 = a_l \frac{\pi}{6}(\rho_p - \rho) g d_p^3 + a_i F_i \tag{2.52}$$

where $a_t K_t = a_l K_l + a_d K_d + a_m K_m$, which is a function of $Re_\star$ as suggested by Greeley & Iversen (Ref. 24). Simplifying Eq. 2.52 gives

$$\rho u_{\star_t}^2 = \frac{a_l K_p}{a_t K_t}\Delta P + \frac{a_l}{a_t K_t}\frac{\pi}{6}(\rho_p - \rho) g d_p + \frac{a_i}{a_t K_t}\frac{F_i}{d_p^2} \tag{2.53}$$

The expression for the threshold friction velocity, $u_{\star_t}$, can then be written as

$$u_{\star t} = A\sqrt{\frac{6}{\pi}\frac{K_p}{\rho}\Delta P + \frac{\rho_p - \rho}{\rho} g d_p + \frac{6}{\pi}\frac{a_i}{a_l}\frac{F_i}{\rho d_p^2}} \tag{2.54}$$

where $A^2 = \dfrac{a_l}{a_t K_t}\dfrac{\pi}{6}$. Using the value of $K_p = \pi/4$, this equation becomes

$$u_{\star t} = A\sqrt{\frac{3}{2}\frac{\Delta P}{\rho} + \frac{\rho_p - \rho}{\rho} g d_p + \frac{6}{\pi}\frac{a_i}{a_l}\frac{F_i}{\rho d_p^2}} \tag{2.55}$$

Notice from this foregoing equation that $u_{\star t}$ decreases with ΔP until $u_{\star t} = 0$. This leads to the concept of a threshold pressure difference, ΔP_t, which determines sediment mobility conditions in the absence of shear forces, i.e., when $u_{\star t} = 0$. The expression of ΔP_t can be written as

$$\Delta P_t = -\frac{2}{3}\left((\rho_p - \rho) g d_p + \frac{6}{\pi}\frac{a_i}{a_l}\frac{F_i}{d_p^2}\right) \tag{2.56}$$

Therefore, if the unsteady pressure difference, ΔP, acting on the particle is smaller than the threshold pressure difference, ΔP_t, then the particle can become mobilized and uplifted from the bed even in the absence of shear effects.

2.3.3.1 Threshold Model Without Pressure Effects

Several models have been developed to simulate the mechanisms of sediment entrainment in simple one-dimensional canonical flow fields (i.e., with $\Delta P = 0$). Some of the

well-known models in this category are those developed by Bagnold (Ref. 23), Greeley-Iversen (Ref. 24), and Shao & Lu (Ref. 75). A brief discussion of these models, along with their assumptions and approximations, is presented in the current section.

Bagnold's Threshold Model

Bagnold (Ref. 23) approximated the terms in Eq. 2.44 by considering the balance of only drag and gravitational forces. Bagnold (Ref. 114) also stated that the initial upward acceleration of a stationary particle from a surface arises because of the lift force that acts on the particle, but this force becomes very small as soon as the particle becomes airborne. Bagnold neglected the lift force and the cohesive forces in the development of his expression for $u_{\star_t}$. In this case, Eq. 2.55 becomes

$$u_{\star t} = A_B \sqrt{\frac{\rho_p - \rho}{\rho} g d_p} \tag{2.57}$$

where $A_B = \sqrt{\frac{\pi}{6} \frac{a_l}{a_d K_d}}$ is a dimensionless number that depends upon the particle-friction-velocity Reynolds number $Re_\star = u_\star d_p / \nu$. The coefficient A_B has also been termed the non-dimensional threshold friction velocity parameter (Ref. 75), and can be written as

$$A_B = \frac{u_{\star t}}{\sqrt{\frac{\rho_p - \rho}{\rho} g d_p}} \tag{2.58}$$

Bagnold (Ref. 23) found that for particles with $Re_\star > 3.5$, the surface becomes "rough," i.e., the downstream particles behave as "obstacles" in the path of the fluid, and small eddies are shed from the lee faces of these particles. For these "rough" flows on the bed, the coefficient A_B was found to have a value of 0.1 in air.

For particles of very small size, or flows with very small friction velocities, the value of $Re_\star$ can become smaller than 3.5. The experimental data from Bagnold (Ref. 23) sug-

gested that for very small-sized particle the value of $u_{\star t}$ increases with a decrease in d_p. Therefore, there is an optimum particle size for which $u_{\star t}$ reaches a minimum. Bagnold suggested that the value of $Re_\star$ for this optimum was 3.5. For $Re_\star < 3.5$ the coefficient A_B is no longer a constant, and its value increases rapidly with decreasing particle size. This effect was explained such that the surface comprising of very small particles becomes "smooth," i.e., the particles do not shed small eddies in this case, and lie in the viscous sub-layer region. Therefore, these particles require higher drag forces to become mobilized.

Greeley-Iversen Threshold Model

Iversen et al. (Ref. 115) suggested that the increase in the threshold friction velocity seen in the experimental data of Bagnold (Ref. 23) and Chepil (Ref. 116) was because of the effects of inter-particle forces, which were neglected in the Bagnold's initial threshold analysis. Greeley & Iversen (Ref. 24) also considered the lift forces on the particle (as shown in Fig. 2.12), which was viscous in origin. However, as also mentioned by Greeley & Iversen (Ref. 24), it is difficult to measure these forces anyway. The aerodynamic forces, which are viscous in origin, i.e., F_l and F_m and F_d, can only be approximated by using Eqs. 2.46, 2.47, and 2.48.

The expression for $u_{\star_t}$, as given by Iversen & White (Ref. 80), can be obtained by writing Eq. 2.55 as

$$A_B = \frac{a_l}{a_t K_t}\frac{\pi}{6}\left(1+\frac{6}{\pi}\frac{a_i}{a_l}\frac{F_i}{(\rho_p-\rho)d_p g}\right) \tag{2.59}$$

Table 2.1: Values of constant A_1 and function $f(Re_{\star t})$ from Iversen & White (Ref. 80).

$Re_{\star t}$	A_1	f($Re_\star$)
$0.03 \leq Re_{\star t} \leq 0.3$	0.2	$(1+2.5Re_{\star t})^{1/2}$
$0.3 \leq Re_{\star t} \leq 10$	0.129	$\left(1.928{Re_{\star t}}^{0.092}-1\right)^{1/2}$
$10 \leq Re_{\star t}$	0.12	$1-0.0858\exp[-0.0617(Re_{\star t}-10)]$

Iversen & White (Ref. 80) hypothesized that

$$A_B = A_1 f(Re_{\star t}) G(d_p) \tag{2.60}$$

where A_1 is a constant, and $f(Re_{\star t})$ is a function of particle friction velocity Reynolds number, i.e.,

$$f(Re_{\star t}) = u_{\star t} d_p / \nu \tag{2.61}$$

The value of $G(d_p)$ depends on particle diameter. The values of these parameters were obtained by Iversen & White (Ref. 80) by fitting curves to their measured data. The values of A_1 and $f(Re_{\star t})$ are given in Table 2.1, and the expression for $G(d_p)$ is

$$G(d_p) = \left(1 + b/\rho_p g d_p^{2.5}\right)^{1/2} \tag{2.62}$$

where $b = 0.006$ gcm$^{0.5}$sec^{-2}. The value of $u_{\star t}$ from this model can be obtained by iteratively solving Eqs. 2.58, 2.60, 2.61 and 2.62, respectively.

Shao & Lu Model

Shao & Lu (Ref. 75) approximated the expression of the inter-particle forces, which com-

prise Van der Waal forces, electrostatic forces, cohesive forces, etc., as

$$F_i = \beta_c d_p \tag{2.63}$$

where β_c is a dimensional parameter that depends on the particle properties (i.e., shape, material, etc) and bed surface properties. Substituting Eq. 2.63 into Eq. 2.55, the expression for $u_{\star t}$ is

$$u_{\star t} = A_B \sqrt{\left(\frac{\rho_p - \rho}{\rho} g d_p + \frac{\gamma}{\rho d_p} \right)} \tag{2.64}$$

where

$$A_B = \sqrt{\frac{\pi}{6} \frac{a_l}{a_t K_t}} \quad \text{and} \quad \gamma = \frac{6}{\pi} \frac{a_i}{a_l} \beta_c \tag{2.65}$$

Shao & Lu curve fitted Eq. 2.64 to the measurements of Iversen & White (Ref. 80) and obtained the following values of A_B and γ for Aeolian flows, i.e.,

$$A_B = 0.1109 \quad \text{and} \quad \gamma = 3 \times 10^{-4} \text{ Nm}^{-1} \tag{2.66}$$

The variation of $u_{\star t}$ as predicted by the three models, i.e., Bagnold (Eq. 2.57), Greeley & Iversen (Eq. 2.60), and Shao & Lu (Eq. 2.64) models, is shown in Fig. 2.14 against a threshold friction parameter ϕ, where ϕ is defined as

$$\phi = \sqrt{\frac{\rho_p}{\rho} g d_p} \tag{2.67}$$

The values of $u_{\star t}$ for silica particles ($\rho_p = 2{,}840$ kg m^{-3}) of different sizes are also shown in this plot. Notice that the values of $u_{\star t}$ as predicted by Bagnold's model decreases with ϕ. However, this model is strictly applicable only for $Re_\star > 3.5$ because, as explained previously, A_B does not remain constant for $Re_\star < 3.5$; for these values of Re_p the value of $u_{\star t}$ will increase with a decrease in d_p.

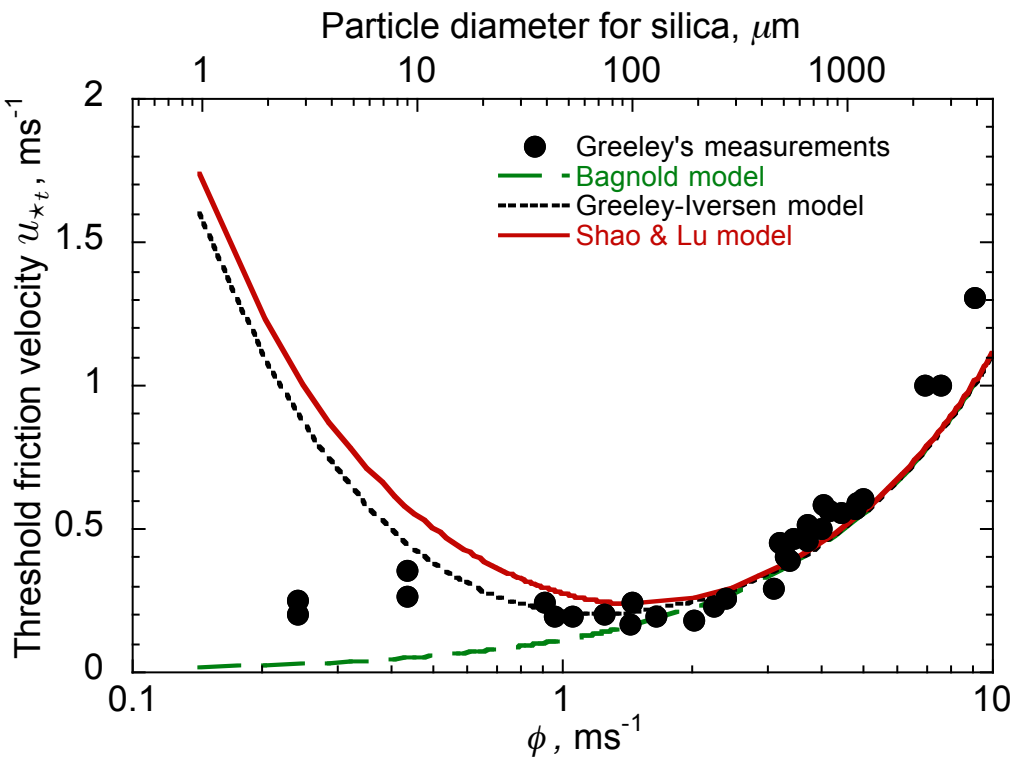

Figure 2.14: Threshold friction velocity as predicted from three models: (a) Bagnold (Ref. 23), (b) Greeley & Iversen (Ref. 24), and (c) Shao & Lu (Ref. 75).

Notice also that for the larger and heavier particles (i.e., with larger values of ϕ), $u_{\star t}$ increases with ϕ, which is because of gravitational forces. For the smaller and lighter particles, $u_{\star t}$ increases with a decrease in ϕ because of the dominance of the inter-particle forces over gravitational forces. Therefore, there exists an optimum value of ϕ at which $u_{\star t}$ is a minimum. A minimum value of $u_{\star t}$ is obtained from Greeley's model at $\phi \sim 1.12$ ms^{-1} or $d_p \sim 60$ μm, and from Shao's model at $\phi \sim 1.5$ ms^{-1} or $d_p \sim 100$ μm. Most (if not all) of the existing brownout dust cloud prediction models (Refs. 22, 39, 40) are based on the use of Shao & Lu's particle mobility criterion.

Figure 2.14 also shows measurements of the particle threshold velocity in vortical flows, as was obtained by Greeley et al. (Ref. 83). These measurements were obtained

for various particles with different sizes and densities. Notice that the measurements of $u_{\star t}$ agree well with the shear stress-based threshold models for the heavier and larger particles with $\phi >\sim 1.5$ ms^{-1} (i.e., for $d_p > 60\,\mu$m with silica). For the smaller and lighter particles with $\phi <\sim 1.5$ ms^{-1} (or for $d_p <\sim 60\,\mu$m with silica), these empirical relations overpredict the threshold velocity. On the basis of these measurements (as shown in Fig. 2.14), Greeley et al. (Ref. 83) concluded that the boundary layer shear mechanism is responsible for the entrainment of the larger and heavier particles. However, the smaller-sized dust particles become mobilized and entrained by the action of the pressure field on the sediment bed caused by the vortices when they are closer to the bed.

The measurements made of $u_{\star t}$ in vortical flows (Ref. 83) also suggest that brownout dust clouds should comprise a larger concentration of smaller and lighter particles, which is confirmed by brownout field tests (Refs. 5 and 6). This observation suggests that the available threshold models that are based on shear effects alone will be insufficient to model sediment mobility in brownout problems, and the inclusion of the unsteady pressure effects will also be important.

2.3.3.2 Model with Unsteady Pressure Effects

As previously discussed, the threshold entrainment models that have been developed thus far have not accounted for unsteady pressure effects, although such effects could potentially play a very significant role in determining the onset of sediment mobility. The threshold model developed in the present work includes the contributions of the unsteady pressure forces in the determination of mobility.

This new model uses the expression for the inter-particle forces as suggested by Shao & Lu (see Eq. 2.63). The resulting expression for $u_{\star t}$ can then be written as

$$u_{\star t} = A\sqrt{\frac{3}{2}\frac{\Delta P}{\rho} + \frac{\rho_p - \rho}{\rho} g d_p + \frac{\gamma}{\rho d_p}} \tag{2.68}$$

Based on Shao & Lu's model (Ref. 75), the value of A and γ were assumed to be equal to 0.1109 and 3×10^{-4} Nm^{-1}, respectively. As mentioned previously, for the values of $|\Delta P| \geq |\Delta P_t|$, a particle can become mobilized even in the absence of shear forces. The value of ΔP_t in this case is

$$\Delta P_t = -\frac{2}{3}\left[(\rho_p - \rho) g d_p + \frac{\gamma}{d_p}\right] \tag{2.69}$$

This value of ΔP_t also depends upon the particle size, diameter, fluid density and inter-particle forces.

Figure 2.15 shows the variation of $u_{\star_t}$ with ϕ (see Eq. 2.67) for different values of ΔP. For $\Delta P = 0$, the model reduces to Shao & Lu's model, as given by Eq. 2.68. With the inclusion of the unsteady pressure term, ΔP, value of $u_{\star_t}$ decreases with a reduction in ΔP; this decrease is clearly significant for particles of intermediate sizes, i.e., those that are not too cohesive or too heavy. Furthermore, the values of $u_{\star_t}$, as given by the new threshold expression (Eq. 2.68), for the smaller values of ϕ do not agree very well with measurements. The reason for this behavior will be discussed later in this section.

Figure 2.16 shows the variation of the threshold shear stress, $\tau_{s_t} = u_{\star_t}^2 \rho$, versus the pressure drop, ΔP, for different values of ϕ. The resulting plots are straight lines with constant slopes of value $\frac{3A}{2}$. The values of $\tau_{s_t} = u_{\star_t}^2 \rho$ for $\Delta P = 0$ is identical to that given by Shao & Lu's model. The shear stress, τ_{s_t}, required to entrain particles decreases with a reduction in ΔP. This result makes intuitive sense because the presence of wall

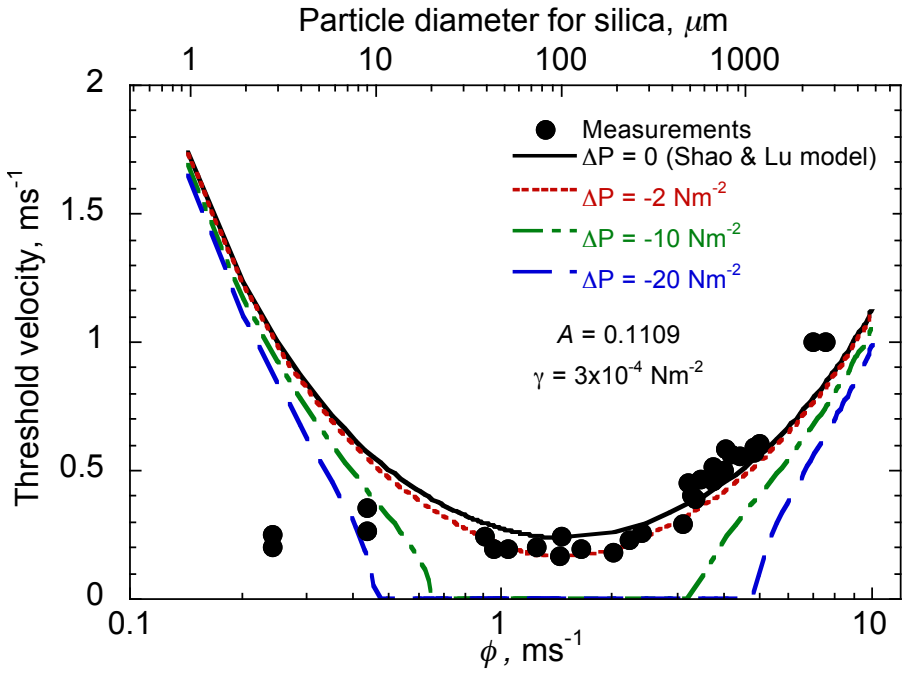

Figure 2.15: Variations of the threshold friction velocity $u_{\star_t}$ as a function of ϕ and ΔP. The value of threshold parameter $\phi = \sqrt{\frac{\rho_p g d_p}{\rho}}$. The corresponding sizes of silica particles with $\rho_p = 2{,}840$ kgm^{-3} are also shown.

normal stresses (produced by the effects of ΔP) will reduce the threshold shear stresses, τ_{s_t}, required to mobilize and entrain a particle. The decrease in the value of τ_{s_t} with ΔP reaches a maximum for medium-sized particles.

Figure 2.17 shows the threshold pressure difference ΔP_t required to mobilize particles in the absence of shear stresses (i.e., when $\tau_{s_t} = 0$). Notice that even a very small decrease in ΔP can be sufficient to mobilize the medium sized particles. For particles with very large or very small values of ϕ, a much larger decrease in ΔP will be required to mobilize them under the conditions where $\tau_{s_t} = u_{\star_t} = 0$.

As previously mentioned, it can be seen in Fig. 2.15 that the predictions from this new model (i.e., Eq. 2.68) do not agree with Greeley's measurements for the smaller and

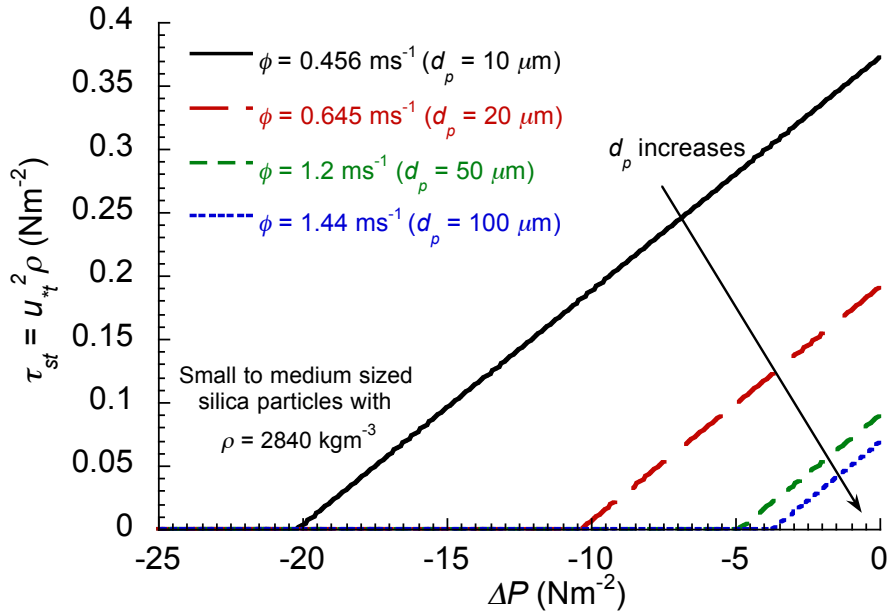

(a) For smaller to medium sized silica particles

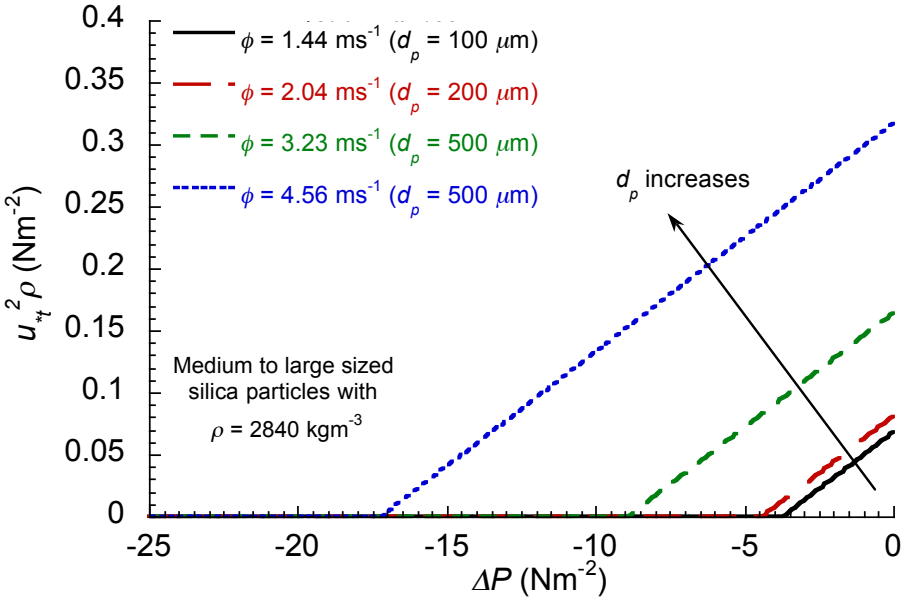

(b) For medium to larger sized silica particles

Figure 2.16: Variation of threshold shear stress $\tau_{s_t} = u_{*_t}^2 \rho$ versus ΔP for: (a) smaller to medium sized particles, and (b) medium to larger sized particles.

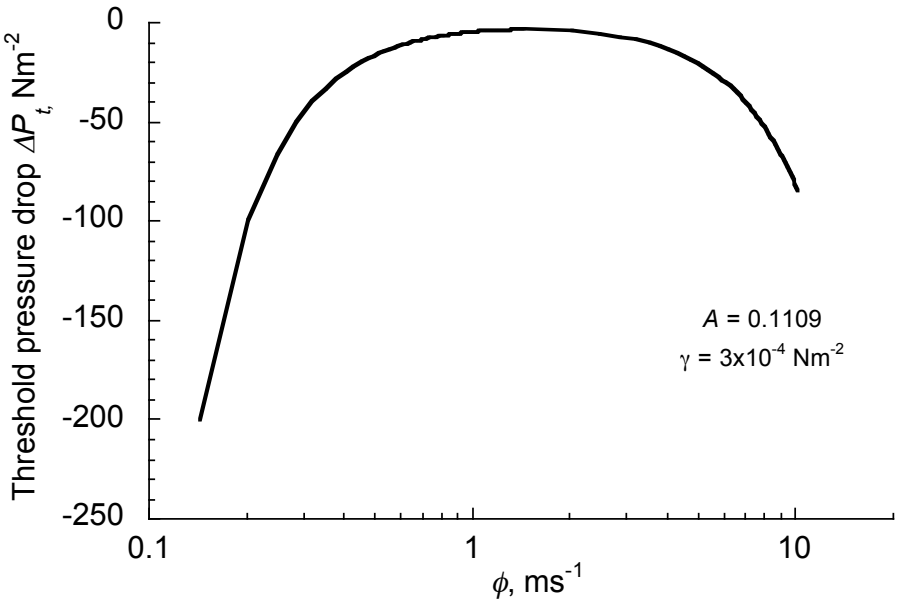

Figure 2.17: Variations of the threshold pressure drop ΔP_t as a function of ϕ and $u_\star$. The corresponding sizes of silica particles with $\rho_p = 2{,}840$ kgm^{-3} are also shown.

lighter particles, i.e., for smaller values of ϕ. This outcome suggests that the cohesive behavior of these particles may also be influenced by the effects of a pressure field. In fact, Greeley & Iversen (Ref. 24) mentioned that the tensile stress τ_s created by cohesive forces can be a different function of particle diameter in vortex-dominated flows compared to boundary-layer flows.

The variation of inter-particle forces with ΔP has been studied in fluidization studies of packed beds comprising of very fine particles with $d_p < 30\,\mu$m, i.e., Geldart C particles. Jaraiz et al. (Ref. 111) has shown that the fluid flowing upwards through a packed bed creates a pressure difference across the bed, which can cause the bed to expand. This effect increases the porosity of the bed and decreases the number of contact points per particle, which results in a decrease in the inter-particle forces. Xu & Zhu (Ref. 112) also showed that inter-particle forces can be sensitive to atmospheric conditions. They studied

the effects of temperature on inter-particle forces, and found that changes in temperature can change the Hamakar constant (Ref. 117), and therefore, the Van der Waal forces. Although enough evidence exists to suggest that the inter-particle forces are sensitive to the value of ΔP on the bed, modeling of this effect is still difficult because of the scarcity of observations of the behavior.

The effects of F_i on $u_{\star t}$ can be shown by representing F_i in Eq. 2.55 as

$$F_i = \beta_c d_p^{n_1} \tag{2.70}$$

The resulting particle mobilization condition then becomes

$$u_{\star t} = A\sqrt{\frac{3}{2}\frac{\Delta P}{\rho} + \frac{\rho_p - \rho}{\rho} g d_p + \frac{\gamma}{\rho d_p^{2-n_1}}} \tag{2.71}$$

Two cases were considered to investigate the effects of different values of γ and n_1 on $u_{\star t}$. Although these two parameters should vary with ΔP, this dependence is, at least for now, unknown. In the first case, the values of $n_1 = 1$, 0.9, 0.8, and 0.7, were used, with the value of γ being 3×10^{-4} Nm^{-1}.

Figure 2.18(a) shows the variation of $u_{\star t}$ for different values of n_1. Notice that n_1 significantly affects the inter-particle forces and, therefore, affects the value of $u_{\star t}$ of the smaller-sized particles. In the second case, the sensitivity of $u_{\star_t}$ to different values of γ is shown in Fig. 2.18(b). Notice that decreasing γ by an order of magnitude decreases $u_{\star_t}$ for the smaller particles. Overall, these results show that the entrainment of smaller and lighter particles is sensitive to the inter-particle forces. Wachspress et al. (Ref. 40) used a value of $\gamma = 3 \times 10^{-4}$ Nm^{-1} in their brownout dust cloud simulations, however, the possible effects of ΔP on particle mobility were ignored.

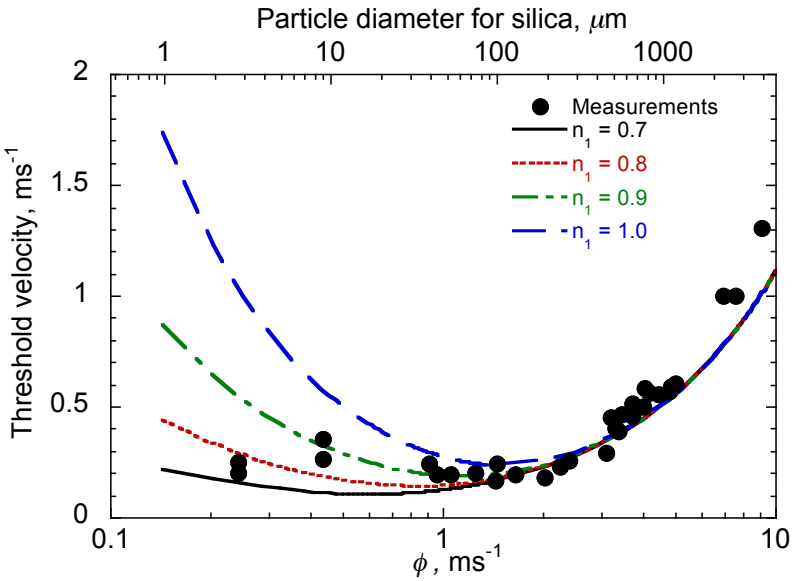

(a) Variation of $u_{\star_t}$ with ϕ for different values of n_1

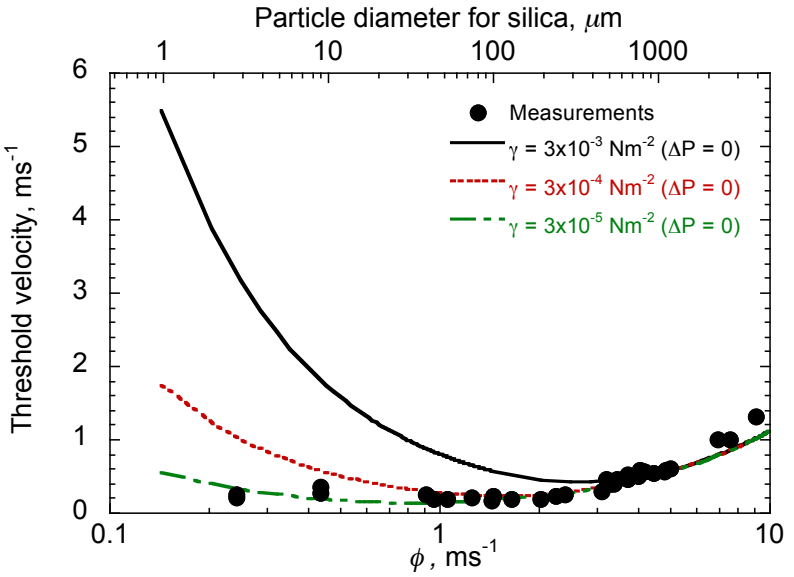

(b) Variation of $u_{\star_t}$ with ϕ for different values of γ

Figure 2.18: Variation of $u_{\star_t}$ with ϕ for different values of: (a) n_1 (with $\gamma = 3 \times 10^{-4}$ Nm^{-1}), and (b) γ (with $n_1 = 1$).

The present work attempts to provide a better understanding of the interdependent effects of different external flow mechanisms in determining sediment mobility. One impediment to doing something more is the difficulty in representing changes in inter-particle forces from pressure difference acting on the bed. These interdependencies can only be understood by making future experiments to identify the needed empirical coefficients. In the present work, the entrainment model as given by Eq. 2.55 was used to obtain the results; this model includes the explicit effects of pressure forces, but the changes in the inter-particle forces from variations in ΔP effects are not modeled.

2.4 Particle Convection

After the particles are entrained into the flow field near the ground, the resulting forces acting upon the particles govern their convective motion. The present section discusses the forces acting on the particles after they become airborne. The development of the particle equations of motion (EOMs) are also discussed, with a description of the associated assumptions that are made in their development. Then, the solution techniques to solve the particle EOMs are discussed, along with details of their stability, accuracy, and convergence characteristics.

2.4.1 Particle Equations of Motion

Figure 1.6(b) (in Chapter 1, Section 1.2.2) showed that the typical ratio of the mass fraction of the dispersed to the carrier phases in a brownout dust cloud is < 0.1 % everywhere except close to the ground. Therefore, it is assumed hereafter that the resulting

two-phase flow is lightly loaded by the particles in that the particle motion is driven by the air but not vice-versa (i.e., an assumption of one-way coupling). This means that the particles are considered as a discrete phase and the path of each individual particle is tracked in time. From the statistics of the particle trajectories, this approach can also be used to calculate particle density concentrations and other useful data such as optical metrics of the dust cloud (Ref. 88).

The forces acting on the uplifted particles are shown in Fig. 2.19, and include a drag force $\mathbf{F}_D$, a lift force $\mathbf{F}_L$, a gravity force $\mathbf{F}_g$, a buoyancy force $\mathbf{F}_b$, an apparent mass force $\mathbf{F}_{\text{am}}$, the Basset forces $\mathbf{F}_{\text{Basset}}$. The Basset-Boussinesq-Oseen (BBO) equation governs the resulting dynamic behavior of the particles. The Basset force, which depends on the time-history of the particle motion, manifests as an apparent drag force. However, it can be neglected because it is important only in flows with very light particles and very steep velocity gradients. Furthermore, apart from drag and gravitational forces, all other forces vary proportionally to the ratio of the gas to particle density, which is of the order of 10^{-3} in air (Ref. 118). Therefore, perhaps with some exceptions, these other forces can be justifiably neglected for brownout problems.

Therefore, the EOMs describing the particles (i.e., the BBO equations) can then be simplified to

$$
\begin{aligned}
m\frac{d\mathbf{V}_p}{dt} &= \sum \mathbf{F} && (2.72)\\
&= \mathbf{F}_D + \mathbf{F}_g + \mathbf{F}_L + \mathbf{F}_{\text{am}} + \mathbf{F}_b + \mathbf{F}_{\text{Basset}} && (2.73)\\
&\simeq \mathbf{F}_D + \mathbf{F}_g && (2.74)\\
&= -\frac{1}{2}\rho\, C_d A \left|\mathbf{V}_p - \mathbf{V}\right| (\mathbf{V}_p - \mathbf{V}) + mg\hat{k} && (2.75)
\end{aligned}
$$

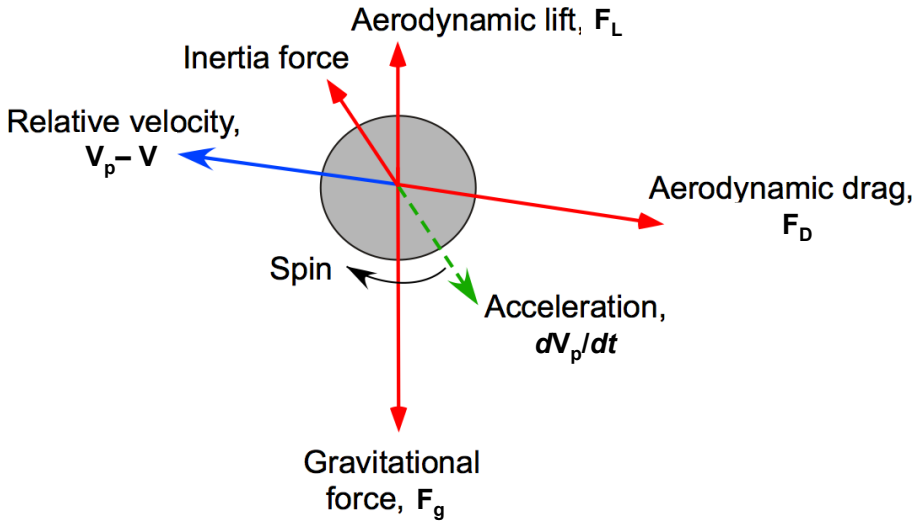

Figure 2.19: Forces acting on an airborne sediment particle.

where $\mathbf{V}_p$ and $\mathbf{V}$ are the particle and flow velocities, respectively. The quantities C_d and A are, respectively, the particle drag coefficient and its cross-sectional area, m is the mass of the particle, g is the acceleration under gravity, and $\hat{k}$ is the unit vector in the vertical z direction. In the present model, monodisperse spherical particles with an equivalent diameter of d_p were assumed, so $A = \pi d_p^2/4$.

The drag coefficient, C_d, is a function of particle Reynolds number, Re_p, i.e.,

$$C_d(Re_p) = \frac{24}{Re_p}\left(1 + 0.15 Re_p^{0.687}\right) \tag{2.76}$$

where

$$Re_p = \frac{\left|\mathbf{V}_p - \mathbf{V}\right| d_p}{\nu} \tag{2.77}$$

Under Stokes flow assumptions, i.e., for $Re_p << 1$, then C_d can be written as

$$C_d = \frac{24}{Re_p} \tag{2.78}$$

Figure 2.20 shows the variation of C_d as given by Eqs. 2.76 and 2.78.

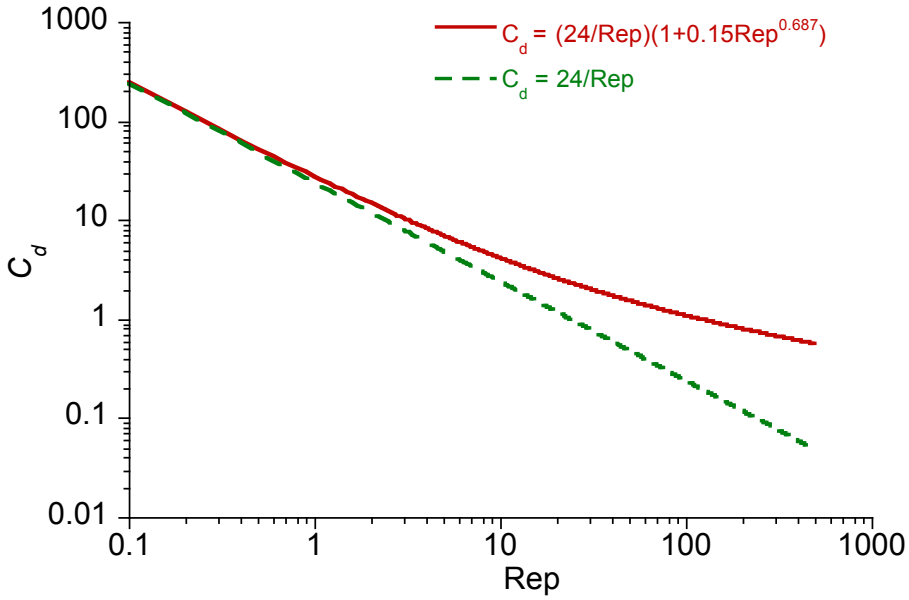

Figure 2.20: Variation of drag coefficient C_d with particle Reynolds number Re_p under: (a) general flow conditions, and (b) Stokes flow assumptions.

The EOMs for the particles then become

$$\frac{d\mathbf{V}_p}{dt} = -\frac{(\mathbf{V}_p - \mathbf{V})}{\tau_p} + g\hat{k} \tag{2.79}$$

$$\frac{d\mathbf{X}_p}{dt} = \mathbf{V}_p \tag{2.80}$$

where $\mathbf{X}_p$ is the particle's position at time t, and τ_p is the particle response time as given by

$$\tau_p = \frac{m}{\frac{1}{2}\rho C_d(Re_p)A\left|\mathbf{V}_p - \mathbf{V}\right|} \tag{2.81}$$

Notice that the particle response time is a function of particle and flow properties. Using Eqs. 2.76 and 2.77 with spherical particles, then τ_p can be written as

$$\tau_p = \frac{\tau_{p_s}}{1 + 0.15Re_p^{0.687}} \tag{2.82}$$

If τ_{p_s} is the particle response time under Stokes flow (with $Re_p << 1$) conditions, then it

can be written as

$$\tau_{p_s} = \frac{\rho_p d_p^2}{18\mu} \tag{2.83}$$

Inserting the value of τ_p from Eq. 2.82 into Eq. 2.79, the particle EOMs become

$$\frac{d\mathbf{V}_p}{dt} = -\frac{(1+0.15Re_p^{0.687})}{\tau_{p_s}}(\mathbf{V}_p - \mathbf{V}) + g\hat{k} \tag{2.84}$$

$$\frac{d\mathbf{X}_p}{dt} = \mathbf{V}_p \tag{2.85}$$

Equation 2.84 is a nonlinear ordinary differential equation and, therefore, must be solved by using iterative methods.

The simulation of brownout dust clouds is already a computational very challenging problem (see Section B), so the use of iterative methods to solve the nonlinear ODE (given by Eqs. 2.84) will dramatically increase the computational cost of the brownout simulations, most likely to the point of being prohibitive. Therefore, in the present work, Stokes flow assumptions were used to linearize Eq. 2.84. A justification of the Stokes flow assumption is given later in Section 3.1.2.3.

Using the assumption of Stokes flow, then the particle EOMs can be written as

$$\frac{d\mathbf{V}_p}{dt} = -\frac{(\mathbf{V}_p - \mathbf{V})}{\tau_{p_s}} + g\hat{k} \tag{2.86}$$

$$\frac{d\mathbf{X}_p}{dt} = \mathbf{V}_p \tag{2.87}$$

Under the further assumptions of dilute gas-particle suspensions, Eqs. 2.79 and 2.80 can be decoupled in the three spatial dimensions. The resulting EOMs then become two sets of first-order ODEs. The components of particle velocities are determined by solving the

set

$$\begin{aligned} \frac{dV_{p_x}}{dt} &= -\frac{(V_{p_x} - V_x)}{\tau_{p_s}} \\ \frac{dV_{p_y}}{dt} &= -\frac{\left(V_{p_y} - V_y\right)}{\tau_{p_s}} \\ \frac{dV_{p_z}}{dt} &= -\frac{\left(V_{p_z} - V_z\right)}{\tau_{p_s}} - g \end{aligned} \tag{2.88}$$

and the particle displacements by solving the subsequent set

$$\begin{aligned} \frac{dX_{p_x}}{dt} &= V_{p_x} \\ \frac{dX_{p_y}}{dt} &= V_{p_y} \\ \frac{dX_{p_z}}{dt} &= V_{p_z} \end{aligned} \tag{2.89}$$

2.4.2 Solution to the Particle Equations of Motion

The decoupled particle equations can be written in a simplified mathematically form as

$$\frac{dV_{p_i}(X_{p_i},t)}{dt} = -\frac{V_{p_i}(X_{p_i},t) - f_i(X_{p_i},t)}{\tau_{p_s}} \tag{2.90}$$

$$\frac{dX_{p_i}(t)}{dt} = V_{p_i}(X_{p_i},t) \tag{2.91}$$

where $i = x$, y, and z, and $\mathbf{f}$ is the forcing function containing the contributions from the flow velocity $\mathbf{V}$ and the gravitational force, and can be written as

$$\begin{aligned} f_x &= V_x \\ f_y &= V_y \\ f_z &= V_z - g\tau_{p_s} \end{aligned} \tag{2.92}$$

Equations 2.90 and 2.91 are three sets of ODEs, where each set can be written as

$$\frac{d}{dt}\begin{Bmatrix} V_{p_i} \\ X_{p_i} \end{Bmatrix} - \begin{bmatrix} -1/\tau_{p_s} & 0 \\ 1 & 0 \end{bmatrix} \begin{Bmatrix} V_{p_i} \\ X_{p_i} \end{Bmatrix} = \begin{Bmatrix} f_i \\ 0 \end{Bmatrix} \tag{2.93}$$

These two sets of ODEs are solved together to compute the positions of the particles, $\mathbf{X}_p$, at different times. First, the particle velocities $\mathbf{V}_p$ are determined using Eq. 2.90 under the influence of rotor flow velocities $\mathbf{V}$, which appear in the forcing function, $\mathbf{f}$, in Eq. 2.92. These velocities will obviously include the induced velocities from all of the vortex elements in the flow field, the maneuver velocities, the free-stream velocities, etc. The computed particle velocities, $\mathbf{V}_p$, are then used to convect the particles to new positions in time, $\mathbf{X}_p$, by using Eq. 2.91.

Because the forcing function $\mathbf{f}$ on the RHS of Eq. 2.90 also contains the wake induced velocities $\mathbf{V}$, which is a nonlinear function of the particle positions, $\mathbf{X}_p$, it is not possible to obtain an exact solution to Eqs. 2.90 and 2.91. Therefore, these ODEs must be solved numerically by using time-marching schemes. The LHS can be discretized by using the most suitable time-marching algorithm. The forcing function $\mathbf{f}$ is computed by using the Biot-Savart law (Ref. 67) as an integral along the length of each vortex segment. This integral cannot be evaluated exactly, therefore, it is approximated using numerical quadrature and straight-line vortex segmentation (Ref. 67), as discussed previously in Section 2.1.1

The time-marching schemes must also be chosen carefully by analyzing their stability and accuracy. In the present work, several time-marching schemes were analyzed. Finally, a modified form of a two point backward difference formula denoted as EI-BDF2-E, as discussed later in Section 2.4.2.2, was used to obtain the results shown in the present

work. This scheme is second-order accurate in time. A detailed analysis of stability and accuracy of the different time-marching schemes is discussed next.

2.4.2.1 Stability of the Time-Marching Integration Schemes

The first requirement of a suitable numerical integration scheme is that it should be stable, i.e., the error caused by discretization should be bounded and not grow with time. The eigenvalues of the coupled ODE system (as given by Eq. 2.93) are $\lambda_1 = -1/\tau_{p_s}$ and $\lambda_2 = 0$. Therefore, these ODEs are inherently stable because λ_1, $\lambda_2 \leq 0$. Because the value of $\lambda_2 = 0$, all time-marching schemes will be unconditionally stable for the ODE in Eq. 2.91. However, the stability of the time-marching schemes must be examined to solve the first ODE, i.e., Eq. 2.90, which can be written in a simplified form as

$$\frac{du}{dt} - \lambda u = f(t) \tag{2.94}$$

The solution of this latter ODE is

$$u(t) = u_0 e^{\lambda t} + e^{\lambda t} \int_0^t f(\sigma) e^{-\lambda \sigma} d\sigma \tag{2.95}$$

where $\lambda = -1/\tau_{p_s}$. Notice that the value of τ_{p_s} will vary with the carrier flow and the particle properties. For silica particles with d_p ~1–1000 μm, the value of τ_{p_s} ranges between 10^{-6} s to 10 s. The corresponding value of λ ranges between -10^6 s^{-1} to -10^{-1} s^{-1}.

Unfortunately, Eq. 2.90 can become "stiff" for very large values of λ. The stiffness ratio (*SR*) of this problem can be defined as the ratio $|\lambda_{\max}|/|\lambda_{\min}|$. For d_p ~1–1000 μm, the value of *SR* = 10^6, which is very large. The ODEs with large values of *SR* possess

some interesting characteristics, which then determine the stability limits of the numerical schemes.

The first term on the RHS of Eq. 2.95, i.e., $u_0 e^{\lambda t} = u_0 e^{-t/\tau_{p_s}}$, is the transient solution, which decays exponentially with time at a rate proportional to λ. The second term is the particular solution, which depends upon forcing function f. After the transient solution decays, the particle starts to moves with the local flow velocity. The transient solution, therefore, acts as a lag, which determines how quickly the particle velocity approaches the flow velocity. Obviously, particles of smaller size have a correspondingly smaller lag compared to larger and heavier particles.

The basic properties of the solution, as given by Eq. 2.95, can be understood by considering a simpler one-dimensional problem in which the external flow velocity is a constant say U. In this case, an exact solution to the ODE is

$$u(t) \quad = \quad u_0 e^{-t/\tau_{p_s}} + U\left(1 - e^{-t/\tau_{p_s}}\right) \tag{2.96}$$

By considering a typical value of the flow velocity found in the rotor wake, say $U = 20$ ms^{-1}, and that $u_0 = 0$ ms^{-1}, the resulting variation of u is shown in Fig. 2.21 for different values of τ_{p_s} (corresponding to particles of different sizes). Notice that the particle velocity exponentially approaches the flow velocity, depending upon the particle size (or the value of τ_{p_s}). The particles with small values of τ_{p_s} have a small lag and, therefore, their velocities quickly approach the flow velocity. The larger particles clearly have a much greater lag. This behavior, in which some components of the solution decay much faster than the others, characterizes the "stiffness" of the problem.

The numerical solution of Eq. 2.94 can be obtained by using different time-marching

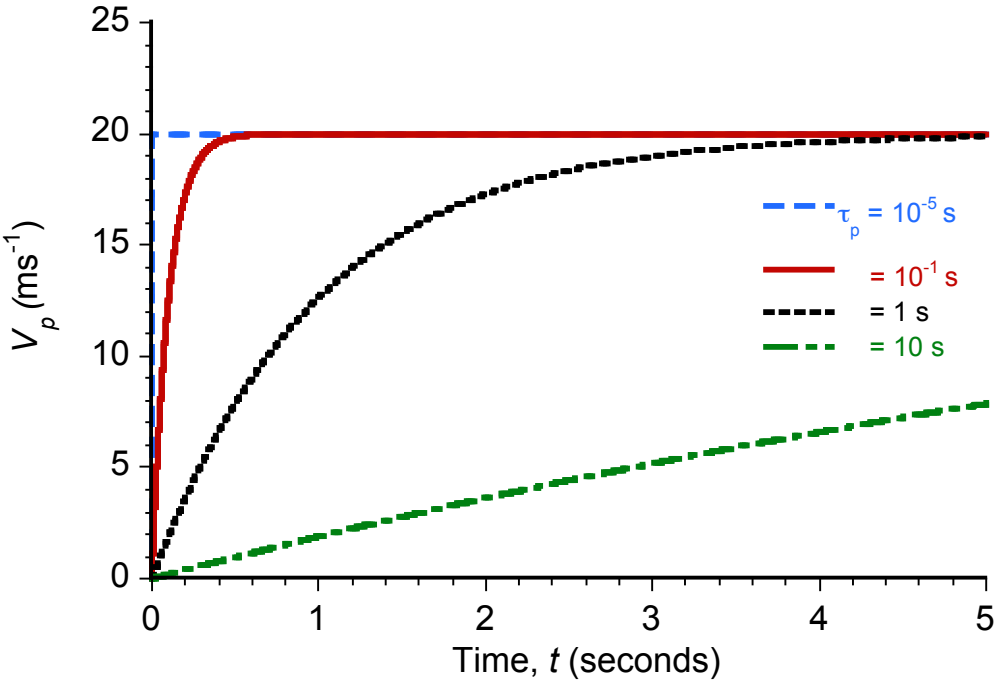

Figure 2.21: Variation of the velocity of particles of different sizes with time in a constant velocity flow field.

integration schemes to solve for the LHS of the equation. The resulting equation is usually referred to as the Ordinary Difference Equation (OΔE). Because Eq. 2.90 is a stiff equation, the stability of the resulting OΔE must be analyzed properly.

In the present work, stability of several time-marching schemes were analyzed. These schemes included: (a) first-order Euler explicit, (b) first-order Euler implicit, (c) explicit second-order Adams-Bashforth method (AB2), (d) implicit second-order BDF2 scheme, and (e) Implicit third-order BDF3 scheme.

The stability regions of these five numerical schemes can be calculated by using the boundary locus method (Ref. 119). The OΔEs corresponding to these four methods can

be written as:

$$\text{Euler Explicit}: \quad u_{n+1} = u_n + hu'_n \tag{2.97}$$

$$\text{Euler Implicit}: \quad u_{n+1} = u_n + hu'_{n+1} \tag{2.98}$$

$$\text{AB 2}: \quad u_{n+1} = u_n + \frac{h}{2}\left[3u'_n - u'_{n-1}\right] \tag{2.99}$$

$$\text{BDF 2}: \quad u_{n+1} = \frac{1}{3}\left[4u_n - u_{n-1} + 2hu'_{n+1}\right] \tag{2.100}$$

$$\text{BDF 3}: \quad u_{n+1} = \frac{1}{11}\left[18u_n + 8u_{n-1} - \frac{3}{2}u_{n-2} + 6hu'_{n+1}\right] \tag{2.101}$$

where $u' = \dfrac{du}{dt}$. Substituting Eq. 2.90 into these Eqs. 2.97, 2.98, 2.99, and 2.100, gives

$$\text{Euler Explicit}: \quad u_{n+1} - (1+\lambda h)u_n = hf(t_n) \tag{2.102}$$

$$\text{Euler Implicit}: \quad (1-\lambda h)u_{n+1} - u_n = hf(t_n) \tag{2.103}$$

$$\text{AB2}: \quad u_{n+1} - (1+\frac{3}{2}\lambda h)u_n + \frac{1}{2}\lambda h u_{n-1} = \frac{3}{2}hf(t_n) - \frac{1}{2}hf(t_{n-1}) \tag{2.104}$$

$$\text{BDF2}: \quad (1-\frac{2}{3}\lambda h)u_{n+1} - \frac{4}{3}u_n + \frac{1}{3}u_{n-1} = \frac{2}{3}hf(t_{n+1}) \tag{2.105}$$

$$\text{BDF3}: \quad (1-\frac{6}{11}\lambda h)u_{n+1} - \frac{18}{11}u_n + \frac{9}{11}u_{n-1} - \frac{2}{11}u_{n-2} = \frac{6}{11}hf(t_{n+1}) \tag{2.106}$$

Placing the difference operator E, i.e., $u_{n+k} = E^k u_n$ into Eqs. 2.102, 2.103, 2.104, and 2.105, the characteristic equations can be obtained as:

$$\text{Euler Explicit}: \quad P(\lambda h) = \sigma - (1+\lambda h) \tag{2.107}$$

$$\text{Euler Implicit}: \quad P(\lambda h) = (1-\lambda h)\sigma - 1 \tag{2.108}$$

$$\text{AB2}: \quad P(\lambda h) = \sigma^2 - (1+\frac{3}{2}\lambda h)\sigma + \frac{1}{2}\lambda h \tag{2.109}$$

$$\text{BDF2}: \quad P(\lambda h) = (1-\frac{2}{3}\lambda h)\sigma^2 - \frac{4}{3}\sigma + \frac{1}{3} \tag{2.110}$$

$$\text{BDF3}: \quad P(\lambda h) = (1-\frac{6}{11}\lambda h)\sigma^3 - \frac{18}{11}\sigma^2 + \frac{9}{11}\sigma - \frac{2}{11} \tag{2.111}$$

where σ is the root of the characteristic equation, i.e., $P(\sigma) = 0$. The stability bounds

of these equations can now be obtained by iteratively solving them by using Newton-Raphson method in the form

$$\lambda h^{\text{new}} = \lambda h^{\text{old}} - \frac{P(\lambda h^{\text{old}})}{dP(\lambda h^{\text{old}})/d(\lambda h^{\text{old}})} \tag{2.112}$$

In general, λh can be a complex number depending upon the value of λ. The stability bounds of explicit (i.e., Eqs. 2.107 and 2.109) and implicit (i.e., Eqs. 2.108 and 2.110) time-marching schemes are shown in Figs. 2.22(a) and 2.22(b), respectively. The numerical solution of the explicit time-marching schemes are stable within the bounded regions shown in Fig. 2.22(a), and those from the implicit schemes are stable outside the bounded regions, as shown in Fig. 2.22(b). Notice that for all of these schemes, the stability regions decrease with an increase in the order of accuracy.

As mentioned previously, for the present problem $\lambda h = -\Delta t/\tau_{p_s}$, which is always real but negative. Therefore, for the explicit scheme to be stable, the value of λh must lie between 0 and -2 for the Euler explicit, and between 0 and -1 for the AB2 method. Therefore, for $\tau_{p_s} = 10^{-5}$ s the value of Δt must be less than 2×10^{-5} s for the Euler explicit method, and must be less than 10^{-5} s for the AB2 method. These time steps are extremely small and, therefore, will tremendously increase the computational cost of obtaining a solution to the dust cloud. However, all of the implicit schemes discussed here are stable for all values of Δt and for real and negative values of λ, which shows that for the present problem an implicit time-marching scheme should be used.

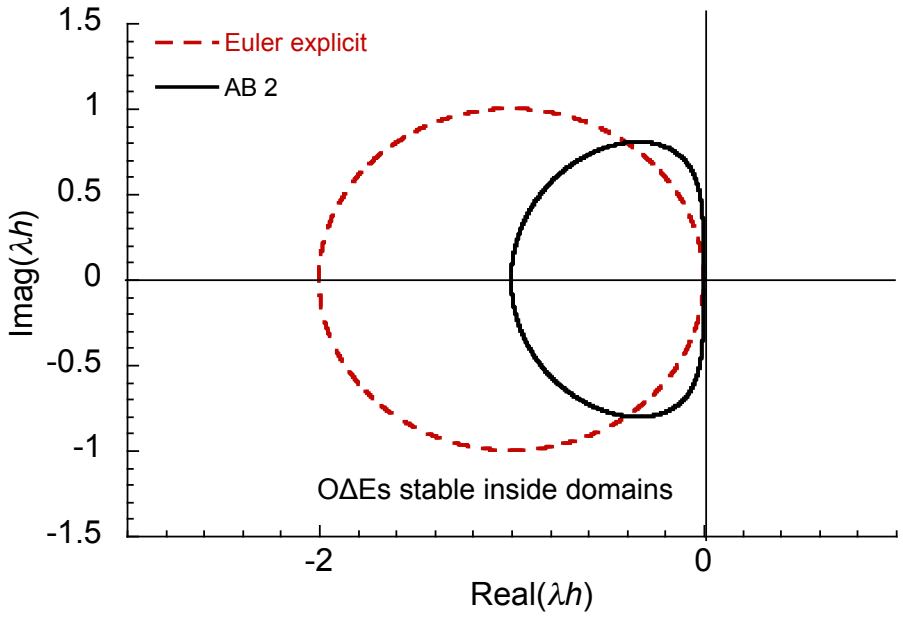

(a) Stability bounds of explicit schemes

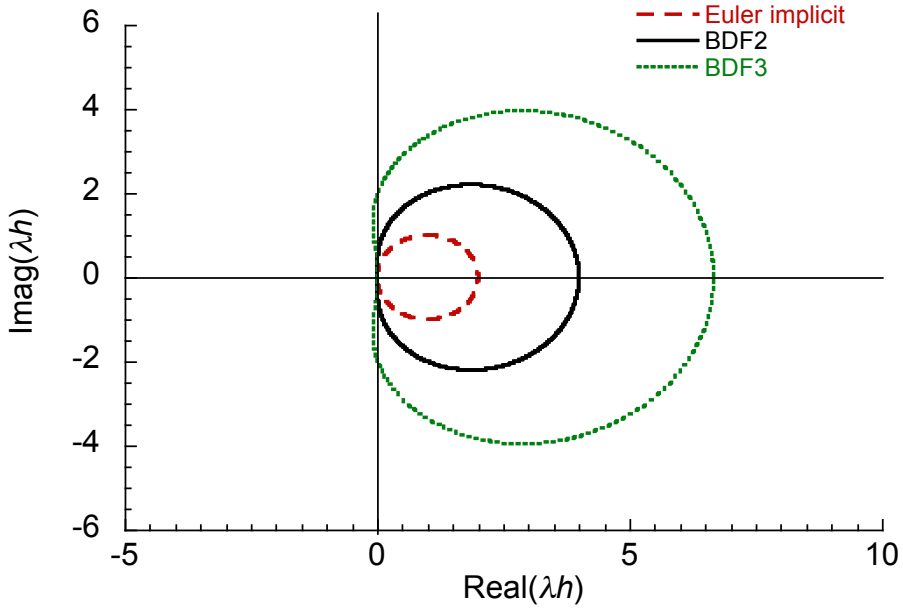

(b) Stability bounds of implicit schemes

Figure 2.22: Stability bounds of: (a) explicit schemes: Euler explicit and AB2, and (b) implicit schemes: Euler implicit, BDF2, and BDF3.

The two values of σ for the BDF2 scheme can be obtained from

$$\sigma = \frac{2 \pm \sqrt{1+2\lambda h}}{3\left(1-\frac{2}{3}\lambda h\right)} \tag{2.113}$$

$$= \frac{1}{3}\left[2 \pm (1+2\lambda h)^{0.5}\right]\left(1-\frac{2}{3}\lambda h\right)^{-1} \tag{2.114}$$

The principal root σ_1 and the spurious root σ_2 can be obtained by using binomial expansions of Eq. 2.114. These roots can be written as

$$\sigma_1 = \underline{1+\lambda h+\frac{(\lambda h)^2}{2!}}+\frac{(\lambda h)^3}{2}+\cdots \text{ higher order terms} \tag{2.115}$$

and

$$\sigma_2 = \frac{1}{3}\left(1-\frac{1}{3}\lambda h+\frac{5}{18}(\lambda h)^2-\frac{7}{54}(\lambda h)^3\right)+\cdots \text{ higher order terms} \tag{2.116}$$

Because the leading error term in the principal root σ_1 is $\frac{(\lambda h)^3}{2}$, the BDF2 scheme is locally third-order accurate, and globally second-order accurate.

Furthermore, for the leading error term to be small, then

$$\Delta t < \tau_{p_s} \tag{2.117}$$

It is known that the value of τ_{p_s} can become small for smaller-sized particles. For example, for a particle with $d_p = 0.1$ μm, the value of $\tau_{p_s} \sim 10^{-7}$ s and, therefore, the value of Δt must also be of the same order of magnitude. For a full-scale helicopter, this value of Δt will correspond to an azimuthal resolution $\Delta\psi$ of the order 0.0001°, which is extremely small and completely impractical in numerical terms. However, notice that the transient term given by $V_{p_0}e^{-t/\tau_{p_s}}$ decays extremely quickly for smaller values of τ_{p_s} and, therefore, the numerical solution of this transient part becomes insignificant for such values of

τ_{p_s}. Therefore, the condition given by Eq. 2.117 can be ignored for all practical purposes; however, the convergence of the numerical scheme must still be properly analyzed.

2.4.2.2 Time-Marching Solution

The stability analysis performed has shown that the BDF2 and BDF3 schemes can be used to solve the particle EOMs given by Eqs. 2.90 and 2.91. Different formulations of the implicit BDF2 (Refs. 120 and 119) and BDF3 methods can be used to solve the particle EOMs (Eqs. 2.90 and 2.91). Numerical implementation of the BDF2 scheme requires a knowledge of the particle velocities and positions from the two previous time steps; the BDF3 scheme requires this information from three previous time steps. Because this information is not available at the first time step of the BDF2 scheme, and at the first two time steps of the BDF3 scheme, lower-order schemes have to be used for these initial time steps. Therefore, multi-step time-marching schemes must be used to obtain the solution to the particle EOMs.

Euler Implicit with BDF2 (EI-BDF2) Scheme

In this scheme, the first time step is calculated using an Euler implicit method, and then the BDF2 scheme is used for the remainder of the time steps. Notice that the BDF2 scheme is an implicit scheme and, therefore, requires a knowledge of the forcing function, **f**, as given by Eq. 2.92, at $n+1^{\text{th}}$ time step. Because f_i is a function of the flow velocity $V_i(X_{p_i},t)$, it is not known at the $(n+1)^{\text{th}}$ time step unless X_{p_i} is also known at this time step. In the EI-BDF2 scheme, f_i is approximated at n^{th} time step. The numerical solution

of $V_{p_i}^{n+1}$ and $X_{p_i}^{n+1}$ can be written as

$$V_{p_i}^{n+1} = \frac{1}{\left(1+\frac{\Delta t}{\tau_{p_s}}\right)}\left(V_{p_i}^{n}+\frac{\Delta t}{\tau_{p_s}}f_i^n\right) \qquad \text{for } n=1 \qquad (2.118)$$

$$V_{p_i}^{n+1} = \frac{1}{3\left(1+\frac{2\Delta t}{3\tau_{p_s}}\right)}\left(4V_{p_i}^{n}-V_{p_i}^{n-1}+2\frac{\Delta t}{\tau_{p_s}}f_i^n\right) \qquad \text{for } n>1 \qquad (2.119)$$

and

$$X_{p_i}^{n+1} = X_{p_i}^{n}+\Delta t V_{p_i}^{n+1} \qquad \text{for } n=1 \qquad (2.120)$$

$$X_{p_i}^{n+1} = \frac{1}{3}\left(4X_{p_i}^{n}-X_{p_i}^{n-1}+2\Delta t V_{p_i}^{n+1}\right) \qquad \text{for } n>1 \qquad (2.121)$$

The accuracy analysis of this scheme is discussed in Section 3.1.2.

EI-BDF2 with Extrapolation (EI-BDF2-E) Scheme

In this scheme, the value of f_i^{n+1} is approximated by quadratic extrapolation. This scheme can also be regarded as a predictor-corrector formulation of the EI-BDF2 scheme. In the predictor step, the value of $X_{p_i}^{n+1}$ is calculated by using quadratic extrapolation of $X_{p_i}^{n}$, $X_{p_i}^{n-1}$, and $X_{p_i}^{n-2}$, which can be written as

$$\bar{X}_{p_i}^{n+1} = 3X_{p_i}^{n}-3X_{p_i}^{n-1}+X_{p_i}^{n-2} \qquad (2.122)$$

The value of f_i^{n+1} is then evaluated at $\bar{X}_{p_i}^{n+1}$. In the corrector step, the calculated value of f_i^{n+1} is used to evaluate $V_{p_i}^{n+1}$ using

$$V_{p_i}^{n+1} = \frac{1}{\left(1+\frac{\Delta t}{\tau_{p_s}}\right)}\left(V_{p_i}^{n}+\frac{\Delta t}{\tau_{p_s}}f_i^{n+1}\right) \qquad \text{for } n=1 \qquad (2.123)$$

$$V_{p_i}^{n+1} = \frac{1}{3\left(1+\frac{2\Delta t}{3\tau_{p_s}}\right)}\left(4V_{p_i}^{n}-V_{p_i}^{n-1}+2\frac{\Delta t}{\tau_{p_s}}f_i^{n+1}\right) \qquad \text{for } n>1 \qquad (2.124)$$

The corrected particle positions $X_{p_i}^{n+1}$ are then evaluated by using Eqs. 2.121.

In a different formulation, the value of f_i^{n+1} can be predicted by extrapolating the velocities at the particle positions at the previous time steps. For example, quadratic extrapolation of f_i^n, f_i^{n-1}, and f_i^{n-2} can be used to compute the value of f_i^{n+1} by using

$$f_i^{n+1} = 3f_i^n - 3f_i^{n-1} + f_i^{n-2} \tag{2.125}$$

One potential challenge in this extrapolation process is that the velocity induced by the rotor wake filaments is a time-dependent and nonlinear function of space ζ and time ψ. Extrapolation of the flow velocity from $V_i(X_{p_i}^n)$, $V_i(X_{p_i}^{n-1})$, and $V_i(X_{p_i}^{n-2})$, therefore, can result in additional errors, which are very difficult to evaluate. Therefore, in the present work the predictor-corrector formulation as given by Eqs. 2.122, 2.123, 2.124, and 2.121 was implemented.

Trapezoidal with BDF2 Scheme Using Extrapolation (TR-BDF2-E)

In this formulation, the first time step was evaluated by using second-order accurate trapezoidal scheme. In this case, Eqs. 2.123 and 2.124 are replaced by the following equations

$$\left[1 + \frac{\Delta t}{2\tau_{p_s}}\right] V_{p_i}^{n+1} = \left[1 - \frac{\Delta t}{2\tau_{p_s}}\right] V_{p_i}^n + \frac{\Delta t}{2\tau_{p_s}} \left(f_i^n + f_i^{n+1}\right) \quad \text{for } n = 1 \tag{2.126}$$

$$X_{p_i}^{n+1} = X_{p_i}^n + \frac{\Delta t}{2} \left(V_{p_i}^n + V_{p_i}^{n+1}\right) \quad \text{for } n = 1 \tag{2.127}$$

Again, f_i^{n+1} in Eq. 2.126 is not known at $n = 1$. However, it can be approximated by first using an Euler implicit scheme at $n = 1$ to calculate $\bar{X}_{p_i}^{n+1}$, and then finding $f_i^{n+1}(\bar{X}_{p_i}^{n+1})$. This calculated value of f_i^{n+1} can then be used in Eq. 2.126 to update $X_{p_i}^{n+1}$ at $n = 1$ using the trapezoidal scheme.

Euler Implicit with BDF3 Scheme Using Extrapolation (EI-BDF3-E)

The formulation of this particular time-marching algorithm is similar to the EI-BDF2-E scheme, except the BDF2 scheme was replaced by the third-order accurate BDF3 scheme. Because the BDF3 scheme requires three previous time steps to march the solution in time, the solution at $n = 1$ was calculated by using an Euler implicit scheme (given by Eqs. 2.123 and 2.120), and the solution at $n = 2$ was calculated by using the BDF2 scheme (given by Eqs. 2.124 and 2.121). For values of $n \geq 3$, the BDF3 scheme was used, which can be written as

$$\left(1 + \frac{6\Delta t}{11\tau_{p_s}}\right) V_{p_i}^{n+1} = \frac{1}{11}\left(18V_{p_i}^{n} - 9V_{p_i}^{n-1} + 2V_{p_i}^{n-2} + 6\frac{\Delta t}{\tau_{p_s}} f_i^{n+1}\right) \quad (2.128)$$

$$X_{p_i}^{n+1} = \frac{1}{11}\left(18X_{p_i}^{n} - 9X_{p_i}^{n-1} + 2X_{p_i}^{n-2} + 6\Delta t V_{p_i}^{n+1}\right) \quad (2.129)$$

The value of f_i^{n+1} was evaluated by using quadratic extrapolation, as given by Eq. 2.122.

Trapezoidal with BDF3 Scheme Using Extrapolation (TR-BDF3-E)

This scheme is also similar to the TR-BDF2-E scheme, where the second-order BDF2 method was replaced by the third-order accurate BDF3 method, as given by Eqs. 2.128 and 2.129.

2.4.2.3 Accuracy of the Numerical Solution

Numerical solutions are obviously approximations to the exact solutions of the ODEs, and can consequently introduce several types of errors. These errors include truncation or discretization errors and round-off errors. Discretization errors, as the name suggests, are introduced while discretizing the original ODE. As the discretization size

approaches zero, the approximate solutions should approach the exact solution. Discretization errors can arise from two reasons: the use of a particular numerical scheme and by the approximation to the induced velocity field. These errors depend upon the discretization time step size Δt, and the numerical scheme chosen, and are usually estimated by using a Taylor error analysis (Ref. 119). The round-off errors arise because of the result of non-exact representation of real numbers on finite-precision computers. The computations in the present work were performed in double-precision with round-off errors of magnitude about 10^{-16}. Therefore, these types of errors are not of practical concern. However, the sources of discretization errors must be analyzed.

The accuracy of the numerical solution can be examined by writing the discretized equations in the form

$$\underline{\frac{\Delta V_p}{\Delta t}} + \frac{V_p}{\tau_{p_s}} = \frac{1}{\tau_{p_s}} \underline{f(\bar{X}_p)} \tag{2.130}$$

$$\underline{\frac{\Delta X_p}{\Delta t}} = \underline{V_p} \tag{2.131}$$

Notice that the subscript i has been omitted in these previous equations for simplicity. The underlined terms are approximated by discretization and, therefore, can produce errors. The two sources of discretization errors in the numerical solution of the particle EOMs are: (a) calculation of the forcing function f_i on the RHS of the Eq. 2.90 by using the Biot-Savart integral, and (b) use of the time-marching schemes to solve these equations. The global error incurred in the numerical solution of the multi-step schemes also depends upon the lower-order time-marching schemes used at the initial time steps.

Accuracy of the Induced Velocity Computations

The velocities induced by the rotor wake at a suspended dust particle can be computed by using the Biot-Savart law; see Section 2.1.1. The accuracy of this velocity computation depends upon the accuracy of the solution of the rotor wake obtained from the FVM. This rotor wake solution is obtained by discretizing the wake vortex filaments into straight line segments, which are convected in space and time by solving the vorticity transport equations under the assumptions of incompressible and inviscid flow fields; see Section 2.1.3. The governing EOMs in this case were solved by using the PC2B scheme (Refs. 64 and 66), which is second-order accurate in both space ζ and time ψ; see Eq. 2.20. Notice that the representation of the temporal coordinate ψ in the FVM is equivalent to time t used in the tracking of the particles such that $\Delta t = \dfrac{\Delta\psi}{\Omega}$, where Ω is the rotational frequency of the rotor. The velocity at the midpoint of the computational domain (i.e., ζ and ψ) was solved by averaging the velocity at four neighboring points, which is also second-order accurate; see Eq. 2.21. Therefore, the rotor wake solution from the FVM is second-order accurate.

Bhagwat & Leishman (Ref. 67) showed that the velocity induced by these straight-line wake filaments at any point in the flow field is also second-order accurate in space, i.e., $O(\Delta\zeta^2)$; see Eq. 2.4. This means that the forcing function $f(\bar{X}_p^{n+1})$ on the RHS of the particle equations of motion (Eq. 2.90) can be computed to second-order accuracy. However, notice that $\bar{X}_p^{n+1}$ is also calculated by using approximations, as discussed in Section 2.4.2.2. Therefore, additional errors can be introduced in the calculation of $f(\bar{X}_p^{n+1})$.

Accuracy of the Time-Marching Schemes

In this section, the errors introduced into the numerical solution through the use of the time-marching schemes, as discussed in Section 2.4.2.2, are examined. The time-marching schemes introduce errors both on the LHS and the RHS underlined terms in Eqs. 2.130 and 2.131.

First, errors introduced by these schemes on the RHS term of Eq. 2.130, i.e., in the calculation of $\bar{X}_p^{n+1}$ are discussed. Recall that in the EI-BDF2 scheme, $\bar{X}_p^{n+1}$ is approximated as

$$\bar{X}_p^{n+1} = X_p^n + O(\Delta t) \tag{2.132}$$

whereas in all the other schemes, i.e., the EI-BDF2-E, TR-BDF2-E, EI-BDF3-E, and TR-BDF3-E schemes,

$$\bar{X}_{p_i}^{n+1} = 3X_{p_i}^n - 3X_{p_i}^{n-1} + X_{p_i}^{n-2} + O(\Delta t)^3 \tag{2.133}$$

Therefore, the calculation of $\bar{X}_p^{n+1}$ is first-order accurate in time for the EI-BDF2 scheme, and third-order accurate for all of the other schemes.

Also, recall that the induced velocity computations using the Biot-Savart integral are $O(\Delta\zeta^2)$. If $\Delta\zeta = \Delta\psi = \Omega\Delta t$, the calculation of $f(\bar{X}_{p_i}^{n+1})$ using the EI-BDF2 scheme will be limited to $O(\Delta t)$ (see Eq. 2.132) and to $O(\Delta t^2)$ by using all the other numerical schemes previously discussed.

Second, the error analysis of the underlined terms on the LHS of these two equations must be performed. These terms are calculated by using different time-marching schemes. The time-marching algorithms as discussed in Section 2.4.2.2 are based on either using the BDF2 or the BDF3 schemes. By using a Taylor error analysis, it can be

shown that the LHS terms in both Eqs. 2.130 and 2.131 are $O(\Delta t^2)$ for the BDF2-based schemes, and $O(\Delta t^3)$ for the BDF3-based schemes.

Furthermore, notice that for the initial time steps, the lower-order schemes of Euler implicit and trapezoidal were used in the BDF2-based schemes, and Euler implicit, trapezoidal and the BDF2 were used in the BDF3-based schemes. This effect can reduce the global accuracy of the time-marching algorithms. The global accuracy of the multi-step schemes must be tested using a convergence analysis, which will be shown later by means of an analysis of different test cases.

To summarize, the accuracy in the calculation of X_p^{n+1} depends upon the accuracy of the computed velocity field V at a point, the time-marching scheme used, and the time step size Δt. Furthermore, the use of lower-order schemes for the initial time steps can reduce the order of accuracy of the overall solution.

2.5 Bombardment Ejection of Particles

Bombardment ejection is another mobilization mechanism that is very important in the formation of brownout dust clouds. Modeling this process is challenging, in part because of the difficulty in representing the mechanical characteristics of the sediment bed and the effects arising from inter-particle forces. The present section explains a simplified model that has been developed to simulate the process of bombardment ejections in the modeling of rotorcraft brownout problem.

Shao (Ref. 28) has shown that the mechanism of bombardment ejections is primarily responsible for the uplift of smaller-sized dust particles, for which the inter-particle

forces are strong enough to prevent them from being dislodged otherwise by the external flow. Recent dual-phase experiments conducted by Sydney et al. (Ref. 17) also showed that bombardment ejections may be an important contributor to sediment mobilization and uplift under the action of rotor wake flows. Representative measurements of the bombardment process, which was obtained through particle image velocimetry (PIV) and particle tracking velocimetry (PTV), are shown in Fig. 2.23. In fact, different forms of bombardment have been observed in this case, as shown in the schematic of Fig. 2.24. For example, particles saltating on the bed follow ballistic-like trajectories and if they gain sufficient velocity can bombard on the bed, ejecting more particles through bombardment. These ejected particles can then become uplifted by the upwash region of a vortical flow, recirculated through the downwash region, and bombarded back onto the bed to eject even more particles. This form of bombardment is called localized reingestion bombardment.

Another form of reingestion bombardment occurs when particles are suspended high enough from the ground to be recirculated through the rotor disk. In this case, the particles can also bombard the bed and eject more particles in a process called global bombardment; see in Fig. 2.24. During all of these bombardment processes, small-sized craters are left on the bed. In some cases, such craters may be big enough to change the topology of the bed and affect the flow, but for a full-scale rotorcraft deviations in the original bed topology are generally small compared to the overall dimensions of the problem.

When a previously suspended particle impacts the underlying bed, it loses part of its kinetic energy to the bed during the collision. Depending upon the size of the particle,

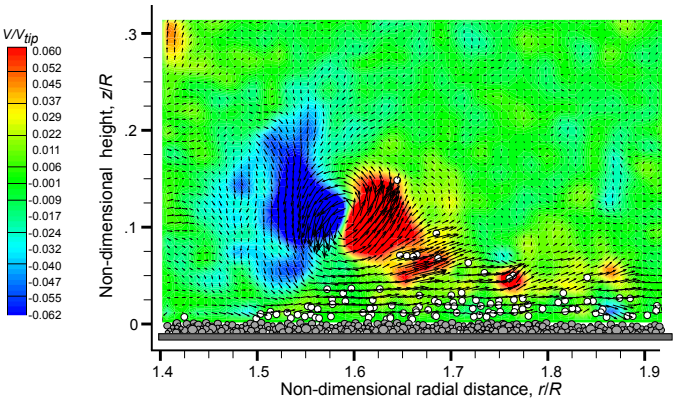

(a) Sediment entrained into vortex upwash

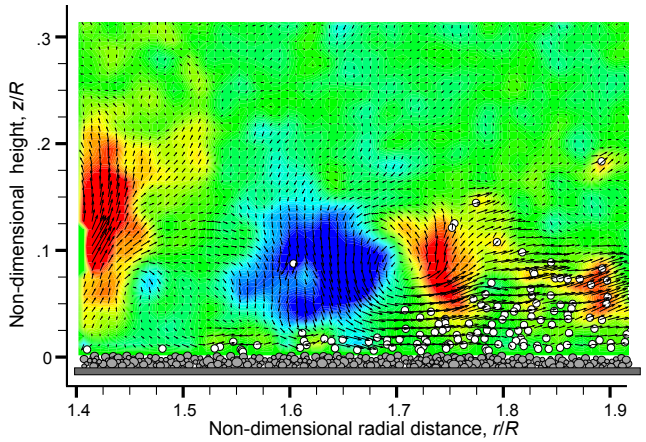

(b) Sediment into downwash flow

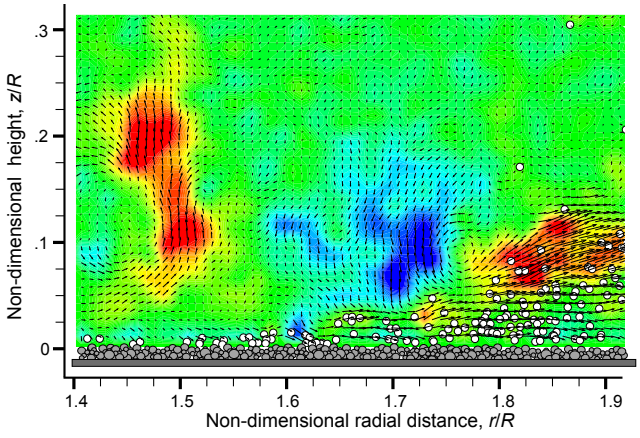

(c) Sediment bombarding bed

Figure 2.23: Sequential schematic and PIV/PTV measurements of sediment particles undergoing the process of bombardment and ejecting new particles from a sediment bed (Ref. 17).

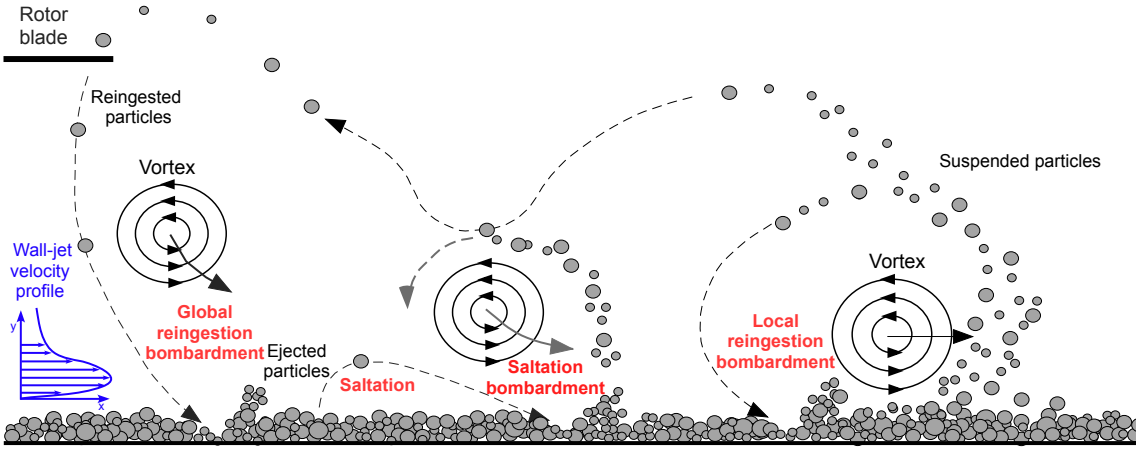

Figure 2.24: Schematic showing the various forms of bombardment in rotor flows.

as well as the elastic force exerted by the bed, the particle rebounds off the bed. During this process, the particle can convert some of its energy to dislodge and eject more particles. As previously discussed, for small-sized dust particles the inter-particle cohesive forces may be strong enough to prevent them from being dislodged from the bed by the mechanisms of direct entrainment, i.e., by the action of shear and pressure. However, when a particle bombards the bed with sufficient energy, it can break the inter-particle bonds between the particles (Ref. 28) and so dislodge and eject more new particles into the flow.

In the present work, the process of bombardment ejection was modeled using a probabilistic approach. The two main components of the model were: (a) finding the volume of crater formed by the impacting particles, and (b) approximating the initial velocities of the ejected particles.

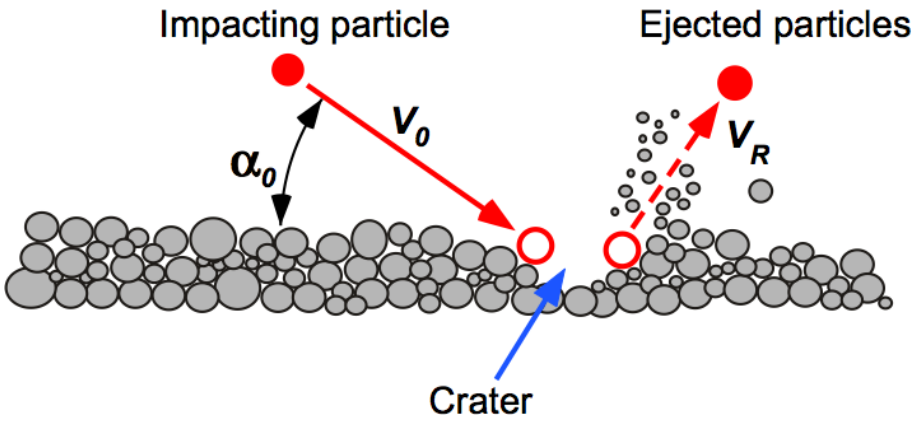

Figure 2.25: Schematic of a sediment particle impacting the ground, forming a crater, and ejecting new particles.

2.5.1 Volume of Crater Formed by Bombardment Ejections

Several assumptions are needed to develop the bombardment ejection model. First, it was assumed that a particle impacting the bed can excavate void-shaped craters, as shown in Fig. 2.25. This assumption is justified based on experimental observations of the mechanism of bombardment ejections seen in dual-phase rotor flows (Refs. 18 and 17). The volume of particles ejected from the bed was assumed to be equal to the volume of the crater formed by the impacting particle. It was further assumed that a constant plastic pressure acts upon the particle impacting the bed, and that the impacting particle does not shatter during the impact. The ratio of the vertical to the horizontal force acting on the particle during its impact with the bed was considered constant, which has a value of about 2 for abrasive grains (Ref. 29).

Under these assumptions, Lu and Shao (Ref. 29) solved the EOMs of each particle that impacts the bed and creates a crater. The resulting volume of the crater, ϑ, was expressed as a function of the velocity $\mathbf{V}_0$, diameter d_p, and mass m_0 of the impacting

particle, as well as of plastic pressure exerted by the bed, i.e.,

$$\vartheta = \frac{\pi \rho_p d_p^3 |\mathbf{V}_0|^2}{12 P_s} \left(\sin 2\alpha_0 - 4 \sin^2 \alpha_0 + \frac{7.5\pi |\mathbf{V}_0| \sin^3 \alpha_0}{\beta_v d_p} \right) \tag{2.134}$$

where $\beta_v = \sqrt{\left(\frac{2\, P_s\, d_p}{m_0} \right)}$ and P_s is the horizontal component of plastic pressure of the bed exerted on the particle. The plastic pressure P_s is a measure of soil erodibility, which depends upon the mechanical properties of the soil such as its cohesion, tensile strength, modulus of elasticity, and aggregate content. While the measurement of such properties is rather difficult, Lu and Shao (Ref. 28) have estimated the range of P_s to lie between 10 to 25×10^5 Nm^{-2} for sandy to loamy beds. For the present analysis, P_s was considered to be 1,000 Nm^{-2}, which was the value also used by Lu and Shao (Ref. 29) for smooth and fine grained unaggregated beds.

2.5.2 Initial Velocity of the Ejected Particles

Several assumptions must also be made to compute the initial velocities of the particles that are ejected during the process of bombardment. In the present work, it was assumed that the particles removed from the bed were tightly packed into the crater volume. All of the ejected particles were assumed to be of the same size as that of the impacting particle. It is recognized, however, that in practice, particles of different sizes could be ejected from the bed, but this is a much more difficult problem to model and is left for future work.

The initial velocities and positions of the ejected particles were determined from the particle rebound velocity, $\mathbf{V}_R$, by using a probabilistic approach, while conserving momentum and energy of the rebounding particle. The rebound velocity of impacting

particles can be computed by using a hard-sphere model after integrating the EOMs and assuming a coefficient of restitution (Ref. 118). The coefficient of restitution was assumed to be 0.6 for the present studies (Ref. 121).

The initial velocities of the particles ejected through bombardment ejections were approximated from the rebound velocity by using a multivariate normal distribution $\Phi(\mu_B, \Sigma_B)$ as given by

$$\Phi = \frac{1}{2\pi^{k/2}|\Sigma_B|^{k/2}} \exp \frac{-1}{2}(\mathbf{V}_n - \mu_B)^T {\Sigma_B}^{-1}(\mathbf{V}_n - \mu_B) \tag{2.135}$$

where $\mathbf{V}_n$ is velocity of the n^{th} ejected particle, μ_B is the mean vector as given by

$$\mu_B = \frac{1}{N_b + 1} \sum_{n=1}^{N_b+1} \mathbf{V}_n \tag{2.136}$$

and Σ_B is the covariance matrix of the normal distribution. The values of Σ_B can be written as

$$\Sigma_B = \begin{bmatrix} \sigma_{xx}^2 & \sigma_{xy}^2 & \sigma_{xz}^2 \\ \sigma_{yx}^2 & \sigma_{yy}^2 & \sigma_{yz}^2 \\ \sigma_{zx}^2 & \sigma_{zy}^2 & \sigma_{zz}^2 \end{bmatrix} \tag{2.137}$$

where

$$\sigma_{ij}^2 = \frac{1}{N_b + 1} \sum_{i=1}^{N_b+1} \left(\mathbf{V}_{n_i} - \mu_{B_i}\right)\left(\mathbf{V}_{n_j} - \mu_{B_j}\right) \tag{2.138}$$

is the variance of i^{th} dimension with j.

The mean and covariance matrices can be estimated using momentum and energy conservation of both the rebounding particle and the ejected particles. Using momentum conservation, the momentum of the particle rebounding with velocity $\mathbf{V}_R$ will be equal to the momentum gained by N_b particles that are ejected through bombardment, i.e.,

$$m_R \mathbf{V}_R = \sum_{n=1}^{N_b+1} m_n \mathbf{V}_n \tag{2.139}$$

where $\mathbf{V}_n$ is the velocity of the nth bombarded particle, and m_R and m_n are the masses of the rebounding and bombarded particles, respectively. Because all of the particles were considered to have the same mass in the present simulations, then $m_R = m_n$.

Using Eqs. 2.136 and 2.139, the mean μ_B of the velocity distribution can be written as

$$\mu_B = \frac{1}{N_b+1}\sum_{n=1}^{N_b+1}\mathbf{V}_n = \frac{\mathbf{V}_R}{N_b+1} \tag{2.140}$$

Furthermore, conservation of the total kinetic energy of the rebounding particle gives

$$E_R = \frac{1}{2}m_R|\mathbf{V}_R|^2 = \frac{1}{2}\sum_{n=1}^{N_b+1} m_n|\mathbf{V}_n|^2 \tag{2.141}$$

where E_R is the total kinetic energy of the rebounding particle. Considering the covariance matrix to be diagonal (i.e., neglecting the coupling between different dimensions in Eq. 2.137), then it can be written as

$$\Sigma_B = \begin{bmatrix} \sigma_{xx}^2 & 0 & 0 \\ 0 & \sigma_{yy}^2 & 0 \\ 0 & 0 & \sigma_{zz}^2 \end{bmatrix} \tag{2.142}$$

where σ_{xx}^2, σ_{yy}^2 and σ_{zz}^2 are the variances along the x, y and z directions, respectively. Using Eq. 2.138, the variance along the x-direction becomes

$$\begin{aligned} \sigma_{xx}^2 &= \frac{1}{N_b+1}\sum_{n=1}^{N_b+1}(V_{n_x}-\mu_{B_x})^2 \\ &= \frac{1}{N_b+1}\left(\sum_{n=1}^{N_b+1}V_{n_x}^2 - 2\mu_{B_x}\sum_{n=1}^{N_b+1}V_{n_x} + \mu_{B_x}^2\right) \end{aligned} \tag{2.143}$$

The first term in Eq. 2.143 can be assumed to be equal to the fraction of the total rebound kinetic energy (as given by Eq. 2.141) along the x-direction, which can be written as

$$\sum_{n=1}^{N_b+1}V_{n_x}^2 = E_R\frac{V_{R_x}^2}{V_{R_x}^2+V_{R_y}^2+V_{R_z}^2} \tag{2.144}$$

Similar expressions can be derived for the y and z dimensions. Using Eqs. 2.140 and 2.144 with Eq. 2.143 gives

$$\sigma_{xx}^2 = \left(\frac{E_R}{N_b+1}\right)\frac{V_{R_x}^2}{V_{R_x}^2+V_{R_y}^2+V_{R_z}^2} - \frac{V_{R_x}^2}{(N_b+1)^2} \tag{2.145}$$

$$\sigma_{yy}^2 = \left(\frac{E_R}{N_b+1}\right)\frac{V_{R_y}^2}{V_{R_x}^2+V_{R_y}^2+V_{R_z}^2} - \frac{V_{R_y}^2}{(N_b+1)^2} \tag{2.146}$$

$$\sigma_{zz}^2 = \left(\frac{E_R}{N_b+1}\right)\frac{V_{R_z}^2}{V_{R_x}^2+V_{R_y}^2+V_{R_z}^2} - \frac{V_{R_z}^2}{(N_b+1)^2} \tag{2.147}$$

Therefore, using the mean μ_B given by Eq. 2.140 and the covariance Σ_B given by Eq. 2.147, the initial velocities of the bombarded particles can be found by using Eq. 2.135.

2.6 Numerical Implementation

Several other simplifications have to be adopted for the numerical modeling of large-scale brownout dust clouds. In the present work, the sediment bed was assumed to have a thickness equal to 2% of the rotor radius. The bed was also assumed to be comprised of spherical particles of the same size and density, which were regularly structured in the form of layers; see Fig. 2.26(a). The number of layers must obviously be limited to contain the computational expense of the problem, which as will be shown, can involve an almost exponential growth in the number of suspended particles resulting from bombardment. Initially, only the particles in the top-most layer of the bed were considered eligible to be entrained under the action of the aerodynamic forces. These particles are termed "active" particles, and are shown in red in Fig. 2.26(a). In general, active particles are those stationary particles that are in direct contact with the flow field, and can become entrained only if the entrainment conditions are satisfied.

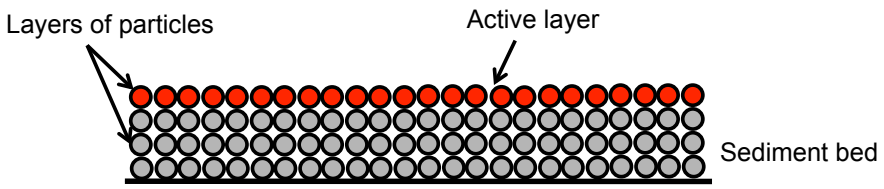

(a) Stationary sediment bed structured in the form of layers

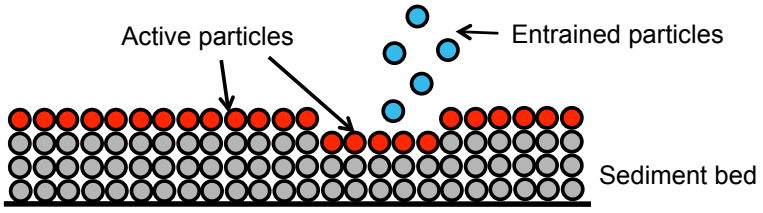

(b) Active and entrained particles

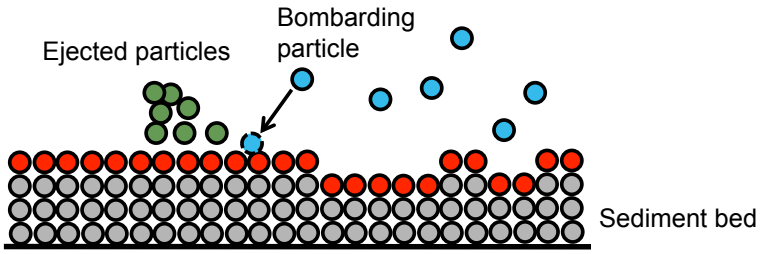

(c) New particles ejected through bombardment

Figure 2.26: Schematics showing the numerical structure of sediment layers, "active" particles, and introduction of new particles on the bed through bombardment ejection.

The initial mobility and entrainment of the particles by the flow was determined by invoking the threshold friction velocity condition, but by using the more general model developed in the present work as given by Eq. 2.55. As an active particle initially stationary on the bed becomes mobilized and entrained into the flow (entrained particles are shown in blue in Fig. 2.26(b)), then the particle beneath this particle becomes exposed to the flow and so now it also becomes eligible to be mobilized, i.e., these particles too now become active; see Fig. 2.26(b). This means that because only a finite number of layers can be computationally modeled, a particle becomes active only after a specified time, say δt, after the particle in the layer just above it became active. This delay time can be justified from videographic results of actual brownout clouds, which show that depending upon the characteristics of the bed (e.g., moisture content, cohesion), the process of mobilization and entrainment of particles is intermittent, not a continuous one. However, modeling representation of this process, for now at least, can only be determined using the assistance of experiments.

From a simulation perspective, a value of δt must be used that can represent the essential details of the dust cloud developments in a practical computational time. In this regard, a sensitivity study was conducted to analyze the effects of δt; details of this study are given in Appendix A. The outcomes show that the process of choosing the best value for δt depends upon the time scales involved with the flight maneuver. For example, for the landing and takeoff maneuvers considered in the present research, it is shown in Appendix A that a value of $\delta t = 1$ s is reasonable in terms of balancing modeling fidelity against computational cost.

The entrained particles that are subsequently uplifted and entrained into the flow

convect under the influence of the rotor-induced flow field. Those particles caught in recirculating flow regions can bombard the sediment bed with enough kinetic energy to eject many more particles through bombardment ejections, as previously described. In the present model, particles ejected through bombardment ejections are treated as new (additional) particles that are introduced into the flow; see Fig. 2.26(c). For example, if N_I is the total number of particles initially comprising the sediment bed and N_b is the total number of particles ejected from the bed from bombardment mechanisms, then the total number particles at the end of the simulation will be $N_I + N_b$; typically N_b will always be much greater than N_I when bombardment occurs.

2.7 Computational Considerations

One of the primary challenges in the numerical modeling of brownout clouds is the tracking of a very large number of suspended particles over the time scales characteristic of the actual flight maneuvers. A rotorcraft landing or takeoff maneuver can involve time scales that are measured in tens of seconds or hundreds of rotor revolutions. The most computationally expensive part of a brownout simulation is the computation of the induced velocity field. The cost of the induced velocity calculations is $O(N_v^2 + N_v N)$, where N_v is the total number of vortex elements $\sim O(10^4)$, and $N = N_I + N_b$ is the total number of particles in the brownout simulation $\sim O(10^{14})$. This cost may translate into weeks or months of computational time, depending upon the time scales of the maneuvers. To contain this cost, two approaches were considered in the present work, namely: (a) utilization of parallel hardware for high-performance computing, and (b) development of

efficient algorithms to reduce computational costs.

In the first approach, the dust cloud simulation methodology was implemented in double precision on graphic processor units (GPUs) by dividing and assigning particle data to each GPU thread and spawning a large number of similar threads (Ref. 97). In this approach, the resulting CPU-GPU computations were nearly found to be 50 times faster without any loss of accuracy. Further details on the specific implementation are given in Appendix B.

In the second approach, particle clustering (Ref. 96) was used to reduce the high computational costs of convecting the particles. In this form of particle clustering, each cluster center is associated with a specified number of particles that have surrounding positions that are determined from a multi-variate Gaussian distribution relative to the velocity of the center of the cluster. Further details on the clustering techniques are given in Appendix C.

2.8 Summary

This chapter has focused on the development of a new methodology to predict the formation of dust clouds produced by rotorcraft operating in ground effect over mobile sediment beds. The main components of this methodology include: modeling of the rotor flow field in ground effect, representation of the viscous flow near the ground, modeling of the onset of particle mobility, and modeling the other particle mechanisms known to occur under brownout conditions. This chapter has also discussed computational techniques that are needed to predict such dust clouds.

The rotor flow field in ground effect was modeled by using an inviscid, incompressible, time-accurate, free-vortex method, which was discussed in Section 2.1. In this method, the rotor blade aerodynamics were modeled using a Weissinger-L model, which was used to solve for the bound vortex strengths by satisfying the flow tangency on the blades. The near wake was modeled as a rigid wake attached to the blade, which rolls up into a tip vortex after a specified distance behind the blade. The strength of the tip vortex was calculated, which is related to the maximum spanwise bound circulation on the blade. This tip vortex was modeled as straight line vortex segments, which were connected by Lagrangian markers. These markers were convected at the local flow velocity, which was calculated by using the Biot-Savart law. The governing convection equation was then solved using a second-order accurate numerical scheme. The effects of diffusion and filament stretching were accounted for by using a semi-empirical viscous core growth model. The rotor flow in ground effect operations was modeled by using the method of images.

The flow computed by using the free-vortex method is inviscid and does not satisfy the no-slip boundary condition at the ground plane. Therefore, the flow conditions in the viscous region near the ground were calculated by using certain approximations. An inviscid-viscous method was discussed in Section 2.2, in which the inviscid and viscous parts of the flow field were coupled at an interface, which was assumed to be at some small distance above the ground. The flow parameters were matched in the viscous region by using a semi-empirical logarithmic velocity profile approximation. This inviscid-viscous approach was then used to estimate the friction velocity on the bed, which in turn was related to the onset of sediment mobility.

The mobilization of sediment particles from the bed was discussed in Section 2.3. The forces acting on a sediment particle stationary on the bed include shear, pressure, inter-particle, and gravitational. The particle mobilizes when the aerodynamic forces acting on it exceed the inter-particle and gravitational forces. Existing sediment mobility models have been developed for simpler external flows and ignore the effects of unsteady pressure forces created by the vortices convecting near the bed. However, recent dual-phase experiments in vortically dominated flows has shown that these effects may be significant in determining particle mobility. Therefore, an improved sediment mobility model was developed by solving for the moment equilibrium at each particle from all of the forces acting upon it. It was found that the effects of unsteady pressures could be very significant, especially for the smaller particles.

The motion of the uplifted particles was tracked by solving their governing equations of motion, as discussed in Section 2.4. Measurements of particle concentration in the brownout dust clouds have suggested that the dust clouds can be assumed to be dilute, at least away from the ground. Therefore, the two-phase problem was assumed to be one-way coupled, i.e., the particles were convected under the influence of rotor flow but the particles do not affect the flow. These assumptions were used to decouple the equations of motion along the three directions, which were then solved numerically using a Stokes flow assumption. The resulting equations were found to be numerically "stiff," so appropriate time-marching schemes were developed by considering the stability and accuracy of the numerical solutions. An implicit, multi-step, two-point backward difference time-marching scheme was finally developed, which was second-order accurate in time.

Recent dual-phase experiments have also suggested that a previously suspended particle can impact the bed, lose a part of its kinetic energy, and then eject many more particles from the bed. As discussed in Section 2.5, a model was developed to simulate this bombardment ejection mechanism. In this model, the volume of the crater formed on the bed was approximated, which was used to approximate the quantity of ejected particles. The spatial positioning of the ejected particles was determined by using a multivariate Gaussian distribution. The mean and variance of the distribution were calculated by solving for the conservation of momentum and energy of the impacting and the ejected particles.

The overall implementation of the brownout methodology was presented in Section 2.6. The sediment bed consists of particles arranged in the form of multiple layers, with each layer containing a fixed number of particles. Particles from one layer were considered to be eligible to be mobilized when the particles in the layer above it were removed. Of course, the eligible particles actually become mobilized when the friction velocities acting on them exceed the threshold values. The particles ejected through bombardment were treated as new particles.

Because of the very large number of particles required to model the brownout dust clouds, the present methodology was designed to be implemented on multiple processors and on graphic processing units, as discussed in Section 2.7. The technique of Gaussian clustering was also used to contain the computational cost of the simulations.

Chapter 3

Results & Discussion

The brownout dust cloud simulation methodology developed in the present work has made significant advancements over existing methodologies (e.g., Refs. 22, 36–40). In particular, new numerical models have been developed to simulate the processes of sediment mobilization and uplift under brownout conditions. The modeling of these physical processes also increases the numerical complexity of the methodology and, therefore, its capabilities need to be validated before the approach can be used to study rotorcraft brownout problems in earnest.

This first part of this chapter shows results from the important components of the dust cloud simulation methodology. These components include the bombardment ejection model and the time-marching algorithms used to convect the particles. These models were analyzed for simpler problems that help to better understand how they must be integrated into the overall brownout simulation. In the second part, a study was undertaken to compare the simulations of brownout dust clouds against actual measurements. Then, the final methodology was used to predict the development of dust clouds for landing and takeoff flight maneuvers. The significance of different mobilization and uplift mechanisms in the developments of the dust clouds was also examined. Finally, an analysis was conducted to explore aspects of brownout mitigation.

3.1 Numerical Methodology

In this section, two important components of the dust cloud simulation methodology are analyzed: (a) the bombardment ejection model, and (b) the time-marching integration algorithms. First, the applicability of the bombardment ejection model to a simpler problem is studied, and the results are used to provide a better understanding of its overall functionality. Second, the applicability of the time-marching algorithms to solve the particle EOMs for several canonical test cases is examined. Finally, a convergence analysis of the simulated dust clouds with the selected time-marching scheme is presented.

3.1.1 Bombardment Ejection Model

An analysis of the model developed to simulate the process of bombardment ejection is presented. This study was conducted to understand the effects of particle size and velocity on the process of bombardment ejections from the sediment bed, and its significance in the eventual creation of brownout dust clouds. Notice that all references to particle size in this study refers to the particle diameter.

This study was conducted in two parts. First, it was assumed that particles of different sizes impacted the sediment bed with the same velocity and trajectory. Second, it was assumed that particles of different sizes had the same flow velocity just before impacting the bed. The overall goals were to explore the sensitivities of the bombardment ejection processes to the size and velocity of the impacting particles.

3.1.1.1 Particles Impacting the Bed with the Same Velocity

Key to the bombardment analysis is in determining the volume of material removed from the bed, which obviously depends upon the size and velocity of the impacting particle. Equation 2.134 shows that the volume of the crater left on the bed increases proportionally to d_p^3, all other parameters being constant; the result in this case is shown in Fig. 3.1(a). The volume of the crater subsequently formed can be used to approximate the total quantity of ejected particles, as was explained previously in Section 2.5. In the present work, it was assumed that particles of the same size were liberated after bombardment.

An analysis was conducted for each bombardment event to compute the total quantity of particles of different diameters representing the crater volume, as shown in Fig. 3.1(b). Each line in this figure shows the total quantity of particles ejected for a given size of impacting particle. The results show that the impact of any given sized particle on the bed will eject a majority of smaller-sized particles. The results also show that the impact of a larger particle on the bed will eject a larger quantity of particles than that ejected by the impact of a smaller particle. A majority of these ejected particles consist of smaller-sized dust.

Overall, it can be seen that under the assumption of particles impacting the bed with the same impact velocities, bombardments will always result in the ejection of a large quantity of smaller-sized dust particles, a result also known experimentally (e.g., Ref. 28).

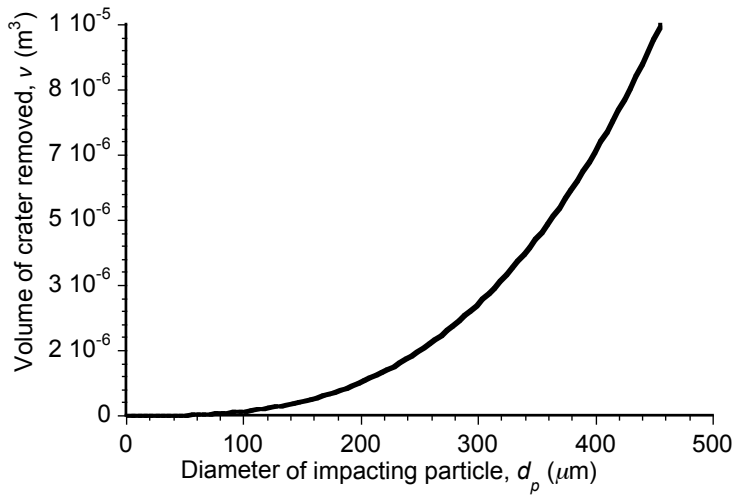

(a) Particle impact velocity

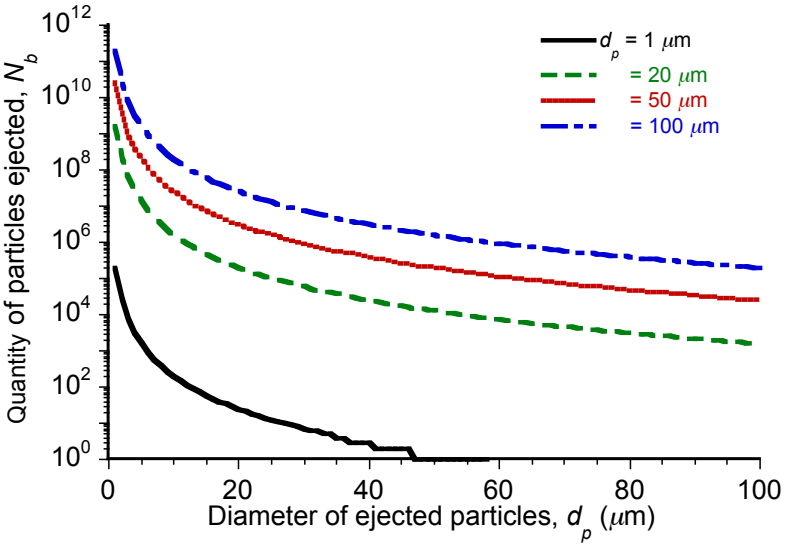

(b) Quantity of ejected particles

Figure 3.1: Results from the analysis of the bombardment ejection model with particles impacting the bed with the same velocity showing: (a) volume of the crater versus the diameter of the impacting particles, and (b) the total quantity particles of different diameters ejected through each impact.

3.1.1.2 Particles at the Same Conditions Before Impacting the Bed

In this case, the assumption was that particles (with diameters in the range 1–500 μm) were located at the same location with the same flow velocity before impacting the bed. The subsequent impact velocities of these particles were computed by solving the particle EOMs, as given by Eqs. 2.90 and 2.91. The results are shown in Fig. 3.2(a). Notice that because of inertial effects, the impact velocity decreases exponentially with an increase in particle size. Specifically, particles with smaller sizes (i.e., "dust" where $d_p < 10$ μm) impact the bed at a velocity approximately equal to the flow velocity, while the larger particles (i.e., with $d_p > 200$ μm) generally impact the bed with smaller velocities because of their higher aerodynamic drag and inertia.

Notice from Eq. 2.134 that the volume of the crater formed varies with d_p^3, but implicitly depends on the particle diameter from the impact velocity, which also varies with d_p, as shown in Fig. 3.2(a). The resulting effect on the volume of the crater is shown in Fig. 3.2(b). For smaller-sized particles, the volume of the crater increases with d_p^3, whereas for the larger particles the volume decreases because the impact velocity of these particles decreases with particle diameter. This, perhaps counterintuitive, result suggests that there exists a maxima, i.e., an intermediate particle size ($d_p \approx 25$ μm in the present case), for which the volume of material removed from the crater reaches a maximum. In practice, the actual particle size for this maximum will obviously depend upon the properties of the flow field, as well as those of the bed.

Figure 3.3(a) shows results from a comparison conducted to compute the total quantity of particles of different sizes that comprise the crater; each case is based on the ejec-

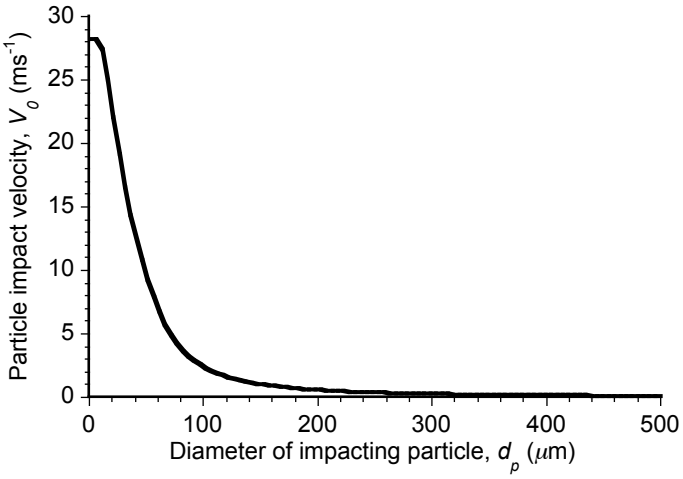

(a) Particle impact velocity

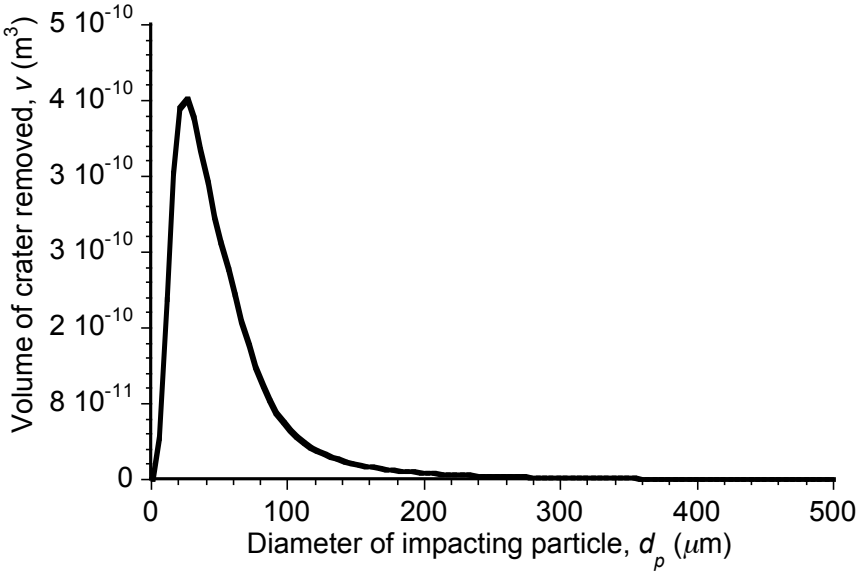

(b) Crater volume

Figure 3.2: Results from the simpler analysis of the bombardment ejection model with the particles of different sizes experiencing the same flow velocity just before impacting the bed: (a) particle impact velocity, and (b) volume of the crater.

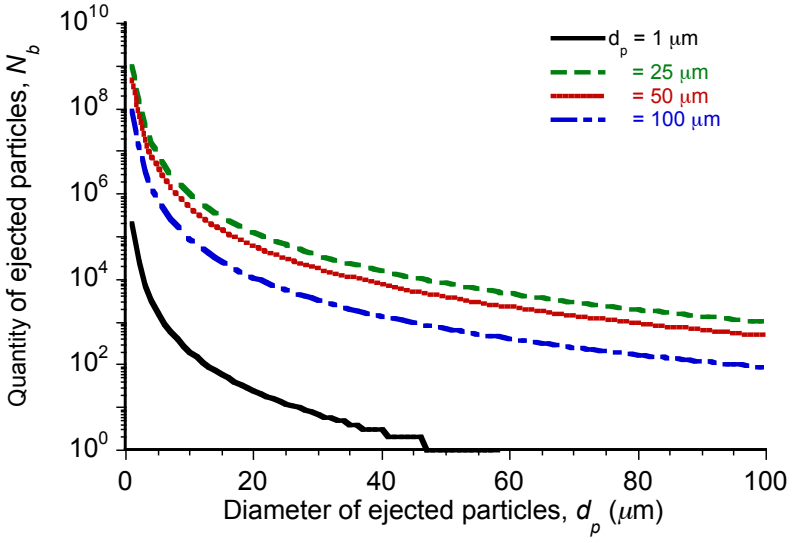

(a) Quantity of particles of various sizes ejected from different impacts

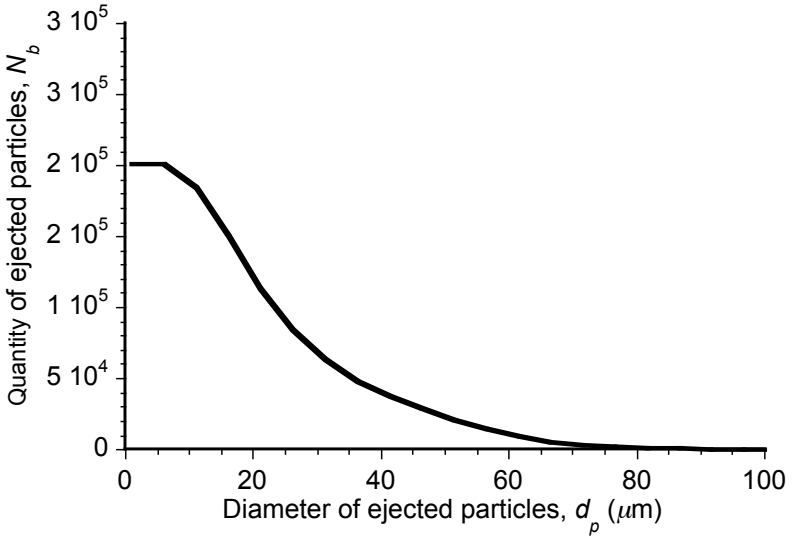

(b) Quantity of particles ejected with size equal to that of the impacting particle

Figure 3.3: Results from the simpler analysis of the bombardment ejection model with the particles of different sizes experiencing the same flow velocity just before impacting the bed: (a) total quantity of particles of different sizes ejected through each impact, and (b) total quantity of particles ejected with the size as that of the impacting particle.

tion of the same-sized particles. It can be seen that each impact yielded a greater quantity of the smaller-sized particles. However, the impact of particles of diameter $d_p = 25$ μm yielded the maximum quantity of ejected particles.

While the eventual integration of this model into the brownout simulation assumed that an impacting particle of a given size can eject particles only of its own size, the variation in the quantity of particles ejected when the same-sized particle bombards the bed is shown in Fig. 3.3(b). Notice that bombardment by a smaller-sized particles will eject a relatively large quantity of the same-sized particles. Also, the bombardment of a larger particle on the bed will result in fewer ejections of particles of its own size.

3.1.2 Convergence of the Time-Marching Algorithms

The convergence characteristics of the different time-marching algorithms to solve the EOMs and to convect the particles (see Section 2.4.2.2) were evaluated by using three test cases: (a) a one-dimensional harmonic velocity field study, (b) a two-dimensional vortex flow, and (c) a three-dimensional brownout simulation.

3.1.2.1 One-Dimensional Harmonic Velocity Field

In the first test case, a one-dimensional problem was considered in which a suspended particle was subjected to a harmonic flow velocity as given by

$$f(t) = V(t) = \sin t + \cos t \tag{3.1}$$

The exact solution of the velocity of the particle is

$$V_p(t) = V_{p_0} e^{-t/\tau_{p_s}} + \left(\frac{1+\tau_{p_s}}{1+\tau_{p_s}^2}\right)\sin t + \left(\frac{1-\tau_{p_s}}{1+\tau_{p_s}^2}\right)\cos t - \left(\frac{1-\tau_{p_s}}{1+\tau_{p_s}^2}\right) e^{-t/\tau_{p_s}} - g\tau_{p_s}(1-e^{-t/\tau_{p_s}}) \tag{3.2}$$

and that of the position of the particle is

$$X_p(t) = X_{p_0} - \tau_{p_s}\left(e^{-t/\tau_{p_s}} - 1\right) V_{p_0} \tag{3.3}$$

where V_{p_0} and X_{p_0} are the initial velocities and positions of the particles at t = 0 s.

Because the flow velocity in this case is not a function of particle position (see Eq. 3.1), the forcing function f^{n+1} (given by Eq. 2.92) can be evaluated exactly and the quadratic extrapolation using Eq. 2.122 is not required. Figures 3.4(a) and 3.4(b) show the maximum relative error in the particle velocity, V_p, and particle position, X_p, at $t =$ 10 s, respectively. For the integration of the particle velocity, V_p^{n+1}, as expected, the EI scheme behaves as first-order accurate, the EI-BDF2 and TR-BDF2 schemes behave as second-order accurate, and the EI-BDF3 and TR-BDF3 schemes behave as third-order accurate.

However, for the integration of the particle position, as shown in Fig. 3.4(b), the EI-BDF3 scheme behaves as second-order accurate instead of being third-order accurate. This outcome is because of the lower-order schemes being used at the first and the second time steps. Recall that for the EI-BDF3 scheme, the first time step is evaluated using the EI scheme, and the second time step is evaluated using the BDF2 scheme. Therefore, the EI-BDF3 scheme becomes overall second-order accurate. Interestingly, the TR-BDF3 scheme still behaves as third-order accurate. Overall, this study shows that the accuracy

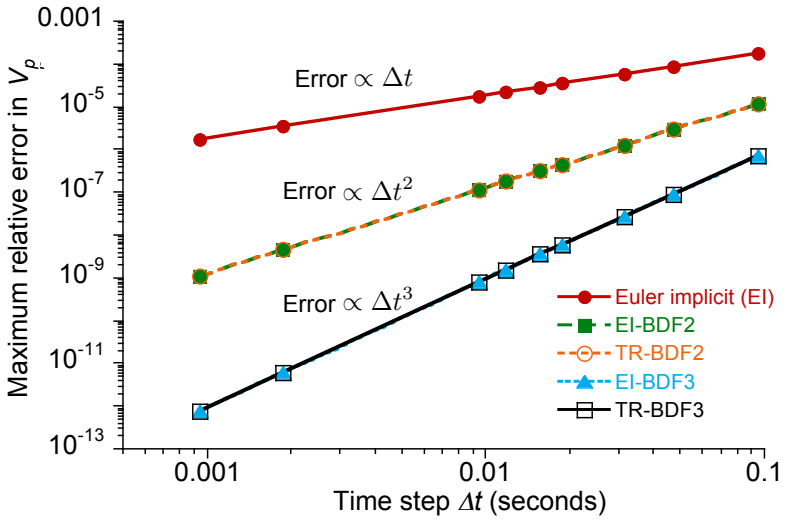

(a) Maximum relative error in particle velocity

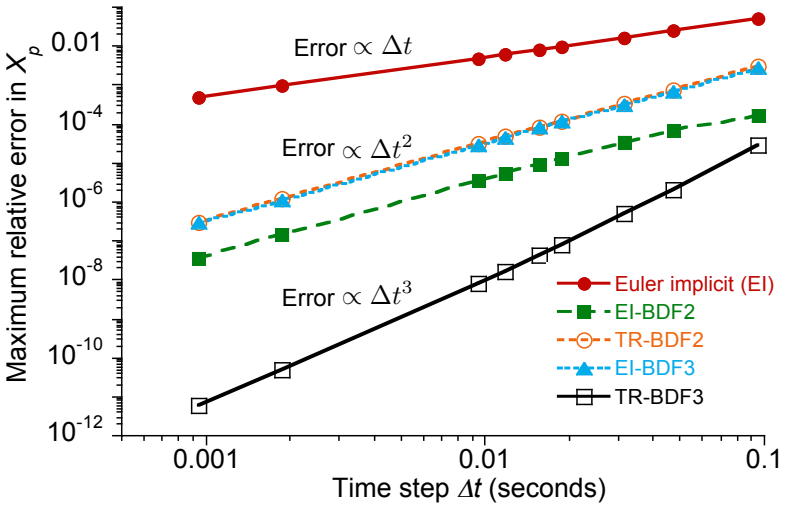

(b) Maximum relative error in particle position

Figure 3.4: Variation of maximum relative error in (a) particle velocity, and (b) particle position, at $t = 10$ s for the Euler implicit (EI), EI-BDF2, TR-BDF2, EI-BDF3, and TR-BDF3 schemes.

of the multi-step schemes can be affected by the lower-order schemes used at the initial time steps.

3.1.2.2 Two-Dimensional Vortex Flow

In the second test case, the convection of a particle in the flow produced by a two-dimensional vortex was considered. A particle of small size will follow a perfect circle under the influence of the flow field generated by a vortex. In this test study, the vortex was assumed to be located at $\{x_v, y_v\} = \{0.5, 0.5\}$ m, and a particle of diameter, $d_p = 10^{-10}$ m was positioned initially at $\{X_{p_x}(t_0), X_{p_y}(t_0)\} = \{0, 0\}$ m. The exact path of this particle under the influence of a stationary vortex is a circle of radius $R_{\text{exact}} = 0.707$ m, which is centered at $\{x_v, y_v\}$.

The numerical solution of the particle position should also follow the circle. Figure 3.5(a) shows the exact circular path and the paths followed by the particle as computed using the EI-BDF2 and EI-BDF2-E integration schemes. Without using extrapolation, the particle follows a spiral path of increasing radius; see Fig. 3.5(b). Using extrapolation of the flow velocity, the particle follows a circle with radius ~ 0.707 m, as shown in Fig. 3.5(b). Therefore, a higher-order approximation of the flow velocity at the $(n+1)^{\text{th}}$ time step is very important in this problem because it can significantly impact the overall accuracy of the solution.

Figure 3.6 shows the maximum relative error in the particle position with respect to the exact solution (i.e., a circular path). Notice that the approximate slope of the EI-BDF2 is 0.5, which is lower than the expected linear slope in this case. The reason for

this outcome is because of the use of the lower-order Euler implicit scheme at the first time step.

Furthermore, notice that all the other schemes are third-order accurate. Again, this is an expected outcome for the EI-BDF3-E and the TR-BDF3-E schemes. However, for the BDF2-based schemes, the coefficient of the error term, which depends upon Δt^2, is approximately zero for this single vortex problem. Therefore, the EI-BDF2-E and the TR-BDF2-E schemes are also third-order accurate. However, the use of the BDF3-based schemes require higher memory storage because at each time step the particle velocities and positions at the three previous time steps have to be stored. Therefore, the EI-BDF2-E scheme was used to obtain the subsequent results shown in the present work.

3.1.2.3 Three-Dimensional Brownout Simulation

The convergence of the particle positions with decreasing time step, $\Delta\psi$, was verified by conducting numerical experiments. To this end, the convergence of the free-vortex solution and the trajectories of the particles were analyzed for a rotor hovering in ground effect at $z/R = 1$.

The specifications of the rotor used in this study are shown in Table D.1 as given in Appendix D. In this case, the rotor was trimmed to a thrust coefficient of $C_T = 0.0018$ for all the cases discussed. The grid resolutions along the spatial and the temporal coordinates were varied between $\Delta\psi = \Delta\zeta = 20^\circ$ to 2.5°. Because the exact solutions of the rotor wake geometry and the particle trajectories are unknown, the solution obtained by using $\Delta\psi = \Delta\zeta = 2.5^\circ$ was considered to be the "exact" solution.

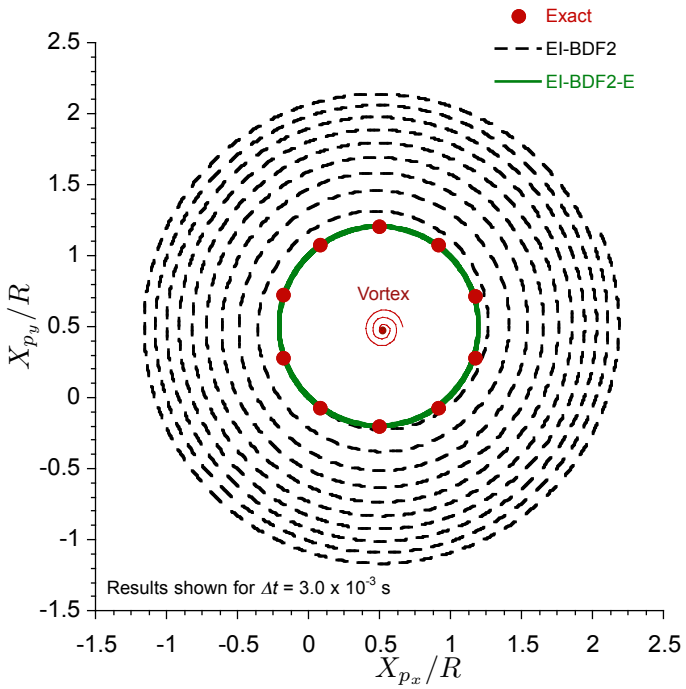

(a) Particle trajectories obtained by using the EI-BDF2 and EI-BDF2-E schemes.

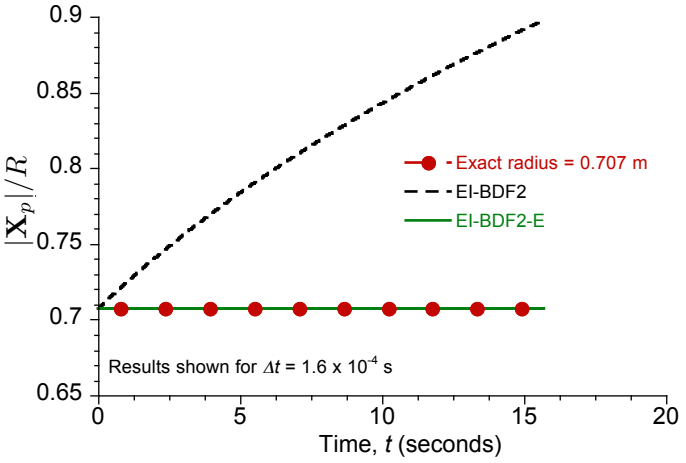

(b) Radius of the particle path at different times using the EI-BDF2 and EI-BDF2-E scheme.

Figure 3.5: Plots showing: (a) trajectory followed by the particle, i.e., X_{p_y} versus X_{p_x}, and (b) the radius of the path, $|\mathbf{X}_p|$ followed by the particle using the EI-BDF2 and EI-BDF2-E schemes.

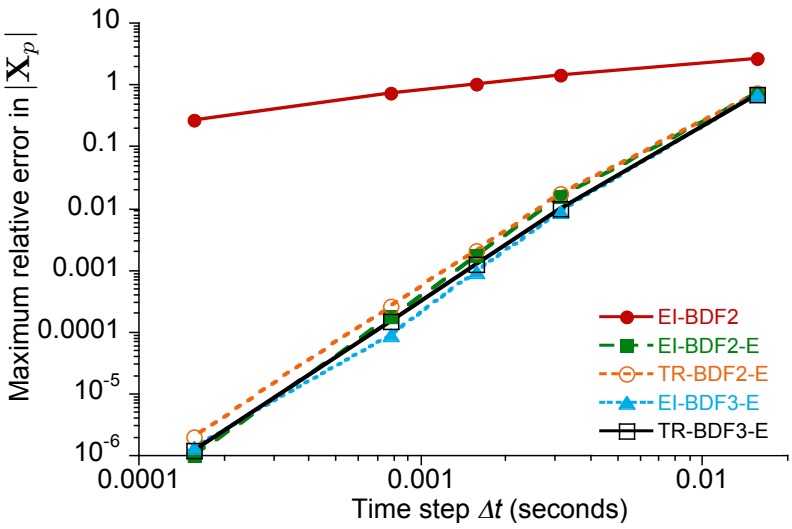

Figure 3.6: Variation of maximum relative error in particle position, $|\mathbf{X}_p|$, at $t = 17$ s using the EI-BDF2, EI-BDF2-E, TR-BDF2-E, EI-BDF3-E, and TR-BDF3-E schemes.

Figure 3.7 shows the radial and axial displacements of the wake filaments as a function of wake age for different grid discretizations. The solution confirms the converging trend with increasing grid resolution. The solutions with grid resolutions of 15° and 20° show considerable differences to the solution with the 2.5° grid resolution. For values of $\Delta\psi = \Delta\zeta$ less than 10°, the radial and axial wake displacements are close to the solution for $\Delta\psi = \Delta\zeta = 2.5°$. This convergent nature of the problem also shows that all of the numerical schemes are convergent.

Figure 3.8 shows the numerical errors in the wake geometry as a function of grid discretization. The results are plotted on logarithmic scales, therefore, the slope of these lines is the order of accuracy of the wake solution. Notice that the slopes of the variations of axial and radial wake displacements are 1.7 and 2.3, respectively. Therefore, the free-vortex wake solution is essentially second-order accurate.

The flow velocities induced at $z/R = 0.02$ above the ground along the longitudinal

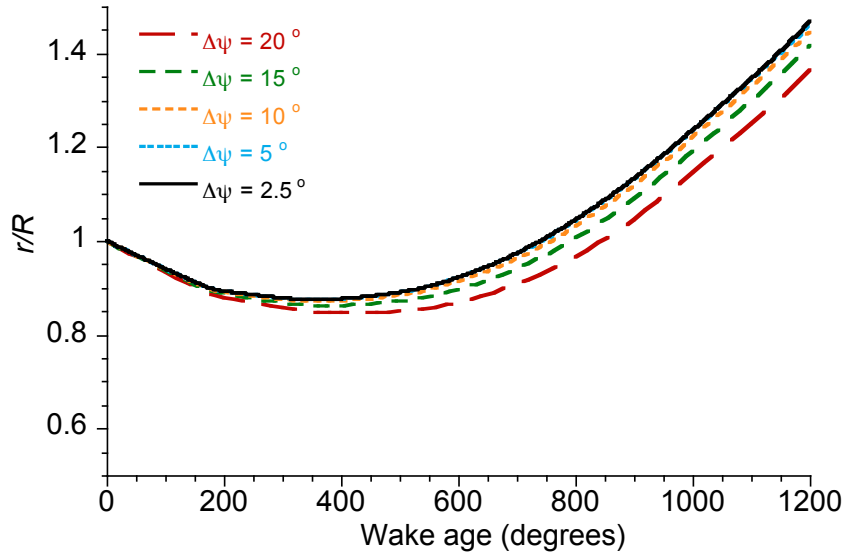

(a) r/R versus wake age

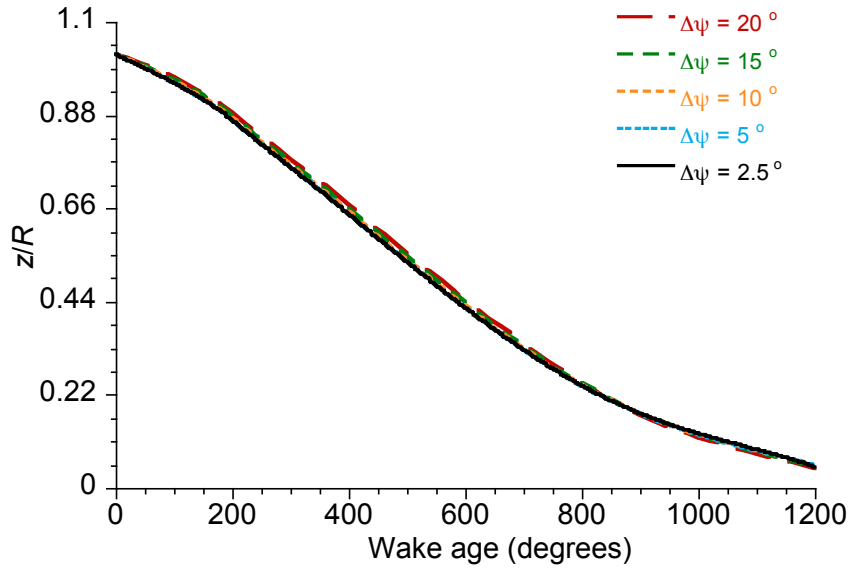

(b) z/R versus wake age

Figure 3.7: Numerical solution from the free-vortex method for different discretization showing grid independence for finer resolution: (a) radial displacements, r/R, and (b) axial displacements, z/R, as a function of wake age.

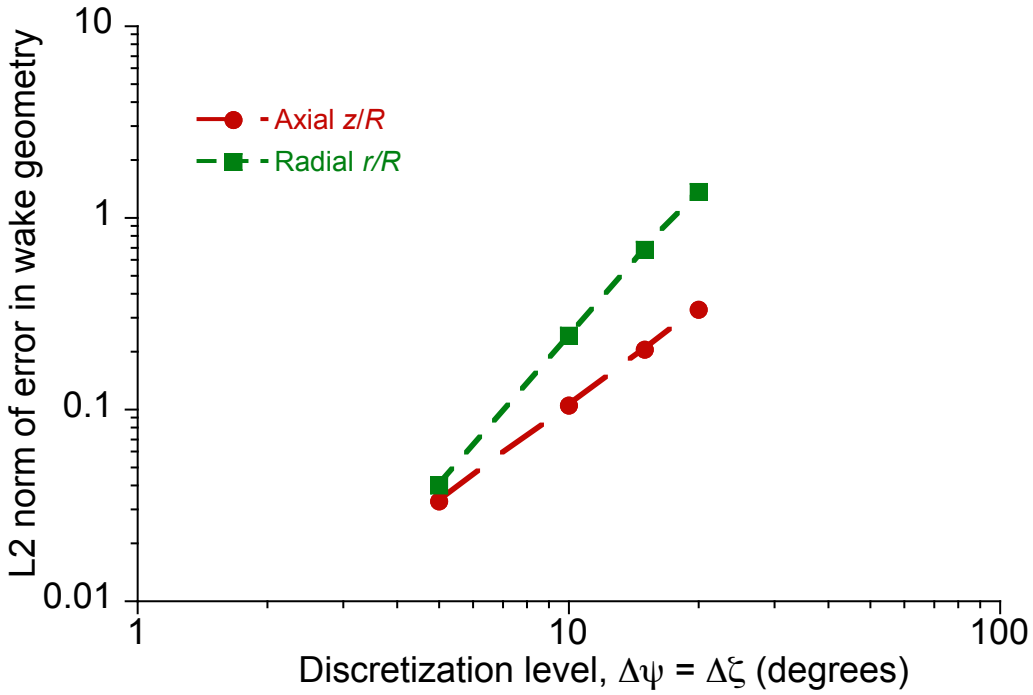

Figure 3.8: Numerical errors in the free-vortex method solution for hover in ground effect with increasing grid discretization.

axis with different grid resolutions are shown in Fig. 3.9. It can be seen that there is a converging trend with increasing grid resolution. The velocities induced with $\Delta\psi = \Delta\zeta \leq 10^\circ$ also show good agreement for smaller values of $\Delta\psi$ and $\Delta\zeta$. Therefore, the subsequent results were obtained by using a 10° discretization in both space and time, i.e., $\Delta\psi = \Delta\zeta = 10\ ^\circ$.

Now that the convergence of the free-vortex solution has been demonstrated, the next step was to examine the convergence of the numerical solution of the particle EOMs. To this end, a simpler case with 100 particles was used where they were positioned at $z/R = 0.02$ along the longitudinal axis (i.e., $y/R = 0$) between $x/R = -5$ to 5. The solution of the particle positions, $\mathbf{X}_p$, obtained by using $\Delta\psi = \Delta\zeta = 2.5^\circ$ was considered

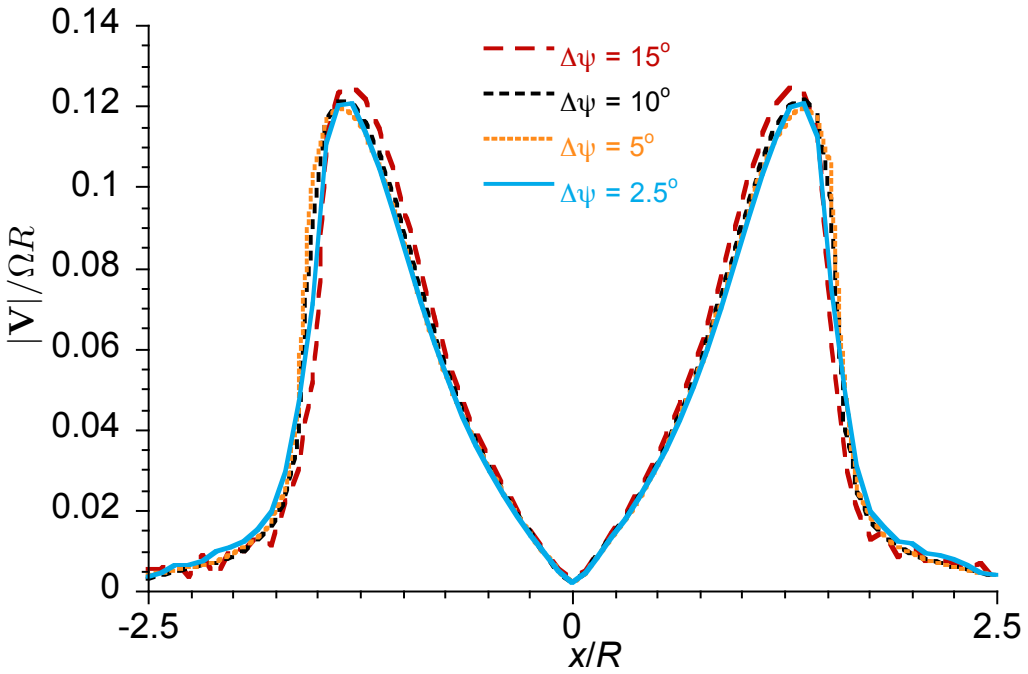

Figure 3.9: Variation of the total induced velocity along a longitudinal axis at $z/R = 0.02$.

to be the exact solution in this case. The solution of the particle positions under the influence of the rotor induced flow was computed for 7 seconds, and the numerical errors for different values of $\Delta\psi$ were analyzed at the end of the simulation.

The errors in the positions of each particle can be compared relative to its position from the solution obtained by using a grid resolution of 2.5°. The error in the simulation for a particular grid resolution was then obtained by finding the maximum error in the positions of all the particles at the end of the simulation, which is shown in Fig. 3.10 as a function of the grid resolution. Notice from the quadratic fit that the error follows a second-order behavior. Therefore, the solution of the particle EOMs is second-order accurate in time.

The corresponding magnitudes of the position vector, $|\mathbf{X}_p|$, for different grid resolutions are plotted in Fig. 3.11 for just two representative particles. In the first case shown

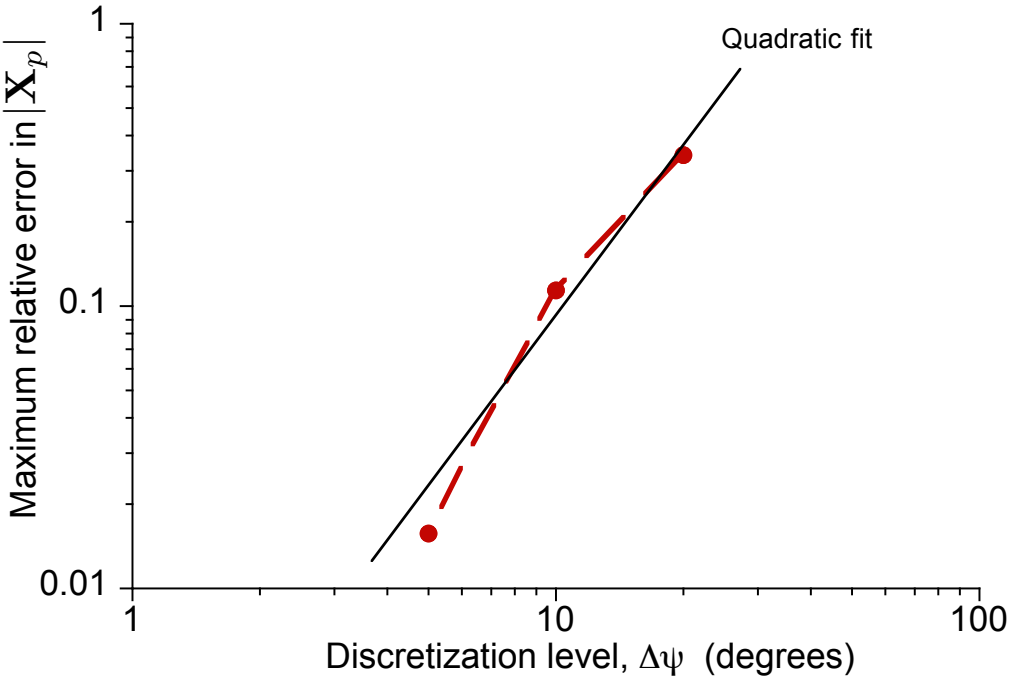

Figure 3.10: Maximum numerical errors in the solution of the particle positions at $t = 7$ s, as a function of grid resolution.

in Fig. 3.11(a), the positions of the particle were well resolved for $\Delta\psi \leq 10^\circ$. This case represents the majority of the particles in the simulation and, therefore, a discretization of $\Delta\psi = 10^\circ$ was subsequently used in the present study. However, for a few particles, it was found that $\Delta\psi = 10^\circ$ was insufficient. One such example is shown in Fig. 3.11(b), for which $\Delta\psi = 5^\circ$ seems to give a more accurate solution. Nevertheless, taking into consideration the computational expense of the bigger problem, a time step size of $\Delta\psi = 10^\circ$ was chosen. All of the subsequent computations in this chapter were obtained by using $\Delta\zeta = \Delta\psi = 10^\circ$.

Recall that the results shown in the present analysis were obtained by using the Stokes flow assumption. This assumption can be justified by considering the particle Reynolds number, Re_p, in the simulated brownout dust clouds. In this case, two brownout

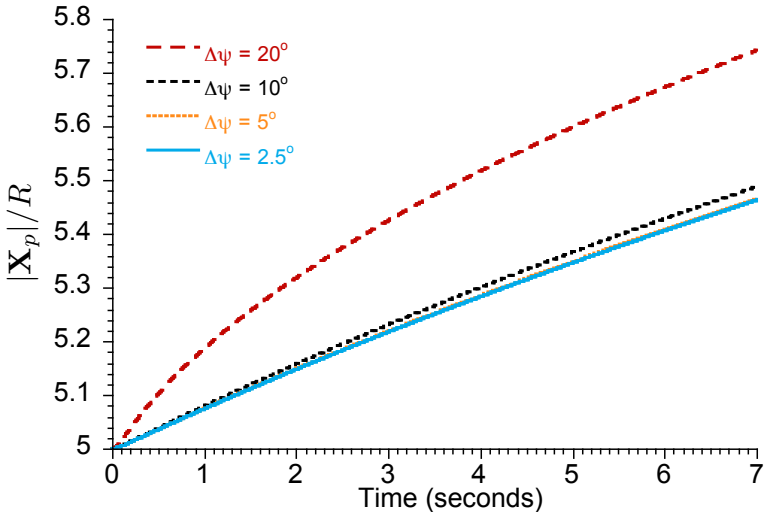

(a) Particle 1

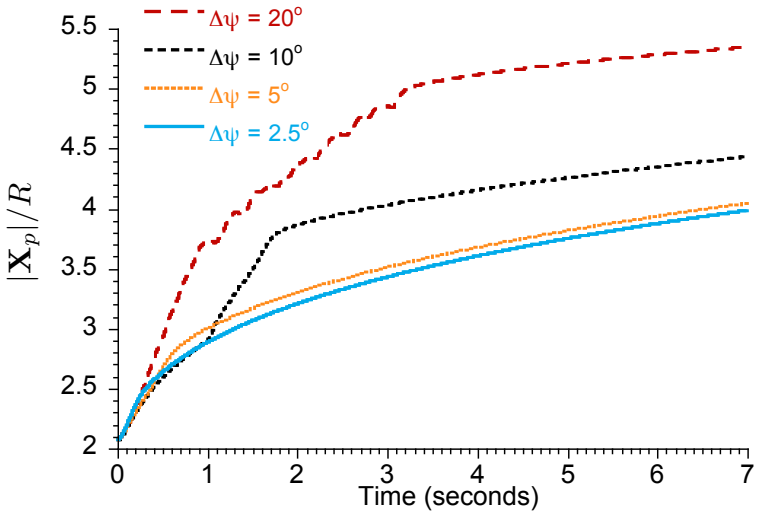

(b) Particle 2

Figure 3.11: Trajectories of two particles obtained using different grid discretizations.

dust cloud were simulated for particles with $d_p = 20\ \mu$m and $100\ \mu$m, respectively. A total of 10^5 particles was used for these simulations.

Figure 3.12 shows contour maps of Re_p at heights of $z/R = 0.02$ and 0.05. At $z/R = 0.02$, the value of Re_p of the majority of particles with $d_p = 20\ \mu$m was less than 3 (see Fig. 3.12(a)), and for particles with $d_p = 100\ \mu$m, it was less than 20 (see Fig. 3.12(b)). However, everywhere else in the flow, the values of Re_p were less than 1; see Figs. 3.12(c) and 3.12(d) for the contour plots of Re_p at $z/R = 0.5$. Therefore, except for the regions very close to the ground, it should be justified to model the brownout dust clouds by using the Stokes flow assumption.

3.2 Comparisons with Measurements

This section presents results from a study conducted to validate the brownout methodology. A prerequisite for validating the formation of such dust clouds is the validation of the rotor flow in ground effect operations. Although performance results from the FVM model for ground effect conditions have been previously validated (see Refs. 99 and 34), the present work focusses on the prediction of the actual flow velocities closer to the ground. To this end, two studies were conducted. In the first study, the flow field generated by a small laboratory rotor hovering at one rotor radius above the ground was compared with the measurements of Lee et al. (Ref. 19) and the CFD predictions from Kalra et al. (Ref. 32). In the second study, the groundwash velocities generated by full-scale UH-1 and CH-54 helicopters were compared to the measurements of Leese et al. (Ref. 122).

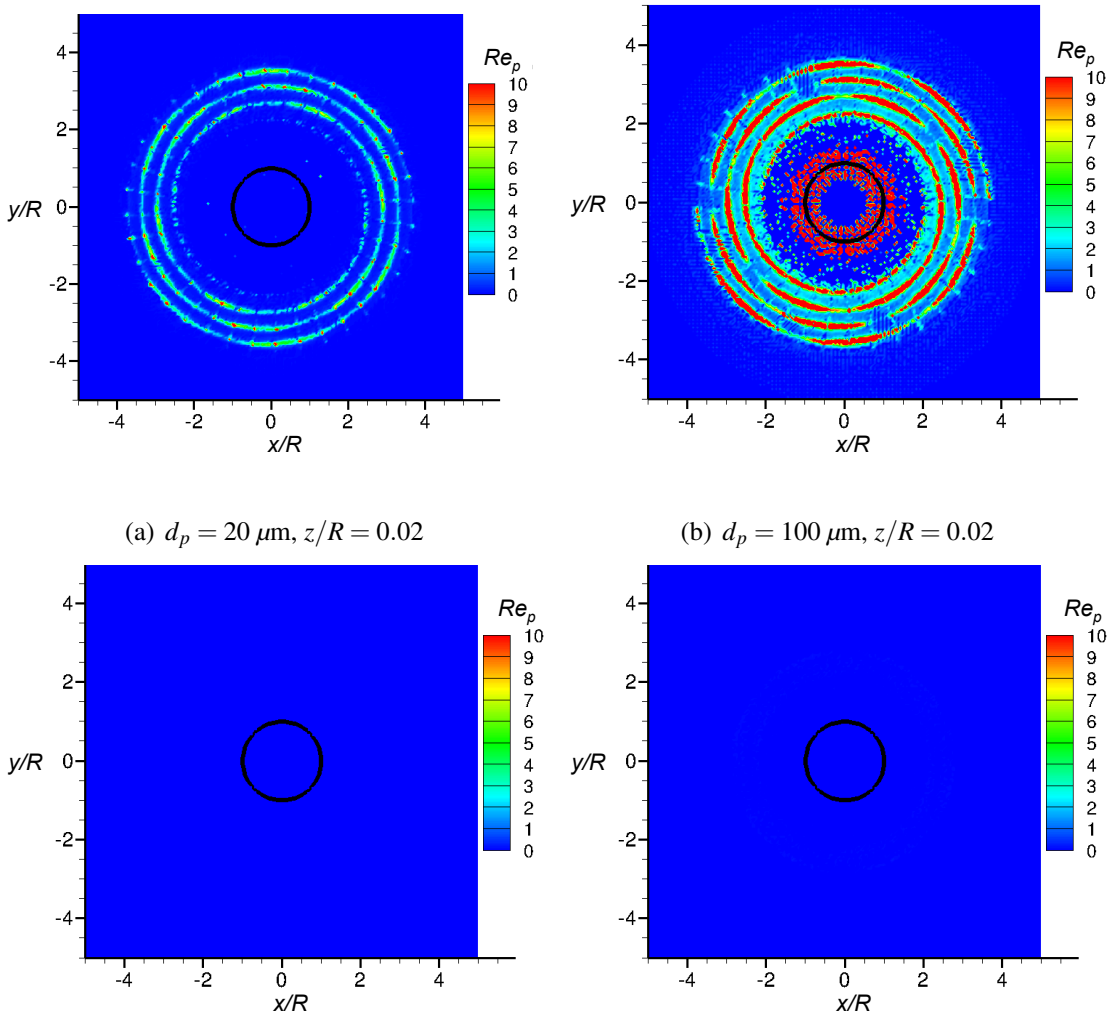

(a) $d_p = 20\ \mu$m, $z/R = 0.02$

(b) $d_p = 100\ \mu$m, $z/R = 0.02$

(c) $d_p = 20\ \mu$m, $z/R = 0.05$

(d) $d_p = 100\ \mu$m, $z/R = 0.05$

Figure 3.12: Contour plots of particle Reynolds number, Re_p, obtained at: (a) $z/R = 0.02$ for particles with $d_p = 20\ \mu$m, (b) $z/R = 0.02$ for particles with $d_p = 100\ \mu$m, (c) $z/R = 0.05$ for particles with $d_p = 20\ \mu$m, and (d) $z/R = 0.05$ for particles with $d_p = 100\ \mu$m.

Validation of the predicted brownout dust clouds is very difficult because of the dearth of actual measurements. However, Wong and Tanner (Ref. 42) have conducted photogrammetry studies to obtain measurements of the sizes and shapes of the brownout dust clouds that were generated by a full-scale helicopter during taxi-pass and approach-to-touchdown maneuvers. Although not all of the data required to validate the numerical simulations were measured or were otherwise available, these measurements were used in the present work to help validate the modeling. A sensitivity study was also conducted to examine the effects of helicopter weight, wind conditions, initial flight profile, and particle sizes, on the development of the brownout dust clouds.

3.2.1 Validation of Flow Predictions

The results from the FVM were validated for a laboratory-scale rotor and for the full-scale UH-1M and CH-54 helicopters. In the first case, the measurements of the flow field were obtained from Lee et al. (Ref. 19). In the second case, groundwash velocity measurements for the UH-1M and CH-54 helicopters were obtained from Leese et al. (Ref. 122).

3.2.1.1 Laboratory-Scale Rotor

Experiments were conducted by Lee et al. (Ref. 19) using a small rotor hovering in ground effect at various heights above the ground. The specifications of this rotor are shown in Table D.2 in Appendix D. The blades had a circular-arc airfoil with thickness of 3.7% and a camber of 3.3%.

Kalra et al. (Ref. 31, 32) also compared the rotor flow predicted using a RANS-based CFD solver with these measurements. Overall, a good agreement was obtained. In the present case, the measurements from Lee et al. (Ref. 19) and the CFD calculations from Kalra et al. (Ref. 32) were both used to validate the results obtained from the FVM. This study was conducted for a rotor hovering at $z/R = 1$. The rotational frequency of the rotor in this case was 50 Hz. The sectional aerodynamics were modeled using airfoil tables generated by CFD, which are shown in Fig. 3.13.

Figure 3.15 shows the top and side views of the wake geometries obtained from the FVM. Notice the significant radial expansion of the wake as it approaches the ground. The vertical and radial displacements of the tip vortices as a function of wake age from the FVM are compared with the CFD predictions in Fig. 3.15, where good agreement is shown. The tip vortex trajectories from the FVM show somewhat larger radial contraction when compared to the CFD, as shown in Fig. 3.16. However, overall the agreement is still acceptable.

A comparison of the corresponding tip vortex strength and core radius versus wake age is shown in Fig. 3.17. The predictions of the vortex strength from the FVM and the CFD agree well with each other, as shown in Fig. 3.17(a). Notice that the FVM predicts somewhat smaller core radius than that from the CFD at younger wake ages, as shown in Fig. 3.17(b). The effects of turbulence from the merging of wake sheets, eddies, relaminarization of vortex core, etc., are modeled in the FVM by using the semi-empirical core growth model (described previously in Section 2.1.3.2), which has been derived from both full-scale as well as model-scale rotary-wing measurements.

The CFD results, as shown in Fig. 3.17(b), were obtained using the Spalart-Allmaras

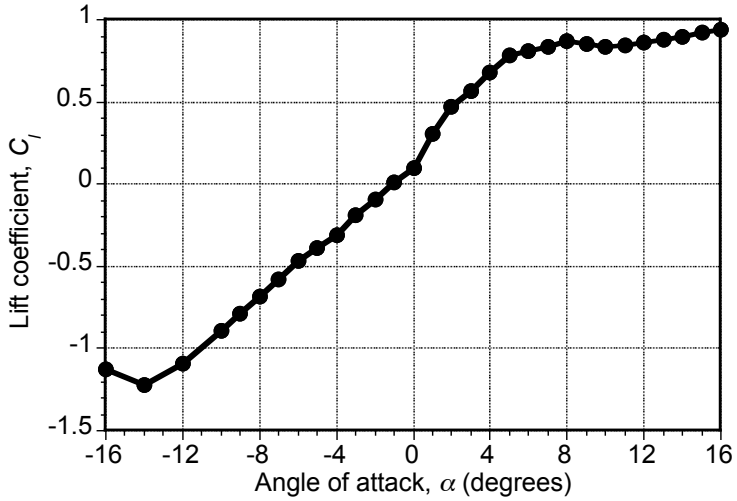

(a) Lift coefficient versus angle of attack

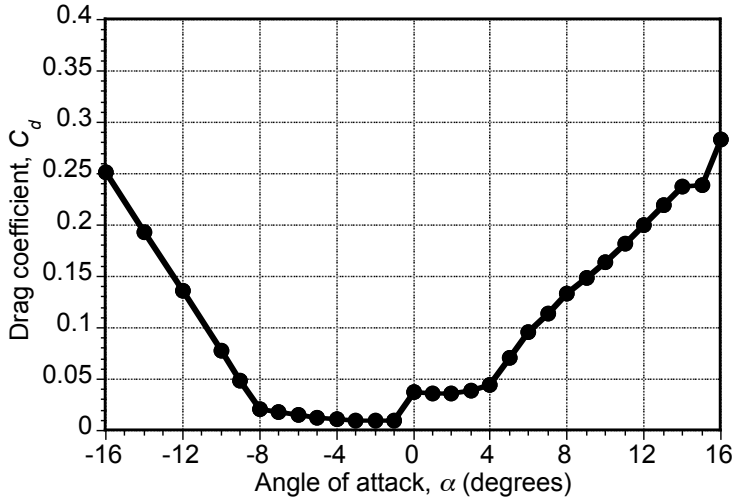

(b) Drag coefficient versus angle of attack

Figure 3.13: Variation of the lift and drag coefficients for the circular-arc airfoil used on the laboratory-scale rotor. Coefficients were generated using CFD.

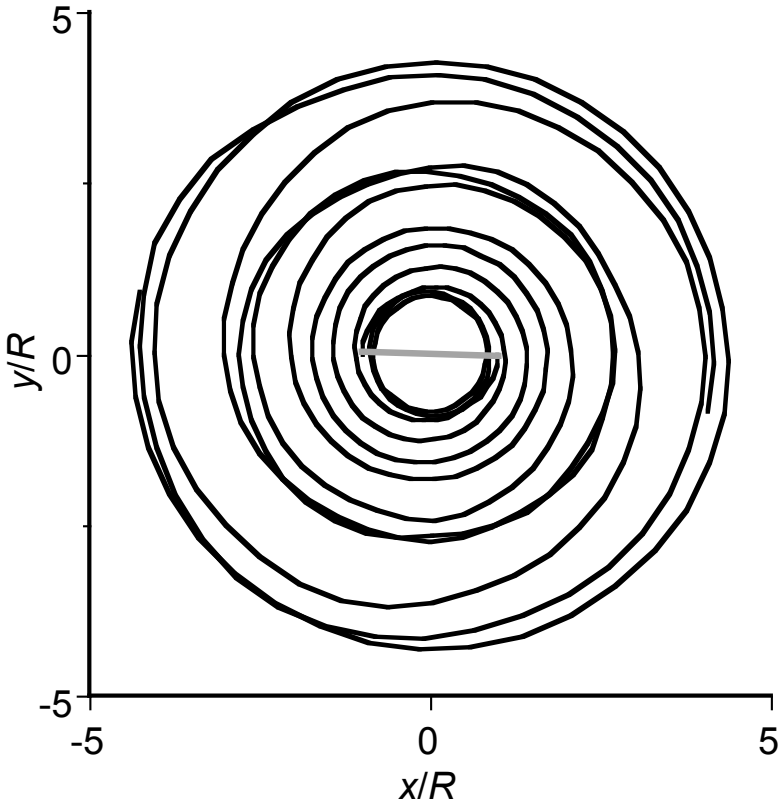

(a) Top view

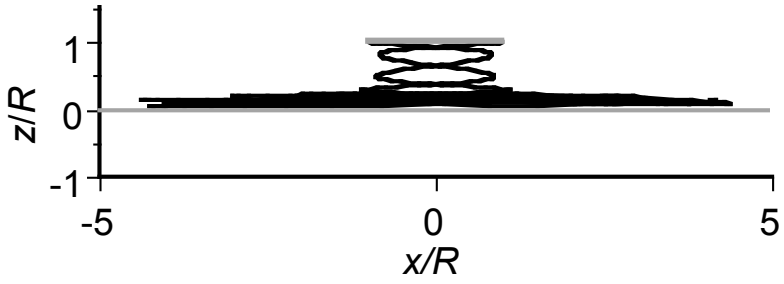

(b) Side view

Figure 3.14: Top and side views of the wake for the laboratory-scale rotor hovering IGE at $z/R = 1$.

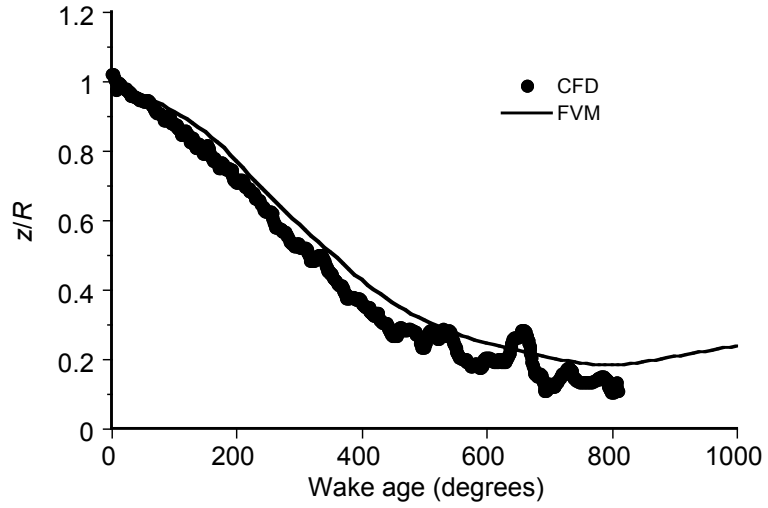

(a) Vertical displacements versus wake age

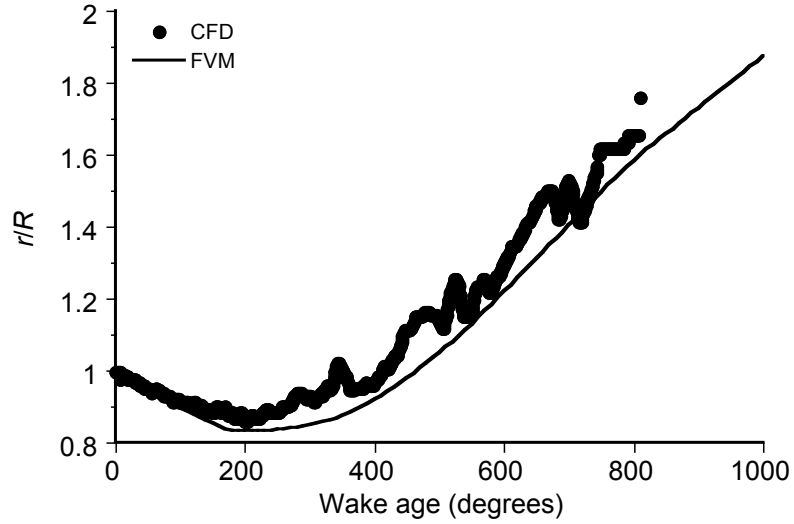

(b) Radial displacements versus wake age

Figure 3.15: Variation of vertical and radial displacements of the tip vortices with wage age for the laboratory-scale rotor hovering IGE at $z/R = 1$.

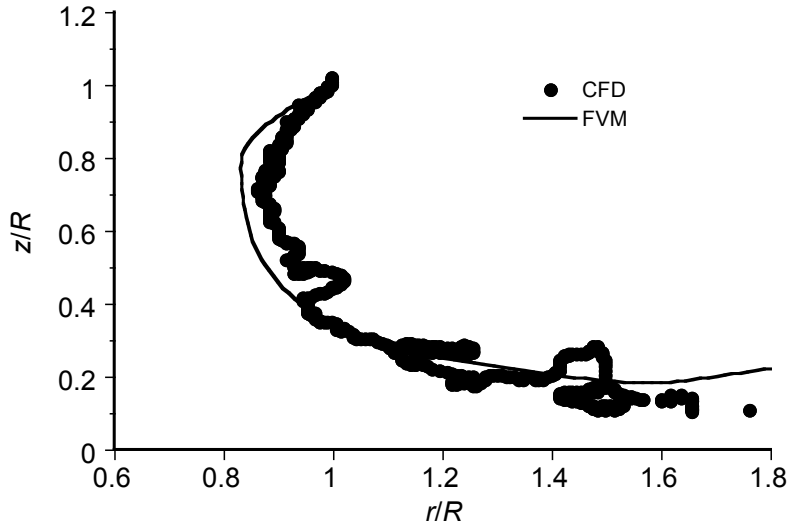

Figure 3.16: Wake boundaries for the laboratory-scale rotor hovering IGE at $z/R = 1$ as predicted by the CFD and the FVM.

(Ref. 54) turbulence model. It is known that the core radius predicted from the CFD can be sensitive to the use of turbulence models, but the effects were not shown in Refs. 31 and 32. Furthermore, the larger value of r_c predicted by the CFD results can be because of the effects of grid size. The use of coarser grids in CFD can result in artificial dissipation of vorticity that can result in a relatively larger core radius. In fact, dependencies of the CFD results on grid size, especially of the core radius, were shown in Ref. 32, and it was clear that refining the grid size reduces the value of the predicted core radius.

Predictions of the time-averaged radial velocity profiles from the FVM and the CFD versus the measurements of Lee et al. (Ref. 19) are shown in Figs. 3.18, 3.19 and 3.20 for $r/R = 0.8$, 1.0, 1.25, 1.5, 1.75 and 2.0, where r is the radial distance from the rotational axis. The radial velocity was normalized by the rotor hover velocity, $v_h = \sqrt{T/2\rho A}$, and the radial r and wall normal distance z were normalized by the rotor radius R.

The results show the formation of wall-jet, which decreases in height at distances

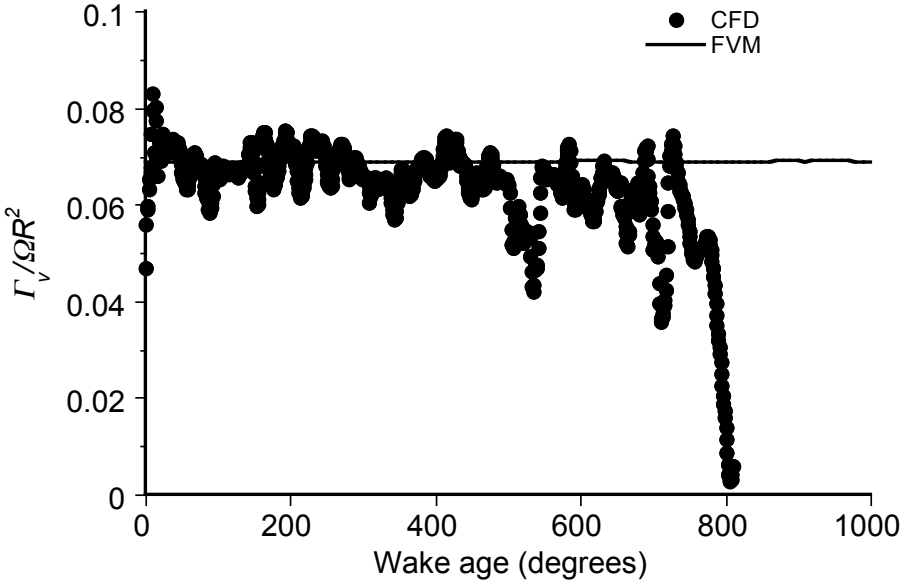

(a) Tip vortex strength versus wake age

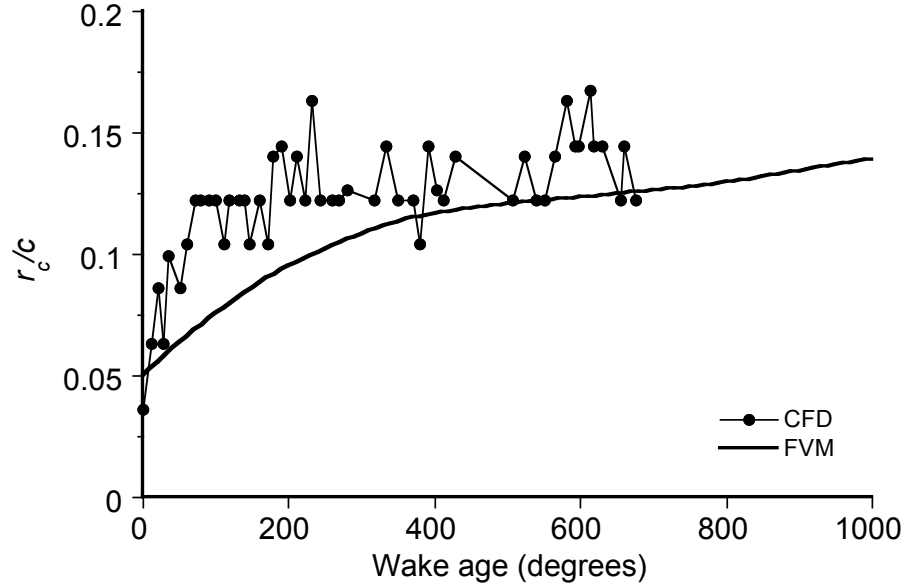

(b) Core radius versus wake age

Figure 3.17: Variation of the normalized: (a) tip vortex strength, and (b) core radius, versus wake age for a rotor hovering IGE at $z/R = 1$.

farther from the rotational axis, as shown in Figs. 3.18, 3.19 and 3.20. The radial velocity in the wall-jet increases with r/R. Notice that there is a reasonable agreement of the predictions from the FVM with the measurements further away from the ground. At greater radial downstream distances, both the CFD and the FVM overpredict the radial velocities of the wall-jet. In particular, notice that the radial velocity predicted by the FVM does not satisfy the no-slip condition at the ground. Therefore, a representation of the flow field closer to the ground was made by assuming a logarithmic boundary layer profile, as explained in Section 2.2. In this approximation, the magnitude of the maximum wall-jet velocity, and the height at which it occurs are important. Notice in Figs. 3.18, 3.19 and 3.20 that these two parameters match well at farther downstream locations, which is where the most of the sediment is usually mobilized (Ref. 17).

It must also be pointed out that proper modeling of the viscous region can only be achieved by either using full viscous CFD solution, as performed by Kalra et al. (Ref. 31, 32), or by coupling the FVM with a full boundary layer or CFD solution in the immediate region of the ground. Both of these techniques will significantly increase the computational cost of the flow solution and their use must ultimately be traded off against better fidelity and cost. This effort, however, is left for future work.

3.2.1.2 Comparison of Groundwash Velocities at Full-Scale

Measurements of the groundwash velocities from Leese et al. (Ref. 122) for full-scale helicopters were used to compare the FVM predictions. The helicopters examined in the present work were the CH-54 and the UH-1, with their specifications being given

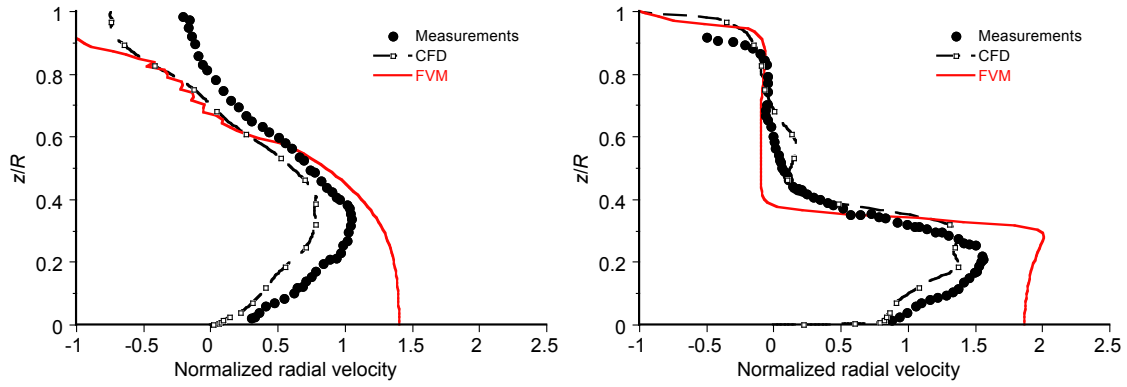

(a) $r/R = 0.8$ (b) $r/R = 1.0$

Figure 3.18: Variation of the time-averaged radial velocity profiles at $r/R = 0.8$ and 1.0 versus normalized height above the ground as obtained from experiments, CFD, and the FVM.

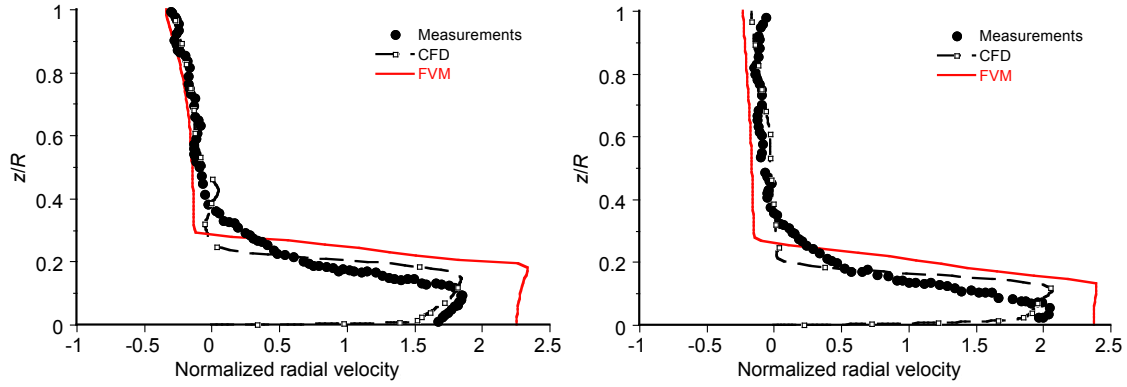

(a) $r/R = 1.25$ (b) $r/R = 1.5$

Figure 3.19: Variation of the time-averaged radial velocity profiles at $r/R = 1.25$ and 1.5 versus normalized height above the ground as obtained from experiments, CFD, and the FVM.

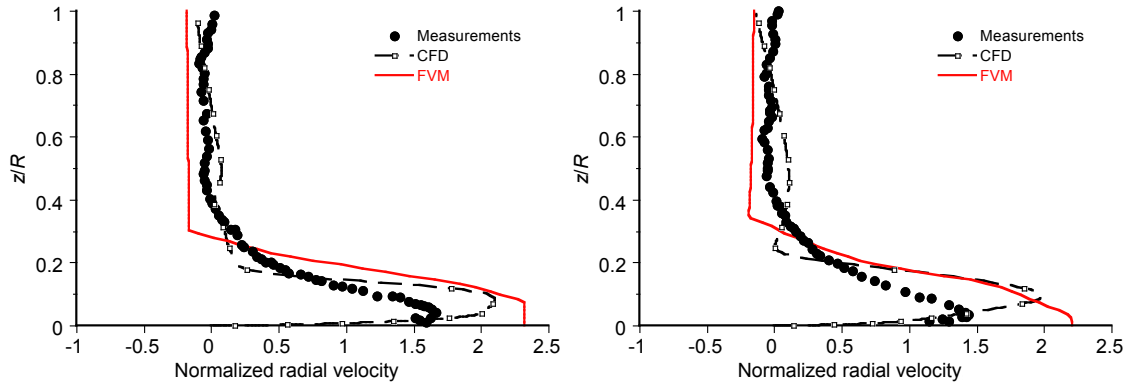

(a) $r/R = 1.75$ (b) $r/R = 2$

Figure 3.20: Variation of the time-averaged radial velocity profiles at $r/R = 1.75$ and 2.0 versus normalized height above the ground, as obtained from experiments, CFD, and the FVM.

in Tables D.4 and D.5, respectively, of Appendix D.

Figures 3.21 and 3.22 show the time-averaged groundwash velocities at 0.3 ft above the ground as produced by the CH-54 helicopter hovering at 80 ft and 40 ft (in terms of rotor height) above the ground, respectively. Similarly, Fig. 3.23 shows the time-averaged groundwash velocities at 0.3 ft above the ground produced by a UH-1M helicopter hovering at 44 ft above the ground. The predicted velocities are in reasonably good agreement with the measurements, especially the peak values and their radial locations, although there are obviously some differences as well. While it is tempting to attribute these deficiencies to the aerodynamic modeling, it must be noted that the measurements themselves are only approximate in that they were made using turbine anemometers. Such anemometers do not respond or measure accurately the time-varying aspects of the three-dimensional unsteady flow field produced by the rotor.

Notice from Figs. 3.21, 3.22 and 3.23 that the peak velocities at the ground occur

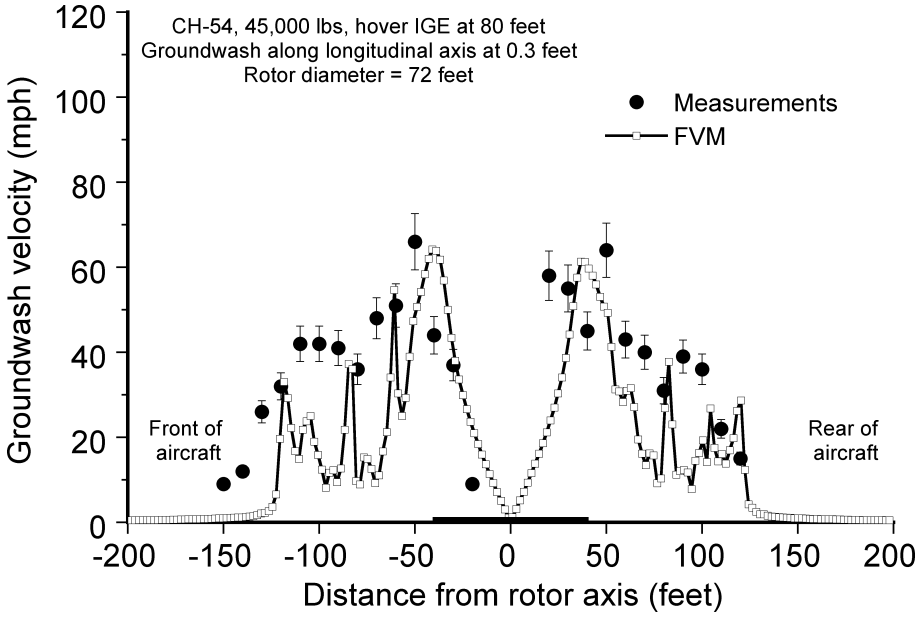

(a) Longitudinal axis

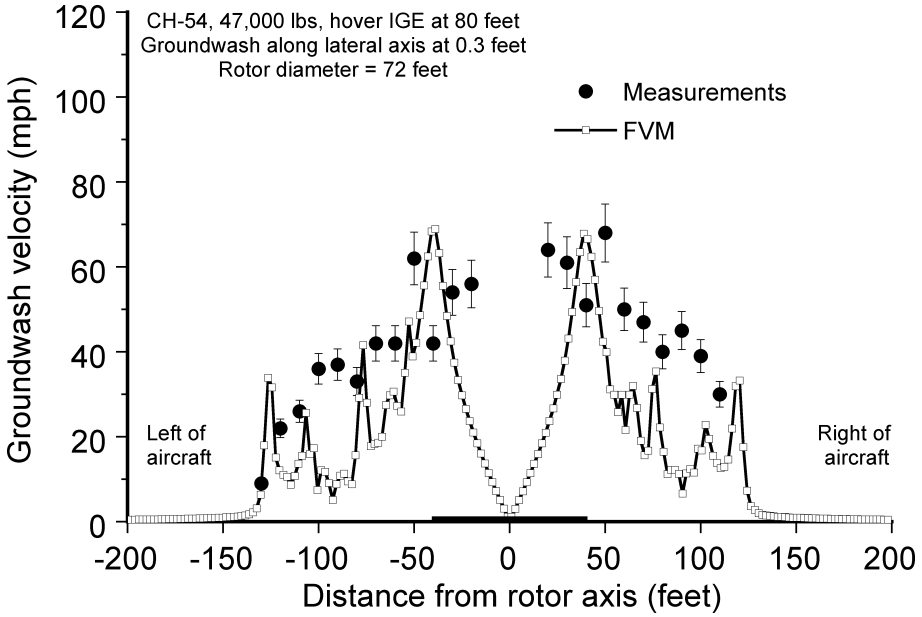

(b) Lateral axis

Figure 3.21: Variation of time-averaged groundwash velocity at 0.3 ft above the ground for a CH-54 helicopter hovering at 80 ft: (a) longitudinal axis, and (b) lateral axis.

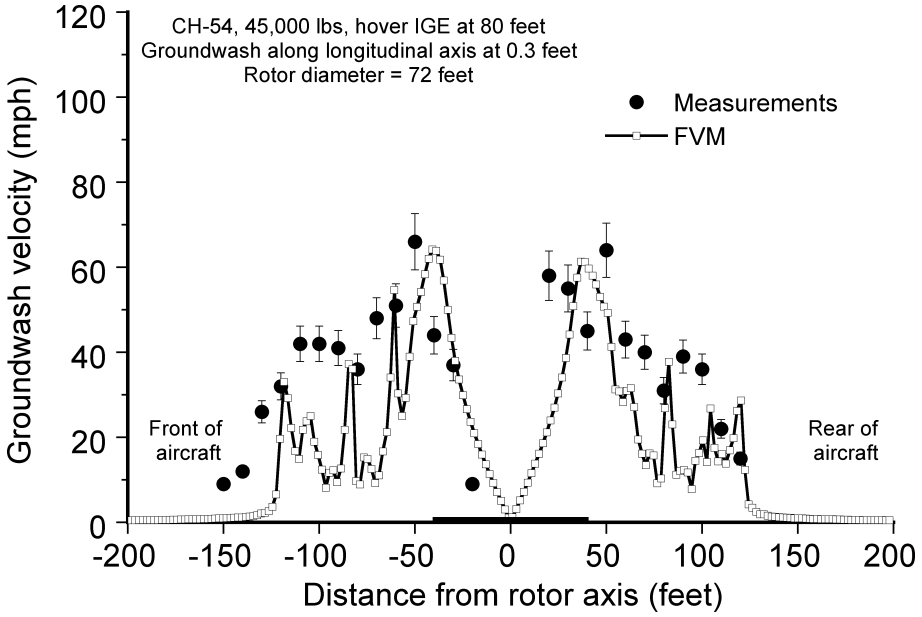

(a) Longitudinal axis

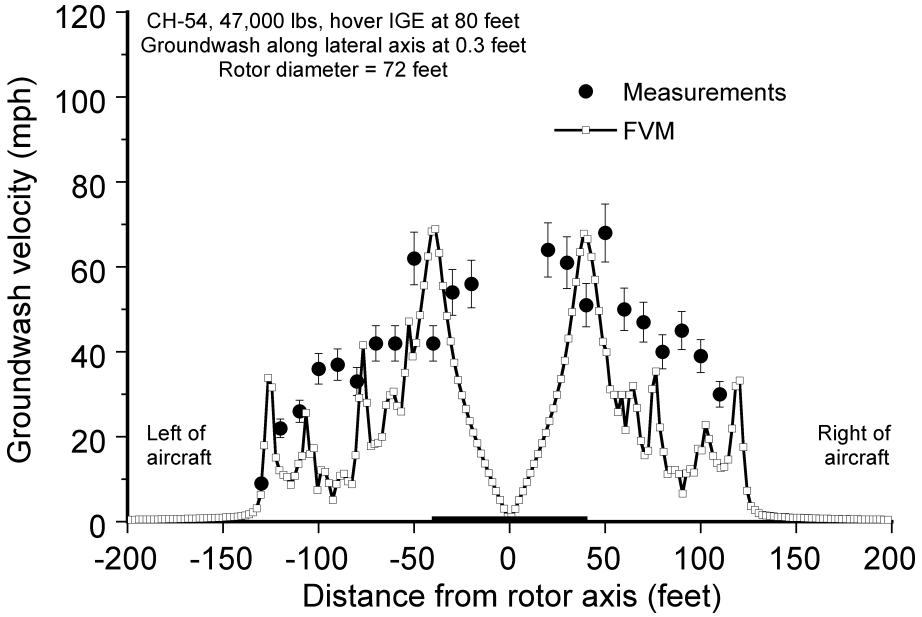

(b) Lateral axis

Figure 3.22: Variation of time-averaged groundwash velocity at 0.3 ft above the ground for a CH-54 helicopter hovering at 40 ft: (a) longitudinal axis, and (b) lateral axis.

just outside of the diameter of the rotor disk, and then decrease quickly as the rotor wake expands radially over the ground away from the helicopter. The time-averaged spatial velocity fluctuations shown in all cases are caused by the local levels of aperiodicity in the flow, which is mainly a result of the bundling of the tip vortex filaments as the wake approaches the ground (discussed later).

3.2.2 Comparisons of the Predicted Brownout Dust Clouds

Unique measurements documenting the evolution of the dust clouds generated by a helicopter operating under brownout conditions have been obtained by Wong and Tanner (Ref. 42). The essential characteristics of the helicopter are given in Table D.3 of Appendix D. A photogrammetric technique was used to measure the shapes and external envelopes of the dynamically evolving dust clouds. These measurements were used in the present work to help establish the efficacy of the current model, and also to determine what additional modeling components may be required to improve the overall fidelity of the brownout simulations.

In the photogrammetric technique, the coordinates of unique features on the external envelope of the dust cloud (e.g., a billow) can be determined by triangulation methods from multiple synchronous images. Wong and Tanner (Ref. 42) used six high-resolution cameras to take photographs of the evolving brownout dust clouds. An example of the images taken using the six cameras at one instant in time is shown in Fig. 3.25.

Measurements of the outer envelope of the clouds (i.e., their size and overall shape) were obtained for two flight maneuvers near the ground: 1. A taxi-pass; 2. An approach

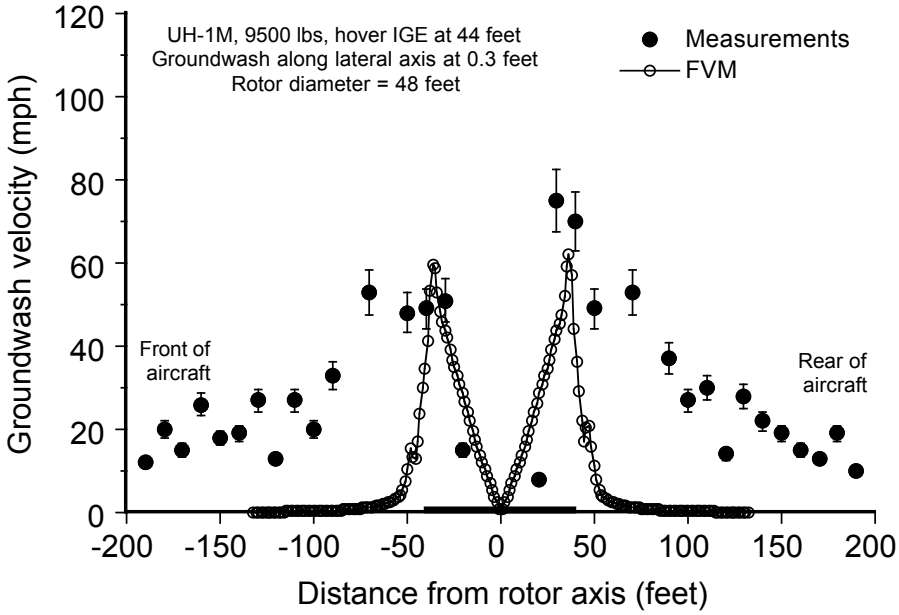

(a) Longitudinal axis

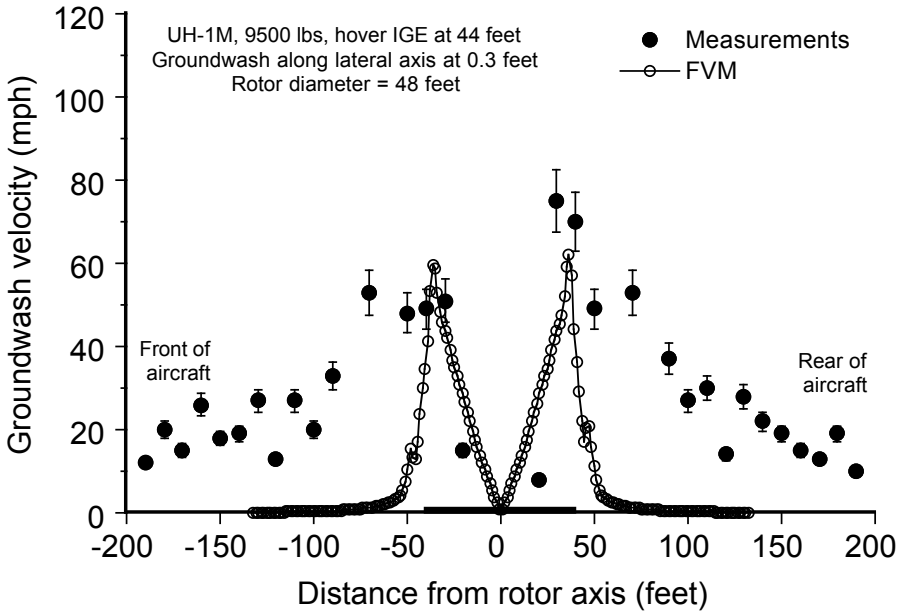

(b) Lateral axis

Figure 3.23: Variation of time-averaged groundwash velocity at 0.3 ft above the ground for a UH-1M helicopter hovering at 44 ft: (a) longitudinal axis, and (b) lateral axis.

to touchdown (but without an actual landing). Measurements for only one side (starboard side of the helicopter) of the dust cloud were available. The layout of the test range used for the brownout measurements is shown in Fig. 3.24, which was divided into seven lanes. The reference coordinate system was located at ground level in lane 7. Lanes 5 and 7 were used for the taxi-pass and approach-to-touchdown flight maneuvers, respectively.

The surface of the range was prepared by tilling before the tests (Ref. 42) to loosen the compacted top layer. A soil sample taken from the range was obtained from the US Army and analyzed by an independent laboratory to determine the mineralogy and particle size distribution. The particles were found to be mostly quartz, plagioclase, mica and various feldspars, with trace amounts of other minerals and some organic materials; see Fig. 3.26(a). The density of the particles subsequently used in the modeling was a weighted-average of the components in the measured sediment sample, i.e., $\rho_p = 2600$ kg m^{-3}. The particles size distribution is shown in Fig. 3.26(b), indicating that a large fraction of particles were in the medium (approximately 100 μm) to small (less than 10 μm) diameter range. Obviously, the larger particles are heavier and more difficult to mobilize, and are also not so easily suspended when (or if) they are mobilized.

All the dust cloud simulations shown here were obtained from a superposition of several separate calculations that used discrete particles of diameters between 1 and 100 μm. While it is recognized that superposition of such monodisperse simulations is not equivalent to what might be obtained by actually tracking all of the particles in a multidisperse cloud, this type of analysis can help to better understand the effects of particle size on the overall development of such dust clouds, i.e., where certain sized particles were mobilized and where they are ultimately convected to, even though in practice some

fraction of these particles may also interact or collide.

The initial sediment bed in each case was comprised of 8.0×10^5 particle clusters arranged in 20 layers. The number of particles used in the simulations was limited by computational time and memory requirements. Therefore, the clouds were advanced at each time step using Gaussian clustering (see Appendix C), which also brings out finer details of the cloud structures. For the present study, each simulation was comprised of over one million cluster centers, each associated with 100 particles. New particles were introduced into the simulations as a consequence of bombardment ejections, as and when they occurred, a typical simulation comprising over 10^{10} particles.

The challenges in making such calculations and comparisons with dust clouds were compounded because of the unavailability of certain parameters that are needed to fully conduct such studies. For example, the exact weight of the helicopter, the actual ambient wind conditions, the flight-path followed by the helicopter leading up to the measurements, and the blade control angles (trim state), were not available from Ref. 42. Therefore, in the present work several sets of results were computed to cover the expected range of variations in these parameters. Standard techniques were used to estimate trim based on force and moment equilibrium along the prescribed flight paths, as described in Section 2.1.6.

3.2.2.1 Taxi-Pass Maneuver

The taxi-pass maneuver was performed with the helicopter at a nominal forward airspeed of 20 kts and at an reference altitude of 30 ft. The positions of the helicopter

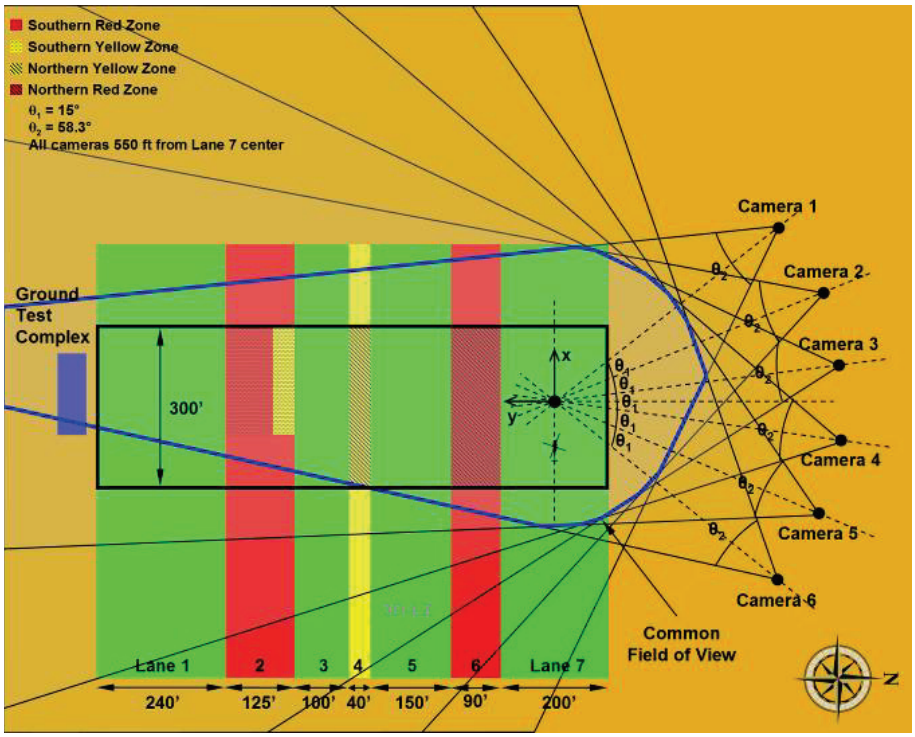

Figure 3.24: Schematic of the landing zone used for the brownout flight test experiments. (Source: Ref. 42)

Camera 1, time t = 0s

Camera 2, time t = 0s

Camera 3, time t = 0s

Camera 4, time t = 0s

Camera 5, time t = 0s

Camera 6, time t = 0s

Figure 3.25: Images of the dust cloud taken using six synchronous cameras during the approach-to-touchdown maneuver at $t = 0$ s. (Source: Ref. 43)

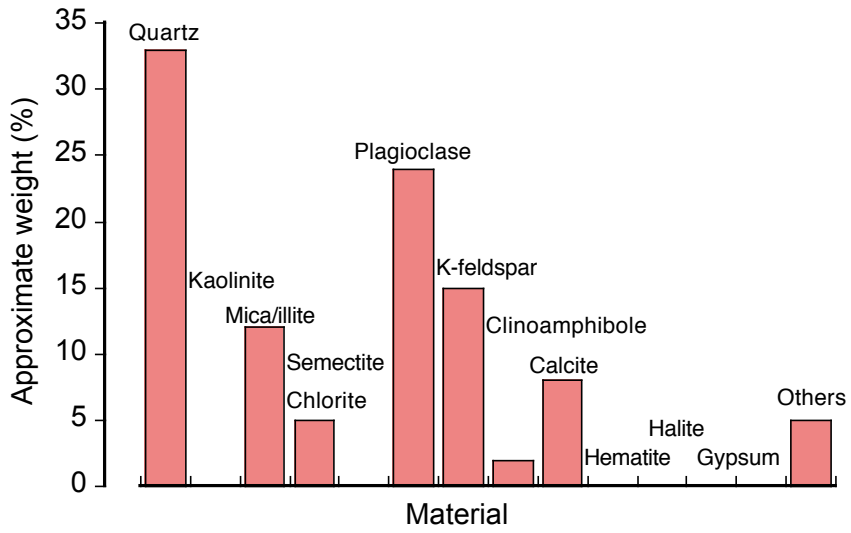

(a) Minerology study of the sample

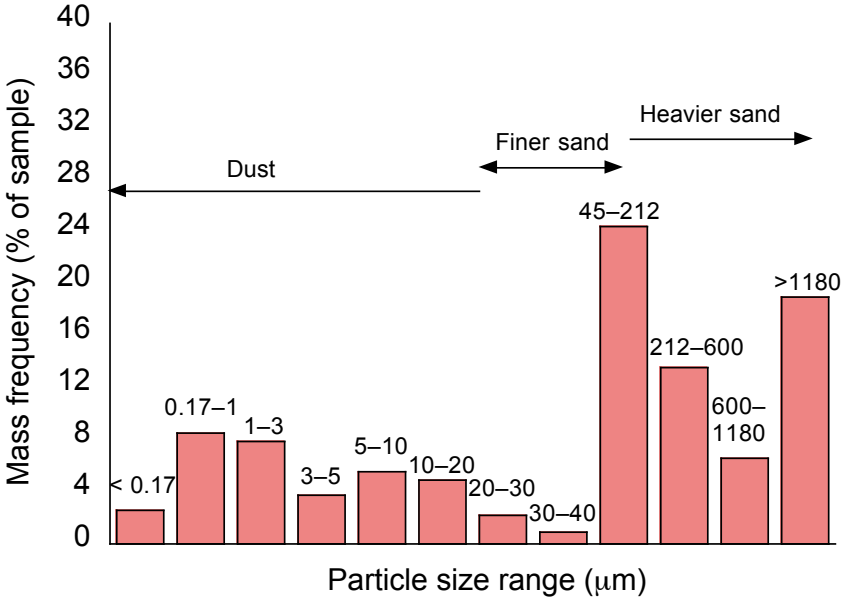

(b) Particle size distribution of the sample

Figure 3.26: Minerology study and particle size distribution of a sample from the range used for the brownout experiments.

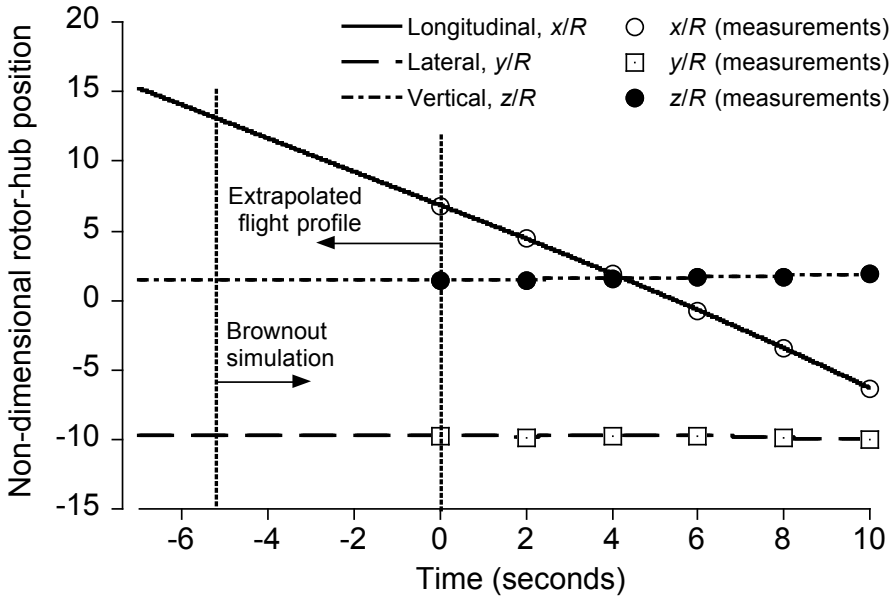

Figure 3.27: Positions of the helicopter at different times during the taxi-pass maneuver. (Positions are defined relative to the rotor hub and are non-dimensionalized by rotor radius.)

(referenced to the center of the rotor hub) are shown in Fig. 3.27, which were also measured using photogrammetry. The measurements (indicated by the markers in Fig. 3.27) showed deviations of the initially prescribed flight-path along all of the longitudinal, lateral and vertical dimensions, i.e., the helicopter actually accelerated from a true airspeed of about 19 kts to 23 kts in 6 s and also climbed from about 35 ft to 55 ft above the ground during the measurement period. These deviations were all modeled in the present simulations.

Measurements of the positions of the helicopter and of the evolving dust clouds were taken for a duration of 10 s. However, the measurements of the flight-path followed by the helicopter before it reached $t = 0$ is also important because both the aerodynamic solution and the dust cloud developments depend on the prior time-history, i.e., the problem cannot be assumed to be quasi-static. Therefore, the flight-path at earlier times was

extrapolated by using the measured velocities from $t = 0$ to 2 s, which is shown by the solid lines in Fig. 3.27. Notice that the aerodynamic solution for this maneuver was obtained by starting from $t = -7$ s, and the brownout solution was started at $t = -5.5$ s. Therefore, a full 15.5 s of the evolving dust cloud was simulated, with measurements being available for the last 10 s of the maneuver.

Instantaneous realizations of the top and side views of the rotor wake geometries during this maneuver are shown in Figs. 3.28 and 3.29. Notice that although the taxi-pass at a constant forward speed may be expected to produce similar wake geometries at different times, the small deviations of the flight path along the three dimensions and the presence of a ground plane generated significantly different wake geometries. The process of vortex bundling can also be seen in Figs. 3.28 and 3.29, which can affect the formation of the dust clouds.

The dust cloud simulations in the taxi-pass case were conducted by using a particle bed covering the area $x/R = -10$ to 15 and $y/R = -18$ to -2. Although the tilled zone on the test range only covered $x/R = -5.6$ to 5.6, both the measurements and the calculations of the evolving cloud suggested that particles were being mobilized and entrained into the rotor flow before the helicopter actually reached this tilled zone.

Effects of Weight

The weight of the helicopter during the brownout measurements was not known precisely, but it was estimated to be between 14,500 lbs and 16,300 lbs based on the initial fuel load and the flight time incurred up to the tests. Because the resulting rotor wake strength and

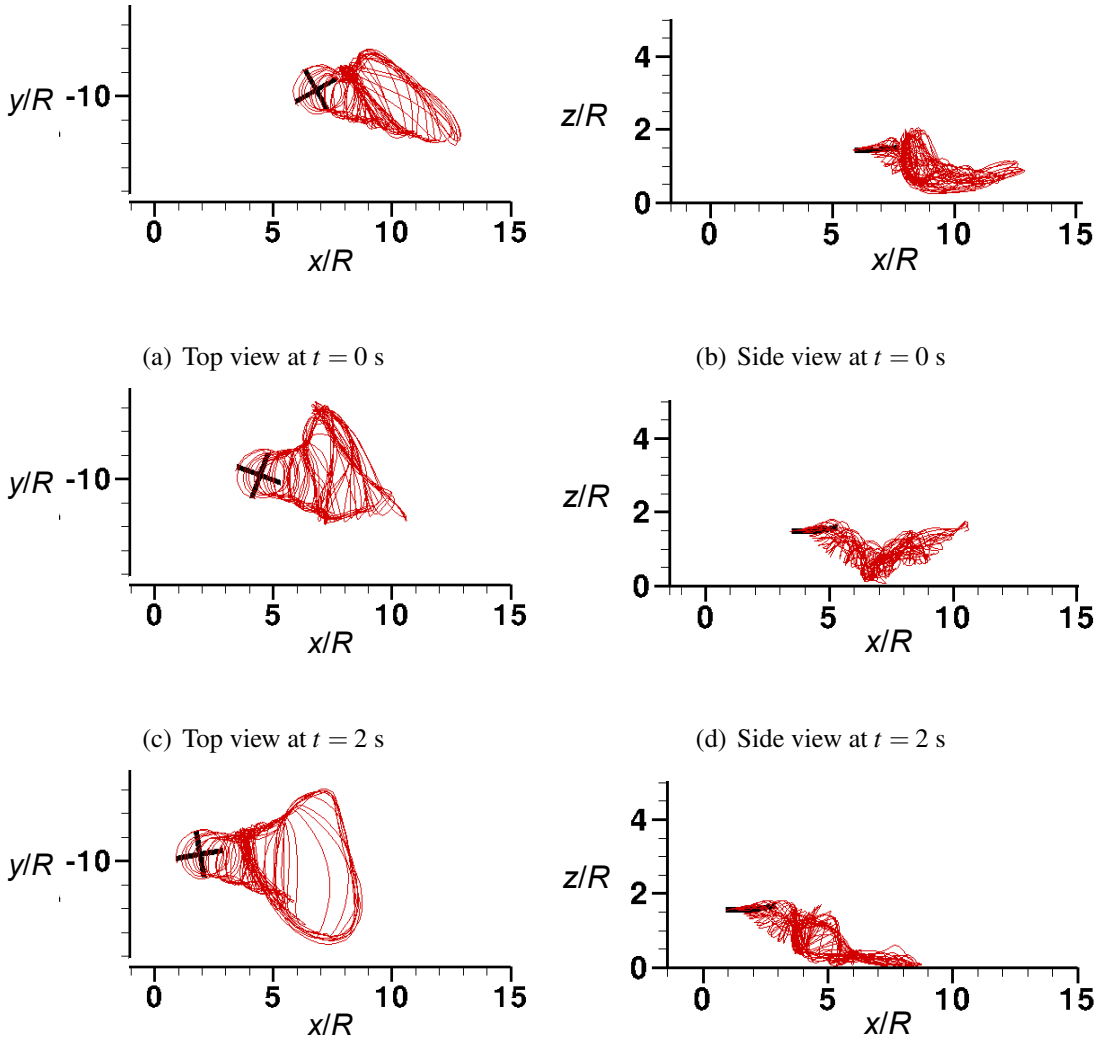

(a) Top view at $t = 0$ s

(b) Side view at $t = 0$ s

(c) Top view at $t = 2$ s

(d) Side view at $t = 2$ s

(e) Top view at $t = 4$ s

(f) Side view at $t = 4$ s

Figure 3.28: Top and side views of the wake geometries at $t = 0$, 2 and 4 s for the taxi-pass maneuver. (Note: these results were obtained from the simulation with $W = 14{,}500$ lbs.)

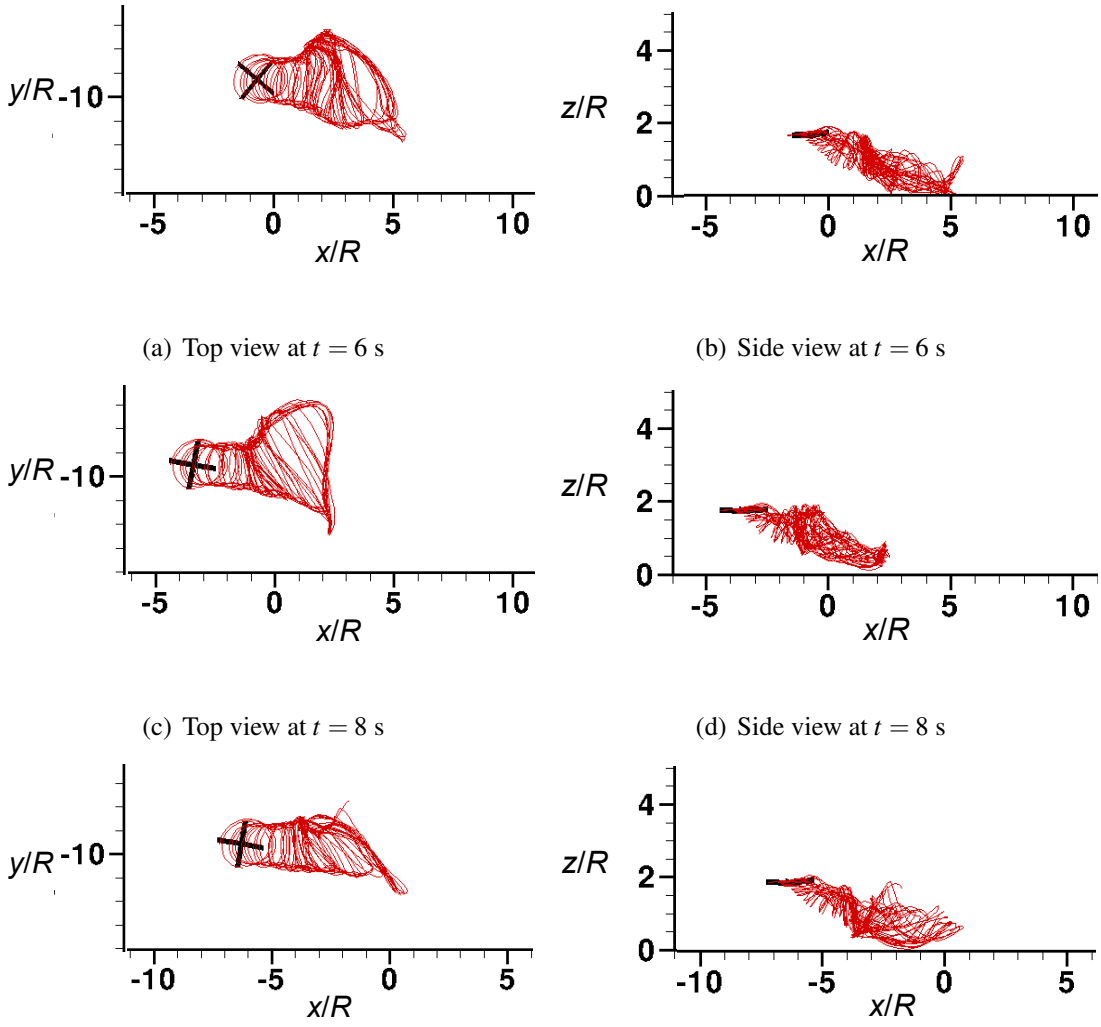

(a) Top view at $t = 6$ s

(b) Side view at $t = 6$ s

(c) Top view at $t = 8$ s

(d) Side view at $t = 8$ s

(e) Top view at $t = 10$ s

(f) Side view at $t = 10$ s

Figure 3.29: Top and side views of the wake geometries at $t = 6$, 8 and 10 s for the taxi-pass maneuver. (Note: these results were obtained from the simulation with $W = 14{,}500$ lbs.)

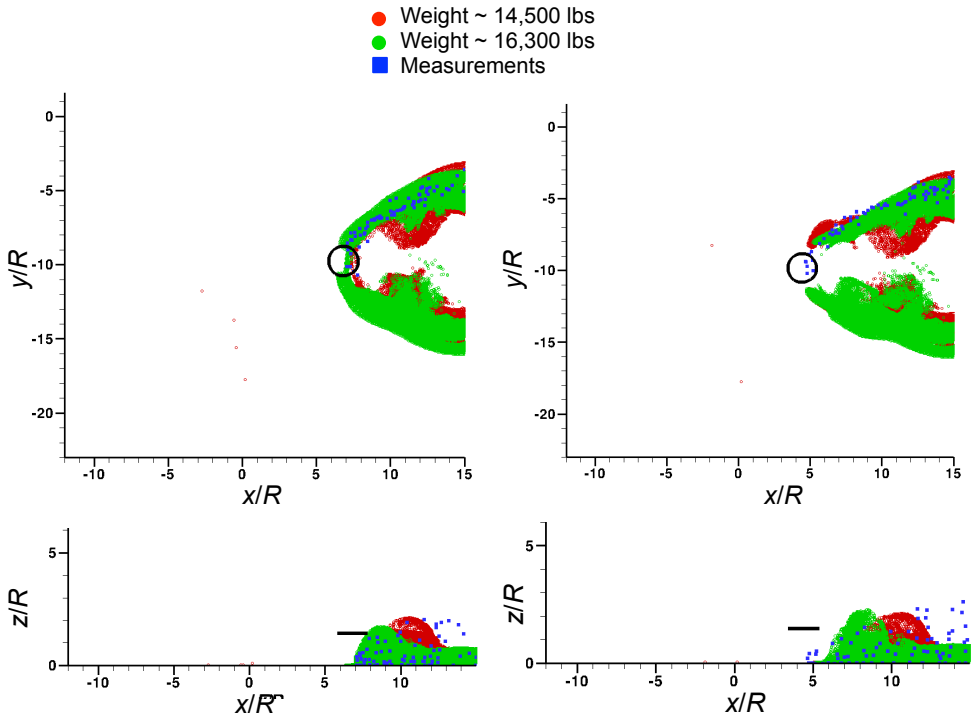

(a) Top and side views at $t = 0$ s

(b) Top and side views at $t = 2$ s

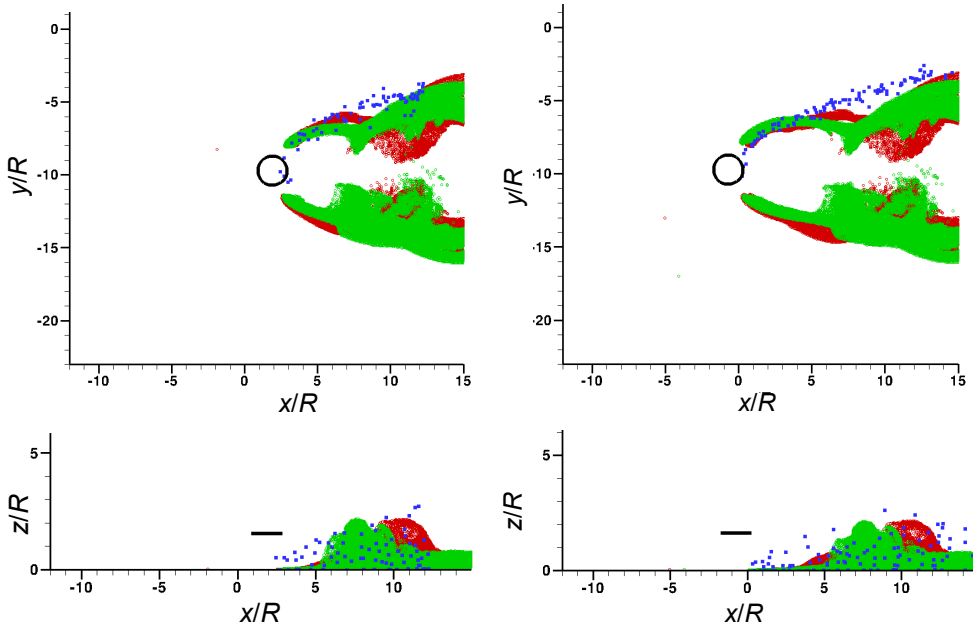

(c) Top and side views at $t = 4$ s

(d) Top and side views at $t = 6$ s

Figure 3.30: Comparison of the predicted dust clouds for weights of 14,500 lbs (shown in red) and 16,300 lbs (shown in green) with photogrammetric measurements (shown in blue) for the taxi-pass maneuver at $t = 0$, 2, 4, and 6 s.

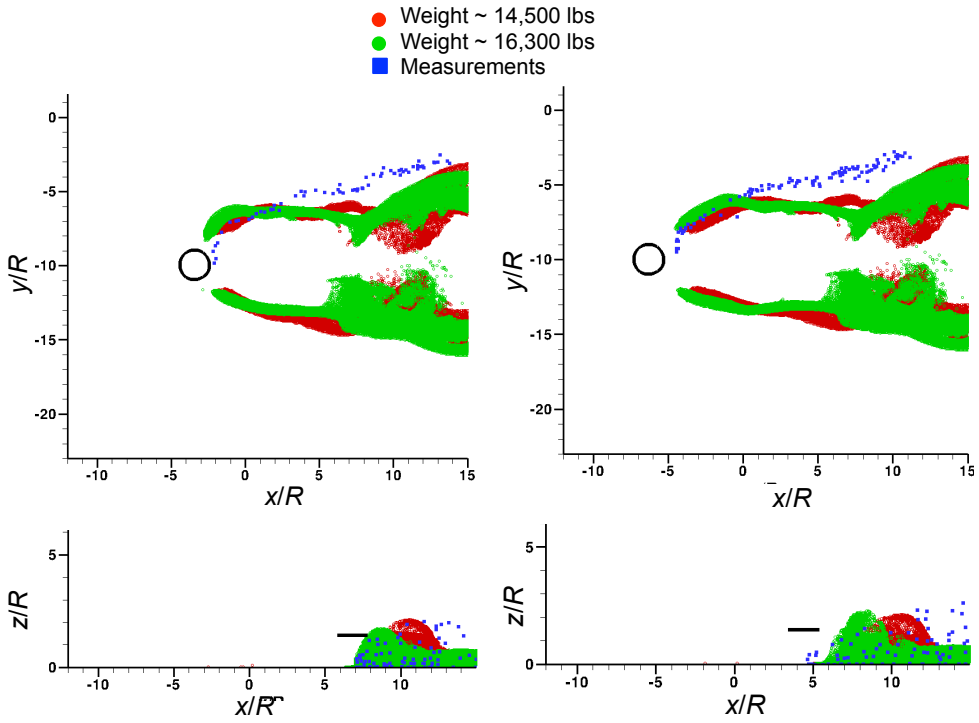

(a) Top and side views at $t = 8$ s

(b) Top and side views at $t = 10$ s

Figure 3.31: Comparison of the predicted dust clouds for weights of 14,500 lbs (shown in red) and 16,300 lbs (shown in green) with photogrammetric measurements (shown in blue) for the taxi-pass maneuver at $t = 8$ and 10 s.

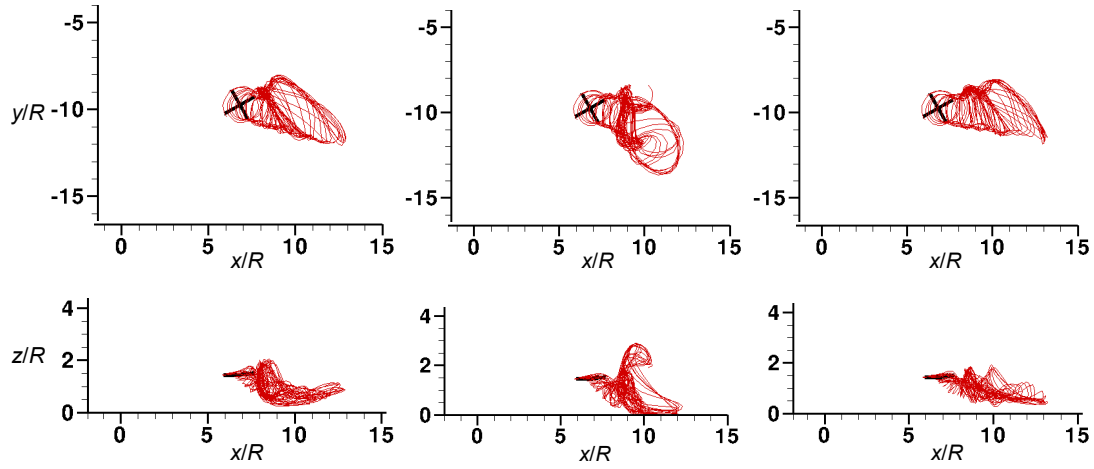

(a) Wake views for $W = 14{,}500$ lbs (b) $W = 16{,}300$ lbs (c) $W = 14{,}500$ lbs (crosswind)

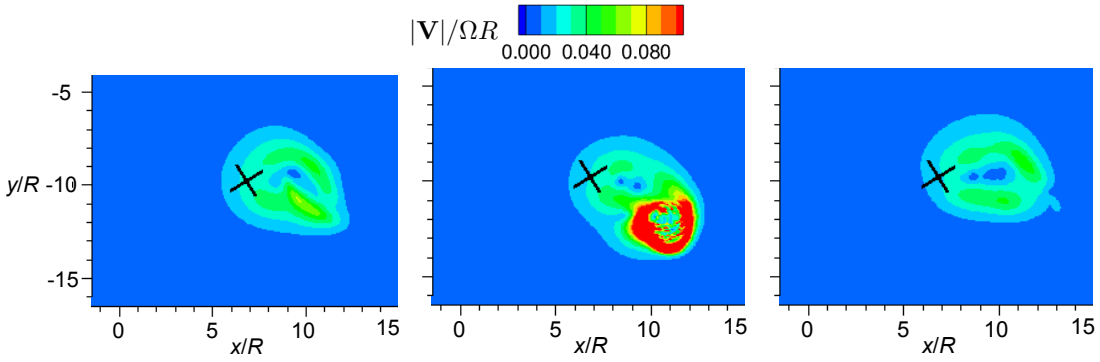

(d) At $z/R = 0.02$ for $W = 14,500$ lbs (e) $W = 16,300$ lbs (f) $W = 14,500$ lbs (crosswind)

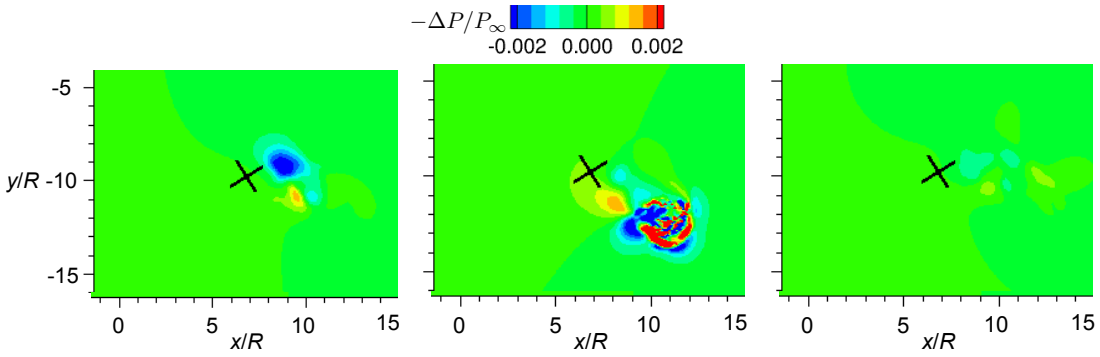

(g) At $z/R = 0.02$ for $W = 14,500$ lbs (h) $W = 16,300$ lbs (i) $W = 14,500$ lbs (crosswind)

Figure 3.32: Comparisons of the wake geometries, normalized induced velocities and unsteady pressure fields at t = 0 s for three taxi-pass cases: (a) W = 14,500 lbs (in calm winds), (b) W = 16,300 lbs (in calm winds), and (c) W = 14,500 lbs (with crosswind).

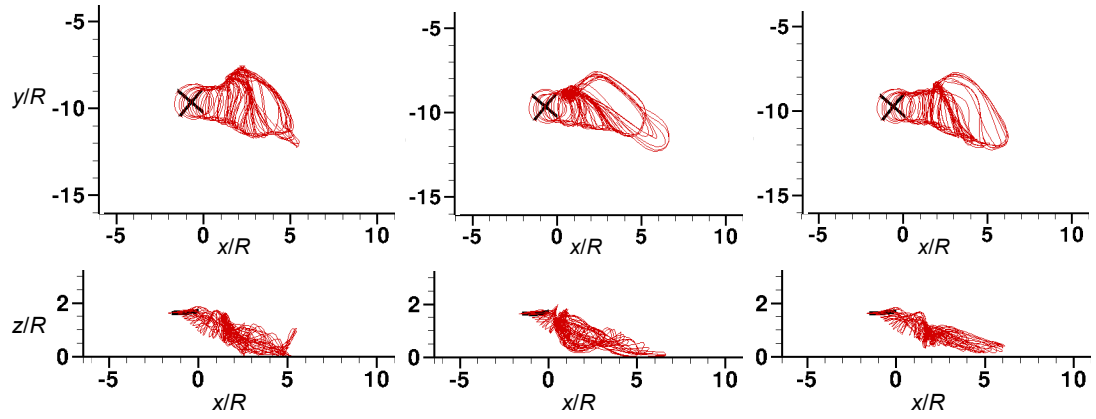

(a) Wake views for $W = 14{,}500$ lbs (b) $W = 16{,}300$ lbs (c) $W = 14{,}500$ lbs (crosswind)

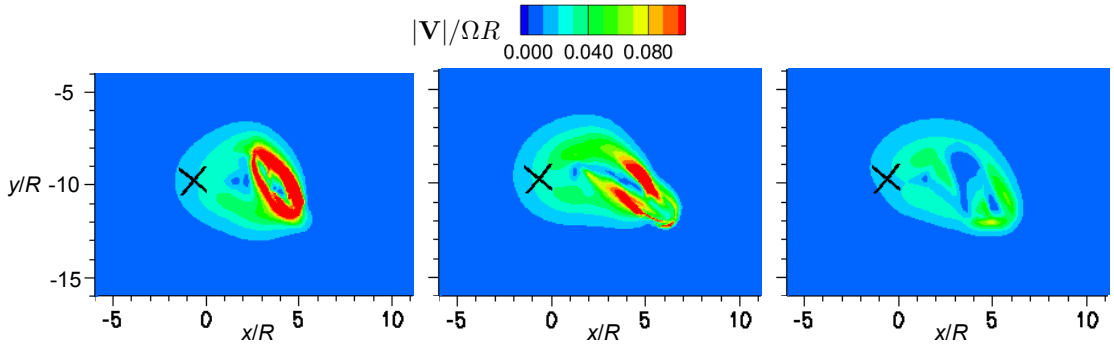

(d) At $z/R = 0.02$ for $W = 14{,}500$ lbs (e) $W = 16{,}300$ lbs (f) $W = 14{,}500$ lbs (crosswind)

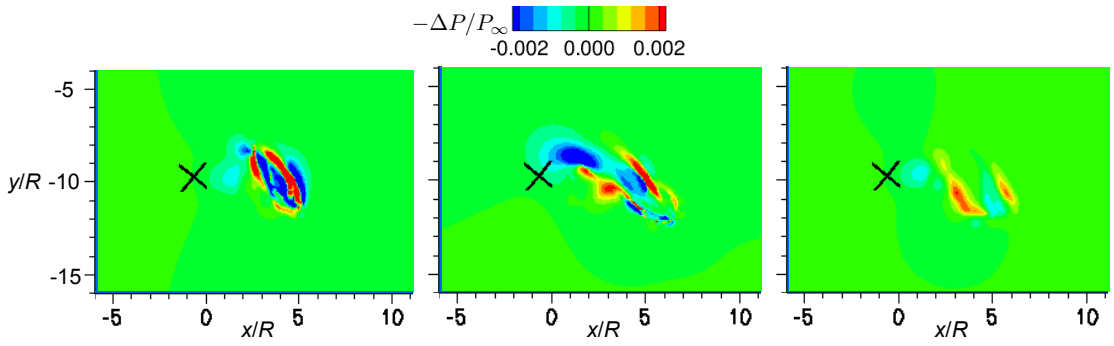

(g) At $z/R = 0.02$ for $W = 14{,}500$ lbs (h) $W = 16{,}300$ lbs (i) $W = 14{,}500$ lbs (crosswind)

Figure 3.33: Comparisons of the wake geometries, normalized induced velocities and unsteady pressure fields at t = 6 s for three taxi-pass cases: (a) W = 14,500 lbs (in calm winds), (b) W = 16,300 lbs (in calm winds), and (c) W = 14,500 lbs (with crosswind).

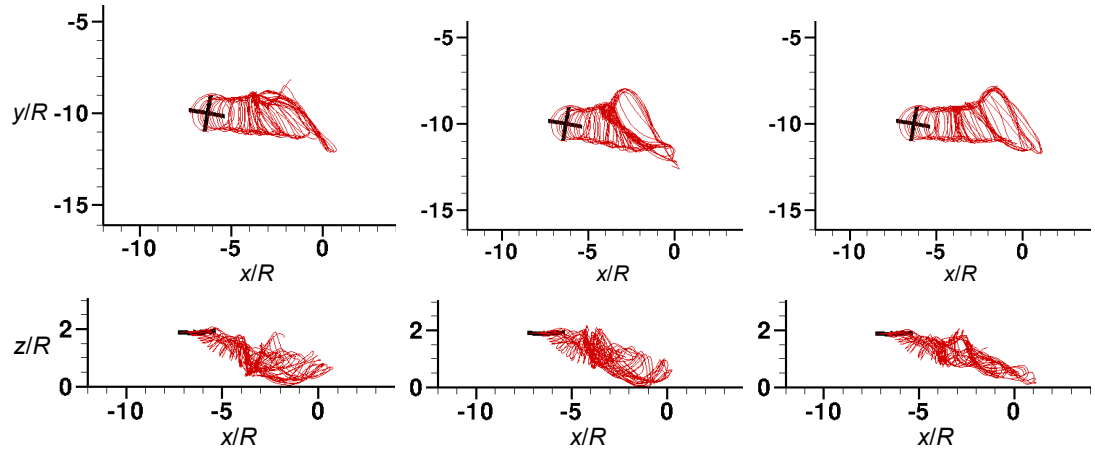

(a) Wake views for $W = 14{,}500$ lbs (b) $W = 16{,}300$ lbs (c) $W = 14{,}500$ lbs (crosswind)

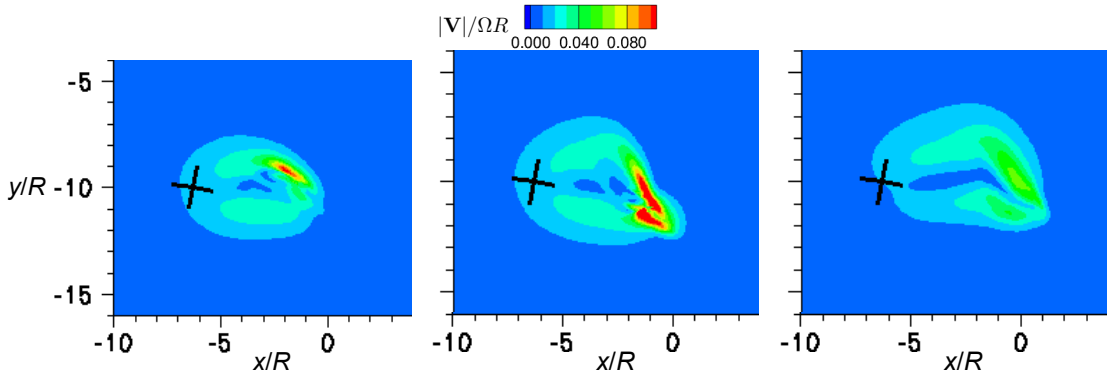

(d) At $z/R = 0.02$ for $W = 14,500$ lbs (e) $W = 16,300$ lbs (f) $W = 14,500$ lbs (crosswind)

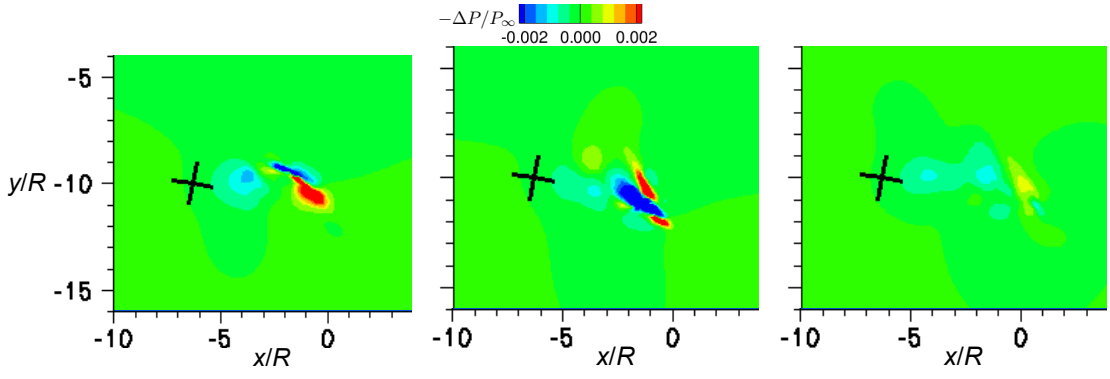

(g) At $z/R = 0.02$ for $W = 14,500$ lbs (h) $W = 16,300$ lbs (i) $W = 14,500$ lbs (crosswind)

Figure 3.34: Comparisons of the wake geometries, normalized induced velocities and unsteady pressure fields at t = 10 s for three taxi-pass cases: (a) W = 14,500 lbs (in calm winds), (b) W = 16,300 lbs (in calm winds), and (c) W = 14,500 lbs (with crosswind).

induced flow field near the ground can be sensitive to aircraft weight, separate calculations of the dust clouds were conducted to encompass a range of expected in-flight weights.

The simulated dust clouds at different times during the taxi-pass are shown in Figs. 3.30 and 3.31 for assumed weights of 14,500 lbs (in red) and 16,300 lbs (in green) versus the photogrammetric measurements (blue symbols). Notice that the vertical scale is magnified by 1.5 times for clarity.

The predictions of the dimensions and shapes of the evolving dust clouds along the longitudinal, lateral, and vertical dimensions all showed fairly good agreement with the measurements for both aircraft weights. It is apparent that at time t = 0 s, the dust cloud was formed closer to the rotor disk. As the helicopter moved further forward, the wake was convected downstream and the dust cloud continued to form behind the rotor. Comparing the results in Figs. 3.30 and 3.31, it is clear that the development of the dust clouds depends on the weight of the helicopter. Notice that the dust clouds generated at the heavier flight weight is formed closer to the rotor, which is at least partly because of the higher downwash velocities. These differences in the dust clouds at different times can be better understood by examining the flow field produced by the simulations at different vehicle weights.

A comparison of the solutions at times $t = 0$, 6 and 10 s are shown in Figs. 3.32, 3.33 and 3.34, respectively, for $W = 14{,}500$ lbs (in calm winds) and 16,300 lbs (in calm winds). These figures show top and side views of the rotor wake geometries, and contour maps of the total induced velocities, $|\mathbf{V}|$, and unsteady pressure difference, ΔP, on the sediment bed. The values of $|\mathbf{V}|$ are non-dimensionalized by the blade tip-speed, and the values of ΔP are non-dimensionalized by ambient pressure. Also, notice that the values

of ΔP in these figures are reversed, i.e., a positive ΔP would signify lift or suction on the particles and a negative ΔP signifies a downward force on the particles.

Differences in the rotor wake geometries are apparent at all times for W = 14,500 lbs and 16,300 lbs. Notice from the side views that the wake skew angle is lower for the simulation at the heavier flight weight. As a consequence, the wake impinges on the ground in regions closer to the front of the rotor disk, and also produces higher flow velocities in these regions. Ultimately, this behavior resulted in the formation of the dust cloud closer to the helicopter.

Bundling of vortex filaments was observed as the helicopter moved forward. The process of bundling is influenced by the rotor operating conditions and its time-history. Therefore, the vortex filaments will bundle in different regions below the rotor. The result of bundling is locally high regions of flow velocity, which in turn influence the mobilization and uplift of particles.

Effects of Ambient Winds

Generally, low winds were reported during the brownout testing in Ref. 42. The actual wind speed and direction were measured in intervals of 15 minutes; the average magnitude and direction was estimated to be 1.9 kts from 216° (see Fig. 3.24), which gives a direct crosswind component of 1.5 kts. Although still a small crosswind (less than 10% of the average airspeed of the helicopter), because of the low speed of the helicopter, it may still affect the development of the rotor wake and the resulting dust cloud. Therefore, a study was conducted to evaluate the sensitivities of the predicted dust clouds to winds, the results being shown in Figs. 3.35 and 3.36.

With the wind, a notable lateral skewness can be observed in the shapes of the dust clouds, confirming that the development of brownout clouds can be sensitive even to light winds. Also, notice that the average height of the dust clouds produced when including the crosswind is lower compared to that obtained in still air. Differences can also be seen in the details of the evolving cloud at the ground, i.e., the winds affect the locations where the sediment particles are actually being uplifted.

Notice from Figs. 3.32, 3.33 and 3.34 that the rotor wake skew angle is larger in the simulation when including crosswind effects. This effect prevents the wake from directly impinging on the ground and, therefore, the induced velocities and pressures on the bed are lower compared to those obtained under calm winds conditions. This outcome produces a lateral skewness in the dust cloud, as discussed previously, which can be seen in Figs. 3.35 and 3.36. The results obtained clearly show that even light winds can affect the formation of the rotor wake and, therefore, the formation of the subsequent dust clouds.

Quantity of Airborne Particles

A comparison of the quantity of suspended particles in the dust clouds is affected by the weight of the helicopter and the crosswind was conducted, the results being shown in Fig. 3.37. In each case, the quantity of suspended particles was normalized by the total quantity of suspended particles at the end of the calm wind simulation of a vehicle weight of 14,500 lbs. It is particularly significant to note from Fig. 3.37 that the average quantity of uplifted particles at the heavier flight weight is much larger (about three times) than at the lighter weight. This outcome occurs because the average downwash velocities in the rotor wake are higher at the heavier weight and the tip vortices are also stronger, which

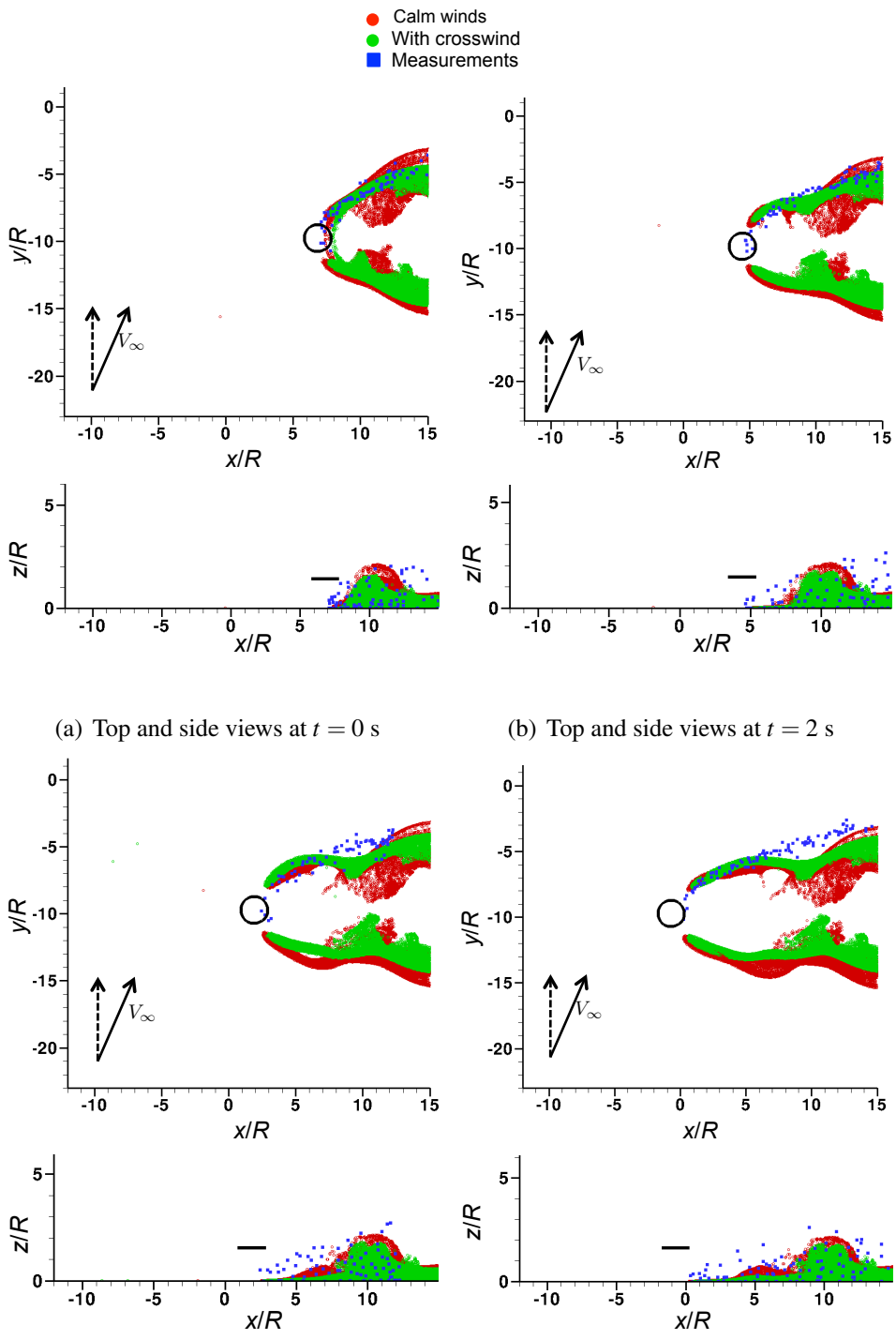

(a) Top and side views at $t = 0$ s

(b) Top and side views at $t = 2$ s

(c) Top and side views at $t = 4$ s

(d) Top and side views at $t = 6$ s

Figure 3.35: Comparison of the predicted dust clouds in calm winds (shown in red) and with the crosswind (shown in green) with photogrammetric measurements (shown in blue) for the helicopter at a weight of 14,500 lbs during taxi-pass maneuver at $t = 0$, 2, 4, and 6 s.

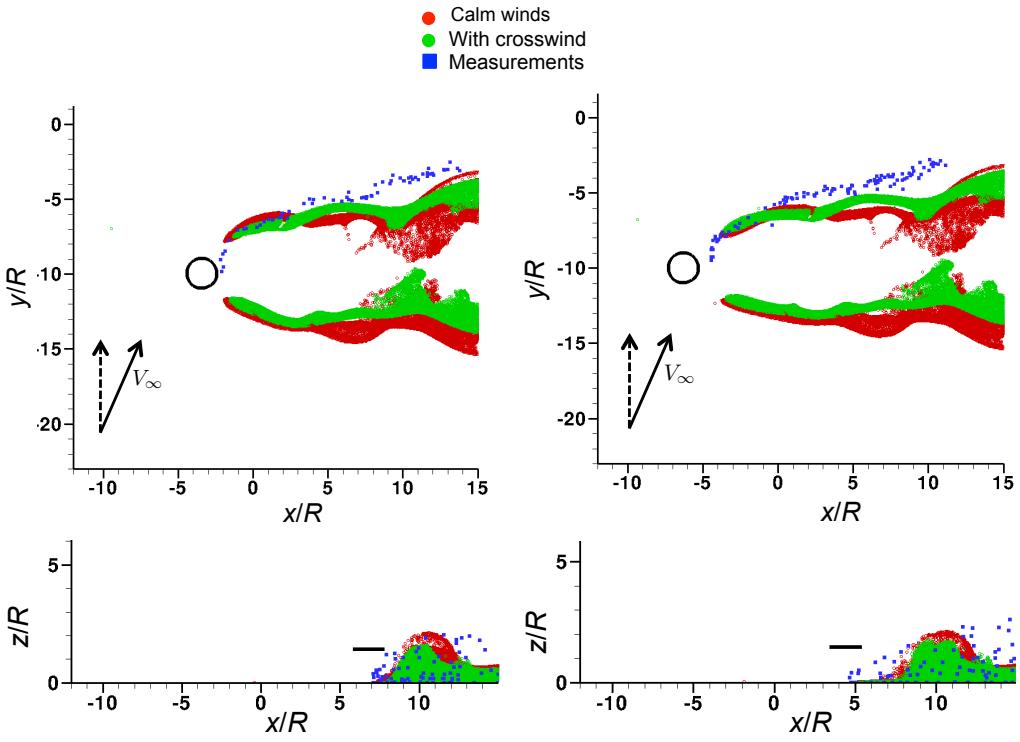

(a) Top and side views at $t = 8$ s

(b) Top and side views at $t = 10$ s

Figure 3.36: Comparison of the predicted dust clouds in calm winds (shown in red) and with the crosswind (shown in green) with photogrammetric measurements (shown in blue) for the helicopter at a weight of 14,500 lbs during taxi-pass maneuver at $t = 8$ and 10 s.

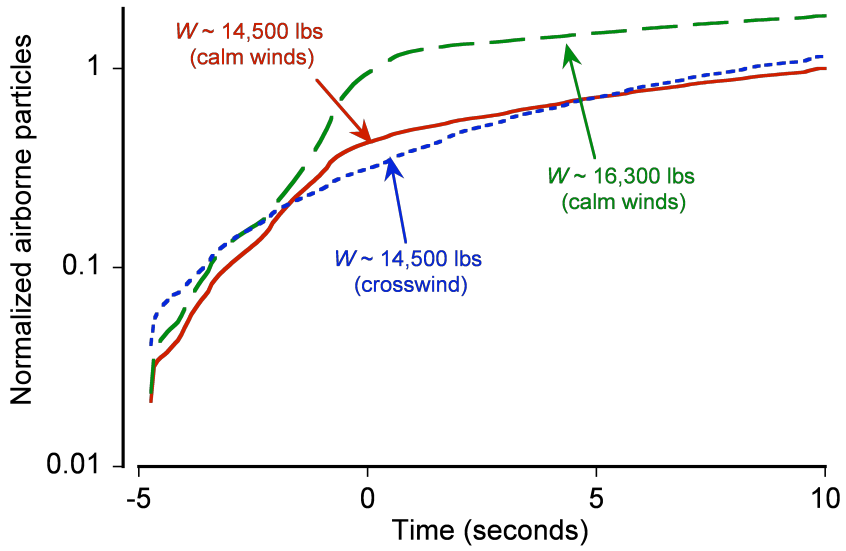

Figure 3.37: Comparison of the time-history of airborne particle count for the taxi-pass maneuver for three cases: (a) W = 14,500 lbs (in calm winds), (b) W = 16,300 lbs (in calm winds), and (c) W = 14,500 lbs (with crosswind).

also induces both higher flow velocities and larger unsteady pressures (see Figs. 3.32, 3.33 and 3.34) that together tend to mobilize and uplift more particles. However, the net quantity of particles entrained under the influence of the wind was still comparable to that found in calm wind conditions. Overall, the net quantity of uplifted particles was found to be more sensitive to changes in aircraft weight than to winds, at least over the smaller ranges examined here.

3.2.2.2 Approach to Touchdown Maneuver

In the approach-to-touchdown maneuver the helicopter approached the ground, the rotor plane reached a height of about 16 ft and then the helicopter climbed rapidly to fly out of the evolving dust cloud. Photogrammetric measurements were obtained over a

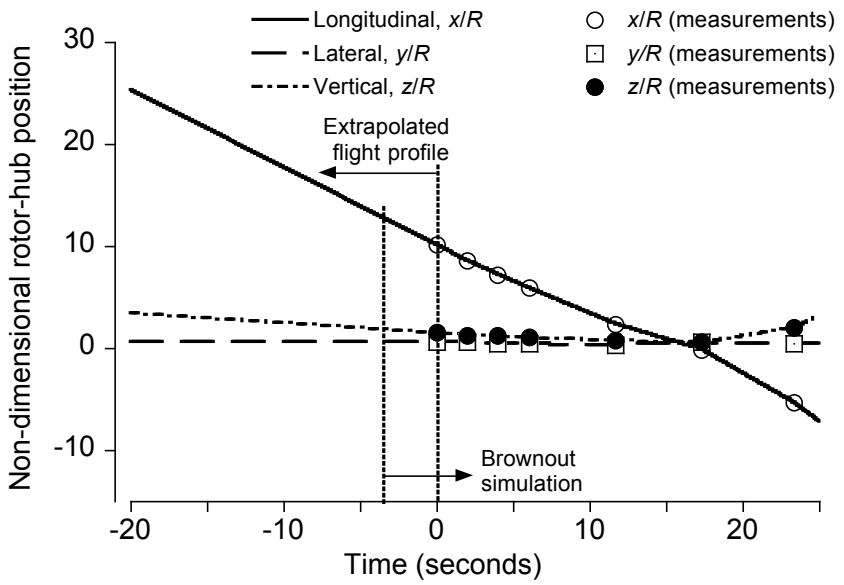

Figure 3.38: Positions of the helicopter during the approach-to-touchdown maneuver. (Positions are defined relative to the rotor hub and are non-dimensionalized by rotor radius.)

duration of about 25 s in this case, the positions of the helicopter being shown in Fig. 3.38 as the markers.

This approach-to-touchdown maneuver is a more complicated one to simulate because the height of the helicopter relative to the ground changed more significantly with time, i.e., the helicopter transitioned between approach-to-touchdown and then touchdown-to-takeoff flight conditions. A proper simulation of this maneuver requires the complete flight profile to be available, including that well upstream of $t = 0$, as indicated in Fig. 3.38. Therefore, because of the unavailability of the initial flight profile, it was extrapolated to earlier times by using the information available from $t = 0$ to 2 s; the solid lines show the flight-path actually used for predicting the dust clouds. Notice in this plot that the flow solution was computed for about 45 s (i.e., from $t = -20$ s to $t = 25$ s) and the dust clouds were simulated for about 28 s (i.e., from $t = -3$ s to $t = 25$ s), whereas the

photogrammetric measurements were available for only the last 25 s.

Instantaneous realizations of the side views of rotor wake geometry are shown in Figs. 3.39 and 3.40. At $t = 0$, i.e., when the first measurement of the flight profile was available, the rotor wake was already undergoing significant restructuring; see Fig. 3.39(a). As the helicopter decelerated further and approached the ground, the rotor wake impinged on the bed; see Figs. 3.39(c) and 3.39(d). The bundling of wake filaments can also be seen at these times. The rotor reached its lowest height above the ground at $t =$ 17 s, and the wake then expanded ahead of the rotor disk; see Fig. 3.40(b). The helicopter then took off and the wake again started to restructure, as shown in Figs. 3.40(c) and 3.40(d). The process of wake bundling can also be observed when the wake undergoes transition from approach to touchdown, and then to to the takeoff conditions. The changes in the wake geometries depend upon the rotor operating conditions, e.g., the weight of the helicopter, the wind conditions, and the initial flight profile (i.e., before $t = 0$ s). All of these effects can affect the formation of the brownout clouds, which will be examined further in the following section.

The brownout dust clouds were obtained by using a computational particle bed that spanned from $x/R = -12$ to 11, and $y/R = -10$ to 10. As for the taxi-pass maneuver, the clouds shown were simulated by using discrete particles with diameters between 1 μm and 100 μm. Again, notice that although tilled zone of the test range spanned from $x/R =$ -5.6 to 5.6, both the measurements and calculations of the dust cloud suggested that dust was entrained into the flow well before this prepared surface was reached.

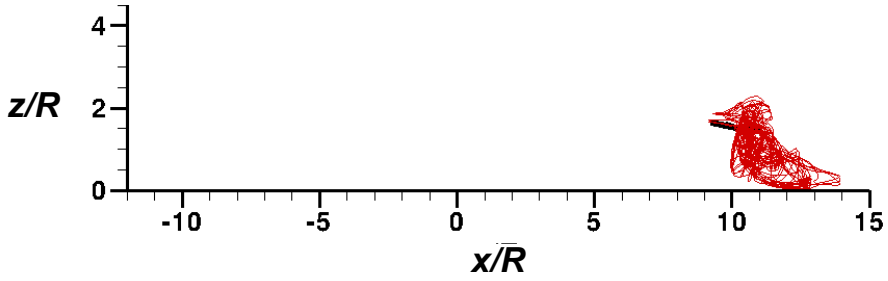

(a) Side view at $t = 0$ s

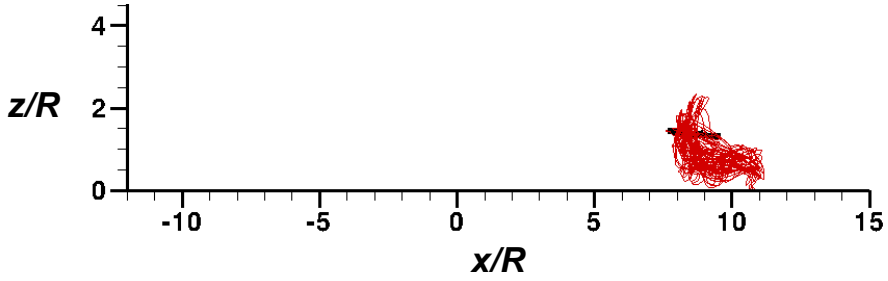

(b) Side view at $t = 2$ s

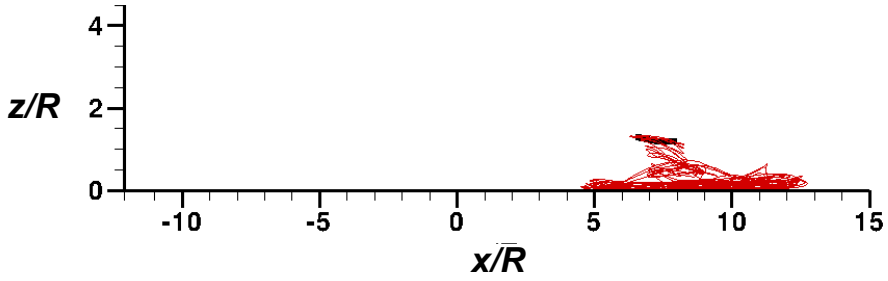

(c) Side view at $t = 4$ s

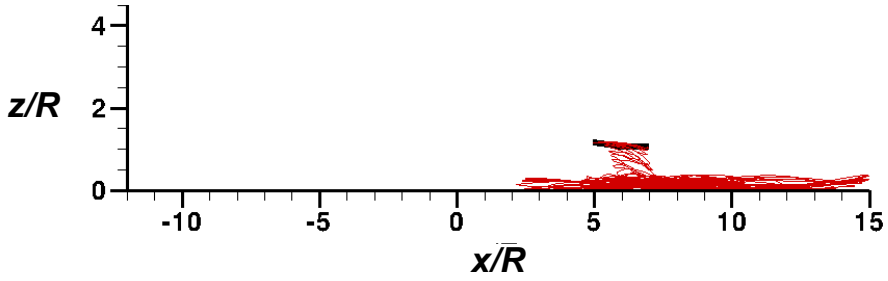

(d) Side view at $t = 6$ s

Figure 3.39: Side views of the wake geometries at $t = 0$, 2, 4 and 6 s for the approach-to-touchdown maneuver. (Note: these results were obtained for the helicopter at $W = 14{,}500$ lbs.)

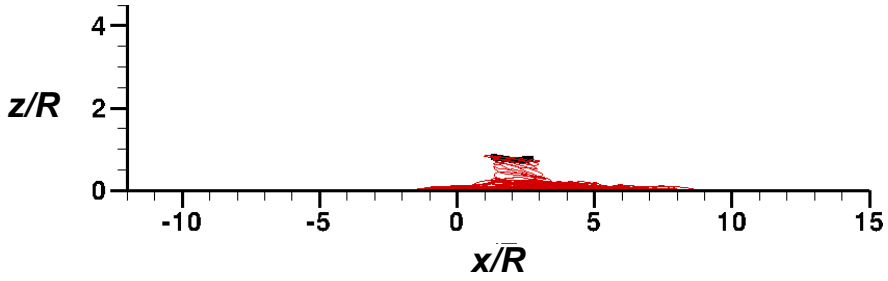

(a) Side view at $t = 13$ s

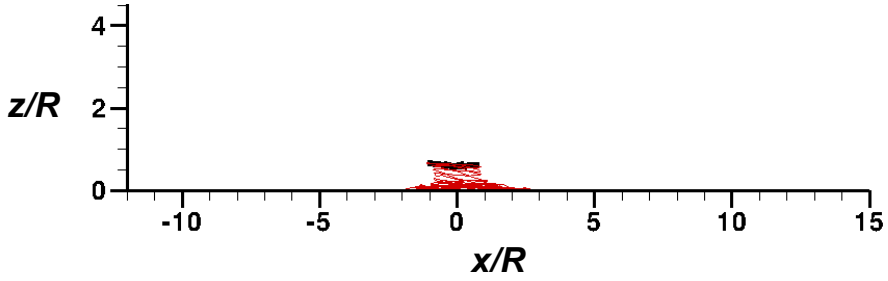

(b) Side view at $t = 17$ s

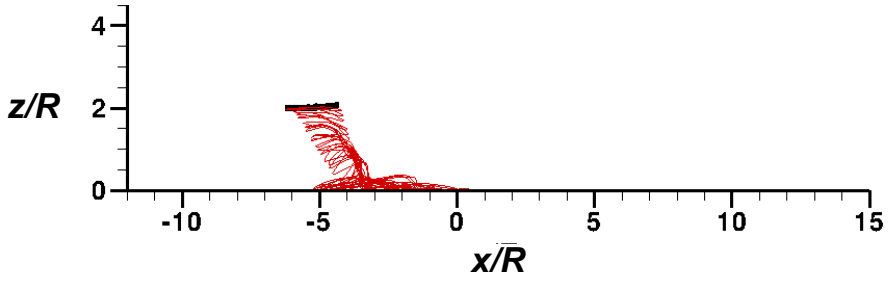

(c) Side view at $t = 23$ s

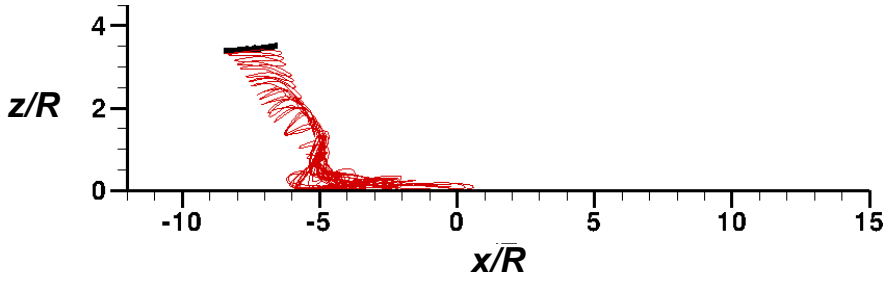

(d) Side view at $t = 25$ s

Figure 3.40: Side views of the wake geometries at $t = 11$, 17, 23 and 25 s for the approach-to-touchdown maneuver. (Note: these results were obtained for the helicopter at $W = 14{,}500$ lbs.)

Effects of Weight

Figures 3.41 and 3.42 show comparisons of the simulated dust clouds with the photogrammetric measurements (shown in blue) for different weights of the helicopter. The results are plotted for the two estimated weights of 14,500 lbs (in green) and 16,300 lbs (in red). The differences in the dust clouds for these cases were analyzed by examining the rotor wake geometries, the contour maps of the total induced velocity $|\mathbf{V}|$ on the sediment bed and along the longitudinal plane passing from $y/R = 0$, and contour maps of the unsteady pressure difference ΔP on the bed. These results are shown at times $t = 0$, 6, 17 and 23 s in Figs. 3.43, 3.44, 3.45 and 3.46, respectively.

As for the taxi-pass maneuver, the results obtained were found to be sensitive to the weight of the helicopter. It can be seen from Figs. 3.41 and 3.42 that the predictions of the cloud of the heavier flight weight are in reasonable agreement with the measurements in the longitudinal and lateral dimensions. However, the vertical development of the predicted clouds are clearly underestimated. Because dust was entrained into the flow field before the helicopter reached the prepared sediment bed, some of these differences may be attributable to the sedimentology of the different beds (i.e., loose versus more compacted), as well as the effects of mixed particle sizes and other characteristics (see later).

It is apparent from Fig. 3.43 that the wake geometries at $t = 0$ s from the simulations with $W = 14{,}500$ lbs and $W = 16{,}300$ lbs are significantly different, even at this early time. The wake of the lighter weight seems to be undergoing restructuring under the influence of the ground, and at the heavier weight the wake has already restructured and is about to impinge upon the bed. The process of vortex bundling also takes place at different

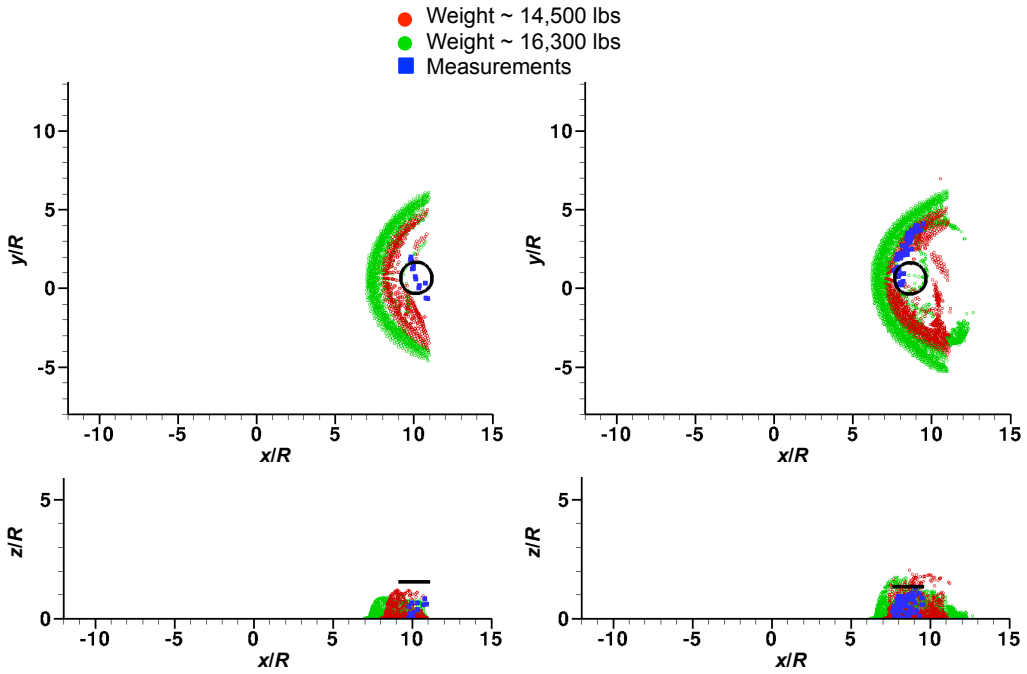

(a) Top and side views at $t = 0$ s

(b) Top and side views at $t = 2$ s

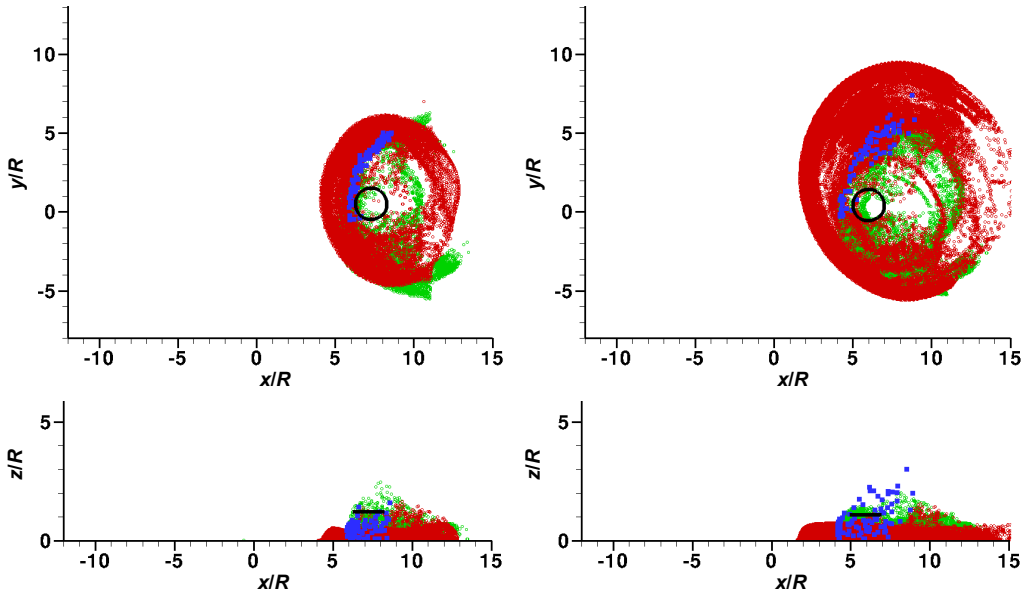

(c) Top and side views at $t = 4$ s

(d) Top and side views at $t = 6$ s

Figure 3.41: Comparison of the predicted dust clouds for the approach-to-touchdown maneuver for weights of 16,300 lbs (shown in red) and 14,500 lbs (shown in green) with photogrammetric measurements (shown in blue) at $t = 0$, 2, 4, and 6 s.

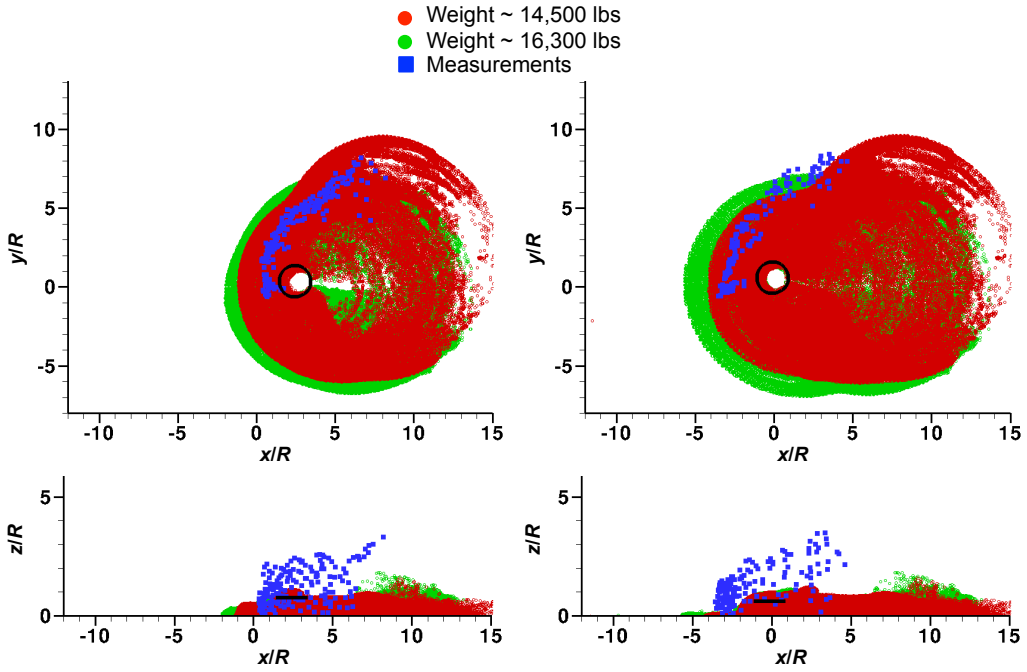

(a) Top and side views at $t = 11$ s

(b) Top and side views at $t = 17$ s

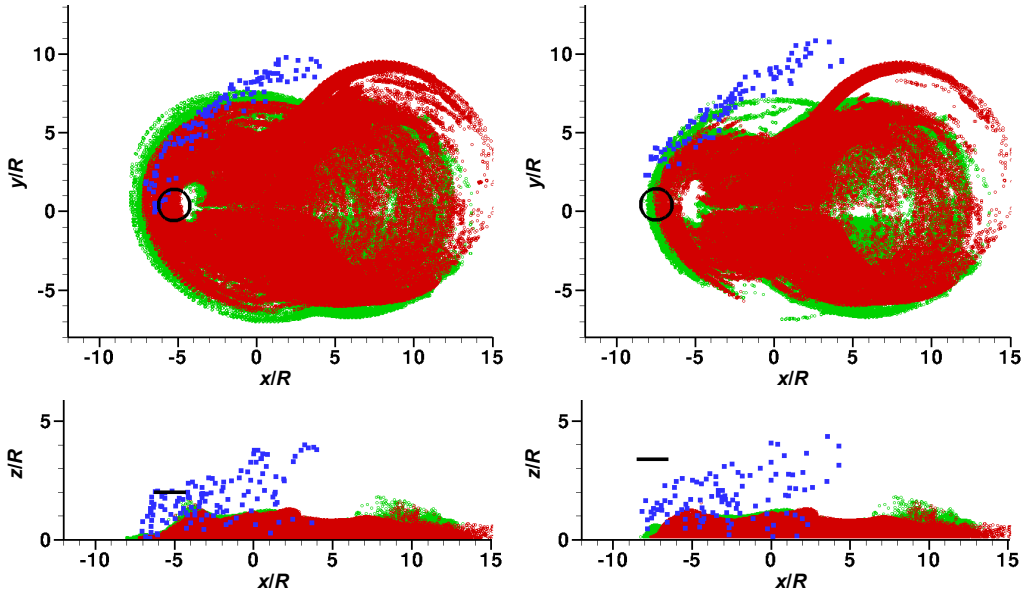

(c) Top and side views at $t = 23$ s

(d) Top and side views at $t = 25$ s

Figure 3.42: Comparison of the predicted dust clouds for the approach-to-touchdown maneuver for weights of 16,300 lbs (shown in red) and 14,500 lbs (shown in green) with photogrammetric measurements (shown in blue) at $t = 11$, 17, 23, and 25 s.

locations relative to the rotor, producing differences in the velocity and pressure fields in these regions. As a consequence, the dust clouds also showed differences even at earlier times in their development.

Notice that at $t = 0$ and 2 s, the frontal boundary of the dust cloud with the helicopter at the lighter weight was formed closer to the front of the rotor disk. Along the vertical dimension, at t = 2 s the dust cloud had convected vertically up above the plane of the rotor disk. The overall agreement of the dust cloud simulations with the measurements is reasonably good.

At t = 4 and 6 s, the wake had expanded ahead of the rotor disk; the wake at the lighter weight shows a more significant expansion than at the heavier weight. The velocity and pressure fields at the lighter weight also show this behavior; see Fig. 3.44 for a comparison at $t = 6$ s. As an outcome, the frontal boundary of the dust cloud at the lighter weight forms farther ahead of the rotor disk; see Fig. 3.41. The formation of ground vortices in the regions just ahead of the rotor disk can be observed at these times; see Fig. 3.44. The simulation for the helicopter at the heavier flight weight produces a stronger ground vortex. Overall, the dust cloud produced at the heavier weight showed better agreement with the measurements along all of the longitudinal, lateral and vertical dimensions.

At $t = 11$ and 17 s, the helicopter undergoes a further deceleration and approaches its lowest height above the ground. The wakes for both weights have expanded ahead of the rotor disk at these times and start to show some similarities; see Fig. 3.45 for a comparison at $t = 17$ s. The induced velocity and pressure fields also show similar features, however, some differences can still be observed. The dust clouds also start to show

similar developments along the longitudinal and lateral dimensions; see Figs. 3.42. The radial distance between the front boundaries of these clouds also start to decrease; see also Fig. 3.42. The predicted dust clouds show reasonable correlation with the measurements along the longitudinal and lateral dimensions, however the correlation along the vertical direction is not so good, where the simulations underpredict the height of the cloud developments.

It must be pointed out here that some of the differences in the predicted dust clouds with respect to measurements can also be because of the inadequate measurements of the flight profile. For example, the flight profile measurements were made by Wong and Tanner (Ref. 42) during approach at $t = 6$, 11 and 17 s. The variations in the flight profile between $t = 6$ and 11 s, and between $t = 11$ and 17 s can result in different flow fields and, therefore, different dust clouds.

After reaching its lowest height at $t = 17$ s, the helicopter begins to take off. Wong and Tanner (Ref. 42) observed that the shape of the dust cloud after this time did not change as much, the dust being convected mainly laterally outward away from the rotor as the helicopter flew along the prescribed flight path. A similar behavior was observed in the simulations; see Fig. 3.42. Overall, the simulations showed good agreement with the measurements at these times along the longitudinal and lateral dimensions, however, the vertical development of the dust clouds was still underestimated.

Effects of Ambient Winds

A wind of about 2.3 kts from 210° (a crosswind component of 2 kts) was reported when the photogrammetric measurements were made during the approach-to-touchdown ma-

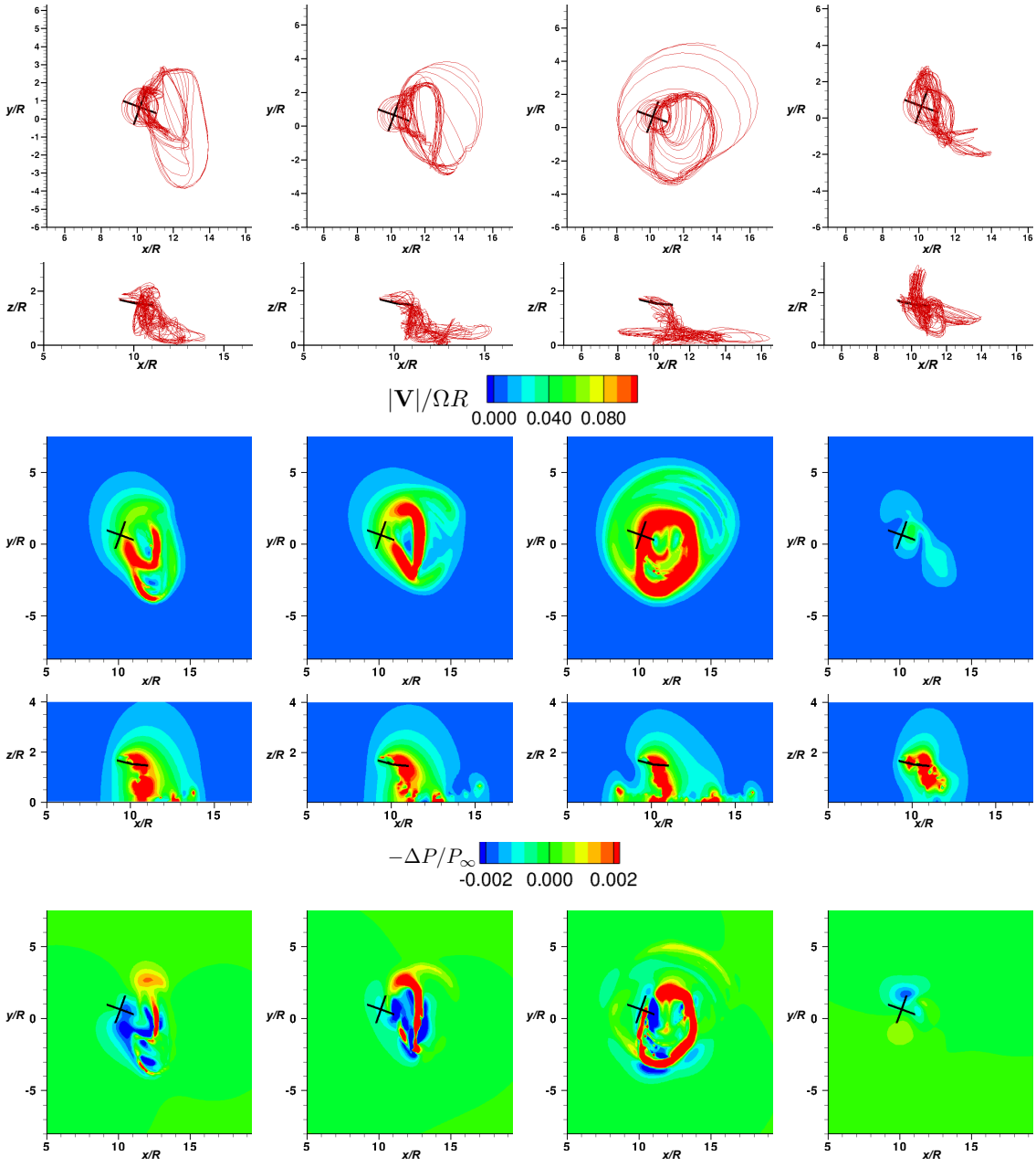

(a) W = 14,500 lbs (b) W = 14,500 lbs (crosswind) (c) W = 16,300 lbs (d) W = 14,500 lbs (initial condition 2)

Figure 3.43: Comparisons of wake geometries, normalized induced velocities and unsteady pressure fields at t = 0 s for the four approach-to-touchdown maneuver cases: (a) W = 14,500 lbs (in calm winds), (b) W = 14,500 lbs (with crosswind), (c) W = 16,300 lbs (in calm winds), and (d) W = 14,500 lbs (second initial condition).

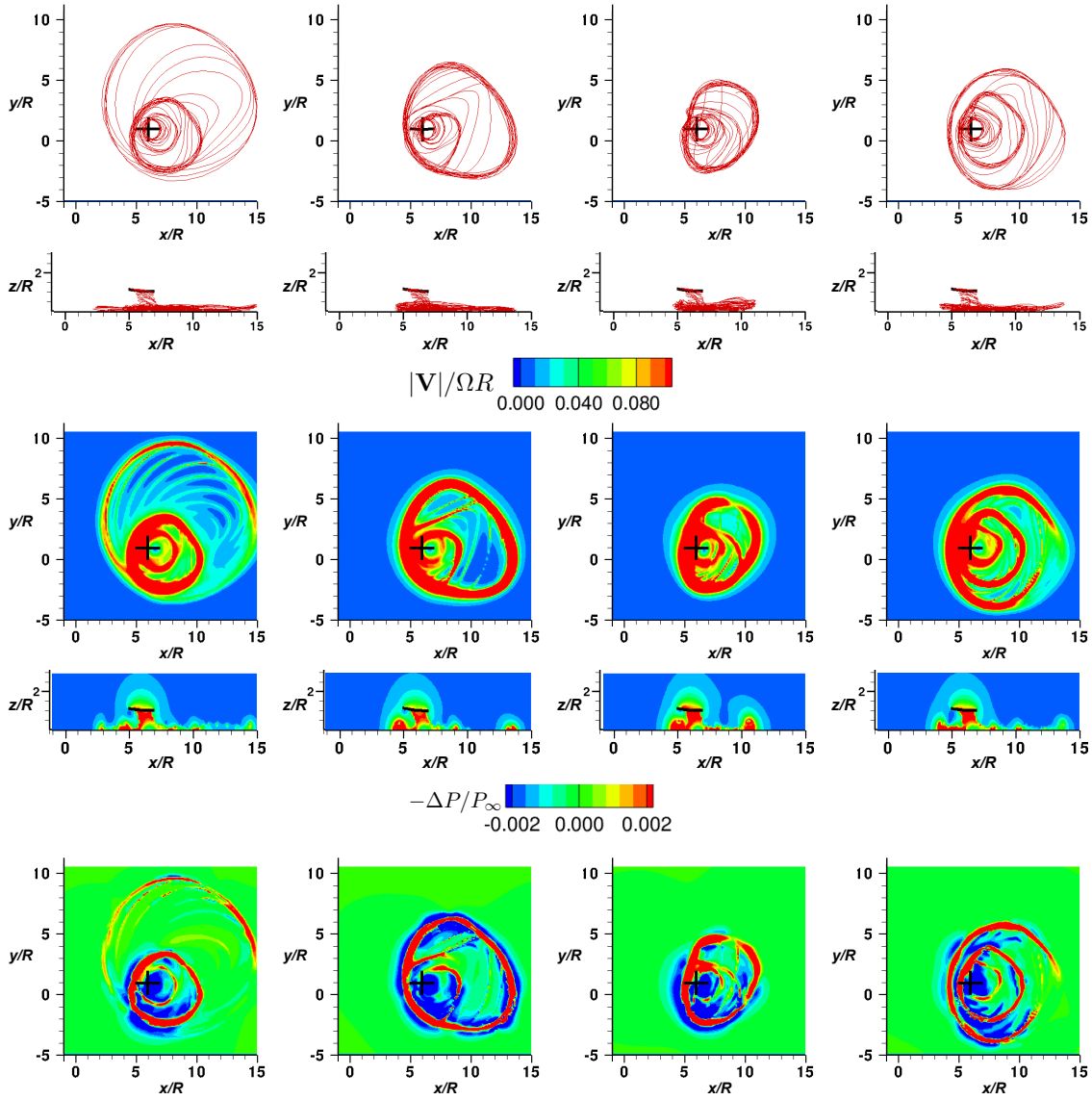

(a) $W = 14{,}500$ lbs (b) $W = 14{,}500$ lbs (crosswind) (c) $W = 16{,}300$ lbs (d) $W = 14{,}500$ lbs (initial condition 2)

Figure 3.44: Comparisons of wake geometries, normalized induced velocities and unsteady pressure fields at $t = 6$ s for the four approach-to-touchdown maneuver cases: (a) W = 14,500 lbs (in calm winds), (b) W = 14,500 lbs (with crosswind), (c) W = 16,300 lbs (in calm winds), and (d) W = 14,500 lbs (second initial condition).

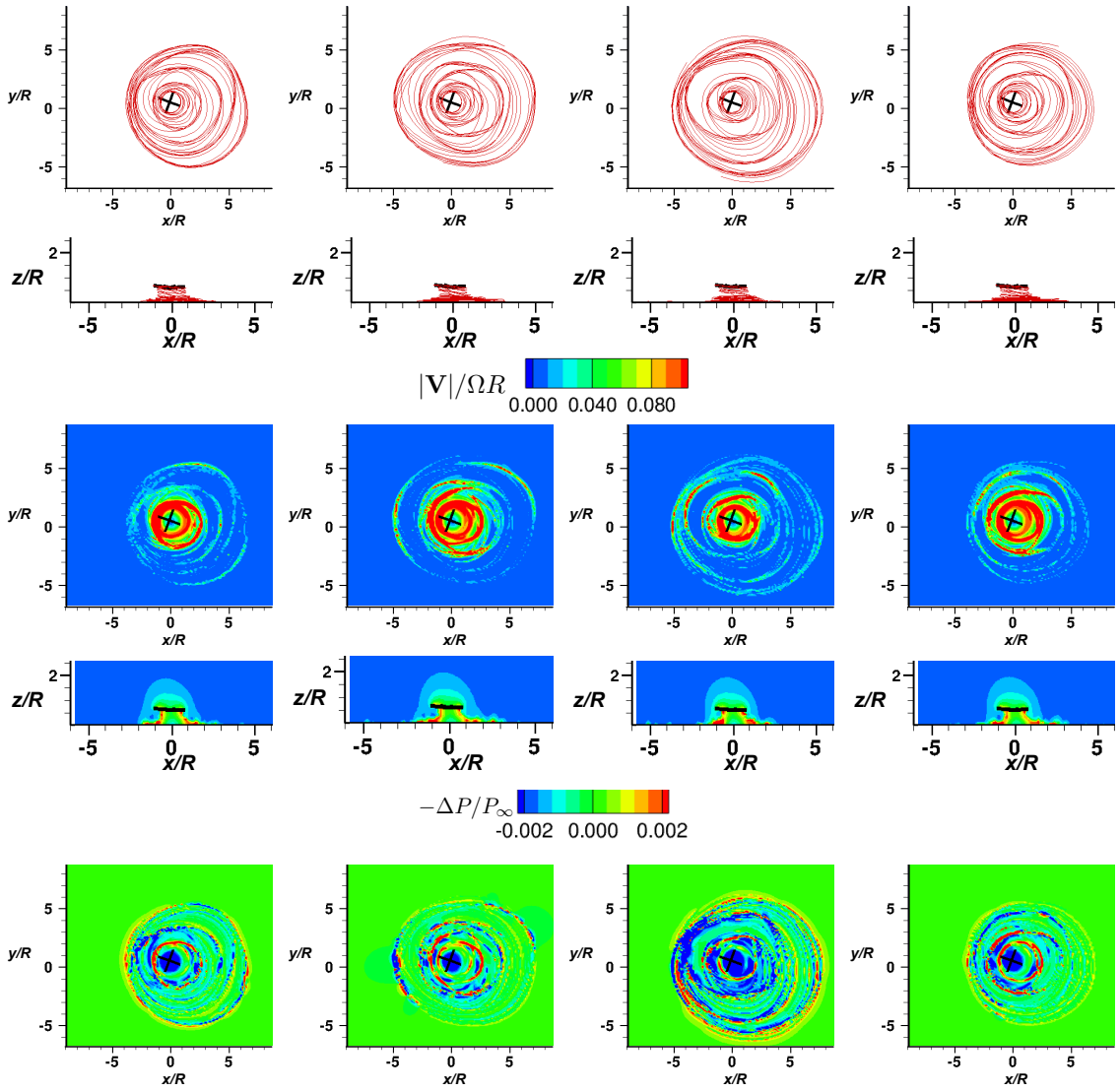

(a) $W = 14{,}500$ lbs (b) $W = 14{,}500$ lbs (crosswind) (c) $W = 16{,}300$ lbs (d) $W = 14{,}500$ lbs (initial condition 2)

Figure 3.45: Comparisons of wake geometries, normalized induced velocities and unsteady pressure fields at $t = 17$ s for the four approach-to-touchdown maneuver cases: (a) W = 14,500 lbs (in calm winds), (b) W = 14,500 lbs (with crosswind), (c) W = 16,300 lbs (in calm winds), and (d) W = 14,500 lbs (second initial condition).

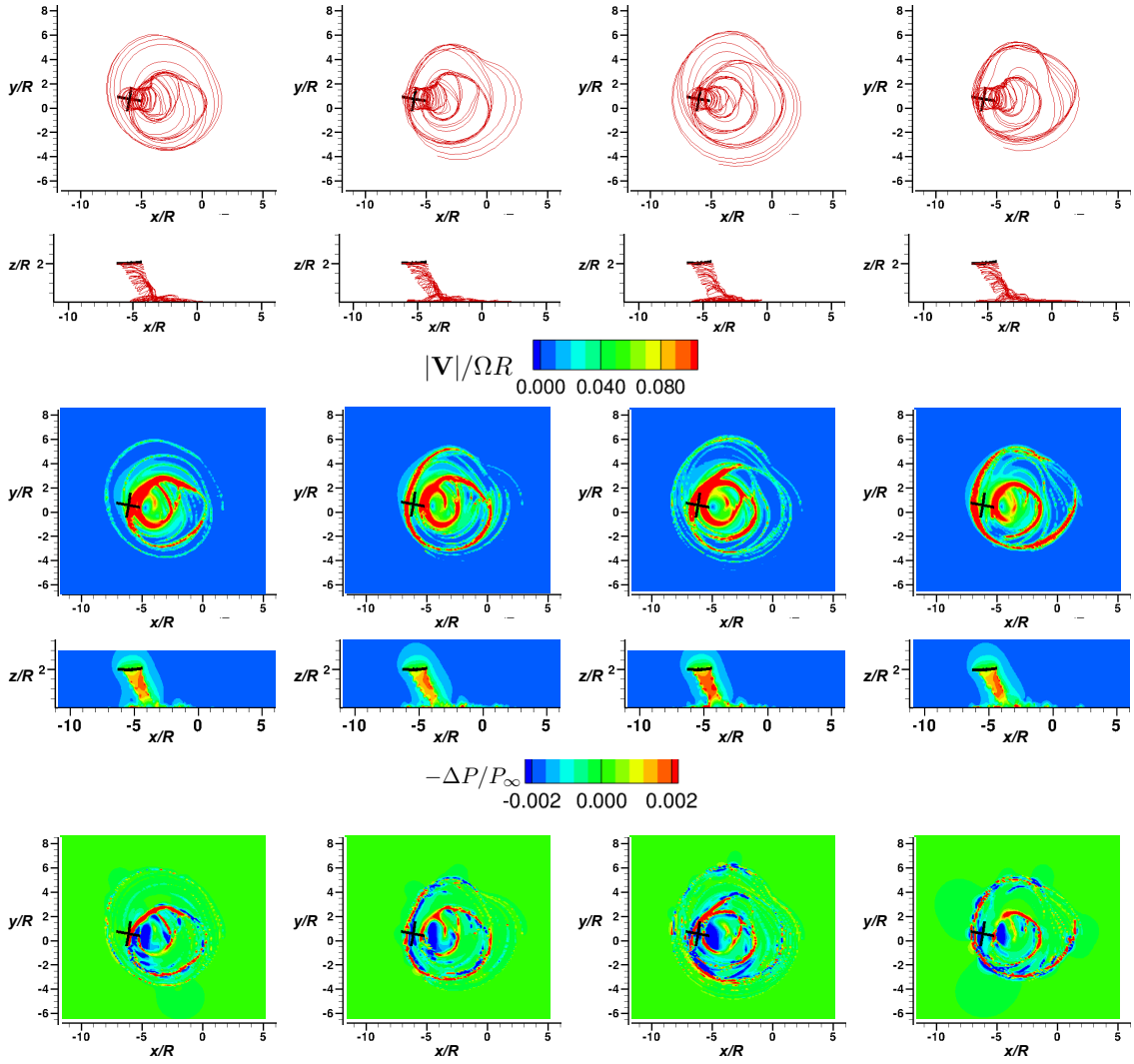

(a) $W = 14{,}500$ lbs (b) $W = 14{,}500$ lbs (crosswind) (c) $W = 16{,}300$ lbs (d) $W = 14{,}500$ lbs (initial condition 2)

Figure 3.46: Comparisons of wake geometries, normalized induced velocities and unsteady pressure fields at $t = 23$ s for the four approach-to-touchdown maneuver cases: (a) W = 14,500 lbs (in calm winds), (b) W = 14,500 lbs (with crosswind), (c) W = 16,300 lbs (in calm winds), and (d) W = 14,500 lbs (second initial condition).

neuver. As for the taxi-pass, however, the exact winds at the time of the tests were not known. A study was conducted to analyze the effects of a small crosswind of 2 kts on the development of the dust clouds, the results being shown in Figs. 3.47 and 3.48 for a weight of 14,500 lbs.

As shown in Figs. 3.47 and 3.48, the crosswind affects the shape of the dust clouds. The dust cloud for the approach-to-touchdown maneuver shows more sensitivity to the crosswind than for the taxi-pass maneuver. While the helicopter approaches the ground, i.e., between $t = 0$ to 6 s, the dust cloud formed with the crosswind is radially closer to the rotor disk; see Fig. 3.47. This means that the wake does not expand as much near the ground for this case as in calm winds; see Fig. 3.44. Up to $t = 6$ s, the simulation with crosswind effects shows better correlation with the measurements along the radial direction. Along the vertical direction, more differences between the simulations and the measurements are apparent, as shown in Fig. 3.44.

As the helicopter decelerates further from $t = 11$ to 17 s, the wake geometries and the dust clouds move radially farther forward of the rotor disk. When the helicopter takes off after $t = 17$ s, the dust clouds begin to look similar, and the sensitivity of the cloud shape to crosswind decreases; see Fig. 3.48. In general, the predicted dust clouds showed better correlation with the measurements along the longitudinal and lateral dimensions when the wind effects were included.

Effects of Initial Conditions

A knowledge of the upstream flight profile of the helicopter before the photogrammetric measurements were actually made is important. The initial condition of the helicopter 20 s

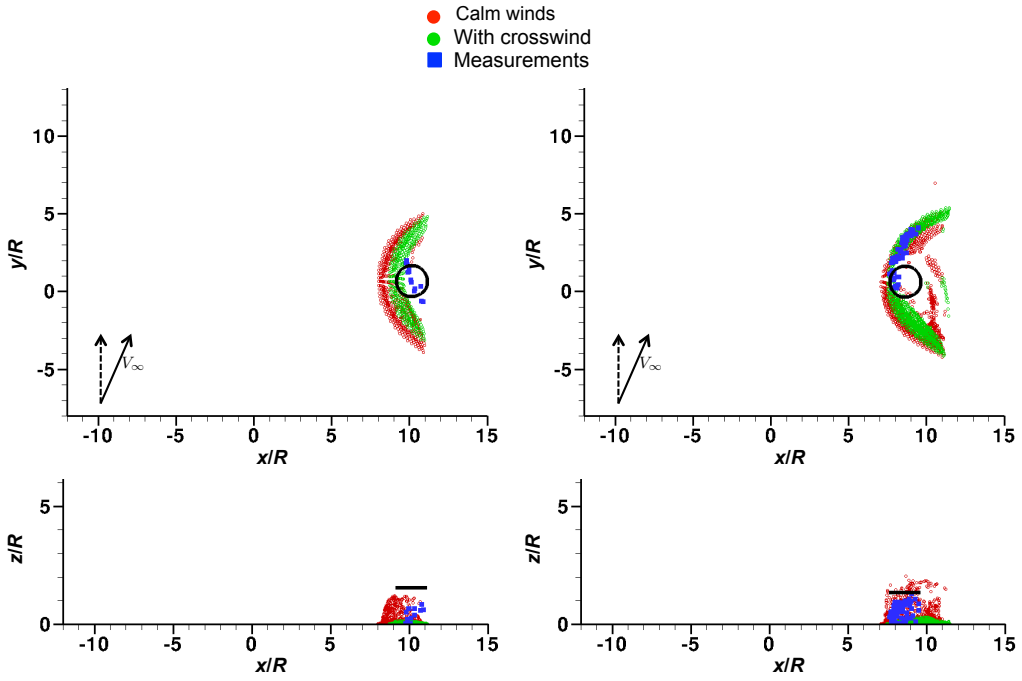

(a) Top and side views at $t = 0$ s

(b) Top and side views at $t = 2$ s

(c) Top and side views at $t = 4$ s

(d) Top and side views at $t = 6$ s

Figure 3.47: Comparison of the predicted dust clouds for the approach-to-touchdown maneuver in calm winds (shown in red) and with the crosswind (shown in green) with photogrammetric measurements (shown in blue) for the helicopter at a weight of 14,500 lbs at $t = 0$, 2, 4, and 6 s.

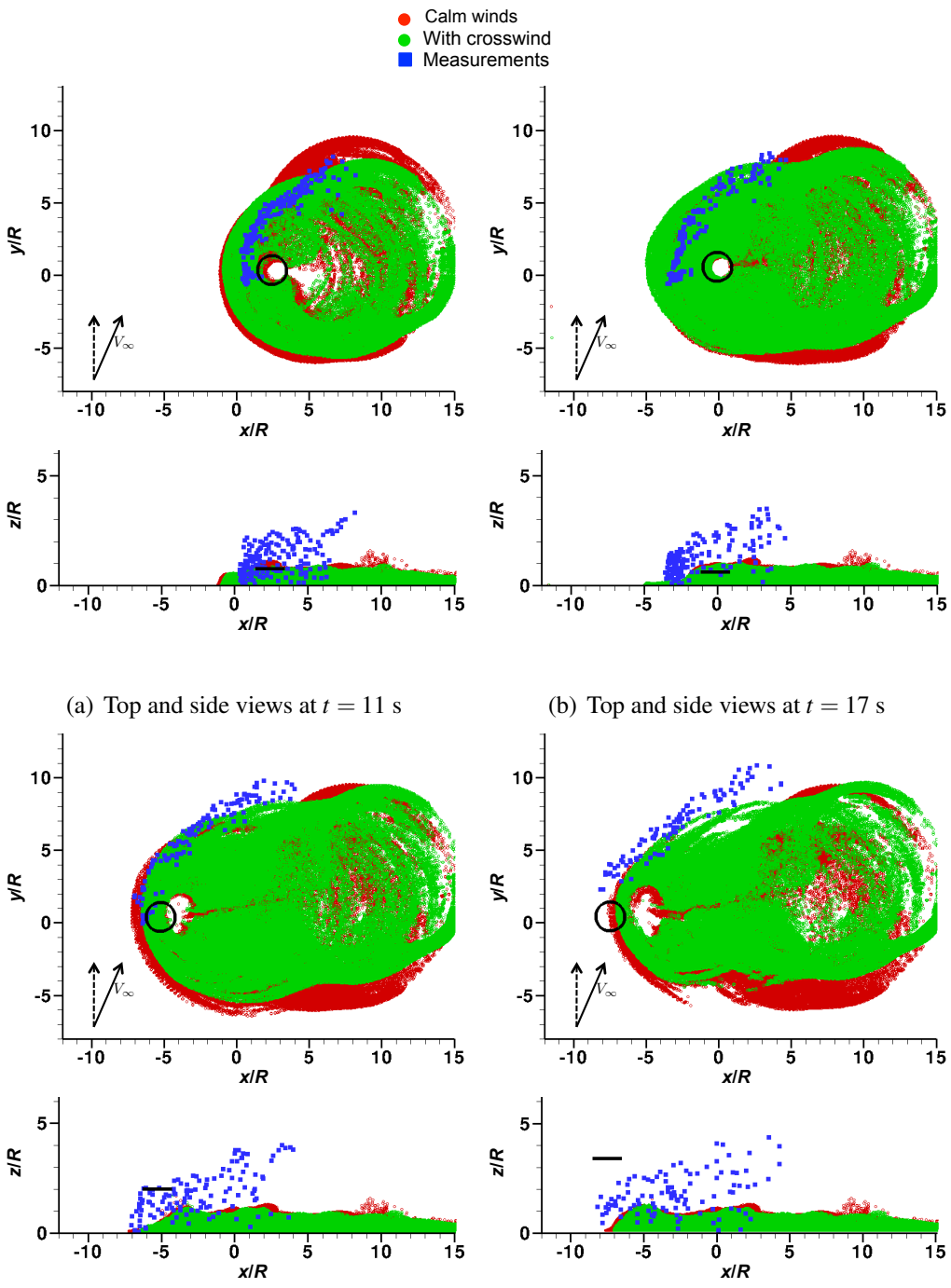

(a) Top and side views at $t = 11$ s

(b) Top and side views at $t = 17$ s

(c) Top and side views at $t = 23$ s

(d) Top and side views at $t = 25$ s

Figure 3.48: Comparison of the predicted dust clouds for the approach-to-touchdown maneuver in calm winds (shown in red) and with the crosswind (shown in green) with photogrammetric measurements (shown in blue) for the helicopter at a weight of 14,500 lbs at $t = 11$, 17, 23, and 25 s.

before the datum at $t = 0$ was estimated by assuming that the helicopter had traveled with the same velocity as it had from $t = 0$ to 2 s; see Fig. 3.38. The sensitivity of the predicted dust clouds was examined by considering a second initial condition, as also shown in Fig. 3.49. In this case, the initial descent velocity (i.e., before $t = 0$ s) was increased from 2.5 ft s^{-1} to 4 ft s^{-1}. These two initial conditions (with descent velocities of 2.5 ft s^{-1} and 4 ft s^{-1}, respectively) are referred to as initial conditions 1 and 2, respectively. These simulation were conducted at a weight of 14,500 lbs, and the effects of the crosswind were also included.

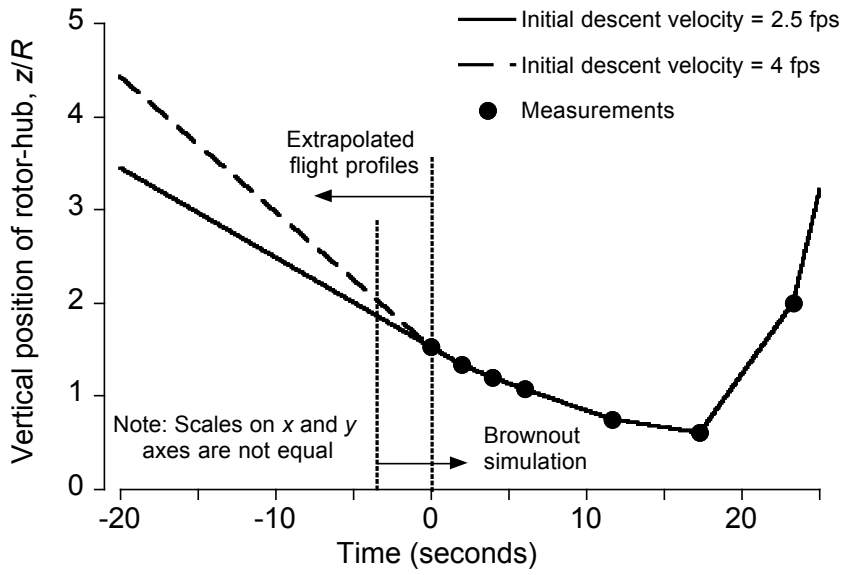

Figure 3.49: Vertical positions of rotor-hub for two different initial conditions, i.e., with initial descent velocities of: (a) 2.5 ft s^{-1}, and (b) 4 ft s^{-1}.

Top and side views of the predicted dust clouds are compared to the photogrammetric measurements in Figs. 3.50 and 3.51. It is apparent from these results that the dust clouds generated using the two initial conditions are significantly different for the first 9 s of the simulation (i.e., until about $t = 6$ s). The wake geometries, velocities, and pressure

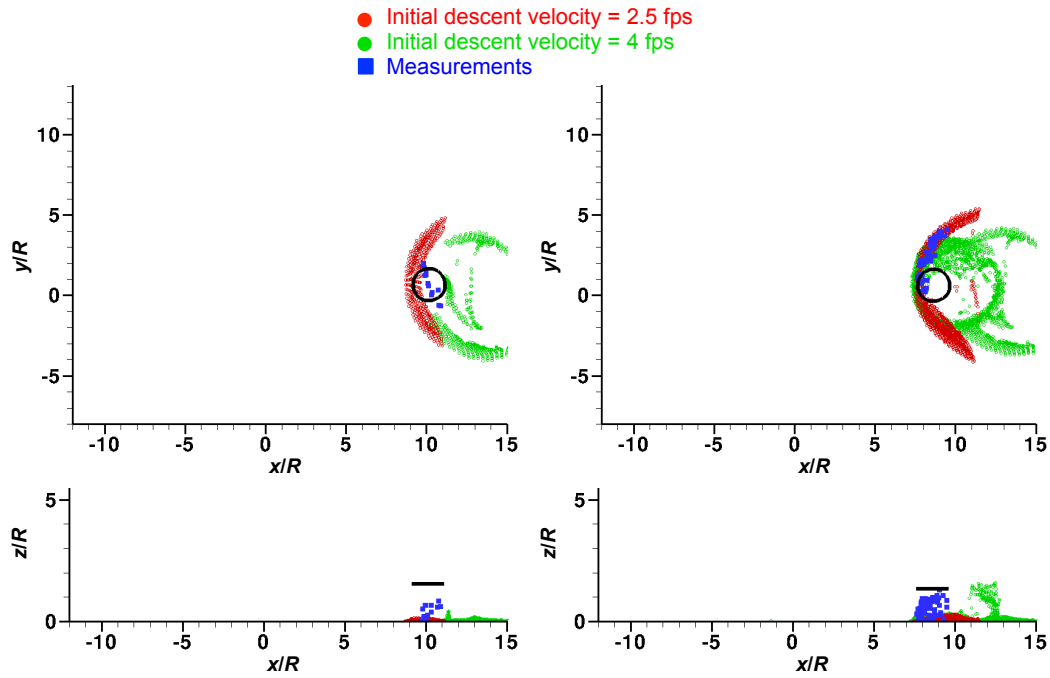

(a) Top and side views at $t = 0$ s

(b) Top and side views at $t = 2$ s

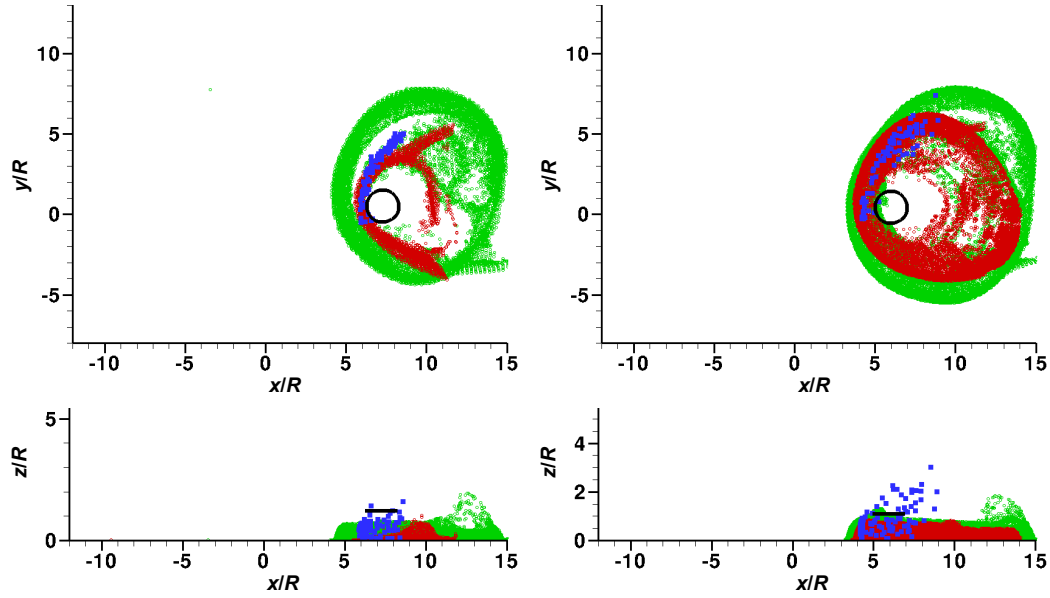

(c) Top and side views at $t = 4$ s

(d) Top and side views at $t = 6$ s

Figure 3.50: Comparison of the predicted dust clouds for the approach-to-touchdown maneuver for the two initial conditions along with photogrammetric measurements (shown in blue) for the helicopter at a weight of 14,500 lbs (with crosswind), at $t = 0$, 2, 4, and 6 s.

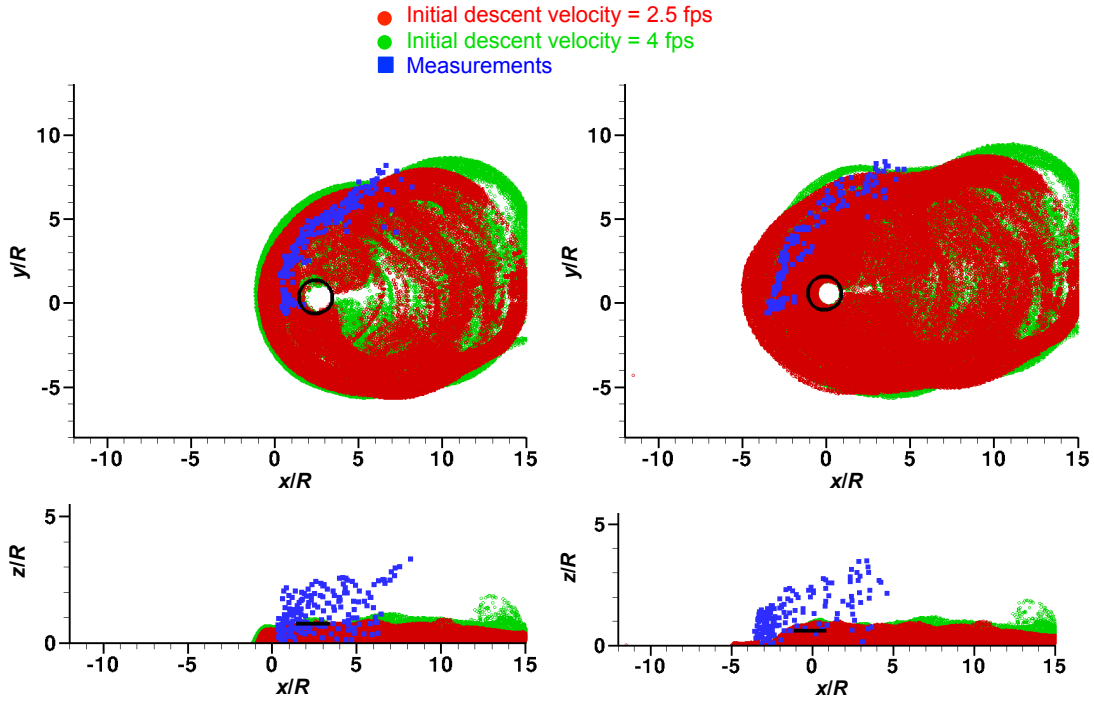

(a) Top and side views at $t = 11$ s

(b) Top and side views at $t = 17$ s

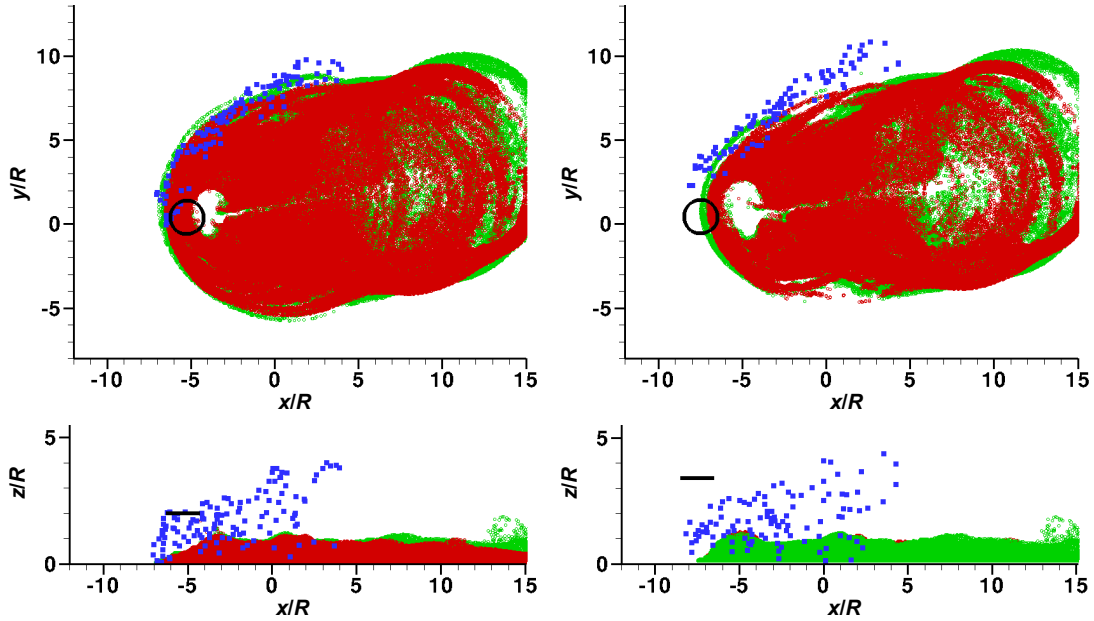

(c) Top and side views at $t = 23$ s

(d) Top and side views at $t = 25$ s

Figure 3.51: Comparison of the predicted dust clouds for the approach-to-touchdown maneuver for the two initial conditions along with photogrammetric measurements (shown in blue) for the helicopter at a weight of 14,500 lbs (with crosswind), at $t = 11$, 17, 23, and 25 s.

fields generated by the two initial conditions are also significantly different at these times, especially at $t = 0$ s; see Figs. 3.43 and 3.44. Although the forward boundaries of the dust clouds are formed at almost same distance ahead of the rotor disk in each case, the details of the clouds are clearly different when the helicopter is approaching the ground. These differences become less apparent as the helicopter reaches its lowest point over the ground and then takes off. After this time, the transients begin to die out and the dust clouds become more similar. However, further away from the rotor disk, the clouds were still substantially different in both shape and in detail. Nevertheless, the boundaries of the dust cloud showed good agreement with the measurement along the longitudinal and lateral dimensions.

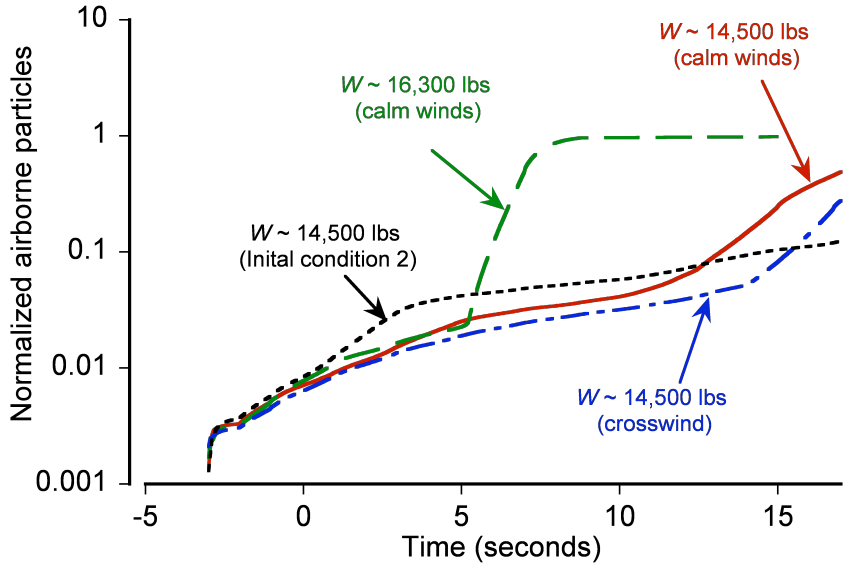

Figure 3.52: Time-history of airborne particle count for the approach-to-touchdown maneuver for the four cases: (a) W = 14,500 lbs (in calm winds), (b) W = 16,300 lbs (in calm winds), (c) W = 14,500 lbs (with crosswind), and (d) W = 14,500 lbs (initial condition 2).

Figure 3.52 shows the variations in the quantity of suspended particles to the weight

of the helicopter, the crosswind conditions, and to the initial flight condition used in the simulations. Clearly, the quantity of particles comprising the dust clouds are sensitive to aircraft weight, especially when the helicopter approaches the ground and the wake impinges on the sediment bed (i.e., $t = 6$ s). An almost exponential growth in the quantity of uplifted dust from pressure effects and bombardment ejections can be seen at this time. It is apparent from Fig. 3.52 that at times t = 4 and 6 s, copious amounts of dust are mobilized when the helicopter is at the heavier flight weight.

The quantity of suspended dust for this approach maneuver was also found to be more sensitive to the crosswind compared to the taxi-pass case, a point previously made. In fact, the average quantity of dust entrained with the crosswind was lower compared to that obtained in calm winds. Again, the sensitivity to initial flight condition appears to be more important when the helicopter comes closer to the ground and when the wake directly impinge on the sediment bed.

Overall, the results obtained suggest that the brownout dust clouds are sensitive to the weight of the helicopter, the wind conditions, and to the flight profile. These sensitivities are more significant when the helicopter approaches the ground, the wake restructures and impinges upon the bed. The developing dust clouds start to show more similarities after the helicopter reaches its lowest point above the ground.

Effects of Particle Size

In the present work, the simulated dust clouds were obtained from a superposition of individual simulations by using particles with diameter, d_p, between 1 and 100 μm. While this type of simulation is not equivalent to one computed simultaneously using a range of

multidisperse particles, an analysis of the resulting dust clouds can help to better understand the effects of particle size on the overall development of the clouds. In this case, the clouds obtained for the approach-to-touchdown maneuver at a weight of 14,500 lbs (in calm winds) were analyzed.

Figure 3.53 shows top and side views of the dust clouds at three time steps of t = 6, 12 and 17 s. The dust clouds for four different particle diameters (i.e., d_p = 1, 20, 70 and 100 μm) are shown in the different colors in Fig. 3.53. Notice that the majority of suspended particles in the clouds are actually the smaller dust particles (i.e., particles with $d_p = 10$ μm and 20 μm), although this is not a surprising result based on the measurements made of particle concentrations in brownout clouds, as shown in Fig. 1.6(a). These smaller particles tend to remain suspended to relatively longer times (see the top and side views, for example) because of their lower terminal velocities, the particles first uplifted at t = 0 s remaining in suspension even to t = 25 s and the helicopter having moved forward by some eight rotor diameters during this period; see Figs. 3.41 and 3.42. The larger particles were noted to be confined to the regions radially closer to the rotor, particularly at the front of the disk; these particles have greater drag and higher terminal velocities so they do not convect as high or as far as the smaller particles.

An analysis of the time-histories of the suspended particle counts for this simulation is particularly interesting because it can help to understand the relative importance of the different entrainment mechanisms. The quantity of particles that are entrained through direct entrainment (i.e., through the action of shear and pressure forces), and bombardment ejection mechanisms is shown in Figs. 3.54(a) and 3.54(b), respectively, with the total particle count being shown in Fig. 3.54(c).

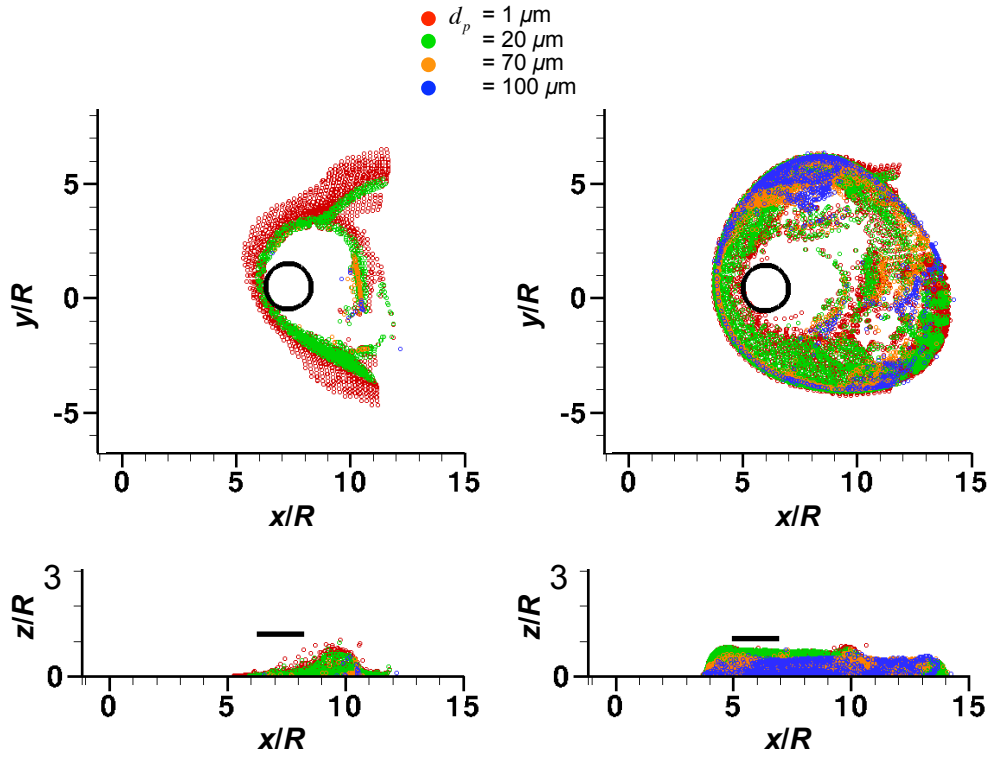

(a) Top and side views at $t = 4$ s

(b) Top and side views at $t = 6$ s

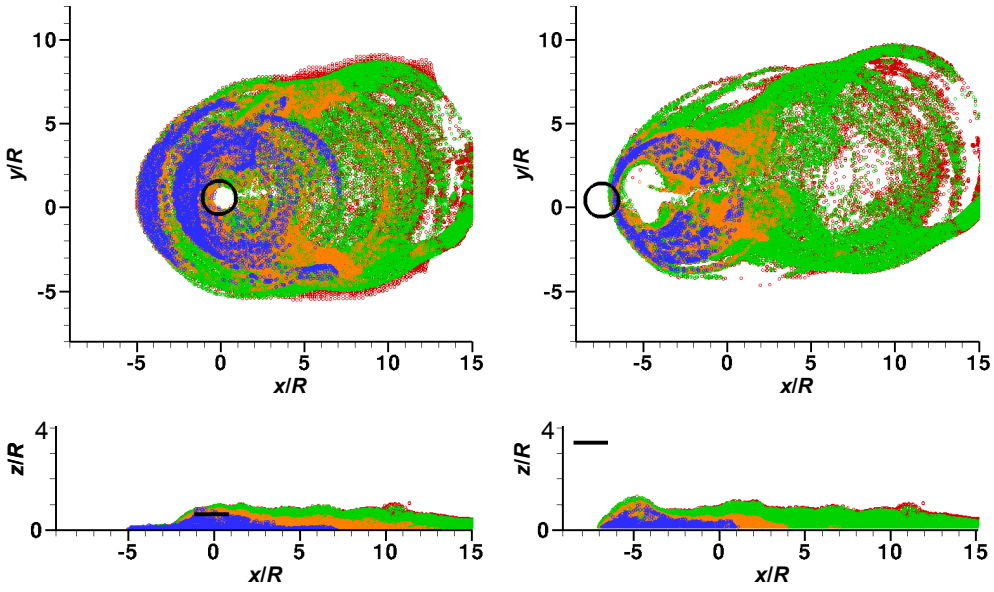

(c) Top and side views at $t = 17$ s

(d) Top and side views at $t = 25$ s

Figure 3.53: Instantaneous realizations of the cloud obtained by superposition of four monodisperse dust clouds (d_p = 10, 20, 70 and 100 μm) during the approach-to-touchdown maneuver for $W = 14{,}500$ lbs.

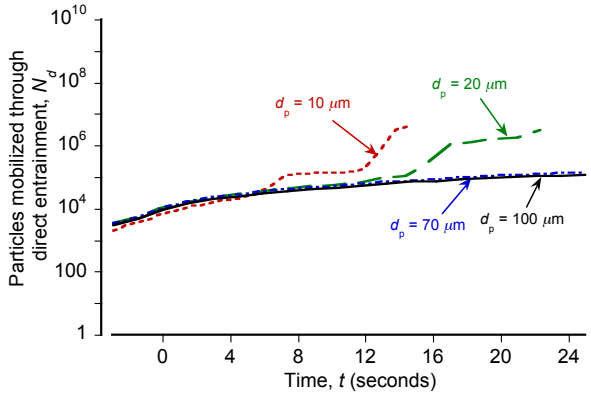

(a) Direct aerodynamic entrainment

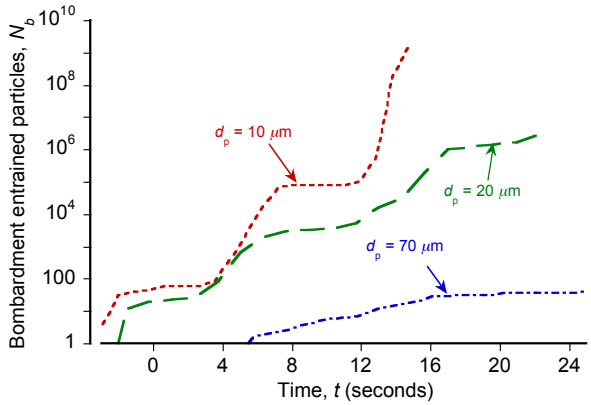

(b) Bombardment ejection

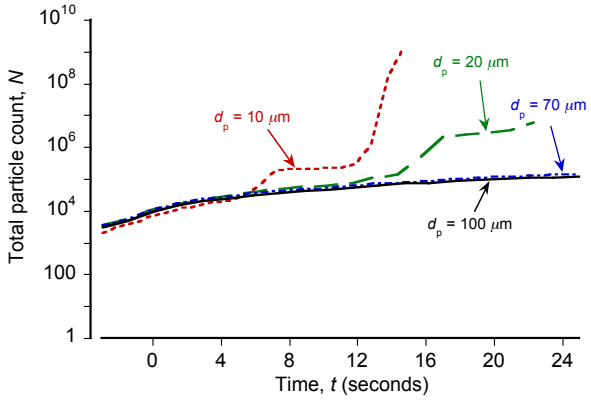

(c) Total entrainment

Figure 3.54: Time-history of the particles entrained via: (a) direct aerodynamic entrainment, (b) bombardment ejection, and (c) total entrained particles. (Note: These results were obtained from the linear summation of monodisperse particles of diameter, d_p = 10, 20, 70 and 100 μm.)

Figure 3.54(a) shows that the shear and pressure forces on the bed are strong enough to overcome the gravitational and inter-particle forces for particle of diameters between 1 μm and 100 μm. However, notice that most of the developing dust field (except closer to the rotor disk) is comprised of the smaller particles (see Fig. 3.53); the larger particles settle out quickly under gravity. A larger quantity of the smaller particles was found to be mobilized and entrained by means of bombardment mechanisms, which is not the case for the heavier particles; see Fig. 3.54(b).

It is apparent from Fig. 3.54(c) that the quantity of suspended particles increases markedly at three discrete times, i.e., at $t \approx 6$, 12 and 17 s. The corresponding wake geometries, induced velocities, and pressures at these three times are shown in Fig. 3.55. At $t = 6$ s, the wake vortices can be seen to impinge on the ground ahead of the rotor disk, the high velocity region corresponding to the position of the ground vortex that forms ahead of the rotor disk. In effect, the ground vortex here can be considered as a "super-vortex," which is formed by the pairing of adjacent parts of the helicoidal wake; more details on the formation of this super-vortex are shown later. The pressure contours on the bed at this time showed large positive and negative regions. The entrained particles in this case were moved almost vertically upwards in the regions of positive pressures (i.e., red contours), whereas bombardment ejections occurred in the other regions. As a consequence, Figs. 3.54(a) and 3.54(c) show that a rapid increase in the quantity of uplifted particles originates at about $t = 6$ s. Notice that this increase is observed for the particles with smaller diameters, i.e., $d_p \sim 10$ μm. In fact, the total number of calculated particles clusters at this time was $O(10^9)$.

At $t = 12$ and 17 s, the rotor is closest to the ground and its wake expands radially

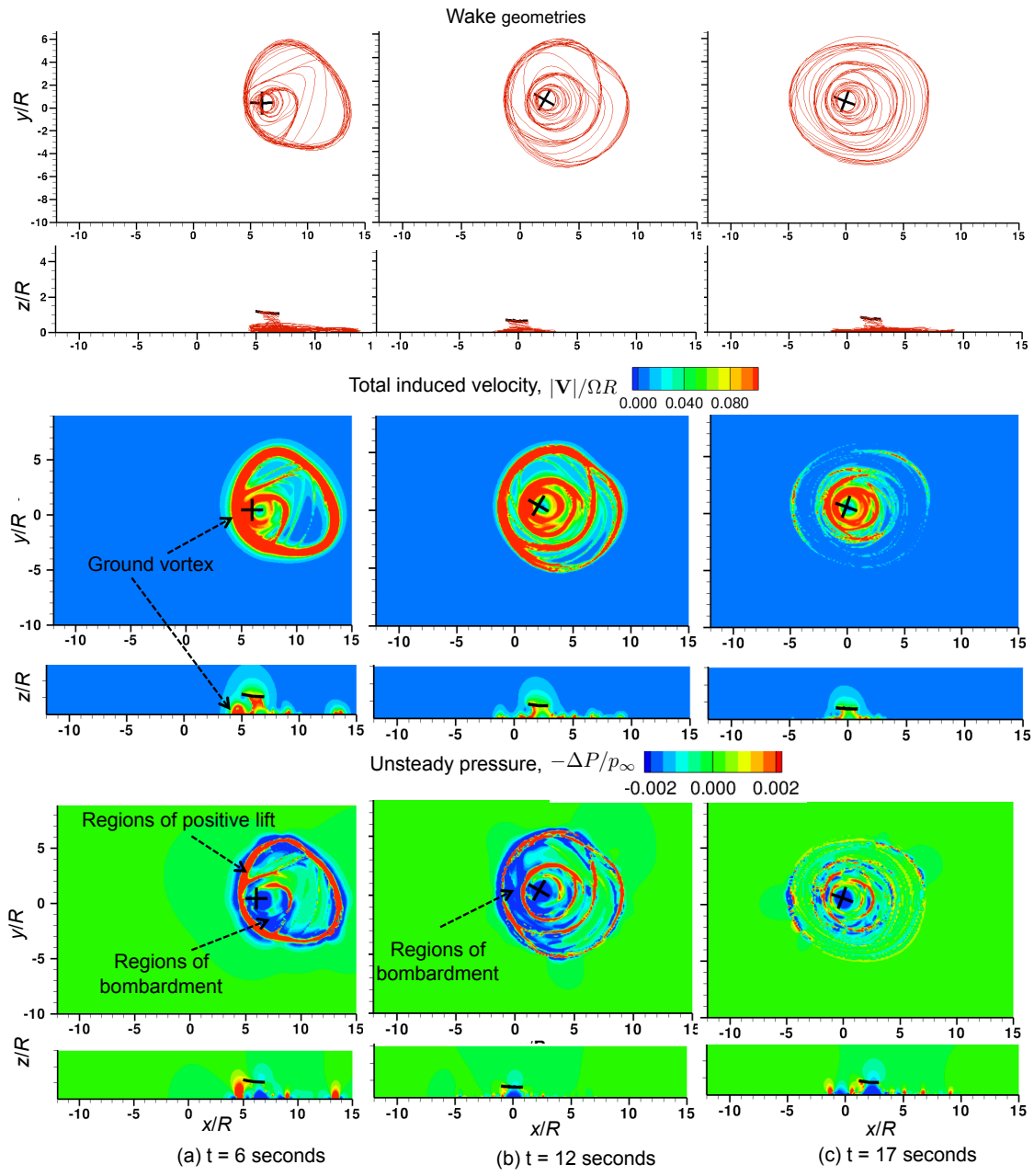

Figure 3.55: Comparisons of the wake geometries (top and side views), contour maps of induced velocity and unsteady pressure at the sediment bed and along the longitudinal axis passing through the rotor hub at t = 6, 12 and 17 s during the approach-to-touchdown maneuver.

outward. The signature of the tip vortices and the bundling of the vortex segments near the ground is shown by the tightly packed induced velocity contours; see Fig. 3.55. Again, the upwash and downwash regions at the ground around the periphery of the rotor disk contribute significantly to the number of bombardment ejections that are produced by the smaller-sized particles.

Finally, Fig. 3.56 shows the predicted average particle count that was produced during the approach-to-touchdown maneuver. This form of presentation confirms that the dust cloud was comprised primarily of the smaller dust-sized particles (i.e., $d_p \leq 20\ \mu$m), which were mobilized both through direct entrainment as well as bombardment ejection mechanisms. Particles larger than $d_p > 70\ \mu$m were primarily mobilized by means of direct entrainment, and only ejected fewer particles of their own size through bombardment ejections. In practice, the bombardment of bigger particles onto the bed may also lead to the ejection of smaller particles, although this interdependent effect needs to be studied in further, before models can be developed for its representation in the brownout simulations.

3.3 Dust Cloud Analysis During Maneuvers

A detailed analysis of the development of the dust clouds is now discussed. First, calculations are presented that show the effects of the different sediment entrainment and mobilization mechanisms that are being modeled. Then, a detailed analysis of the formation of the dust clouds that are formed during different flight conditions is presented; these flight conditions are: (a) hover IGE at $z/R = 1$, (b) a representative landing maneuver, and

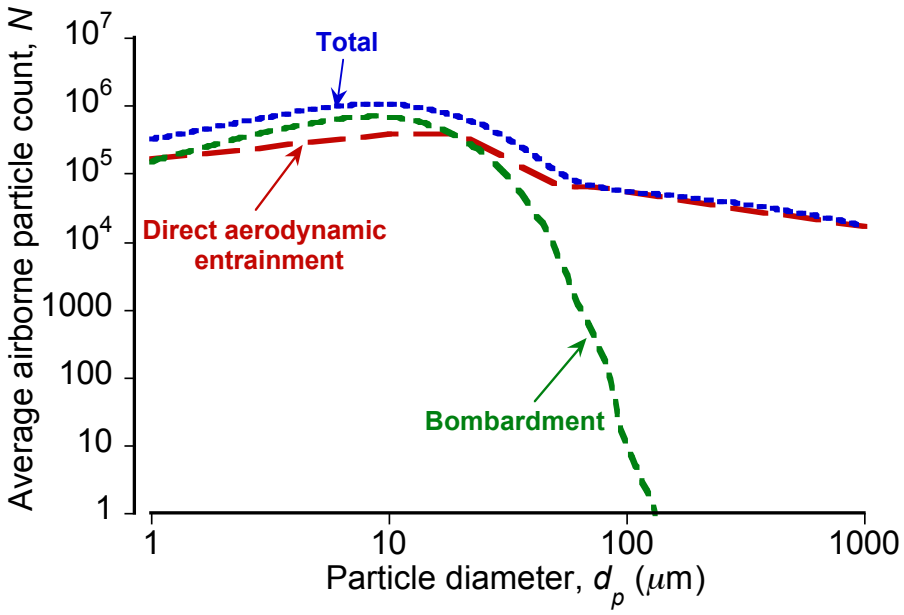

Figure 3.56: Variation of the average airborne particle count as a function of particle size during the approach-to-touchdown maneuver.

(c) a takeoff maneuver.

The specifications of the helicopter considered in this study are given in Table D.3 of Appendix D. The loaded weight of the helicopter was 22,000 lbs, and the FVM computations were performed by using 10 free wake turns of the rotor.

3.3.1 Particle Motion in the Dust Cloud Simulations

An analysis of the details of the sediment mobilization and subsequent motion in the brownout clouds is presented. For this study, the helicopter performing a takeoff maneuver; details of this maneuver are given later. Notice that the actual flight profile was not critical in this case because the objective was to reveal more about the details of the underlying uplift and mobilization mechanisms.

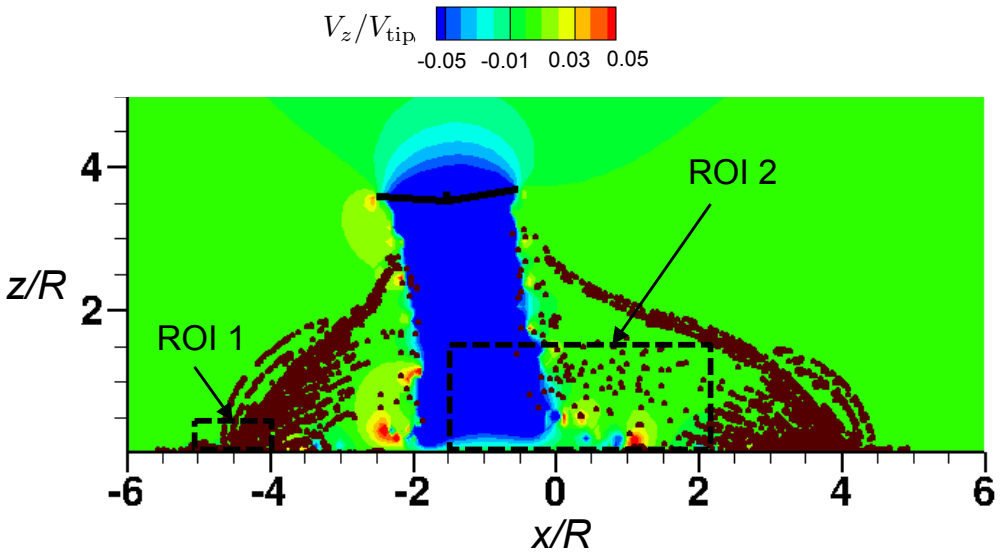

Figure 3.57: Instantaneous realization of a representative flow field chosen to highlight the fundamental sediment dynamics.

An instantaneous realization of the representative flow field that was used to extract the sediment dynamics is shown in Fig. 3.57. Two regions of interest (ROI) were chosen: ROI 1 was selected to show most of the sediment uplift and mobilization processes, with ROI 2 being chosen to highlight the process of global reingestion bombardment.

The resulting dynamics of the sediment motion closer to the ground in ROI 1 is shown in Figs. 3.58 and 3.59. The particles are represented as small circles with background contour being of the vertical component of velocity. The red and blue colors show regions of upwash and downwash velocities, respectively, with the presence of a red-blue pair indicating the signature of a coherent vortex.

Initially, six particles were stationary on the sediment bed in ROI 1 and one particle was creeping, as shown in Fig. 3.58(a). Creeping particles move along the bed under the groundwash produced by the rotor flow, which produces sufficiently high friction

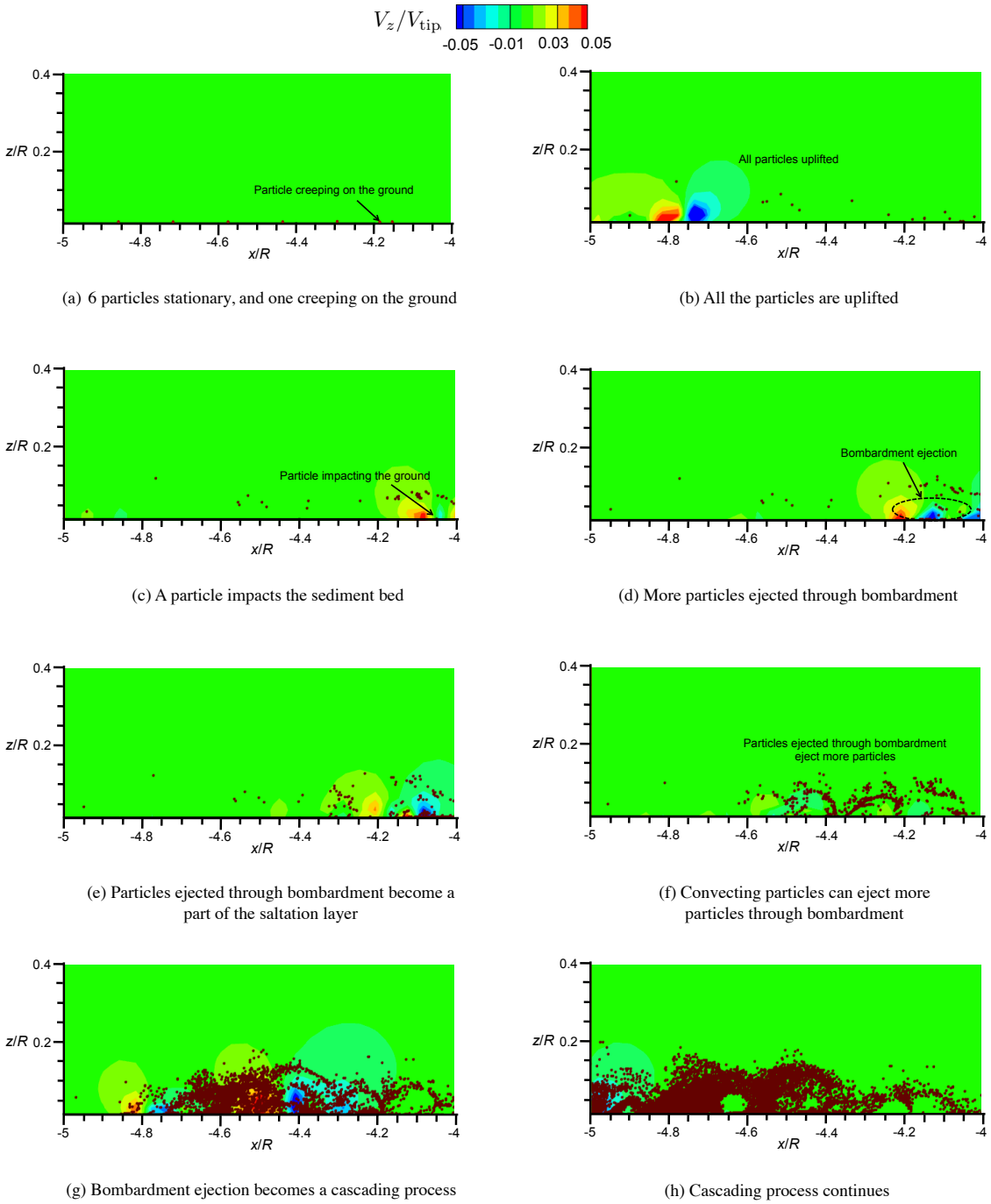

(a) 6 particles stationary, and one creeping on the ground

(b) All the particles are uplifted

(c) A particle impacts the sediment bed

(d) More particles ejected through bombardment

(e) Particles ejected through bombardment become a part of the saltation layer

(f) Convecting particles can eject more particles through bombardment

(g) Bombardment ejection becomes a cascading process

(h) Cascading process continues

Figure 3.58: Instantaneous realizations of the sediment dynamics for the takeoff maneuver showing the details of particle motion in a ROI close to the ground. The background contours are of vertical velocity.

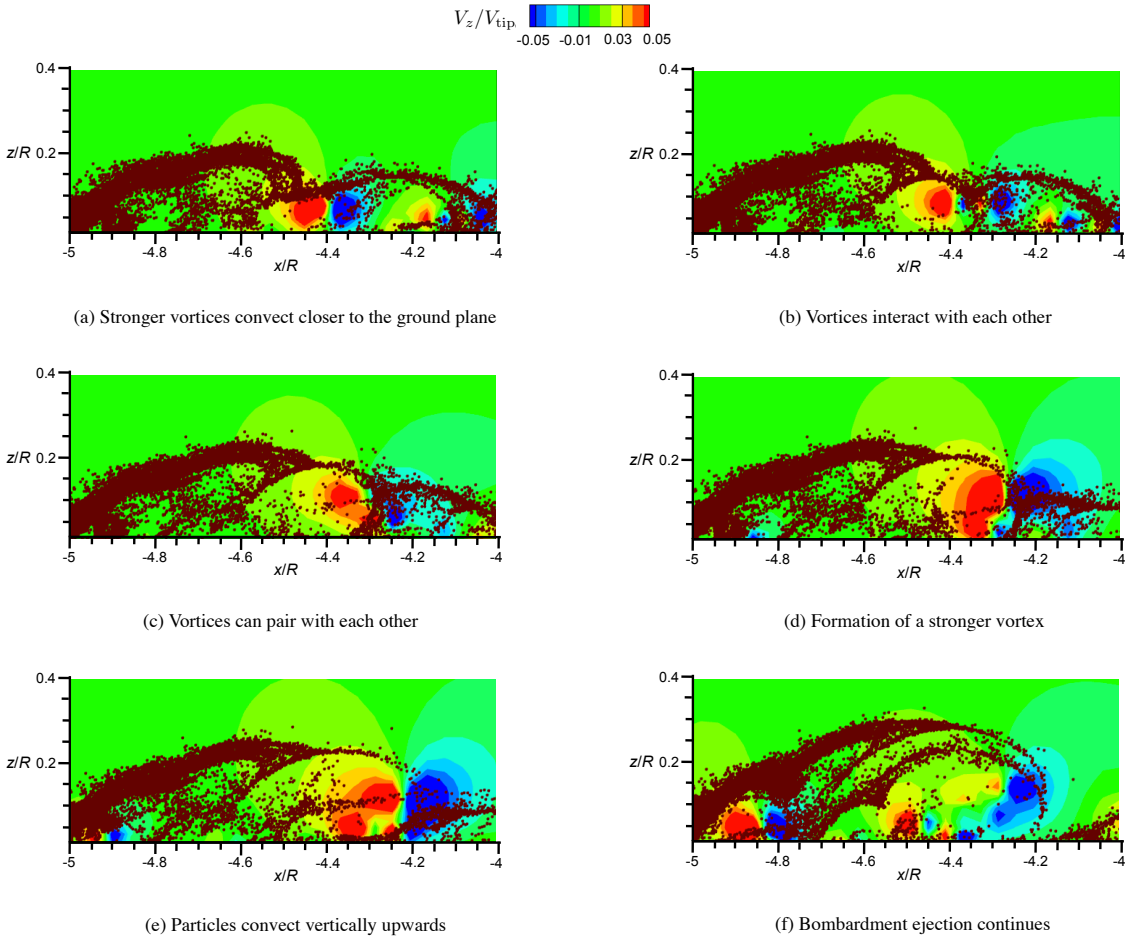

(a) Stronger vortices convect closer to the ground plane

(b) Vortices interact with each other

(c) Vortices can pair with each other

(d) Formation of a stronger vortex

(e) Particles convect vertically upwards

(f) Bombardment ejection continues

Figure 3.59: Instantaneous realizations of the sediment dynamics showing the details of the time-history of bombardment induced by the rolling up and bundling of tip vortices near the ground, where the repeated impact of uplifted sediment particles eject more particles through a cascading mechanism.

velocities to mobilize the particles. However, the vertical velocities are still too low to uplift the particles into the flow. With the passage of a vortex through this region, higher vertical velocities are induced into the flow at the ground, causing all of the particles in the ROI to be uplifted; see Fig. 3.58(b). Some of these uplifted particles then move into saltation, where the particles that were initially uplifted follow ballistic-like trajectories back onto the bed under gravity, as shown in Fig. 3.58(b). Other particles may remain suspended in the flow because of the secondary induced flow from another nearby vortex flow; see Fig. 3.58(c). This phenomenon, which has been termed secondary suspension (Ref. 17), continues to uplift and suspend particles as long as vortices continue to convect through the flow in the vicinity of the bed.

Of more interest in this case, is that some of these suspended particles are trapped in the downwash regions of a vortex flow, as shown in Fig. 3.58(c), and then bombard the bed, as shown in Fig. 3.58(d). This process was termed in Ref. 17 as local reingestion bombardment. Similarly, some of the particles that are uplifted high enough can become reingested through the rotor disk and can then also bombard the bed. This latter process has been termed global reingestion bombardment, and is shown in Fig. 3.60 in ROI 2. Both of these processes initiate a cascading mechanism of bombardment ejections; see Figs. 3.58(e) to 3.58(h). The ejected particles may also become part of the saltation layer, as shown in Fig. 3.58(f), and these saltating particles can again be uplifted when the upwash region of a vortex passes close by, as shown in Fig. 3.58(g), which is a process called vortex-induced trapping (Refs. 18 and 17). Clearly, bombardment ejections increase rapidly the total quantity of particles that are suspended in the developing dust cloud.

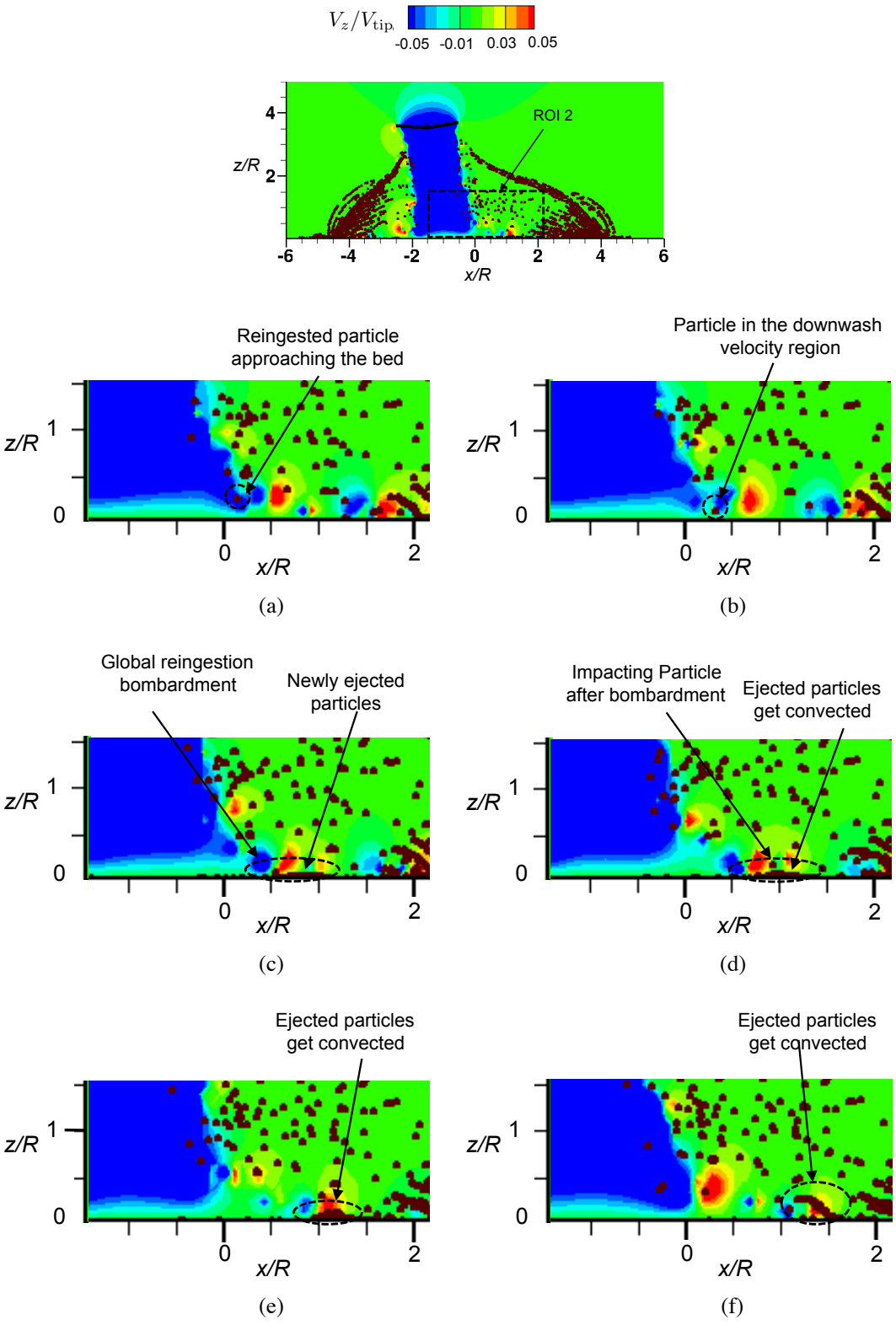

Figure 3.60: Instantaneous realizations of the sediment particles and contours of vertical velocity showing the process of global reingestion bombardment in region of interest (ROI) 2.

Pairing and bundling of the vortices closer to the ground plane can also increase the number of bombardment ejections. For example, Figs. 3.59(a) to 3.59(f) are realizations when the vortices convect through the ROI. In this case, adjacent vortices undergo pairing, which increases the upwash and downwash regions close to the ground and so increases the quantity of particles that are uplifted from bombardment ejections. These results show that the processes of bombardment ejections are closely related to the presence of vortices near the ground, and will become more intense when these vortices interact and pair-up to produce higher upwash and downwash velocities.

3.3.2 Analysis of Dust Clouds in Hover

An analysis of the development of dust clouds was conducted for a rotor hovering IGE at $z/R = 1$. While this is not a realistic brownout condition, it serves to simplify the issues in understanding the underlying mechanisms. Instantaneous realizations of the top and side views of the rotor wake are shown in Figs. 3.61(a) and 3.61(c), respectively. While a simplified flight condition, the results help to illustrate the fundamental behavior of the rotor wake and the subsequent development of the particle motions. The corresponding contours of total velocity in the rotor wake are shown in Figs. 3.61(b) and 3.61(d), respectively. Notice from Figs. 3.61(a) and 3.61(c) that the wake expands as it approaches the ground plane, this process causing stretching of the vortex filaments and a reintensification of vorticity that balances or even counters the process of diffusion (Refs. 20 and 19). In this case, the tip vortices persisted in the flow for up to six rotor revolutions without diffusing significantly, a result consistent with experimental findings

(Ref. 20).

Also, notice from Fig. 3.61(b) that the velocity field induced at the bed was aperiodic because of the pairing and bundling of vortex filaments as they approached the ground plane. Ultimately, it is the proximity of these vortices to the sediment bed that contributes significantly to the mobilization and entrainment of sediment particles in the developing brownout cloud.

For the brownout simulations in this case, the initial sediment bed was comprised of 4.0×10^5 monodisperse particle clusters (in 10 layers with each layer comprising 4.0×10^4 clusters) spread uniformly over a grid of size 200 ft in both the longitudinal and lateral directions, which gave a total of 4.0×10^7 potential particles on the sediment bed. Of course, additional particles could be (and are) ejected through bombardment mechanisms. As mentioned previously in Section 2.6, as each sediment layer was activated the layer beneath it was activated every subsequent second. The dust clouds were obtained by a superposition of monodisperse simulations of particles with d_p between 1–100 μm, as described in Section 3.2.2.

3.3.2.1 Particle Uplift Analysis

A study was conducted to evaluate the relative importance of different mobilization and uplift mechanisms; two cases were considered. In Case 1, particles were mobilized by the action of shear forces alone, i.e., the expression for $u_{\star_t}$ as given by Eq. 2.55 was used with $\Delta P =$ set to zero, and the process of bombardment was ignored. This threshold model has been used in all previous brownout simulation methodologies (Refs. 22, 36–40). In

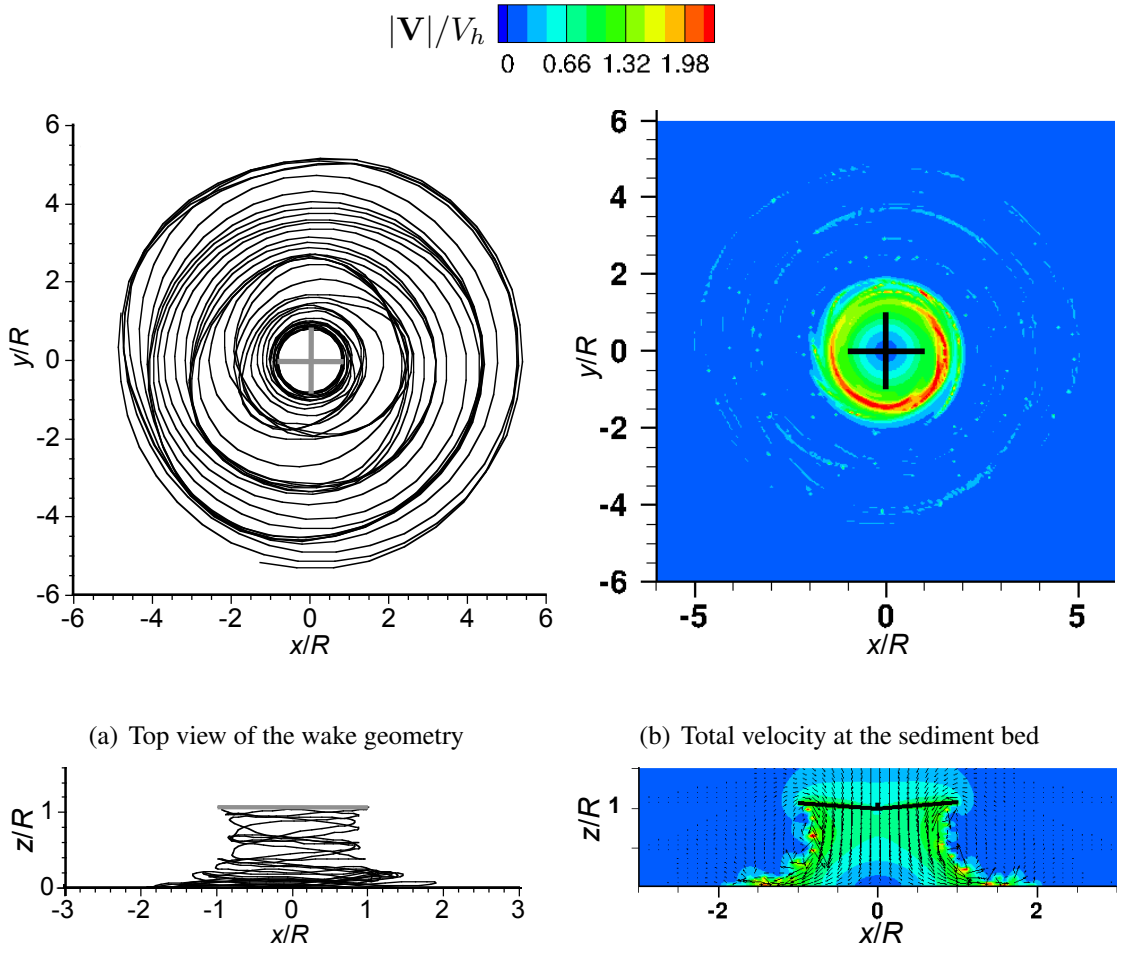

(a) Top view of the wake geometry

(b) Total velocity at the sediment bed

(c) Side view of the wake geometry

(d) Total velocity along a longitudinal plane

Figure 3.61: Wake geometries and contour map of the total velocity produced by the rotor hovering in ground effect at $z/R = 1$: (a) top view, (b) contour plot of the total velocity at the sediment bed (i.e., $z/R = 0.02$), (c) side view, and (b) contour map of the total velocity along a longitudinal plane passing through the rotor disk.

Case 2, the entrainment mechanisms modeled in the present work were used. These mechanisms included: (a) the effects of shear and unsteady pressure forces by using Eq. 2.55, and (b) bombardment ejections.

Figure 3.62 shows the time-history of the total quantity of particles in the dust

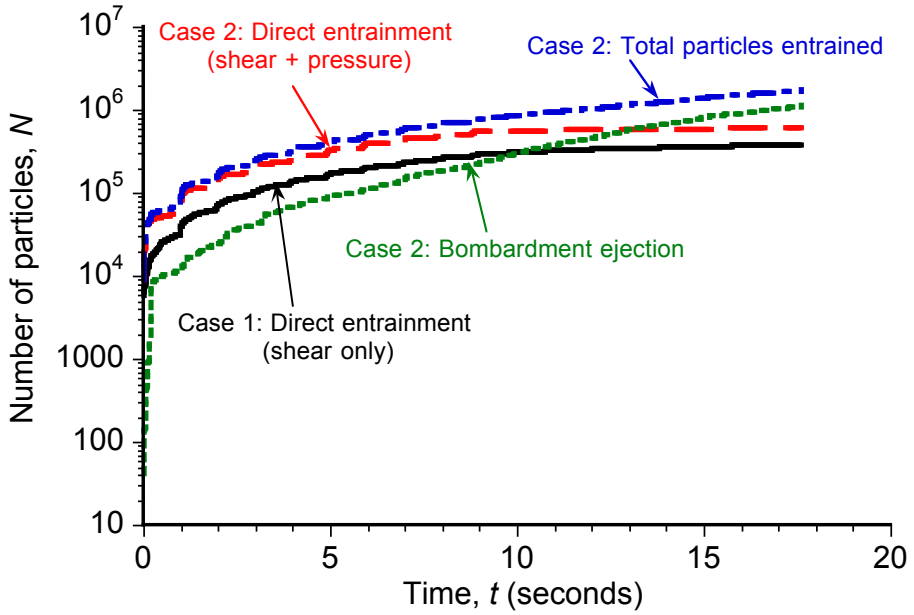

Figure 3.62: Time-history of the total quantity of particles entrained through the mobility conditions defined by Cases 1 and 2, for a rotor hovering IGE at $z/R = 1$.

clouds obtained for a rotor hovering at $z/R = 1$. Notice that the inclusion of the unsteady pressure effects in Case 2 has mobilized approximately twice the total quantity of particles as were mobilized by the action of shear alone in Case 1. The quantity of particles ejected through bombardment in Case 2 also increased with time. At the end of the simulation, the total quantity of particles mobilized by the inclusion of all the mobilization mechanisms (i.e., shear, pressure and bombardment) were an order of magnitude larger than with only the effects of shear.

Figure 3.63 shows the quantity of particles of different sizes in the dust clouds at $t = 17$ s. A large quantity of particles of diameters, d_p, between 30 and 1000 μm were entrained through the action of shear forces in Case 1; see Figure 3.63(a). The smaller sized dust particles require higher friction velocities to mobilize because of the higher inter-particle forces. These friction velocities are affected by unsteady pressure forces, which

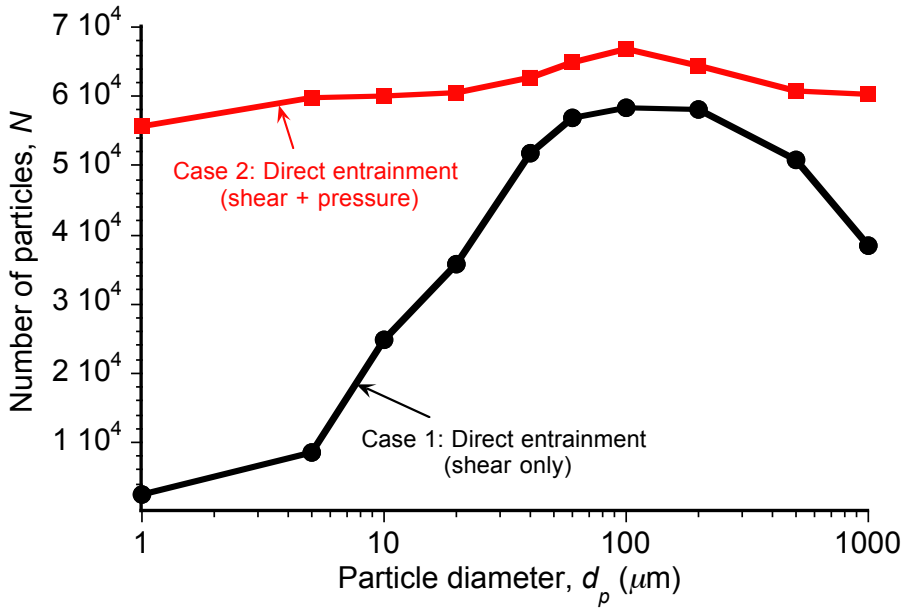

(a) Particles of different sizes entrained through direct entrainment

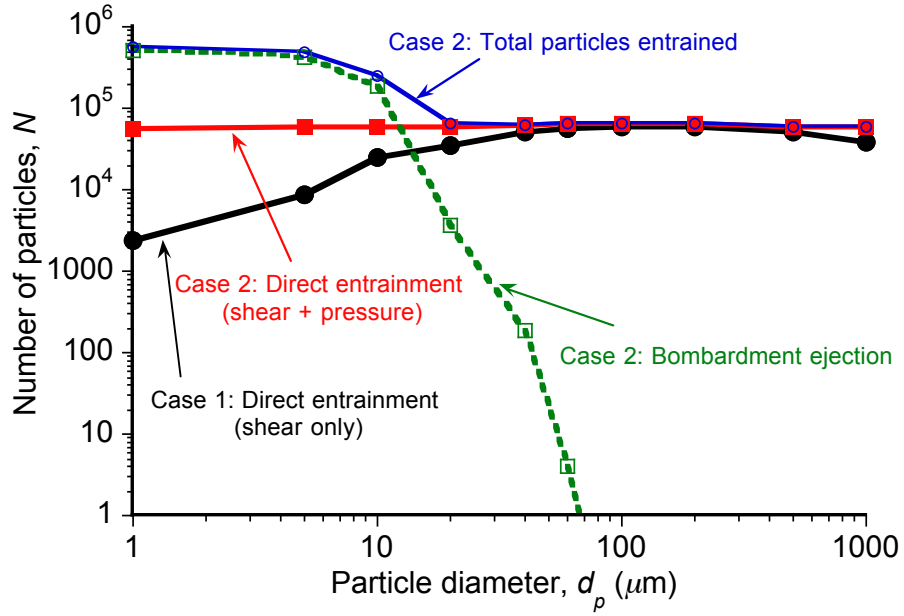

(b) Total particles entrained through Cases 1 and 2 versus particle diameter

Figure 3.63: Comparisons of the total quantity of particles of different sizes present in the brownout cloud at $t = 17$ s: (a) total particles entrained through direct entrainment from Cases 1 and 2, and (b) total quantity of particles entrained through direct entrainment as well as bombardment ejection in Case 2 versus those from Case 1.

result in the mobilization of these particles, as shown in Fig. 3.63(a). Furthermore, a large quantity of small-sized dust particles are also entrained through bombardment ejections; see Fig. 3.63(b). Also, notice that the larger particles did not eject particles of their own sizes through bombardment, a result explained previously in Section 3.1.1. Overall, the results obtained here show that the inclusion of all the mobilization mechanisms is important for the modeling of the dust clouds.

3.3.2.2 Development of Brownout Dust Cloud in Hover

Figure 3.64 shows details of the rotor flow field and corresponding dust cloud for the rotor in hover IGE at $z/R = 1$. The particles are shown as circles, with only the particles initially lying between $y/R = -0.1$ and 0.1 being identified in this case. The rotor flow field is shown using the background contour of the vertical velocity induced along a longitudinal plane passing through $y/R = 0$.

Figure 3.64(a) shows that the particles in the first sediment layer start to mobilize from the regions where stronger upwash velocities are induced by the vortices near the bed, i.e., for r/R approximately between 1.5 and 2. The velocity and pressure fields in these regions induce sufficient friction velocities to overcome the effects of gravity and interparticle forces. The mobilized particles then begin to saltate on the bed, and can also eject new particles through saltation bombardment; see Fig. 3.64(b). Details of these processes are shown in Fig. 3.65.

After the particles in the first sediment layer are removed, the next sediment layer becomes eligible to be mobilized. Notice from Fig. 3.64(c) that the particles from the sec-

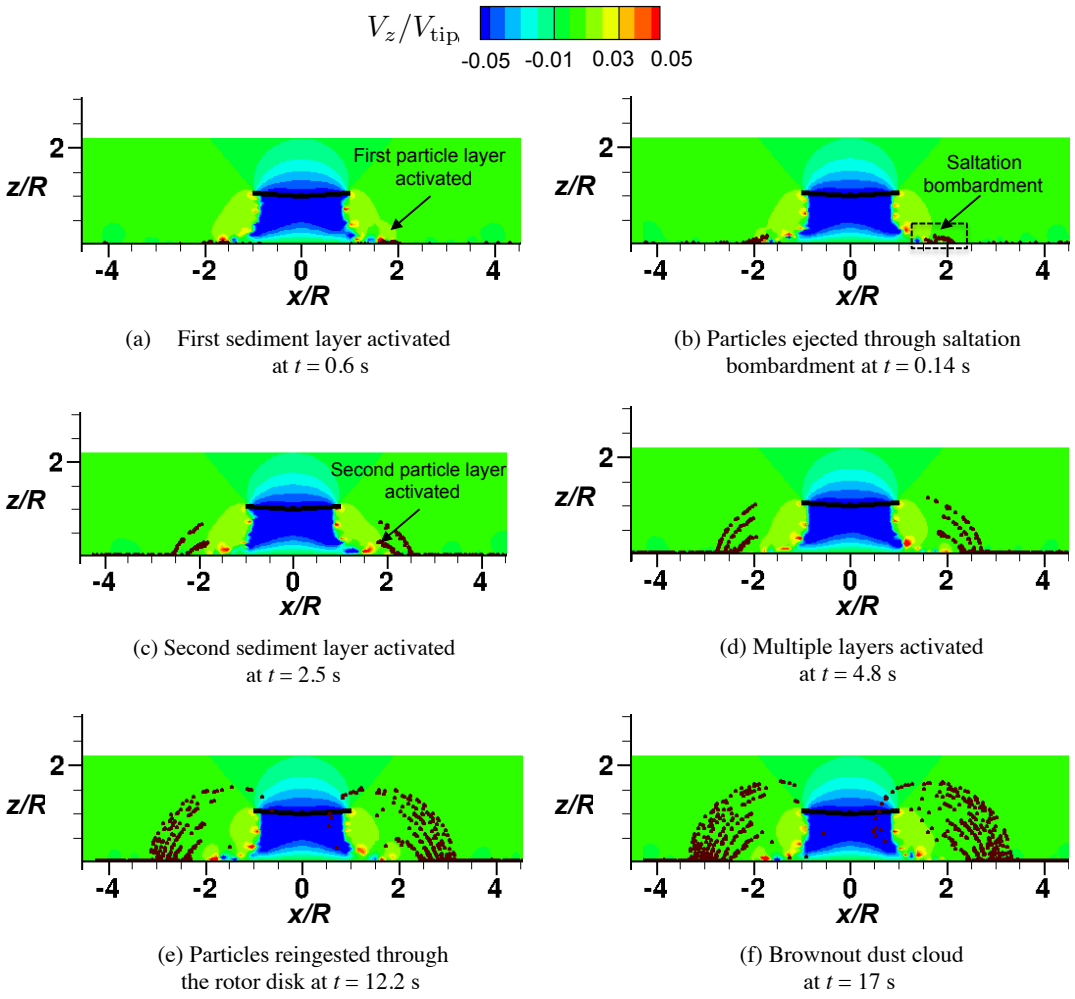

(a) First sediment layer activated at $t = 0.6$ s

(b) Particles ejected through saltation bombardment at $t = 0.14$ s

(c) Second sediment layer activated at $t = 2.5$ s

(d) Multiple layers activated at $t = 4.8$ s

(e) Particles reingested through the rotor disk at $t = 12.2$ s

(f) Brownout dust cloud at $t = 17$ s

Figure 3.64: Development of the dust cloud for a rotor hovering at $z/R = 1$ at times t = 0.05, 1.4, 2.5, 4.8, 12.2 and 17 s. (Note: Only the particles initially positioned between $y/R = -0.1$ and 0.1 are shown for clarity).

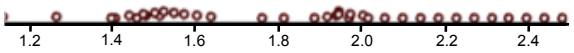

(a) Initiation of saltation

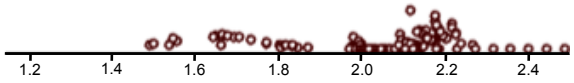

(b) Saltation bombardment

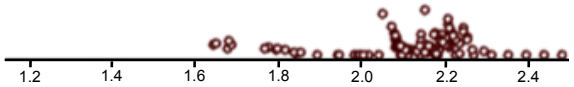

(c) Saltation and bombardment continues

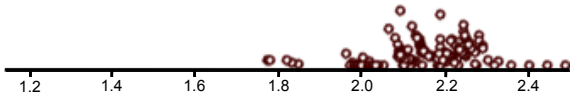

(d) Saltation and bombardment continues

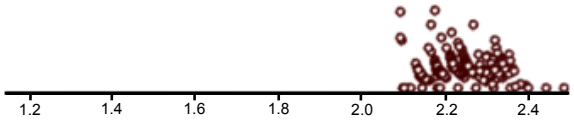

(e) New sediment ejected and more bombardment

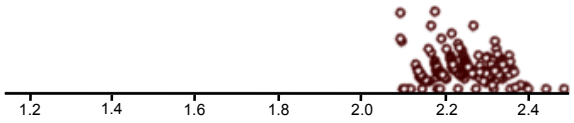

(f) More sediment ejected

Figure 3.65: Instantaneous realizations of the sediment dynamics in the ROI for a rotor hovering at $z/R = 1$, showing the details of saltation bombardment where sediment particles move in saltation and then eject more particles.

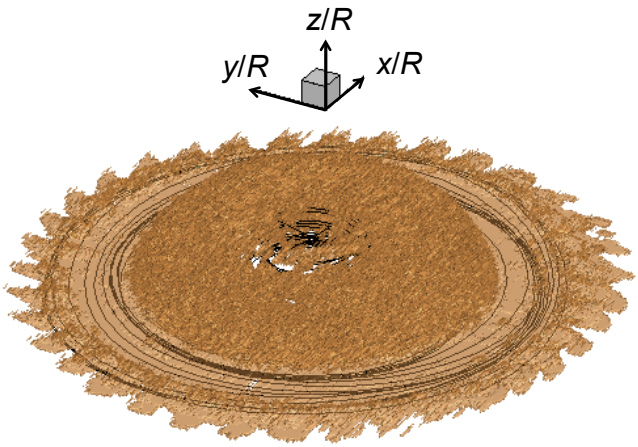

(a) 3-dimensional view of the dust cloud

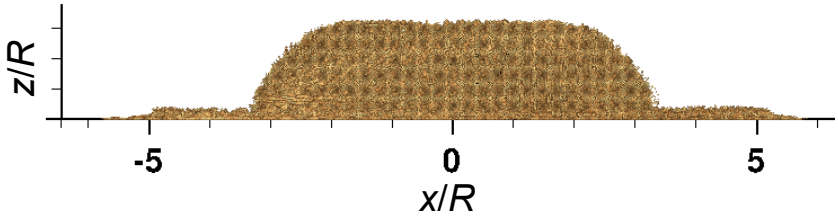

(b) Side view of the dust cloud

Figure 3.66: Instantaneous realization of a fully developed brownout cloud for a rotor hovering in-ground-effect at $z/R = 1$, showing: (a) an isometric view, and (b) a side view.

ond layer are mobilized, and a second wave of particles is formed in the dust cloud. Figures 3.64(d) and 3.64(e) show more particles being entrained into the cloud, and the cloud grows radially outwards as well as vertically upwards. Notice also from Figs. 3.64(e) and 3.64(f) that some particles are reingested through the rotor disk, and can further bombard the bed and eject more particles. Eventually, a fairly symmetric dome shaped brownout cloud is formed, which is a characteristic of brownout conditions. Instantaneous realizations of both a three-dimensional view and a side view of the final brownout cloud are shown in Figs. 3.66(a) and 3.66(b), respectively.

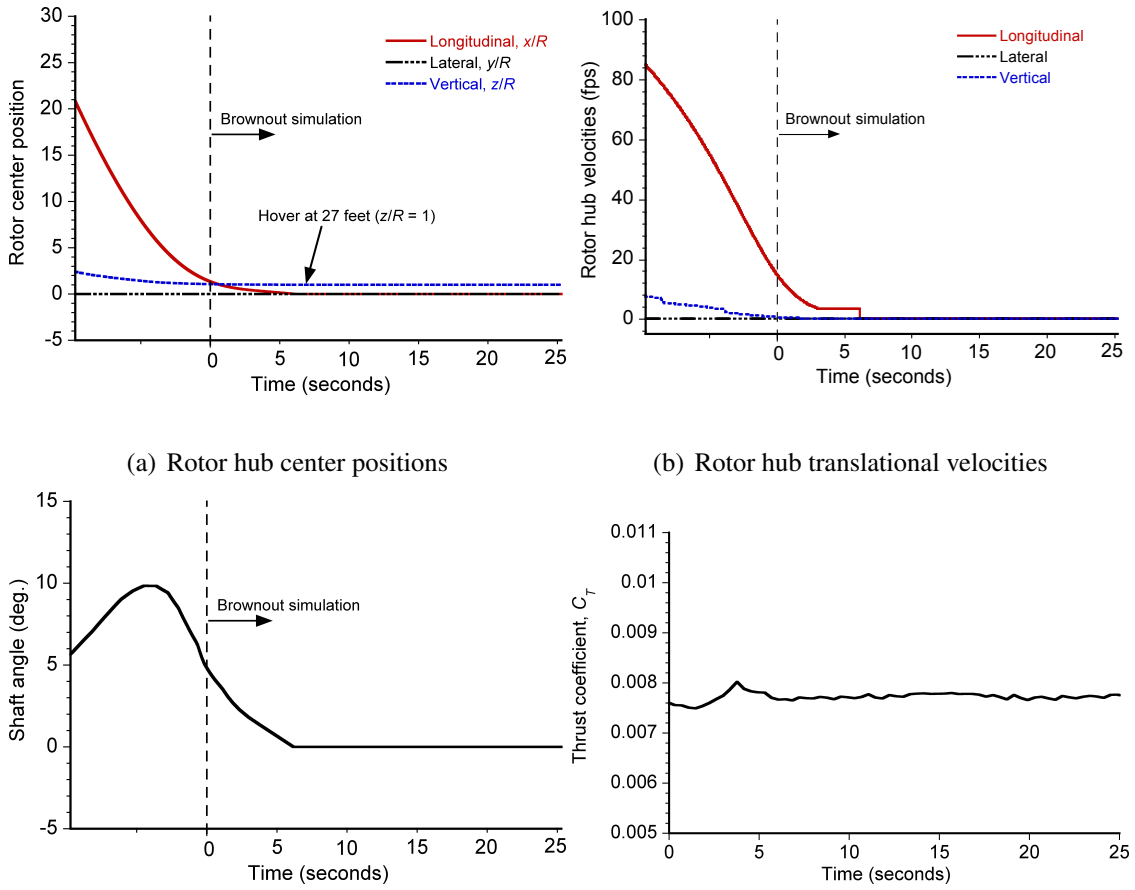

(a) Rotor hub center positions

(b) Rotor hub translational velocities

(c) Rotor shaft tilt angles

(d) Rotor thrust

Figure 3.67: Approach profile of the landing approach: (a) rotor hub center positions, (b) rotor hub translational velocities, (c) shaft tilt angles, and (d) rotor thrust.

3.3.3 Analysis of Dust Clouds Formed During a Landing Maneuver

The nominal landing profile used in the present work was developed from Moen et al. (Ref. 123), and is shown in Fig. 3.67. It travels along the longitudinal direction at a descent rate of 100 ft/min. The helicopter then executes a flare maneuver and decelerates into hover at a height of one rotor radius above the ground. The flow field solution was conducted for 45 s (or about 200 rotor revolutions) although the dust cloud simulation was performed only for the last 33 s. In the following results, time is referenced to the

start of the simulation, as shown in Fig. 3.67.

The sediment bed consisted of 27 layers of particle clusters that were evenly distributed from $-7R$ to $9R$ longitudinally and from $-7.5R$ to $7R$ laterally. In each layer, 4×10^4 particle clusters were eligible for pickup, giving a total of 1.08×10^6 uplift-eligible clusters or 1.08×10^8 particles. Again, additional particles were entrained into the solution as a consequence of evolving bombardment ejections.

3.3.3.1 Details of Rotor Flow and Particle Dynamics

A detailed analysis of the development of the brownout dust cloud during the landing maneuver was conducted by examining the rotor wake geometries, velocity fields, and the convection of the sediment particles. Instantaneous realizations of the wake geometry at different times are shown in Figs. 3.68, 3.69 and 3.70. The positions of the sediment particles in the dust cloud are shown in Figs. 3.71, 3.72 and 3.73; only the particles initially lying between $y/R = -0.1$ and 0.1 are shown for clarity. Also shown in these figures are the contours of vertical velocity along the longitudinal plane passing through the rotor disk.

Between the times t = 0 and 4.4 s, the rotor is decelerating and transitioning from descending to hovering flight; it is descending with an initial descent rate of 1.7 ft/s (100 ft/min) with a backward shaft tilt angle of 6°. As the helicopter approaches the ground plane, the wake restructures and starts to impinge on the sediment bed, as shown in Fig. 3.68(a). This behavior results in the bundling of vortex filaments that creates regions of high velocity near the bed, and forms a ground vortex below the leading edge

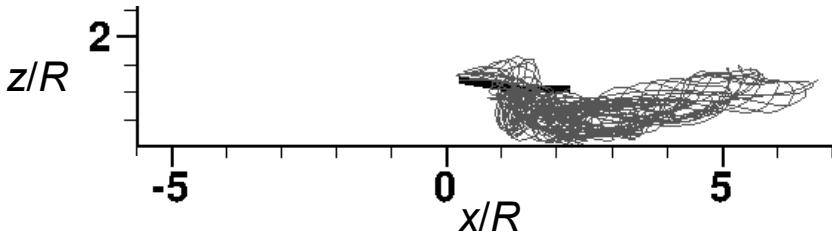

(a) t = 0.3 s

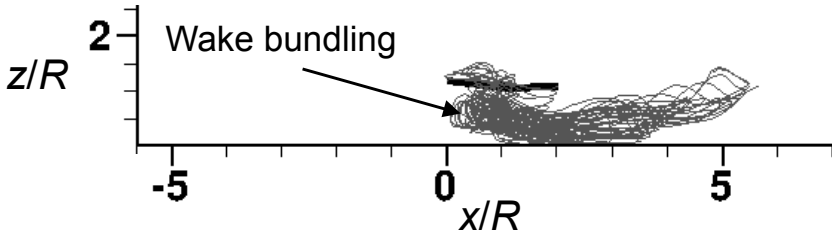

(b) t = 0.76 s

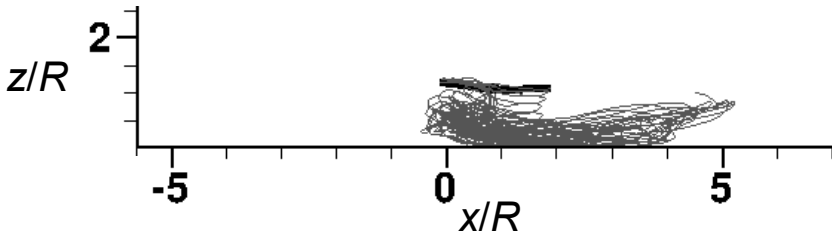

(c) t = 1.0 s

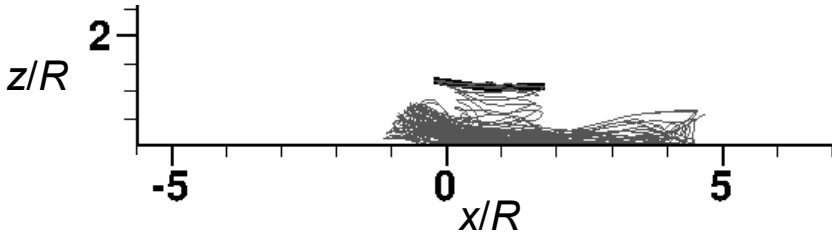

(d) t = 1.5 s

Figure 3.68: Predicted wake geometries during the landing maneuver at times t = 0.3, 0.76, 1.0 and 1.5 s.

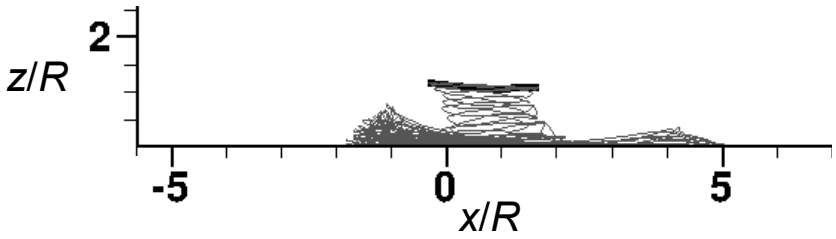

(a) t = 1.9 s

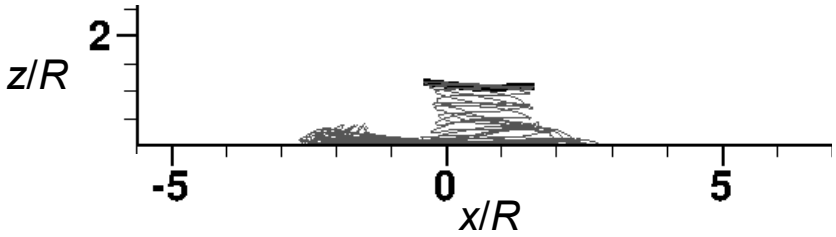

(b) t = 2.2 s

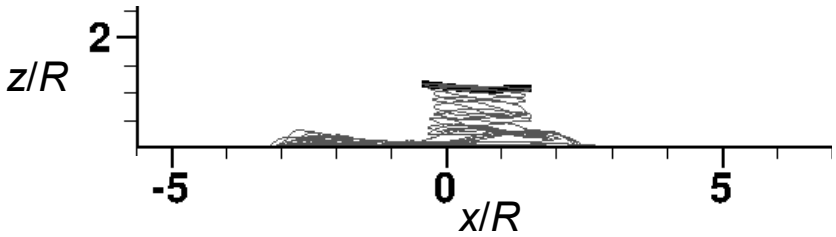

(c) t = 2.4 s

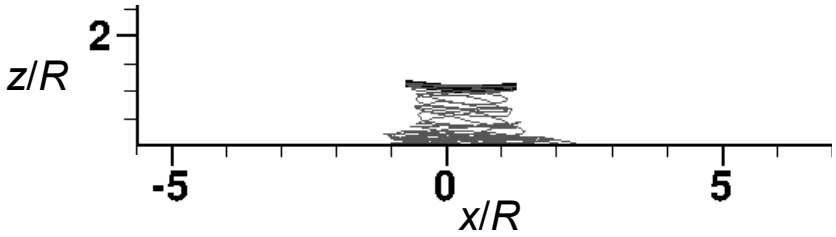

(d) t = 4.4 s

Figure 3.69: Predicted wake geometries during the landing maneuver at times t = 1.9, 2.2, 2.4 and 4.4 s.

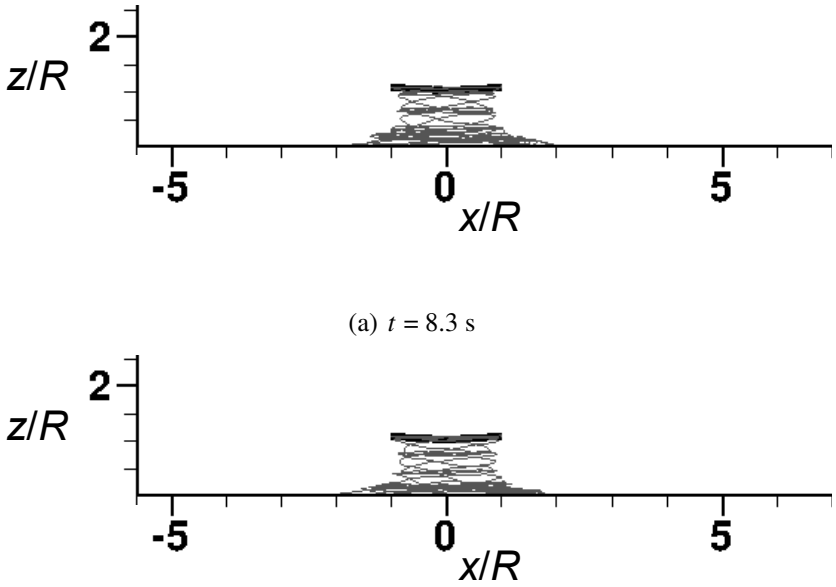

(a) t = 8.3 s

(b) t = 26 s

Figure 3.70: Predicted wake geometries during the landing maneuver at times t = 8.3 and 26 s.

of the rotor disk; see Fig. 3.71(a). The threshold conditions for particle mobilization are mostly satisfied in all of these regions.

With the further deceleration of the helicopter, the bundled wake below the rotor disk starts to expand toward the leading edge of the disk; see Fig. 3.68(b). The ground vortex also starts to move upstream toward the front of the rotor disk, and interacts with the tip vortices trailed by the rotor blades. This interaction results in the merging of vortices into a powerful "super-vortex" that contains the net circulation of all the vortex filaments that comprise it, as shown in Figs. 3.71(b) and 3.71(c). Notice that the formation of the super-vortex correlates to the so-called "recirculation" regime observed by Curtiss et al. (Ref. 13) and Nathan & Green (Ref. 21) at low advance ratios.

The formation of the super-vortex also results in a flow detachment point on the bed

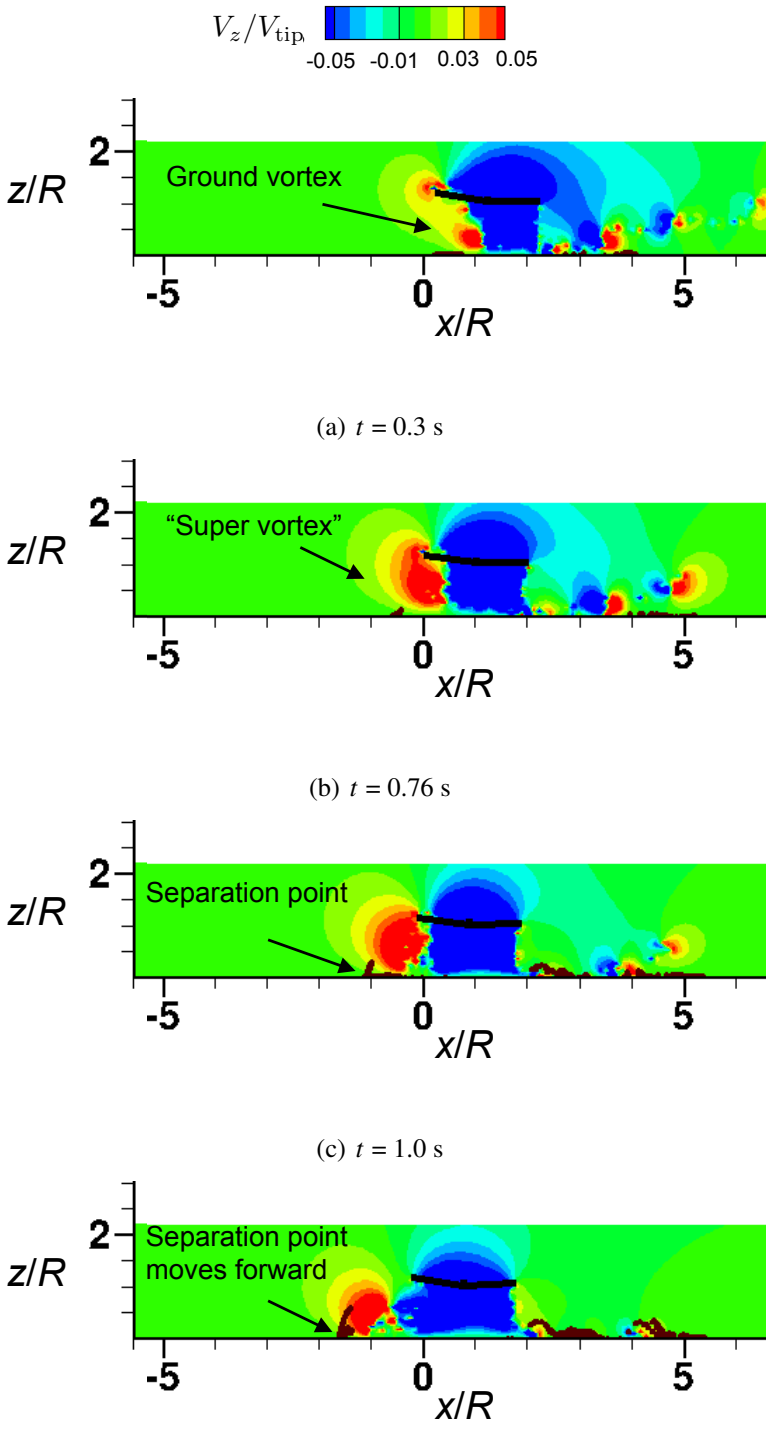

Figure 3.71: Development of the dust cloud during the landing approach at times t = 0.3, 0.76, 1.0, and 1.5 s. (Note: Only the particles initially positioned between $y/R = -0.1$ and 0.1 are shown for clarity).

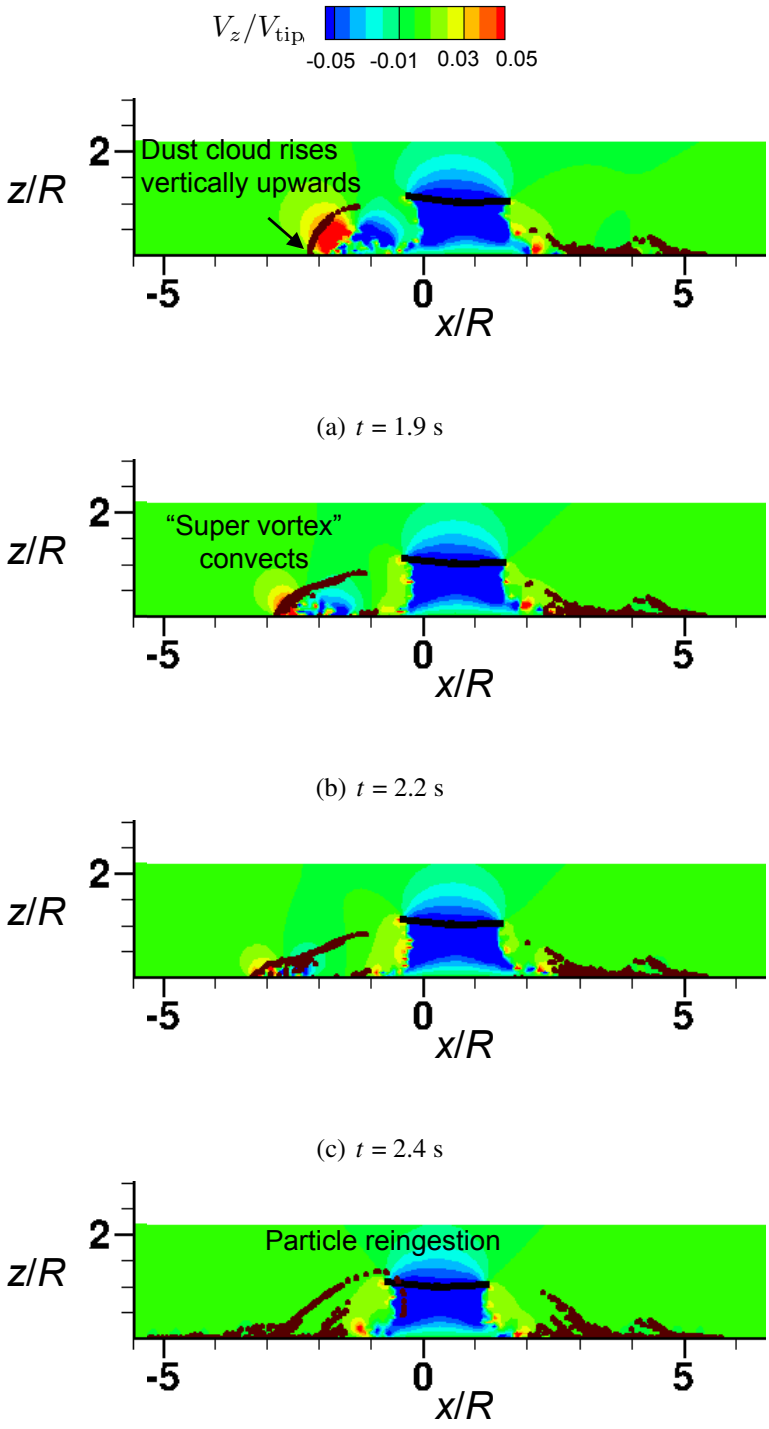

Figure 3.72: Development of the dust cloud during the landing approach at times $t = 1.9$, 2.2, 2.4, and 4.4 s. (Note: Only the particles initially positioned between $y/R = -0.1$ and 0.1 are shown for clarity).

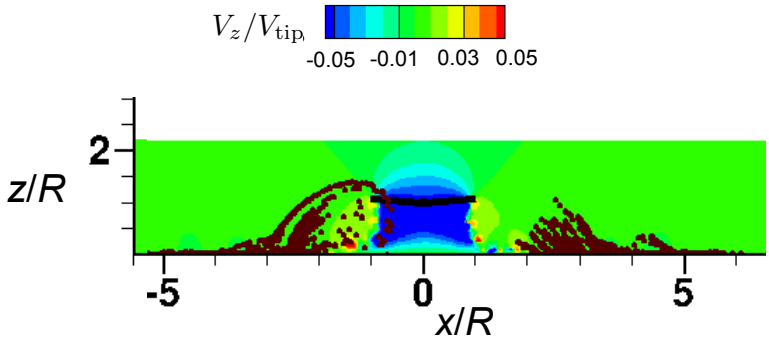

(a) t = 8.3 s

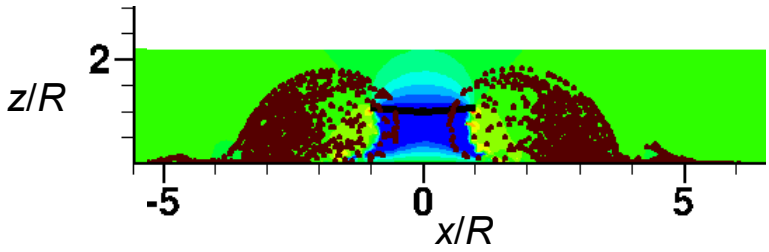

(b) t = 26 s

Figure 3.73: Development of the dust cloud during the landing approach at times t = 8.3 and 26 s.

(Note: Only the particles initially positioned between $y/R = -0.1$ and 0.1 are shown for clarity.)

ahead of the front of the rotor disk, as shown in Figs. 3.71(c) and 3.71(d), which causes the particles to lift more vertically upwards from the bed. This phenomenon was also observed by Nathan & Green (Ref. 21). This upward movement of the particles forms a wave crest like structure that defines the forward boundary of the dust cloud. These structures, i.e., the bundled wake, the super-vortex, the detachment point, and the frontal boundary of the dust cloud, all move forward with the forward motion of the helicopter; see Figs. 3.71(c), 3.71(d) and 3.72(a).

With the further deceleration of the helicopter, the wake bundle then settles toward the ground (see Figs. 3.69(b) to 3.70(b)), and the individual vortices forming the super-vortex undergo diffusion that also diffuses the super-vortex, which occurs at the same rate as that of the individual vortices; see Figs. 3.72(b) to 3.72(d). Notice the FVM does not include any representation of the viscous effects that might be associated with the bundling and amalgamation of the individual vortices. The frontal boundary of the dust cloud grows faster both radially outwards as well as vertically upwards. The dust particles then become reingested into the front of the rotor disk, as shown in Fig. 3.72(d).

At $t = 6$ s, the helicopter begins to reach the hover state with the rotor disk at $z/R = 1$ above the ground. The dust cloud now starts to develop at the back of the rotor disk as well, as shown in Fig. 3.73(a). Eventually, the dust cloud grows and becomes more symmetric as the helicopter continues to hover; see Fig. 3.73(b).

3.3.3.2 Development of the Three-Dimensional Dust Cloud

In the second set of results, as shown by Figs. 3.74, 3.75 and 3.76, instantaneous realizations of the three-dimensional dust cloud during the landing maneuver are shown. Each figure is comprised of four sub-figures; the top left figure shows contour maps of the total flow velocity at the sediment bed, while the bottom left figure shows the total velocity field along the longitudinal plane passing through the rotor disk. The top right figure shows an isometric-view of the instantaneous dust cloud (with the wake geometry), with the bottom right figure showing a side-view of the brownout cloud (along with the corresponding wake geometry).

Figures 3.74(a) and 3.74(b) show the development of the cloud at t = 1 and 1.5 s, respectively, when the wake began to directly impinge on the bed and induces locally high flow velocities. The signature resulting from the vortex impingement on the ground can be correlated in Fig. 3.74(a) to the regions of particle entrainment. Between t = 1 and 2.3 s, the wake has expanded ahead of the rotor disk, and an expansive velocity field was seen to be induced in these regions, as shown in Figs. 3.74(b) and 3.75(a). The bundling of individual blade tip vortices and the formation of the super-vortex manifests as a horse-shoe shaped around the rotor disk. Uplifted particles in these regions become trapped in the strong upwash and downwash regions, and subsequently impact the bed resulting in a rapid increase in the suspended sediment by means of bombardment ejections (see later). The subsequent convection of the super-vortex moves the particles radially away from the rotor, and they start to form a toroidal shaped cloud.

At time t = 2.3 s, as shown in Fig. 3.75(a), the wake expands radially ahead of the

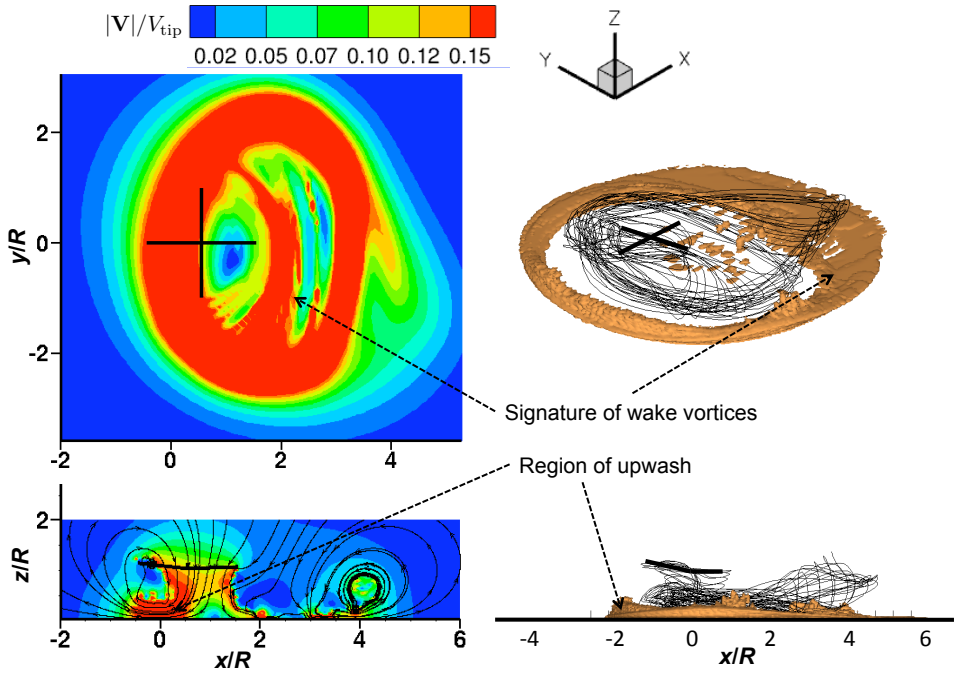

(a) $t = 1$ s

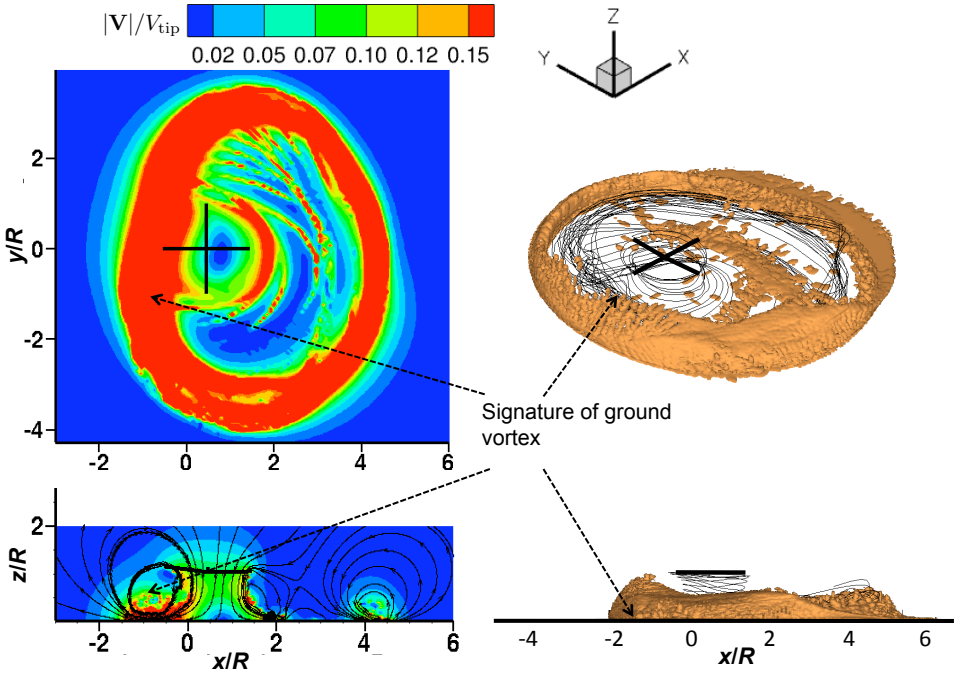

(b) $t = 1.5$ s

Figure 3.74: Development of the dust cloud during the landing approach at times $t = 1$ and 1.5 s.

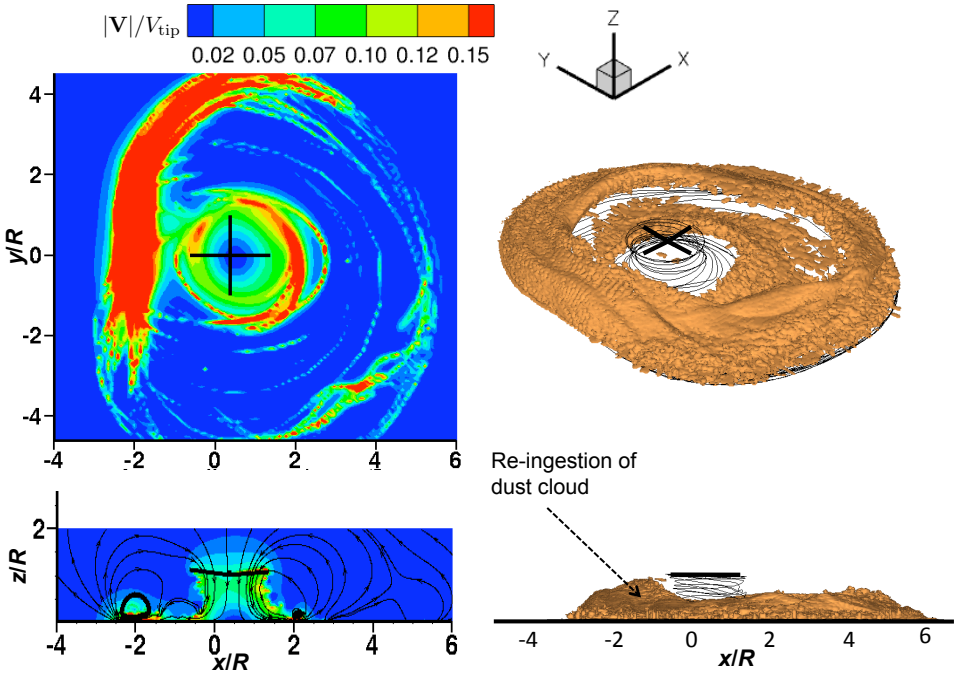

(a) $t = 2.3$ s

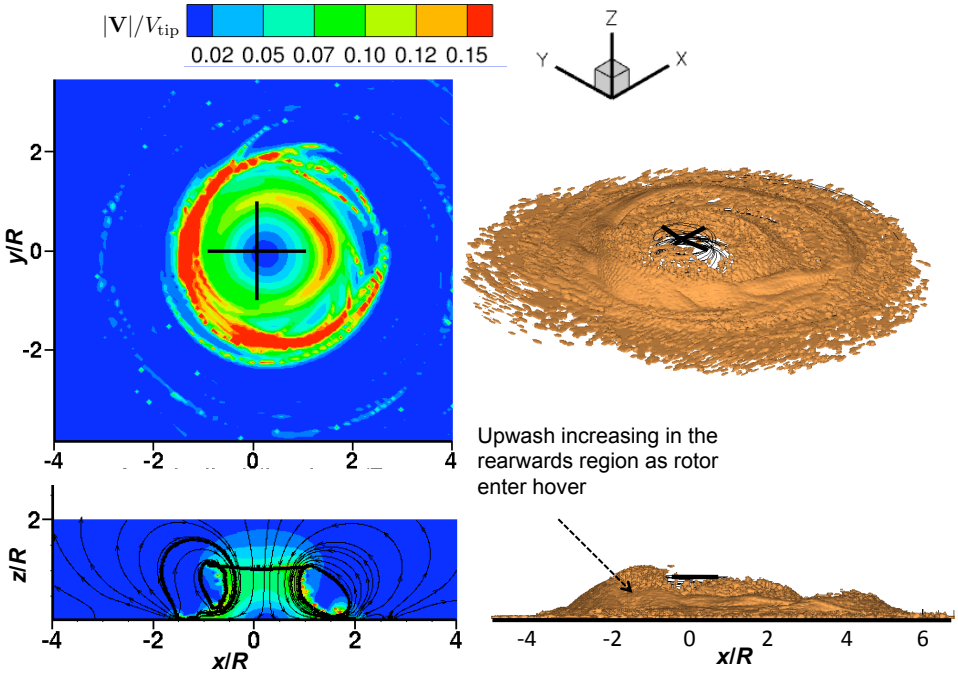

(b) $t = 6$ s

Figure 3.75: Development of the dust cloud during the landing approach at times $t = 2.3$ and 6 s.

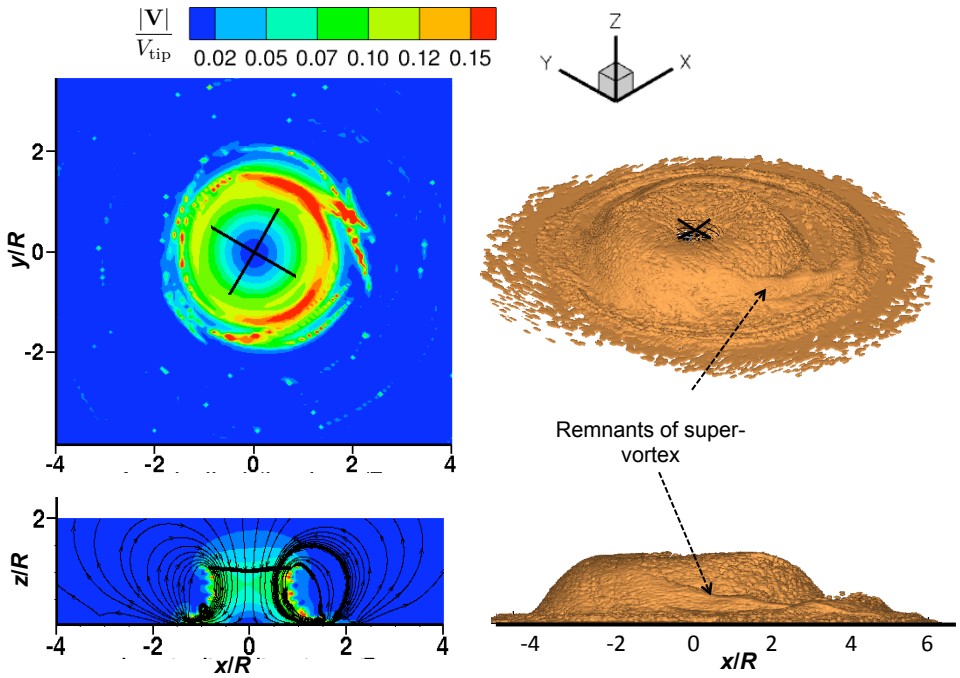

(a) t = 17 s

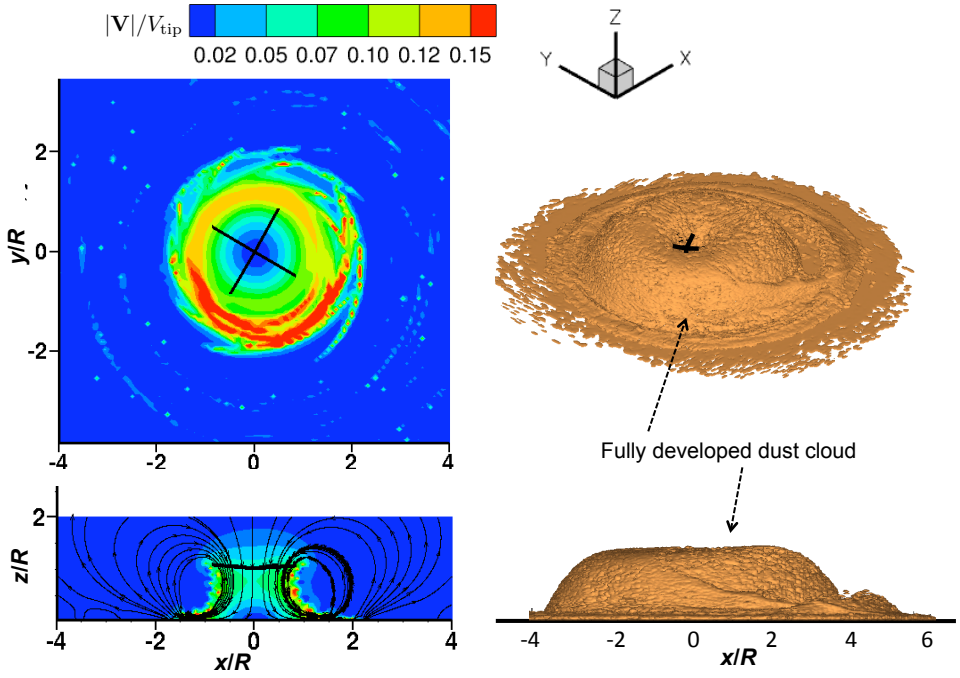

(b) t = 26 s

Figure 3.76: Development of the dust cloud during the landing approach at times t = 17 and 26 s.

disk as the rotor decelerates to enter into hovering flight at a fixed height off the ground. Because of the radial expansion of wake along the ground, the regions of high velocity shift radially away from the rotor, as does the development of the dust cloud. This cloud also shows the residual signature of the diffusing horseshoe vortex. The signature of the individual tip vortices can be clearly seen in the velocity field at the ground. Significant particle bombardment also takes place at this time step, especially toward the front starboard side of the rotor disk. It was noticed that the dust cloud also develops quicker in this region as dust begins to accumulate through the process of bombardments.

A better understanding of the bombardment process can be determined by plotting the locations of just those particles separately, as shown in Fig. 3.77. The contour map shows the vertical component of flow velocity at the sediment bed, and the sediment particles shown with red dots are the particles that are undergoing bombardment at this time step. Clearly, there is a direct correlation between the regions of bombardment and the regions where the wake vortices impinge on the ground.

Figure 3.75(b) shows an instantaneous realization of the dust cloud and the velocity fields at t = 6 s; the rotor now has very small forward velocity and is essentially operating in hover. In this case, there was clear evidence of the dust being reingested at the front of the rotor disk. The flow field also becomes somewhat more axisymmetric, and the dust cloud rises vertically upwards over regions toward the rear of the disk as well. As the cloud grows in size at the front of the helicopter, the dust encroaches over regions that are closer to the rotor.

Figures 3.76(a) and 3.76(b) show the results for the dust cloud at $t = 17$ and 26 s, respectively. By this point, the cloud has become more developed, and is now expand-

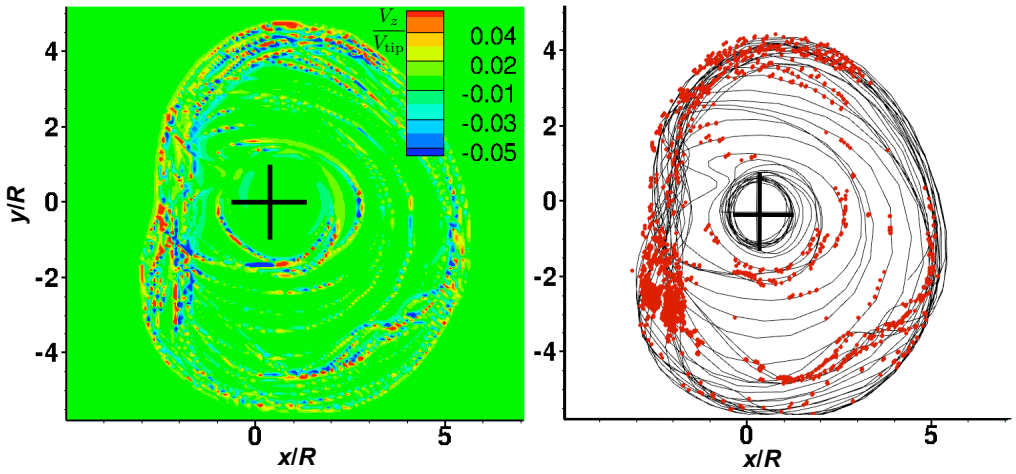

Figure 3.77: Particles uplifted through the process of bombardment (shown by red dots) at time t = 3 s can be correlated to the vertical component of velocity induced at the ground by the wake vortices.

ing into a characteristic dome-shaped cloud. However, the signature associated with the remnants of the horseshoe vortex can still be observed, as shown in Figs. 3.76(a) and 3.76(b).

3.3.3.3 Particle Quantity Analysis

Time-histories of the quantity of particles that were entrained by direct aerodynamic entrainment (i.e., through the action of shear and pressure forces) and bombardment ejections are compared in Fig. 3.78. Initially, particles stationary on the bed were mobilized through the action of shear and pressure forces. Some of these particles impinged on the bed in the regions of high velocities created by the formation of the ground vortex near the bed, and ejected further more particles through the mechanism of bombardment ejections, as shown in Fig. 3.78. The ejection of particles by bombardments decreased as the rotor

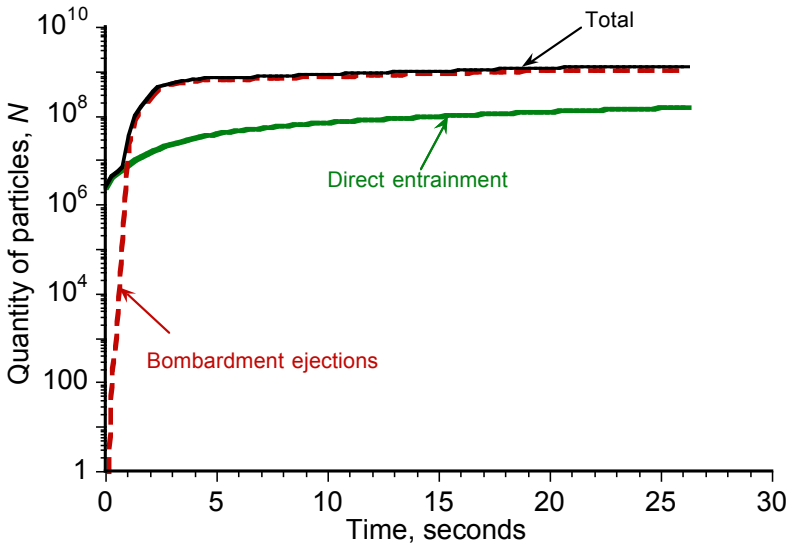

Figure 3.78: Time-history of the quantity of particles entrained during the landing maneuver through friction velocity and bombardment mechanisms, as well as the total number of particles in the flow field.

entered into hover, however, the quantity of particles in the dust cloud still continued to increase slowly by means of the direct entrainment.

3.3.4 Analysis of Dust Clouds Formed During the Takeoff Maneuver

A representative maximum performance takeoff maneuver was simulated, the flight profile being shown in Fig. 3.79. This maneuver is often utilized when tall obstacles obstruct a portion of the flight path or in instances when the pilot recognizes the potential for visual obscuration that may compromise the ability to maintain safe separation from obstacles. In this representative maneuver, the helicopter sits "light on the skids" for about 3 s, until the pilot pulls up on the collective pitch to 24° in about 4 s such that most of the available engine power is called upon to climb out of ground effect. Once the helicopter

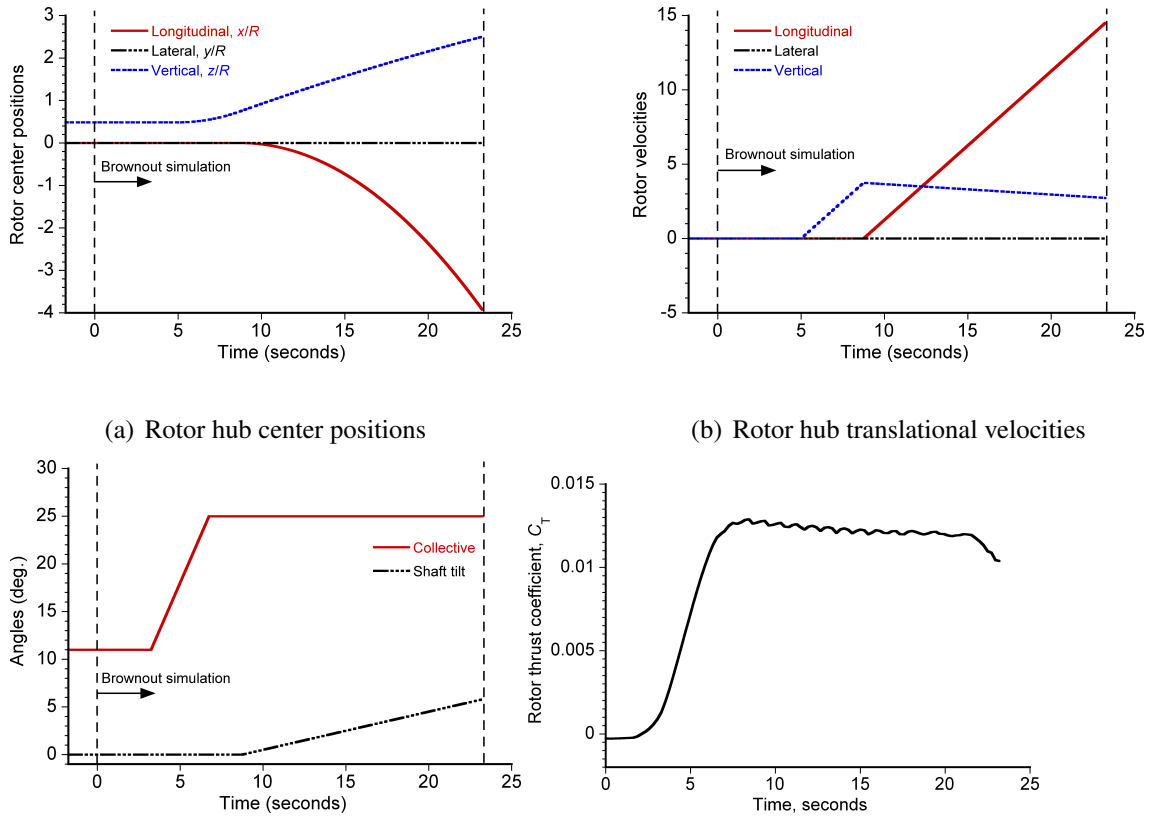

(a) Rotor hub center positions

(b) Rotor hub translational velocities

(c) Rotor shaft angles

(d) Rotor thrust

Figure 3.79: Maximum performance takeoff profile showing: (a) rotor hub center positions, (b) rotor hub translational velocities, (c) shaft tilt angles, and (d) rotor thrust.

is out of the obstacle zone, the pilot tilts helicopter nose-down and moves forward, in the present case with an acceleration of about 1 fts^{-2}. The total duration of this simulated maneuver was about 23 s.

The sediment bed used for this simulation in this case ranged from $-8R$ to $7R$ longitudinally and $-8R$ to $8R$ laterally. A total of 25 layers of particles was assumed with 4×10^4 particle clusters, giving a total of 1×10^6 uplift-eligible particle clusters and a total of 1×10^8 particles. Again, this initial number of particles did not include the quantity of particles that were ultimately entrained into the flow by means of bombardment ejections.

3.3.4.1 Details of Rotor Flow and Particle Dynamics

Instantaneous realizations of the rotor wake geometry at times t = 0.35, 3, 5.0, 8.2, 10.2, 13.9, 19.6 and 20 s are shown in Fig. 3.80. The corresponding positions of the particles are shown in Figs. 3.81 and 3.82, with the background contours being vertical velocity along the longitudinal axis passing through the rotor disk (i.e., $y/R = 0$).

At t = 0.35 s, the helicopter was on the ground with blades in flat pitch and the rotor thrust was very low; Fig. 3.80(a) shows the wake geometry and Fig. 3.81(a) shows the flow field along with the developing dust cloud at this time. Because of the low thrust condition, weaker vortices were trailed from the blade tips. However, the proximity of the rotor blades to the ground produced stretching of the tip vortices as they approached the ground plane, intensifying their vorticity and increasing the local flow velocities there. The tendency of the wake vortices to roll-up and bundle as they reached the ground also increased the groundwash velocity, which was enough to mobilize and entrain some par-

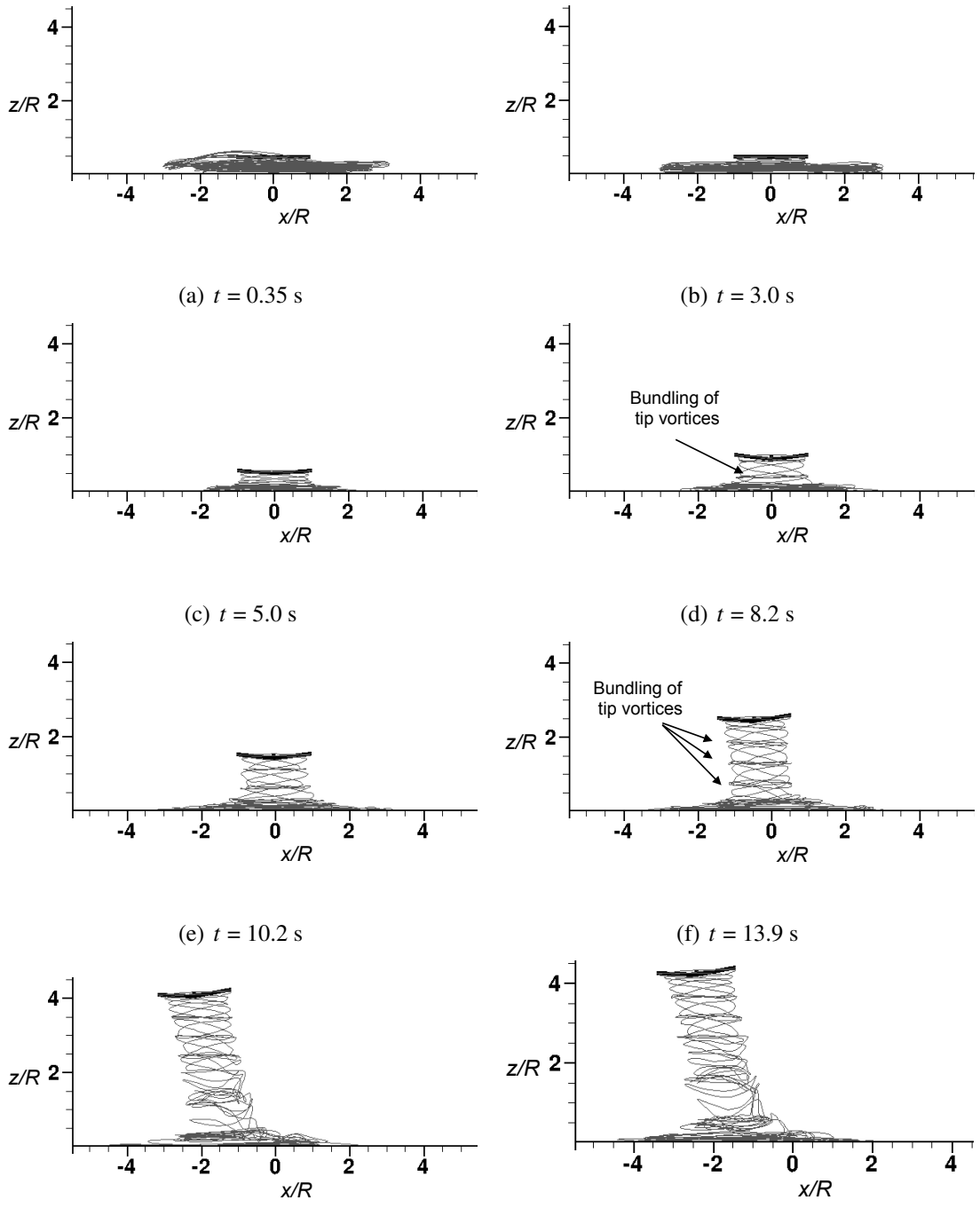

(a) t = 0.35 s

(b) t = 3.0 s

(c) t = 5.0 s

(d) t = 8.2 s

(e) t = 10.2 s

(f) t = 13.9 s

(g) t = 19.6 s

(h) t = 20 s

Figure 3.80: Predicted wake geometries during the takeoff maneuver at times t = 0.35, 3.0, 5.5, 8.2, 10.2, 13.9, 19.6, and 20 s.

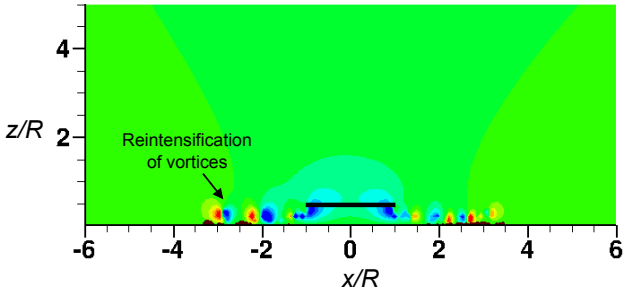

(a) $t = 0.35$ s

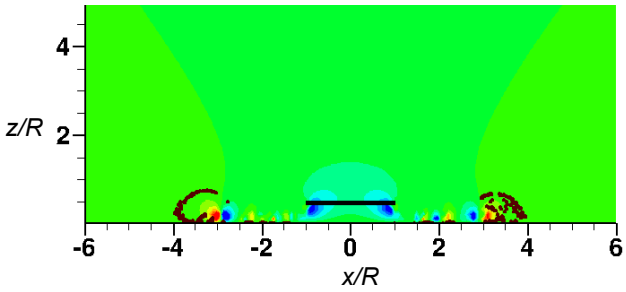

(b) $t = 3.0$ s

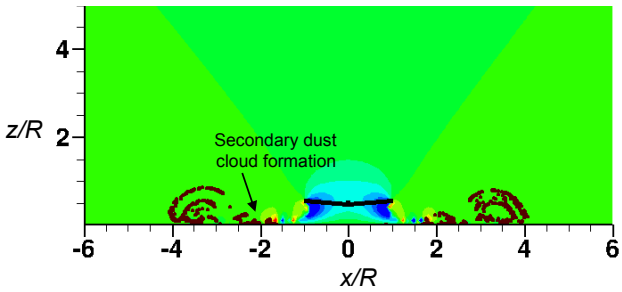

(c) $t = 5.0$ s

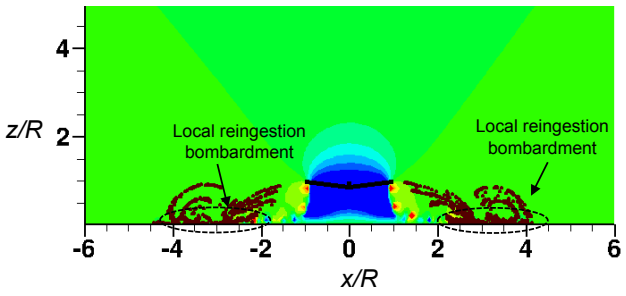

(d) $t = 8.2$ s

Figure 3.81: Development of the dust cloud during the takeoff maneuver at times $t = 0.35$, 3.0, 5.0 and 8.2 s. (Note: Only the particles initially positioned between $y/R = -0.1$ and 0.1 are shown.)

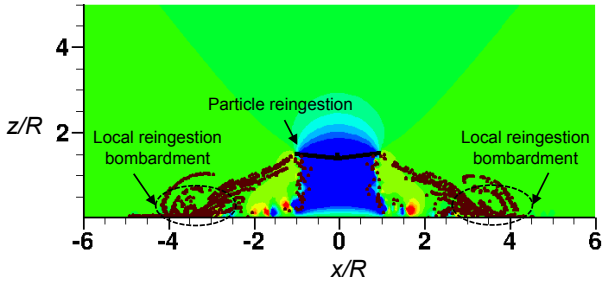

(a) t = 10.2 s

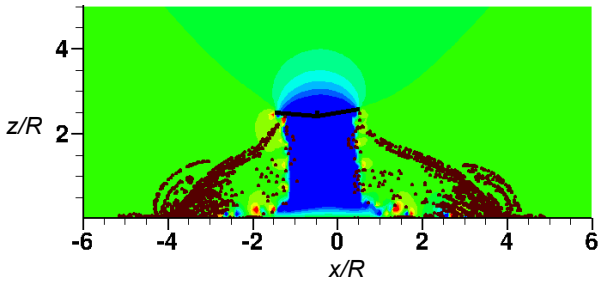

(b) t = 13.9 s

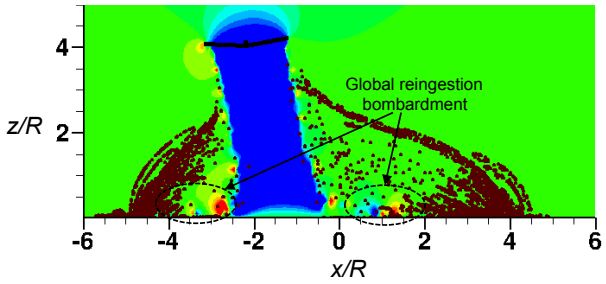

(c) t = 19.6 s

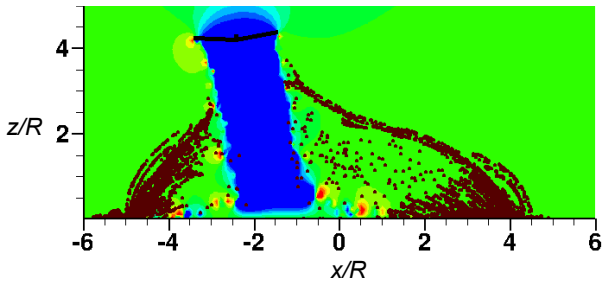

(d) t = 20.0 s

Figure 3.82: Development of the dust cloud during the takeoff maneuver at times t = 10.2, 13.9, 19.6 and 20.0 s. (Note: Only the particles initially positioned between $y/R = -0.1$ and 0.1 are shown.)

ticles. However, it was noticed that the velocity fields produced at this time step were just not intense enough to produce bombardment ejections.

At t = 3.0 s (see Figs. 3.80(b) and 3.81(b)), the collective pitch was raised and the rotor wake started to strengthen, which meant that a higher downwash was produced and the tip vortices had greater strengths. At this point, ejections of newer particles from bombardments were first observed.

At $t = 5$ s (see Fig. 3.80(c) and 3.81(c)), the thrust produced by the helicopter was high enough to lift it off the ground into a climb. The wake was now much stronger, with a powerful downwash flow and stronger tip vortices. Significant sediment uplift was produced both by direct entrainment and bombardment. Because the helicopter was in a climb at this time, the wake boundary was formed radially closer to the rotor disk; see Fig. 3.80(c). This behavior resulted in the entrainment of particles in regions closer to the rotor disk and to the formation of a stronger secondary cloud closer to the rotor; see Fig. 3.81(c).

At $t = 8.2$ s, the collective pitch was set to a maximum value of 24°. Changes in the collective pitch settings on the rotor blades result in wake restructuring and bundling of the tip vortices below the rotor disk; see Fig. 3.80(d). This bundling of the tip vortices was caused by the changes in the bound circulation at the rotor blades (because of the increasing collective pitch); as the collective pitch was increased, the strength of the tip vortices also increased. This effect resulted in a faster downward convection of the younger tip vortices. However, the vortices that were released at the lower thrust values still convected at lower velocities. This difference in the convection velocities resulted in the bundling of adjacent filaments, as shown in Fig. 3.80(d). A vortex ring type of

structure of higher vorticity was produced because of this tendency toward bundling, and was then convected towards the ground. This effect was also observed by Carpenter & Friedovich (Ref. 124) in experiments, and by Ananthan (Ref. 99) in free-vortex wake calculations. As this bundle of tip vortices convected to the ground, it produced regions of higher velocities, which resulted in the mobilization and entrainment of a larger number of particles. Figure 3.81(d) shows that at this point the dust cloud began to develop much faster in vertical extent.

At t = 10.2 and 13.9 s the helicopter was moving forward while still climbing upwards. The thrust produced was at a maximum (to provide the accelerating forces) at this time step and so too was the strength of the tip vortices; when they convected downward and impinged on the bed they generated regions of high velocity, as shown in Fig. 3.82(a). An even greater increase in the number of particles mobilized through bombardment ejections was observed. Notice from Fig. 3.82(b) that the dust particles had now started to become reingested into the rotor disk, and some of these particles had even reached the ground.

At t = 19.6 and 20 s (see Figs. 3.80(g), 3.80(h), 3.82(c) and 3.82(d)), the helicopter was moving slowly forward at an approximate advance ratio of 0.01. In this transitional flight condition (i.e., mostly axial to mostly forward flight), the process of vortex bundling was again found to increase sediment mobilization by both direct entrainment and bombardment ejections. The process of vortex bundling is again seen in Fig. 3.83. As the helicopter moved forward, the process of bundling continued and the regions of strong upwash and downwash were formed near the bed that resulted in many bombardment ejections.

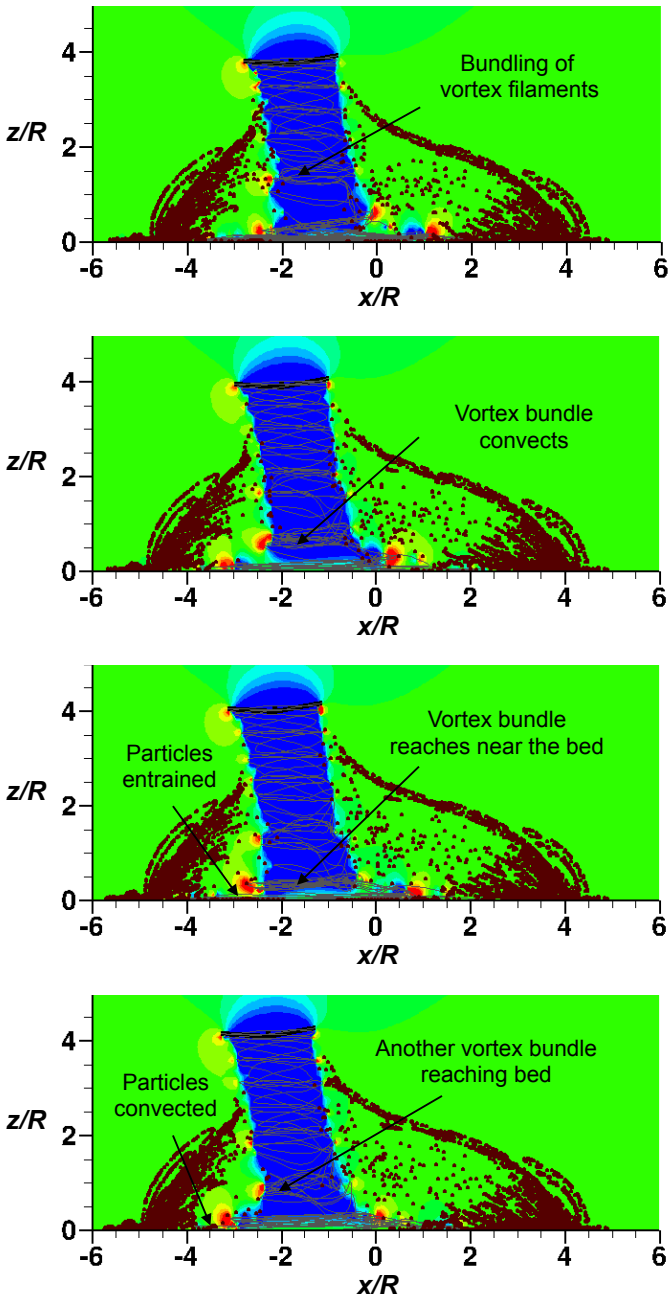

Figure 3.83: Effects of vortex bundling on particle entrainment from the bed between $t = 18.7$ and 20 s.

3.3.4.2 Development of the Three-Dimensional Dust Cloud

Instantaneous realizations of the dust clouds are shown in Figs. 3.84, 3.85 and 3.86 at times $t = 1$, 3, 5, 11, 17 and 21 s. Four sub-figures are used at each time showing: contour maps of the total velocity induced on the sediment bed (top left) and along the longitudinal plane passing through the rotor disk (bottom left), the isometric view of the dust cloud (top right), and the side view of the dust cloud (bottom right).

Figure 3.84(a) shows the brownout cloud at $t = 1$ s. The rotor thrust was very low at this time, however, the bundling and stretching of the vortices still resulted in sufficient velocities to mobilize sediment particles from the bed. The dust cloud had already started to develop and extended out to $r/R = 4$. Notice that the vertical convection of the sediment particles was greater at distances radially farther from the rotor than closer to it.

Figure 3.84(b) shows the dust cloud and induced velocity field at $t = 3$ s, when the dust cloud was still developing radially farther from the rotor disk. The dust cloud had now reached locations that were above the rotor disk, however, it was still radially away from the rotor.

At $t = 5$ s, the blade collective has increased to 18° and the rotor wake impinged on the bed radially closer to the rotor disk. The signature of wake impingement on the bed at $r/R = 2$ can be seen in Fig. 3.85(a) by the regions of high velocity and the formation of the secondary dust cloud, which can also be seen in the isometric view. At $t = 11$ s, the helicopter was climbing upwards, and also starting to move forward. The signatures of the bundling of tip vortices on the bed can be seen in Fig. 3.85(b). The dust cloud at

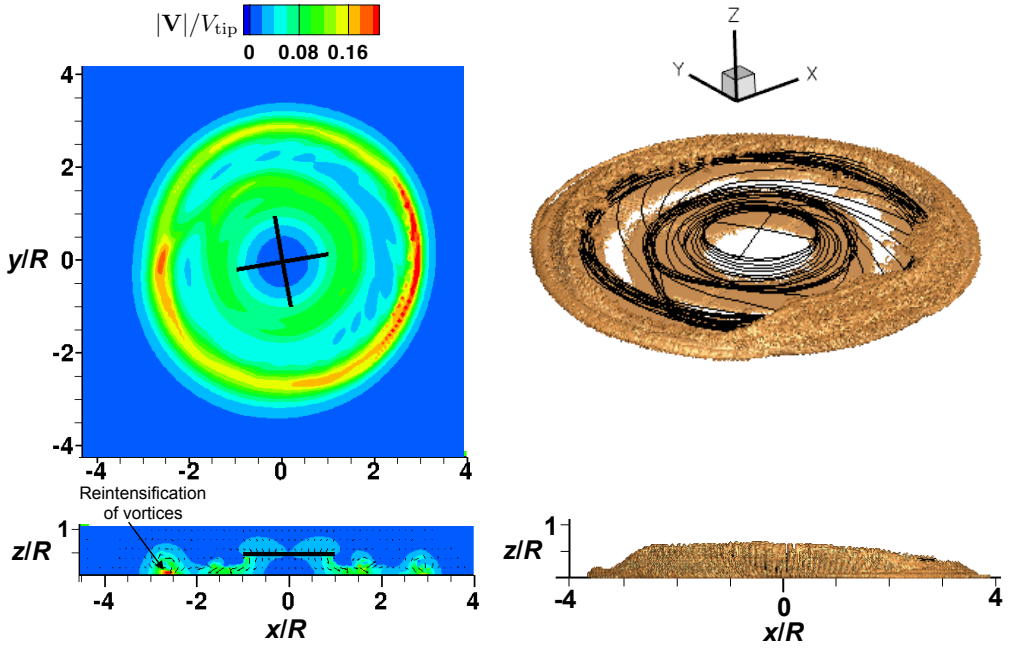

(a) At time, $t = 1$ second

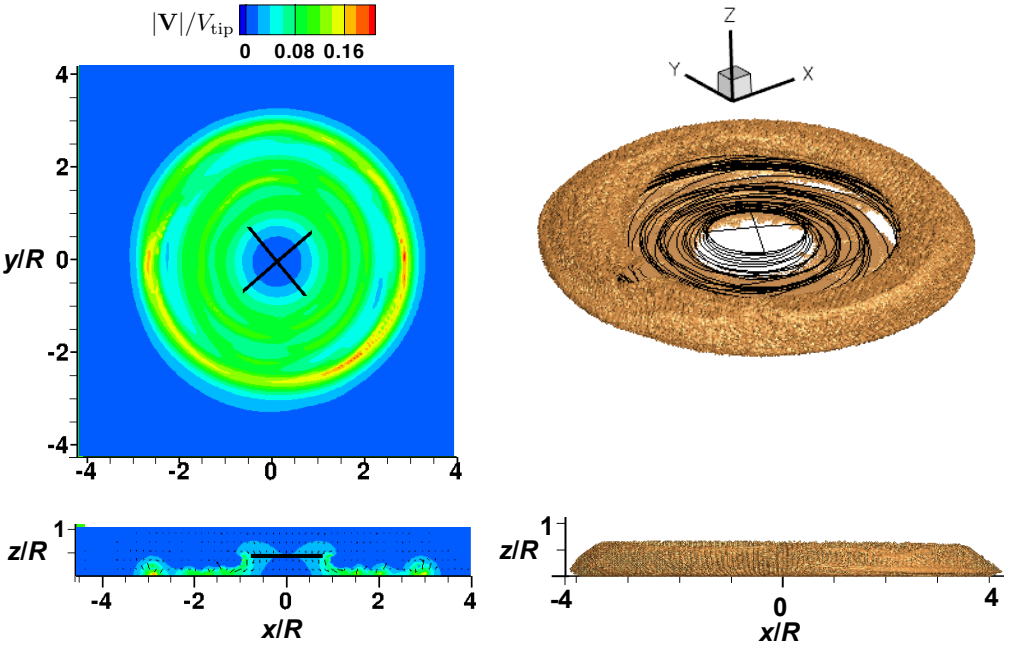

(b) At time, $t = 3$ s

Figure 3.84: Development of the brownout cloud during the takeoff maneuver at times $t = 1$ and 3 s.

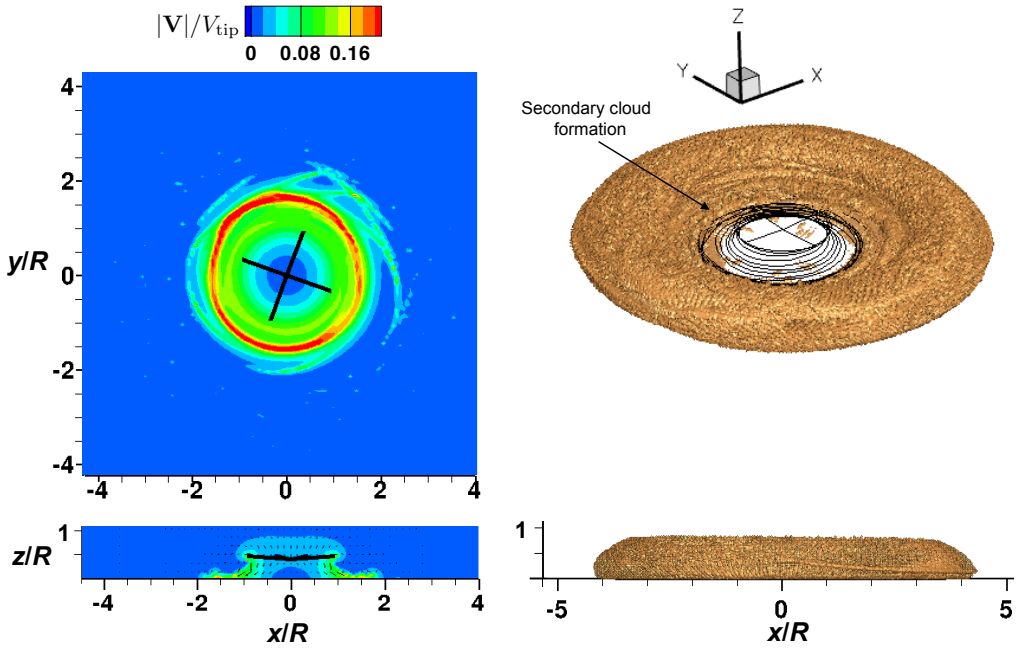

(a) At time, $t = 5$ second

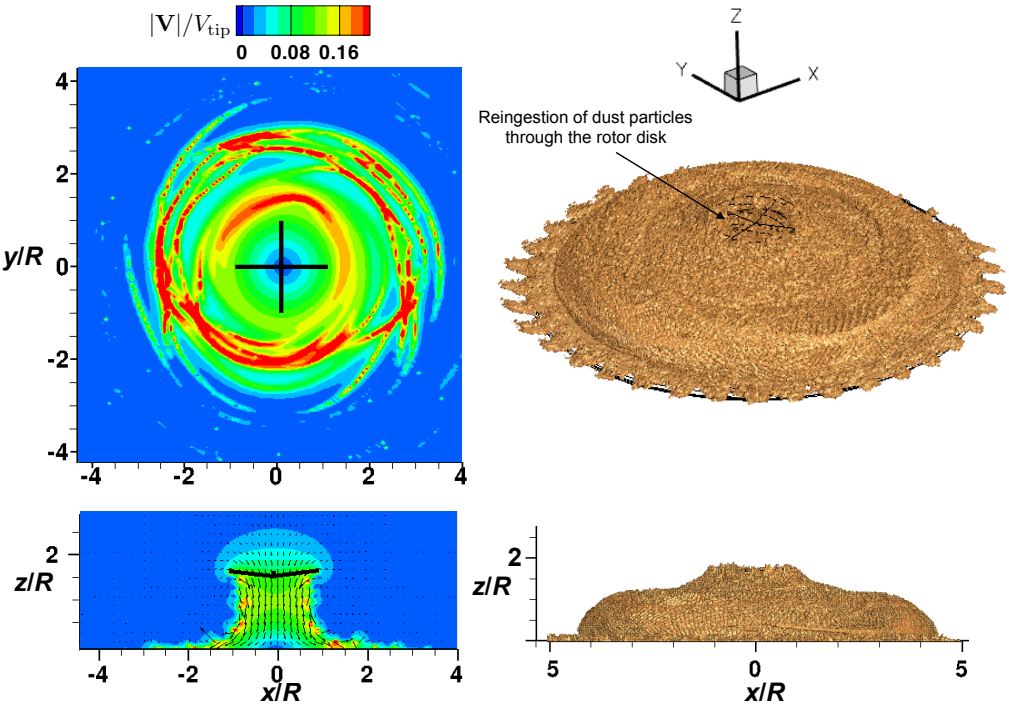

(b) At time, $t = 11$ s

Figure 3.85: Development of the brownout cloud during the takeoff maneuver at times $t = 5$ and 11 s.

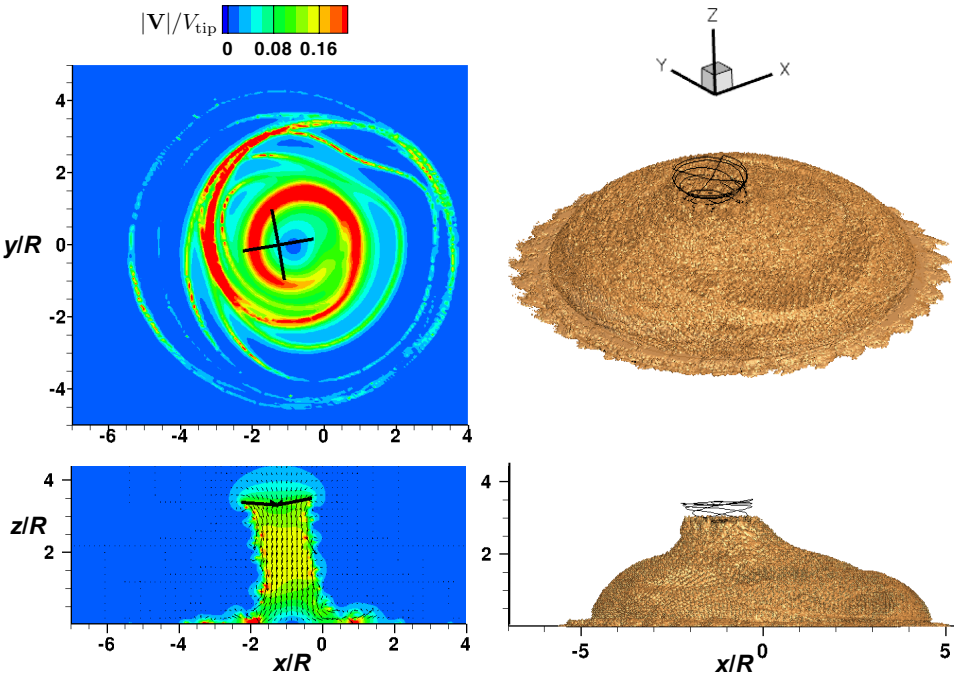

(a) At time, $t = 17$ second

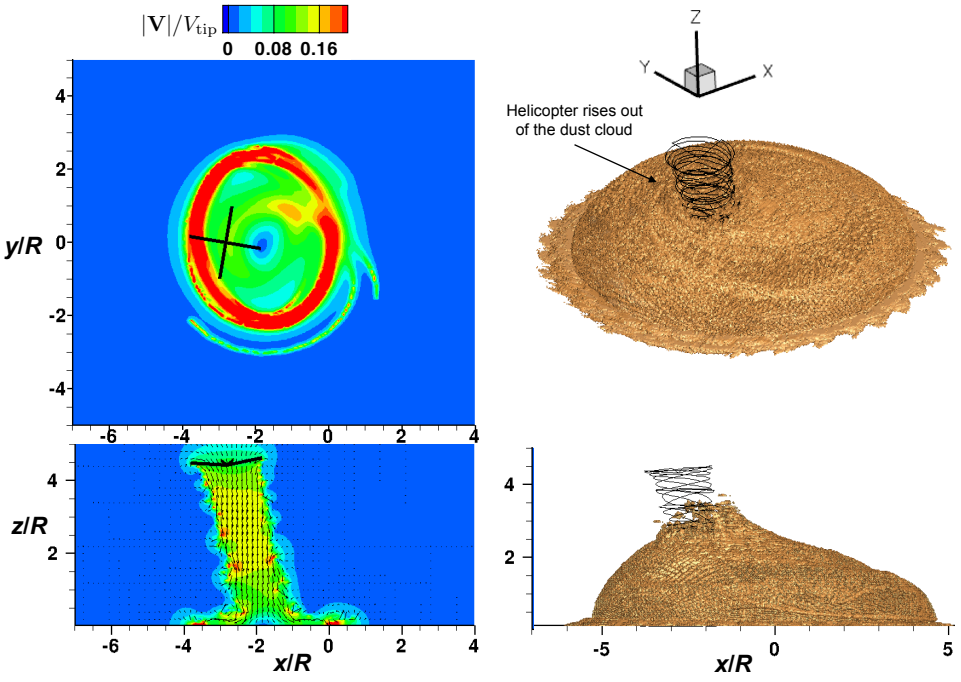

(b) At time, $t = 21$ s

Figure 3.86: Development of the brownout cloud during the takeoff maneuver at times $t = 17$ and 21 s.

this point has developed such that the rotor was completely immersed in it.

At t = 17 s, the helicopter was accelerating forwards, and the rotor plane was just out of the top of the developing dust cloud; see Fig. 3.86(a). However, the wake vortices continued to impinge on the sediment bed, resulting in the further mobilization of particles, mainly by bombardment mechanisms. Such ejections tend to occur until the rotor is a considerable distance away from the ground. The overall dust cloud then grows quickly in both volume and dimensions, as shown in Fig. 3.86(b), however, the climb velocity of the helicopter was high enough in this case to bring it out of the dust cloud as it was developing.

3.3.4.3 Particle Quantity Analysis

The time-histories of the total number of particles that were entrained by direct entrainment and by bombardment ejections are shown in Fig. 3.87. Notice that initially all of the particles were entrained by direct mechanisms. The process of bombardment ejections was only initiated as the collective pitch was raised above 11° at about t = 3 s, which resulted in the bundling of vortex filaments below the rotor disk, as shown previously in Fig. 3.80(d).

Between t = 3 and 11 s, the quantity of particles ejected through bombardment increased to $O(10^7)$. After t = 11 s, the helicopter started to transition from a mostly vertical climb to forward flight, while still climbing upwards. As shown in Fig. 3.83, the phenomenon of vortex bundling was observed at these times as well; see Fig. 3.83. As an outcome, the ejection of particles through bombardment continued, although at a lower

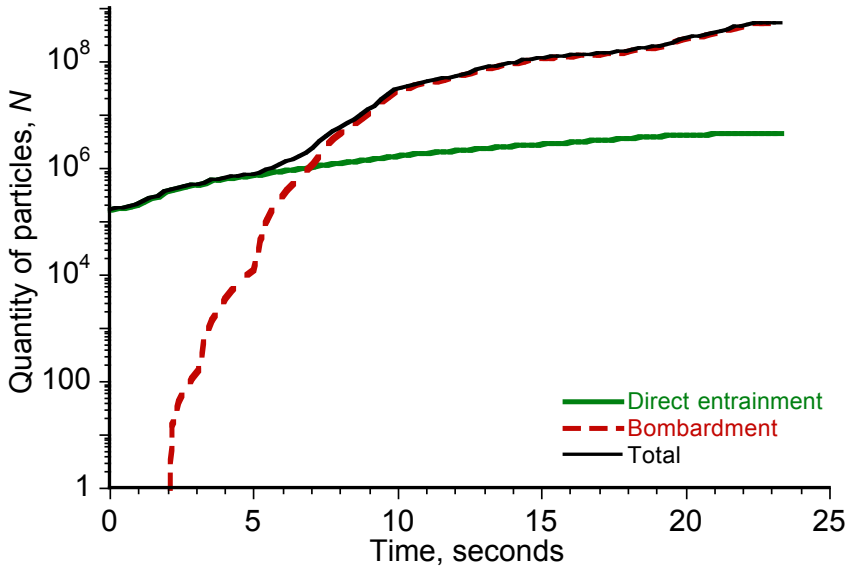

Figure 3.87: Time-history of the quantity of particles entrained during the takeoff maneuver through friction velocity and bombardment mechanisms, as well as the total quantity of particles entrained into the flow field.

rate. By the end of the simulation, the total quantity of particles in the brownout cloud that had originated from bombardment was $O(10^9)$, whereas only $O(10^6)$ particles were uplifted by direct entrainment.

3.4 Effects of More Diffused Tip Vortices on the Dust Clouds

This section describes the effects of artificially diffusing the rotor tip vortices on the development of the dust clouds. The results presented previously have shown that the tip vortices play a critical role in the brownout problem. As they approach the sediment bed, they create transient increases in the flow velocity that, in turn, generate locally large values of shear stress and pressure on the bed that mobilize the particles. The tip vortices can also produce more ejections of particles by means of bombardments. Therefore, more

rapidly diffusing the tip vortices may play a significant role in the process of brownout mitigation.

To this end, the single-phase rotor in ground effect experiments conducted by Milluzzo et al. (Ref. 20) showed that a slotted-tip blade can be effective for diffusing the vorticity contained in the tip vortices, and also in reducing the velocity fluctuations near the ground. Such effects are desirable from a brownout perspective. The results presented in this section examine the potential role of such a blade for the mitigation of brownout. The diffused tip vortices from the slotted-tip blades were modeled by more rapidly diffusing the core of the tip vortex. The different dust clouds that were generated are then analyzed in terms of the differences in the flow structures produced on the ground, the quantity of dust mobilized and uplifted, the overall rate of development of the dust clouds.

3.4.1 Slotted-Tip Blade Geometry

The slotted-tip blade was originally designed for reducing blade vortex interaction noise (Ref. 91). This blade tip comprises four internal slots that pass through the blade tip and connect the leading edge of the blade to its side edge. A schematic of the design is shown in Fig. 3.88. The slotted-tip design is a passive system that is designed to inject small-scale vorticity and turbulence into the otherwise laminar tip vortex core and radially diffuse the otherwise concentrated vorticity, as shown in Fig. 3.88. It has been shown by means of experimental studies (Ref. 91) that the slotted-tip is highly effective in diffusing the blade tip vortices with only a small penalty in terms of rotor power requirements.

The experiments performed by Milluzzo et al. (Ref. 20) confirmed that the creation

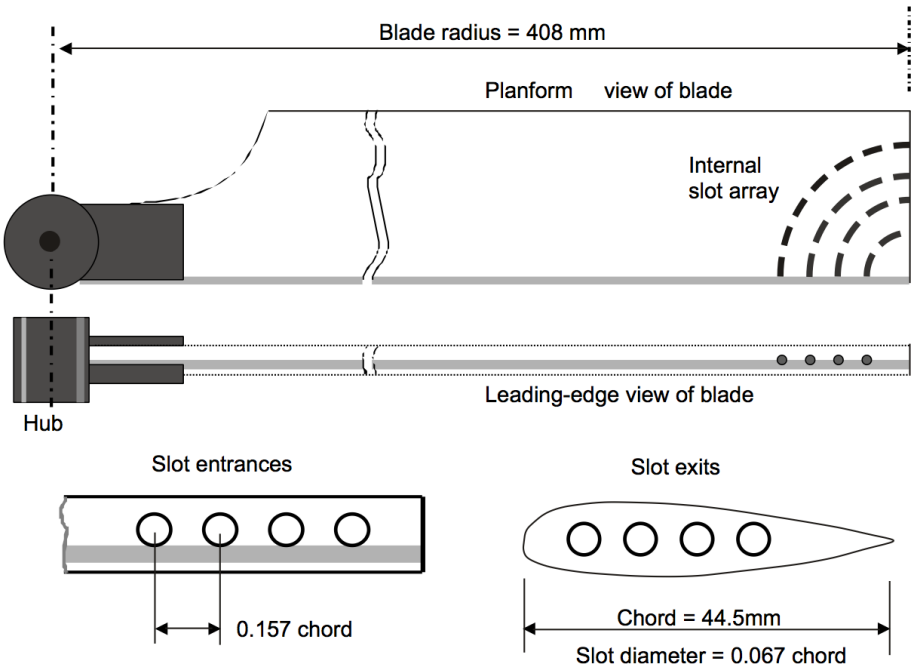

(a) Blade with the slotted tip

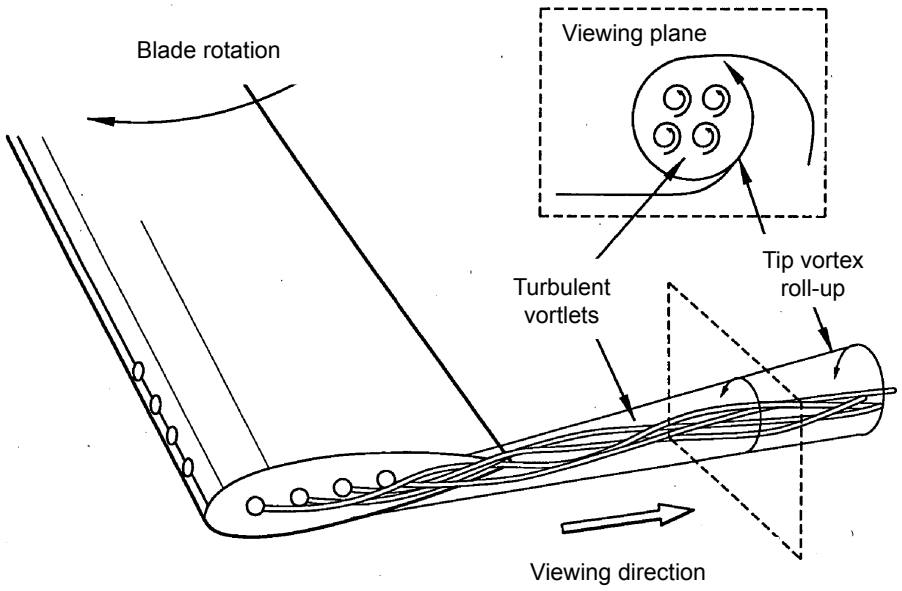

(b) Functionality of the slotted tip

Figure 3.88: Slotted tip blade geometry: (a) the four interior slots connecting the leading edge to the side edge of the blade, and (b) ejecting vortlets (small-scale vorticity and turbulence) into the tip vortex core.

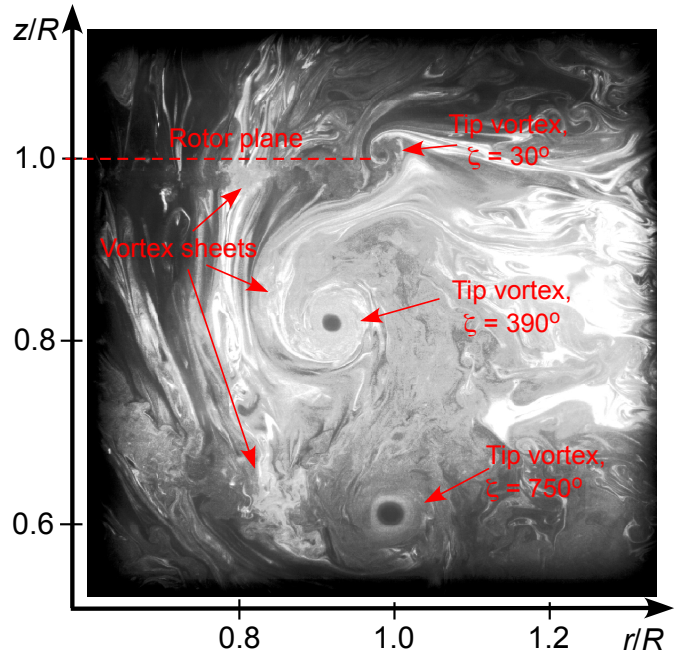

(a) Rectangular blade

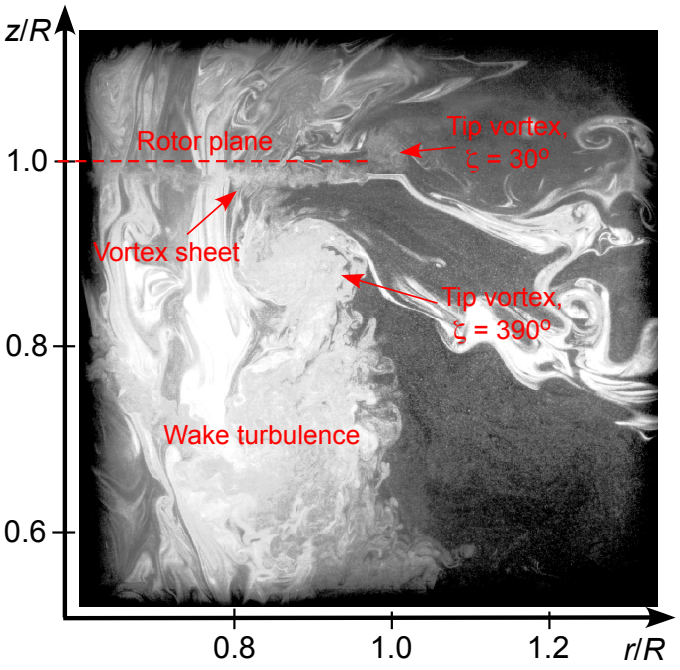

(b) Slotted-tip blade

Figure 3.89: Flow visualization image of tip vortices generated by: (a) rectangular, and (b) slotted-tip blades a wake age of 30°. (Source: Ref. 20).

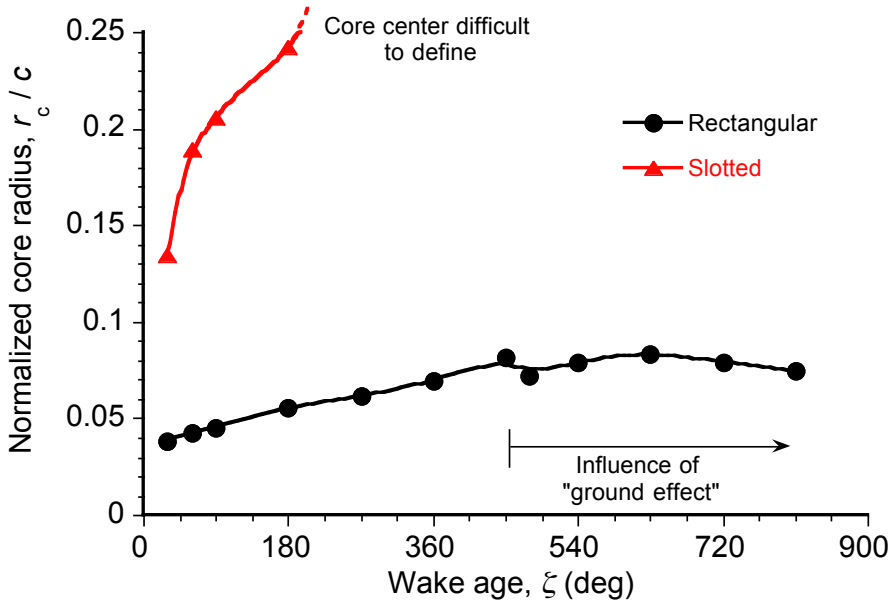

Figure 3.90: Tip vortex growth characteristics in terms of the core radius (normalized by blade chord). (Source: Ref. 20).

of turbulence in the cores of the tip vortices trailed from the slotted-tip resulted in a much higher radial diffusion of vorticity and less distinct vortex cores, even at relatively young wake ages (see Fig. 3.89). Substantially lower swirl velocities were also produced when compared to the vortices from the rectangular blade. The core radius obtained with this blade (as far as it could be measured) was also considerably larger than that for the rectangular blade; see Fig. 3.90. Measurements of the flow field near the ground (Ref. 20) revealed that the vortices trailed from the slotted-tip blade were also significantly diffused by the time they reached the ground. This outcome resulted in a much weaker upwash velocity field near the ground compared to that produced by the rectangular blade; see Fig. 3.91. The instantaneous velocity excursions in the region near the ground were also found to be less pronounced for the slotted-tip blade.

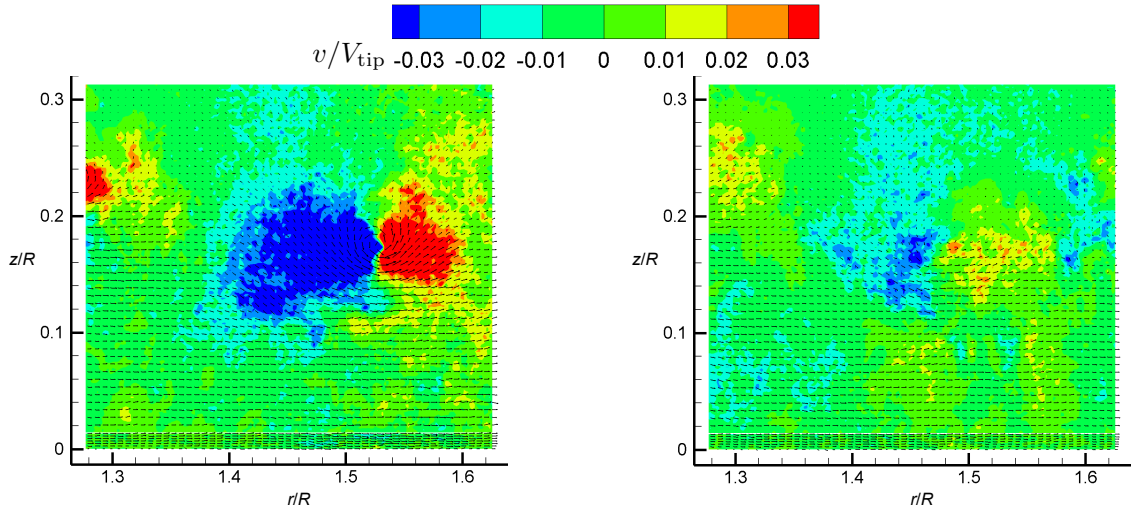

(a) Rectangular tip

(b) Slotted tip

Figure 3.91: PIV measurements of the rotor wake at the ground: (a) rectangular tip; (b) slotted tip. Background contours are based on the vertical component of instantaneous velocity normalized by blade tip speed V_{tip}. (Source: Ref. 20).

3.4.2 Modeling of Vortex Diffusion in the Free-Vortex Method

Because the FVM is an inviscid, potential flow model, the initial viscous properties and subsequent growth characteristics of the tip vortices cannot be explicitly modeled within this construct. However, with a priori knowledge of the core radius from experimental measurements, a semi-empirical model for the effects of the different tip shapes can be established.

As mentioned previously in Section 2.1.3.2, the FVM uses a vortex Reynolds number based model (Ref. 70) to account for the changes in vorticity resulting from diffusion, as well as from filament stretching near the ground (Refs. 69 and 110). This model can

be written as

$$r_c(\zeta,\varepsilon) = \sqrt{r_{c_0}^2 + \frac{4\alpha\delta(Re_v)\nu}{\Omega}\int_0^{\zeta}(1+\varepsilon)^{-1}\,d\zeta} \tag{3.4}$$

The growth of viscous core radius, r_c, over time is a function of the initial (measured) core radius r_{c_0} (i.e., at $\zeta = 0$), and average eddy viscosity coefficient, δ (also estimated from measurements), the latter being a function of vortex Reynolds number, Re_v, and can be written as

$$\delta = 1 + a_1\left(\frac{\Gamma_v}{\nu}\right) = 1 + a_1 Re_v \tag{3.5}$$

The experiments conducted by Milluzzo et al. (Ref. 20) have shown that the slotted-tip blade is very effective in increasing both the initial core radius, r_{c_0}, and the diffusion rate, δ, of the tip vortices; see Fig. 3.90. Therefore in the present study, the value of r_{c_0} for the slotted-tip blade was considered to be 3.5 times that of the value of r_{c_0} for the rectangular blade. The value of δ for the slotted-tip blade was found by increasing the value of a_1 in Eq. 3.5 to 2×10^{-5} from the value of 2×10^{-4} used for the rectangular blade.

3.4.3 Computational Results

Computations were performed for a representative helicopter with the specifications given in Table D.3 of Appendix D. The loaded weight of the helicopter was 22,000 lbs. The flow field and dust clouds produced by the rectangular and slotted-tip blades were analyzed when the rotor was operating in a steady hover at one rotor radius above the ground (i.e., at $z/R = 1$). The rotor thrust was kept constant in these simulations for both the rectangular and slotted-tip blade geometries.

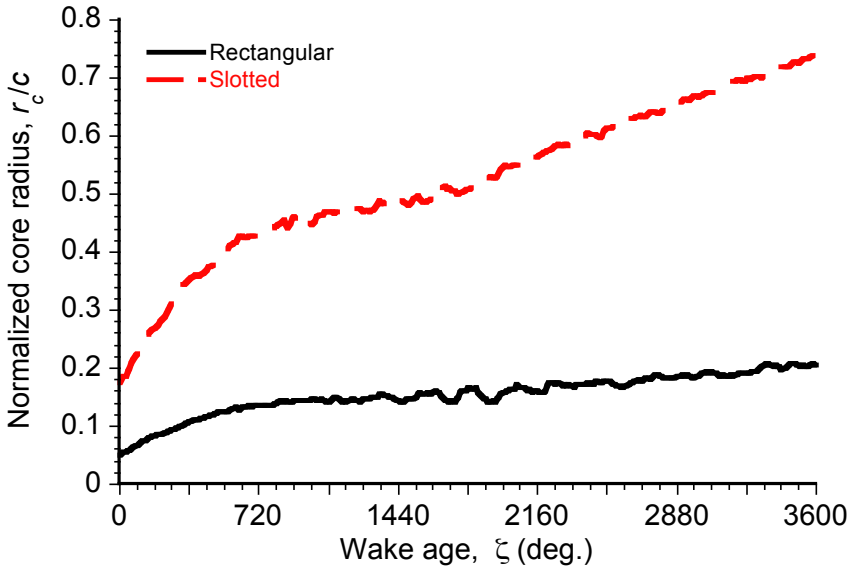

Figure 3.92: Variation of vortex core radius with wake age for the rectangular and slotted-tip shapes as obtained with the modeling for hover in ground effect at $z/R = 1$.

3.4.3.1 In Ground Effect Aerodynamics

A comparison of the rotor flow fields produced by the rectangular and the slotted-tip blades is presented first. In this respect, the rotor wake geometries, spanwise airloads, and the induced velocity and pressure fields were examined.

Vortex Core Radius and Circulation Strength

The predicted variations of the tip vortex core radii in the hover condition is shown in Fig. 3.92. As shown by the experiments, the core growth obtained with the slotted-tip blade is much quicker than for the rectangular blade. Both cases showed stretching effects on the vortex filaments as they approached the ground. These effects resulted in a reduction in the value of r_c at older wake ages, i.e., at $\zeta = 720°$, as shown in Fig. 3.92. This stretching process can cause a significant reintensification of vorticity. For the values

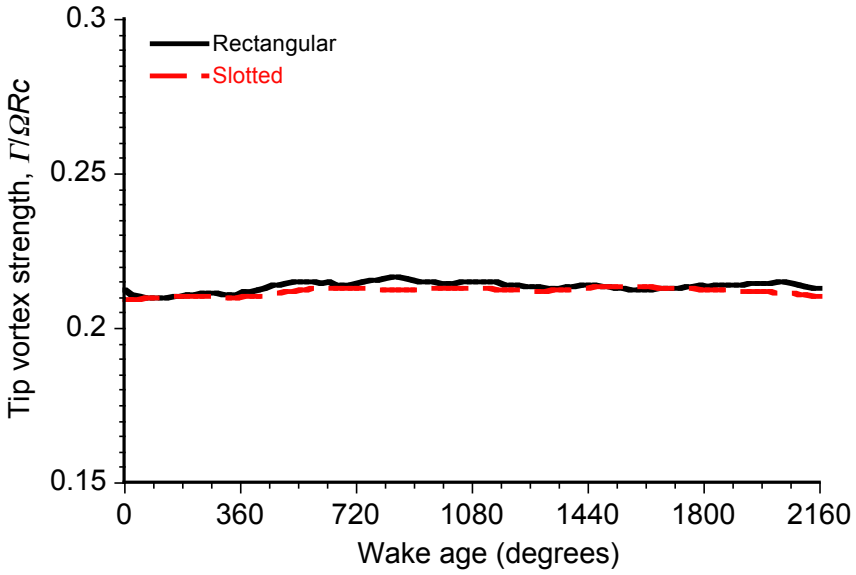

Figure 3.93: Variation of strength of vortex segments with wake age for the rectangular and slotted-tip shapes as obtained with the modeling for hover in ground effect at $z/R = 1$.

of ζ greater than 720°, the calculations with the rectangular blade showed that the value of r_c remains relatively constant, i.e., the processes of diffusion and reintensification were almost in balance. However, the tip vortex produced by the slotted-tip blade experienced little in the way of vorticity reintensification and, therefore, the effects of diffusion in this case remained dominant even at older wake ages, as shown in Fig. 3.92.

The resulting strength of the vortex segments as obtained from the FVM for both the blade tip shapes was almost equal, as shown in Fig. 3.93. This is an expected result in hover because the rotor thrust was kept constant in both of the simulations.

Wake Geometries and Performance Predictions

Figure 3.94 shows the top and side views of the wake geometries for the rotors hovering in ground effect at $z/R = 1$. Notice that the wake from the blade with the slotted-tip did

not expand radially as far as that produced by the rectangular blade. This effect arises because of the lower swirl velocities generated by the slotted-tip blade, which resulted in a smaller radial wake expansion near the ground compared to that obtained with the rectangular blade.

The effects of diffusing the tip vortex on the spanwise loads on the blades were also examined. The induced velocity distribution over the slotted-tip blade was found to be slightly lower than that produced by the rectangular blade; see Fig. 3.95. The spanwise thrust distribution on the rectangular and slotted-tip blades remained the same for up to $r/R = 0.7$, and it then decreased slightly for the slotted-tip blade, as shown in Fig. 3.96. As an outcome, the slotted-tip blade produced somewhat lower induced power than the rectangular blades, as shown in Fig. 3.97.

The integrated spanwise loads on the rectangular and slotted-tip blades are given in Table 3.1. Because of the lower tip-losses with the slotted-tip blade, its induced power coefficient, C_{P_i}, was actualy lower by about 2% when compared to that of the rectangular blades in hover. The profile losses, C_{P_0}, remained the same for the two blade tip shapes, as shown in Table 3.1. Notice that, in reality, the presence of slots in a rotor blade will probably increase the profile drag; Han & Leishman (Ref. 91) have shown that the slots can increase the profile power by about 2%. Overall, the total power requirements from the rotors with the rectangular and slotted-tip blades then remain approximately the same.

Velocity and Pressure Fields

Instantaneous realizations of the total velocity induced by the rectangular and slotted-tips along a longitudinal plane passing through the rotor hub are shown in Figs. 3.98(a)

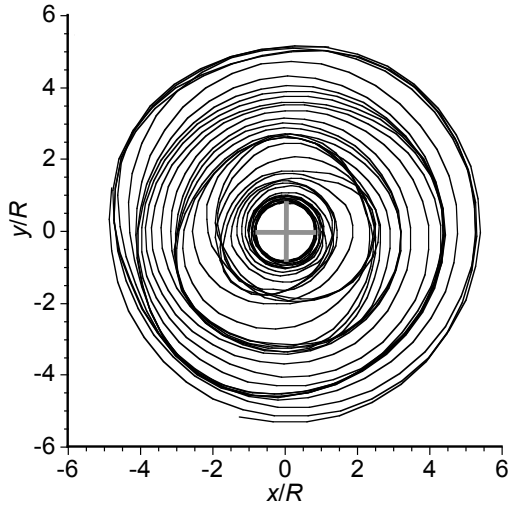

(a) Top view of the wake geometry for the rectangular blade

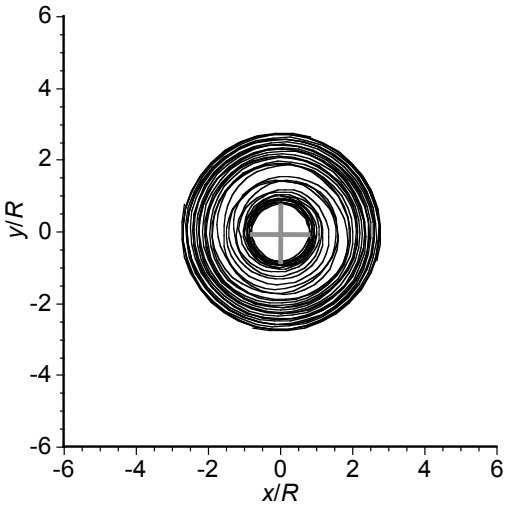

(b) Top view of the wake geometry for the slotted-tip blade

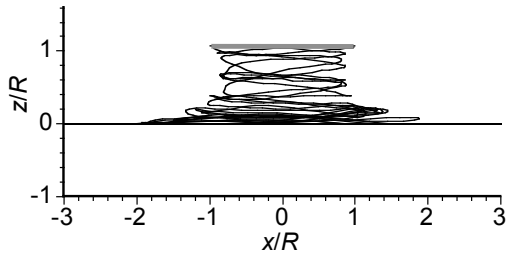

(c) Side view of the wake geometry for the rectangular blade

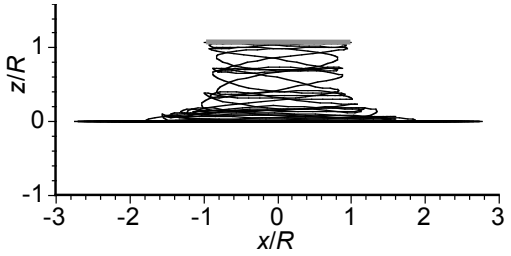

(d) Side view of the wake geometry for the slotted-tip blade

Figure 3.94: Wake geometries produced by the rectangular and slotted-tip blades: (a) top view from the rectangular blade, (b) top view from the slotted-tip blade, (c) side view from the rectangular blade, and (d) side view from the slotted-tip blade, for hover in ground effect at $z/R = 1$.

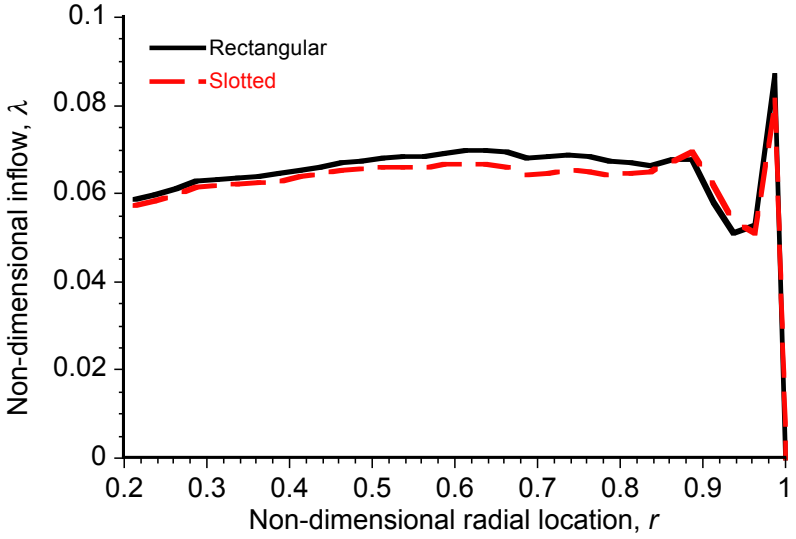

Figure 3.95: Spanwise variation of induced inflow over the rectangular and slotted-tip blades.

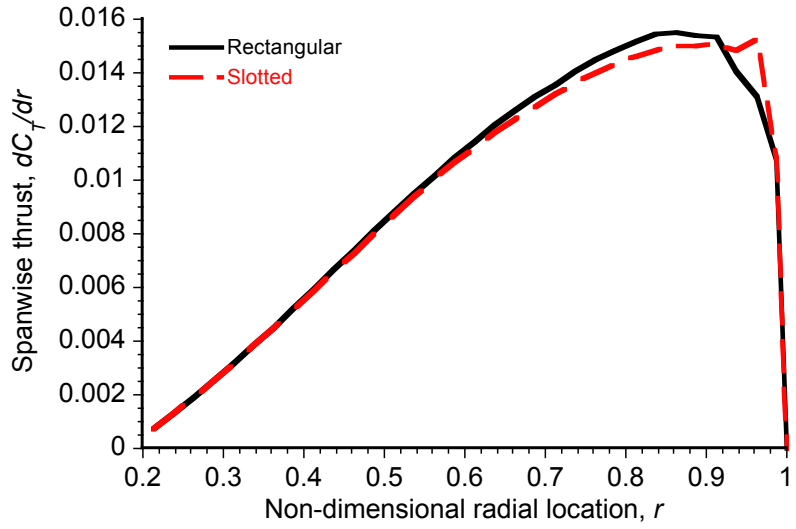

Figure 3.96: Spanwise thrust distribution over the rectangular and slotted-tip blades.

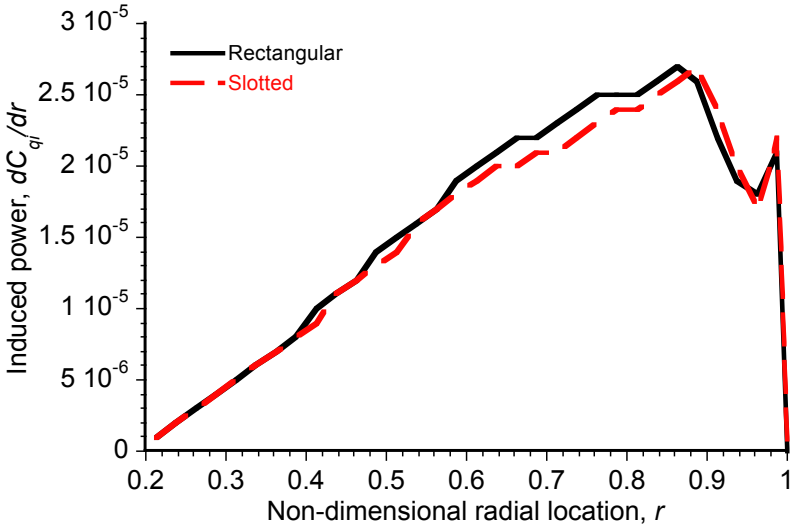

Figure 3.97: Spanwise variation of induced power over the rectangular and slotted-tip blades.

Table 3.1: Comparisons of the core growth parameters and performance predictions for the rectangular and slotted-tip blades at $C_T = 0.0078$.

	Rectangular	Slotted-tip
r_{c_0}/c	0.05	0.175
δ	26	245
C_T	0.0078	0.0078
θ_0	19°	18.8°
C_{P_i}	0.0005919	0.0005778
C_{P_0}	0.0000775	0.0000775
C_P	0.000669	0.0006553

and 3.98(b), respectively. The total velocity was non-dimensionalized by the average hover induced velocity, v_h, as given by the simple momentum theory (Ref. 16). The results confirm that the overall velocity field produced by the slotted-tip blade has lower excursions when compared to those produced by the rectangular blade.

The corresponding contour plots of unsteady pressure are shown in Fig. 3.99. Notice in this figure that the red color indicates regions where the local pressure is lower than ambient, and the blue color shows regions with pressure higher than the ambient. In this case, it is clear that the unsteady pressure field obtained with the slotted-tip blade was significantly reduced and, therefore, would be expected to uplift fewer dust particles by the action of unsteady pressure forces.

Figures 3.100(a) and 3.100(b) show contour plots of instantaneous vertical velocity components along with the radial velocity profiles in a smaller region close to the ground in the longitudinal plane passing through the rotor disk. Notice that the slotted-tip blade produced lower upwash and downwash velocities because of the more diffused vortices. The excursions in the velocity profiles were also found to be lower in comparison to those found with the rectangular blade, an outcome consistent with the experiments described in Ref. 20.

Figures 3.101(a) and 3.101(b) show contours of time-averaged total velocity. Because the calculations for the two blade tips were made at the same disk loading (i.e., the same T/A), the mean velocity fields are similar to each other. However, the instantaneous velocity fields are clearly different, as shown in Figs. 3.98(a) and 3.98(b).

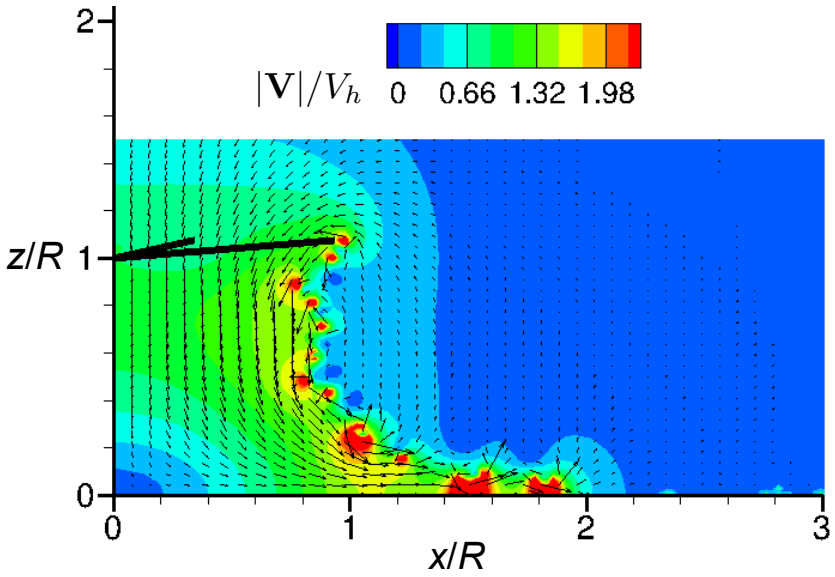

(a) Rectangular tip blade

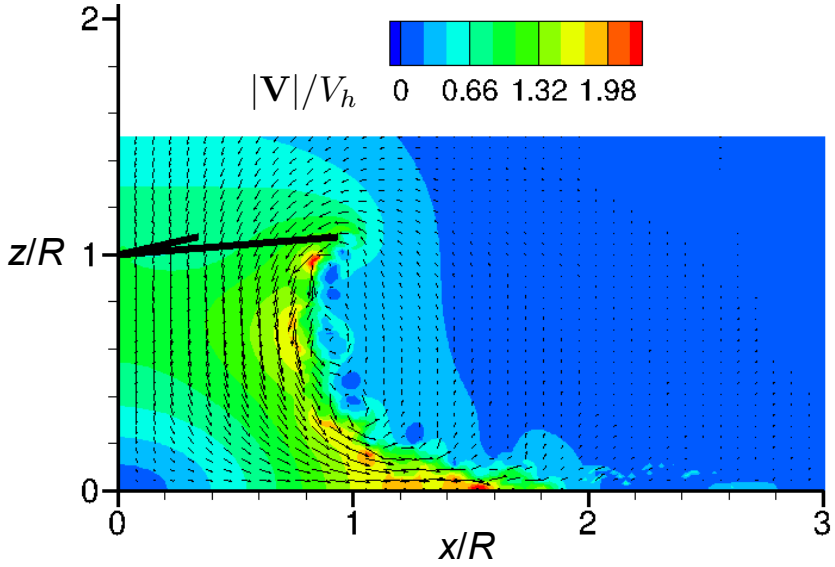

(b) Slotted-tip blade

Figure 3.98: Contour plots of total instantaneous velocity induced in a longitudinal plane by the rectangular and slotted-tip shaped rotor blades for hover in ground effect at $z/R = 1$. Velocities normalized by mean hover induced velocity.

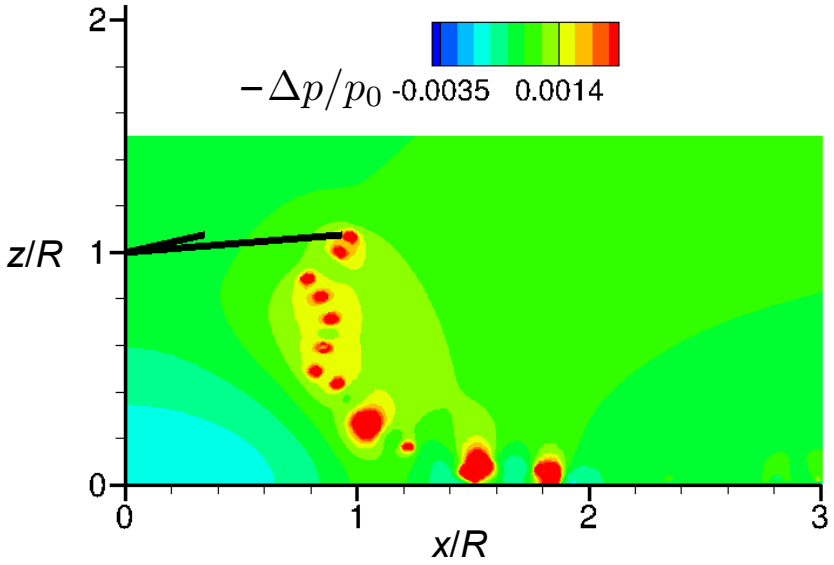

(a) Rectangular tip blade

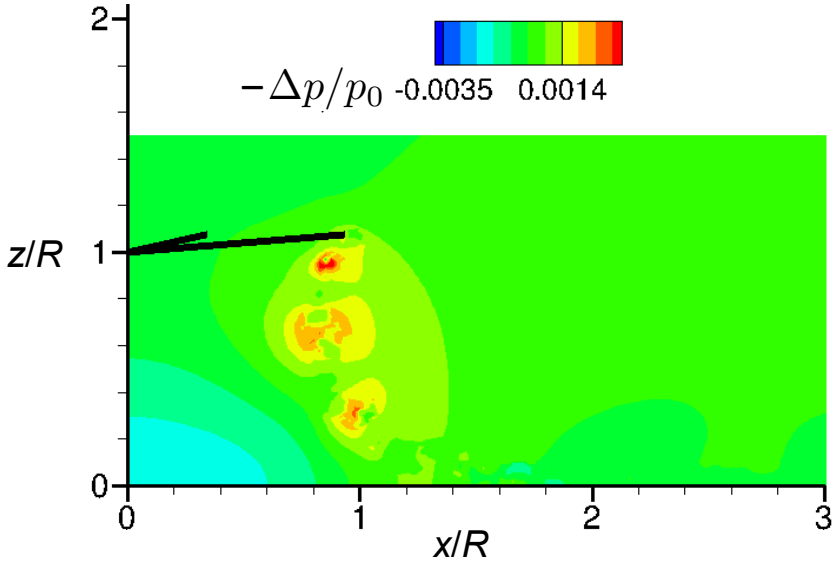

(b) Slotted-tip blade

Figure 3.99: Instantaneous pressure contours in a longitudinal plane as generated by the rectangular and slotted-tip shaped rotor blades for hover in ground effect at $z/R = 1$.

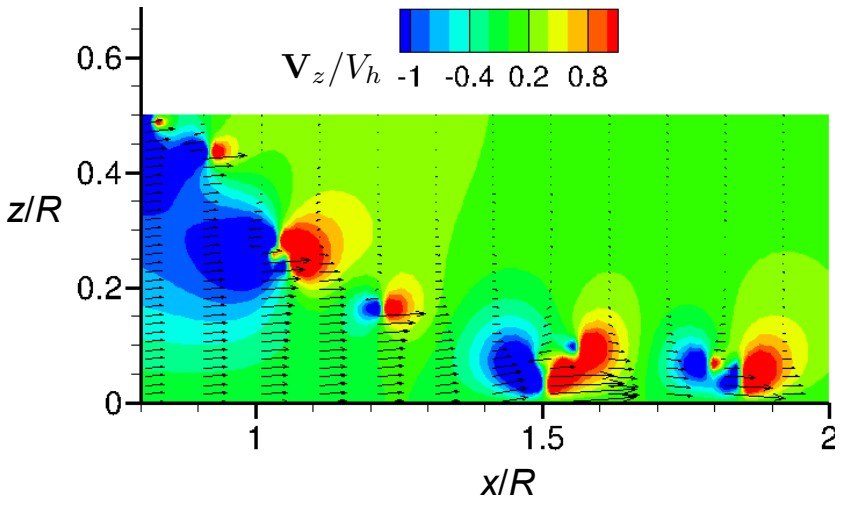

(a) Rectangular tip blade

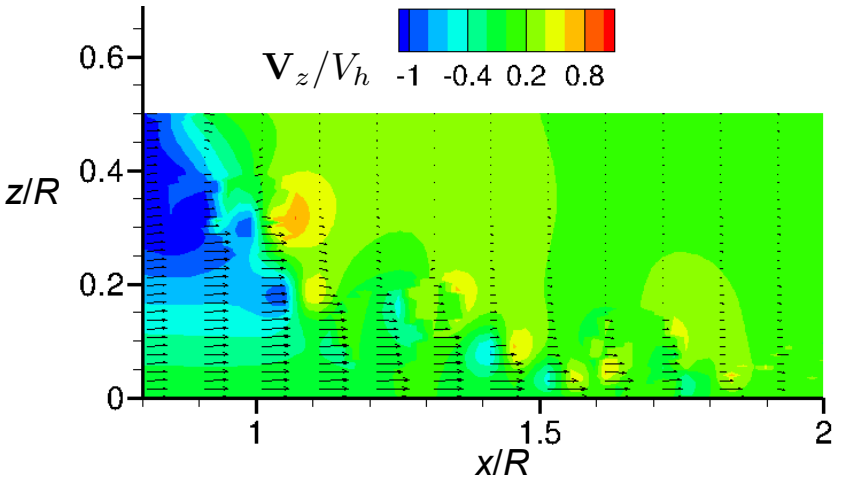

(b) Slotted-tip blade

Figure 3.100: Radial velocity profiles plotted with background contours showing the instantaneous vertical velocity component in a longitudinal plane closer to the ground for the rectangular and slotted-tip blades for hover in ground effect at $z/R = 1$. Velocity normalized by mean hover induced velocity.

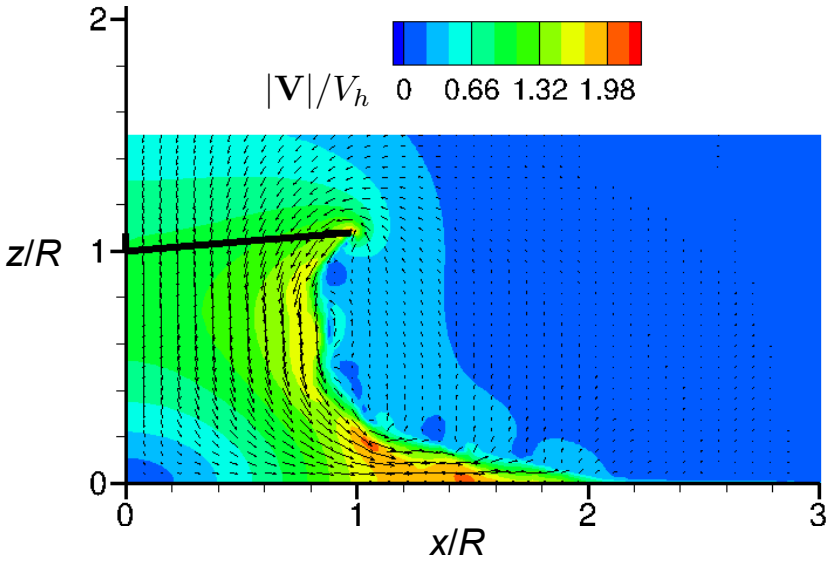

(a) Rectangular blade tip shape

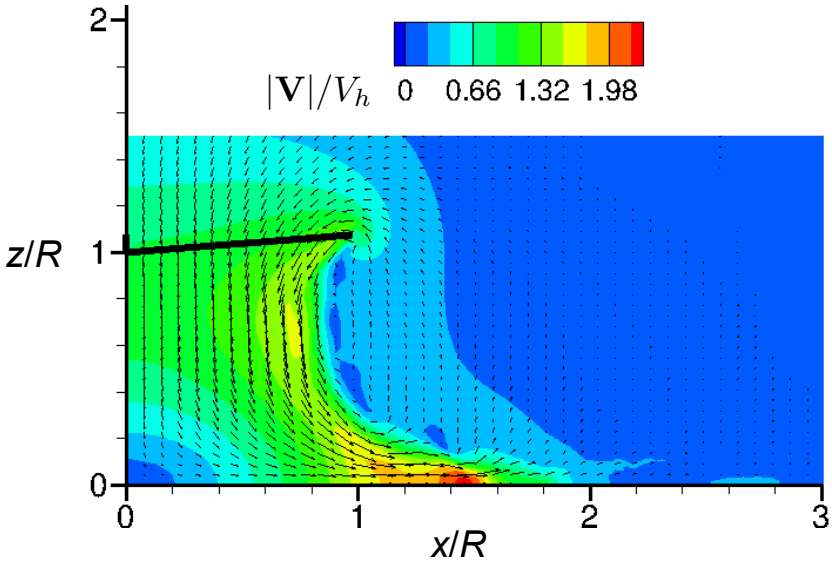

(b) Slotted blade tip shape

Figure 3.101: Time-averaged total velocity in a longitudinal plane for the rectangular and slotted-tip blades for hover in ground effect at $z/R = 1$. Velocity normalized by mean hover induced velocity.

3.4.3.2 Analysis of the Predicted Brownout Clouds

Dust clouds generated by the rectangular and slotted-tip blades were calculated from a superposition of multiple monodisperse simulations with particle sizes ranging between d_p = 1 μm and 100 μm. The dust clouds were post-processed by using the Gaussian clustering method, as explained in detail in Appendix C. For the present study, each simulation comprised over one million cluster centers, each being associated with 50 particles, giving an average of about 50 million particles in the calculations at each time step.

The three-dimensional instantaneous realizations of the dust clouds produced by the rectangular and slotted-tip blades are shown in Figs. 3.102(a) and 3.102(b), respectively. Figures 3.103(a) and 3.103(b) show the top and front views of these dust clouds. Notice that the fuselage in the top views is shown for illustrative purposes only, and the aerodynamic analysis only modeled an isolated rotor. The dashed concentric circles are plotted at integer multiples of the rotor radius for reference purposes. The differences in the geometry of the dust clouds can be clearly seen in these figures, which suggests that the formation of dust clouds are sensitive to the structure of the vortices.

The densities of the dust clouds can be compared by dividing the region surrounding the rotor into volumetric "bins," and calculating the quantity of dust in each bin. Figure 3.104 shows the difference between the densities of the clouds produced by the rectangular and slotted-tip blades; red indicates a region where the cloud produced by the slotted-tip is more dense than that produced by the rectangular blade, green indicates a region where the cloud is less dense, and white indicates a region where there is no

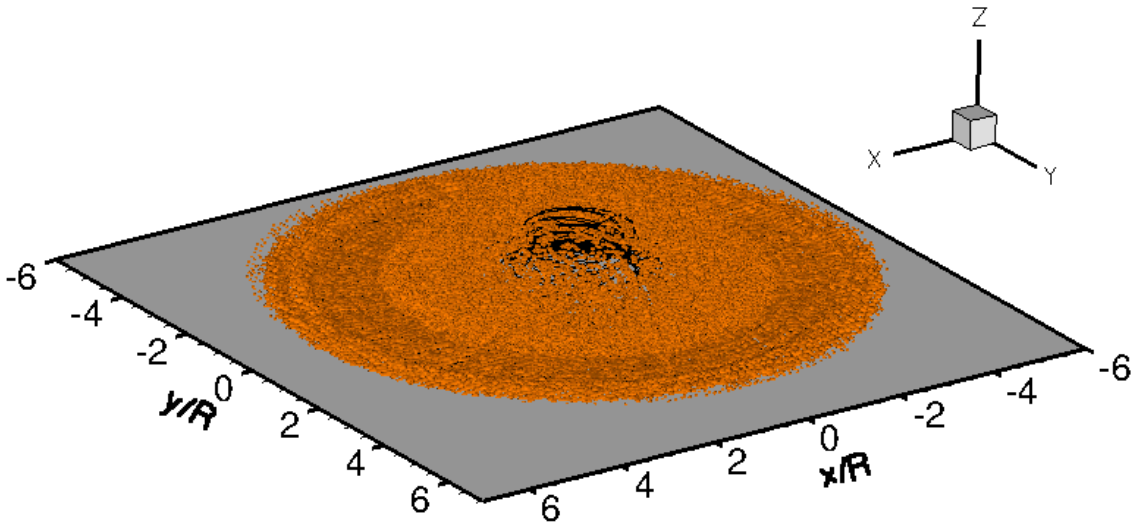

(a) Dust cloud from the rectangular blade

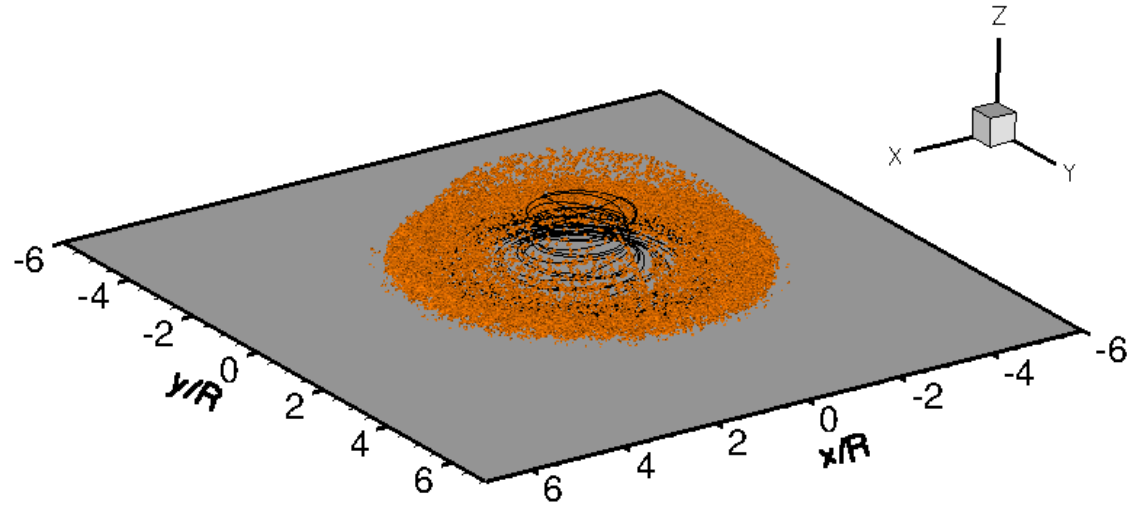

(b) Dust cloud from the slotted-tip blade

Figure 3.102: Three-dimensional instantaneous realizations of the brownout dust clouds produced by the rectangular and slotted-tip blades.

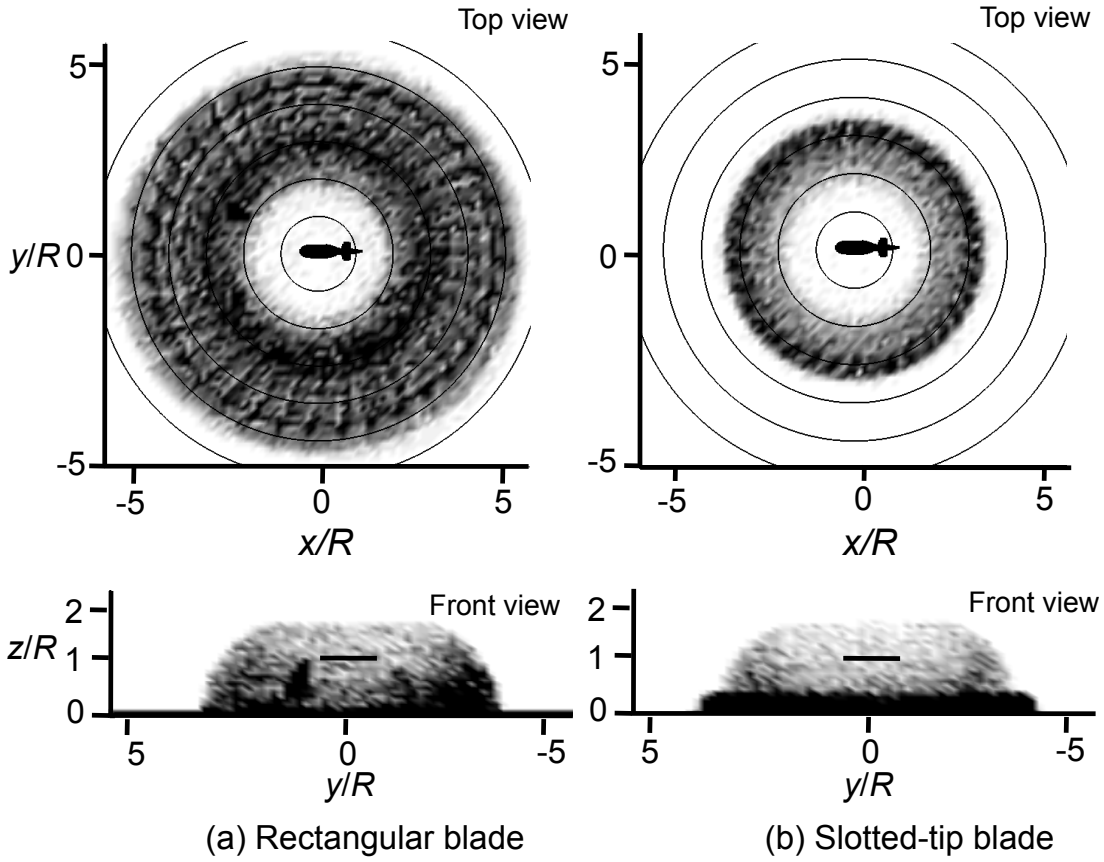

Figure 3.103: Top and front views of the simulated dust clouds for the rectangular and slotted-tip blades at t = 13 seconds.

appreciable difference in cloud density. The predominance of the green color seen in Fig. 3.104 shows that the overall dust cloud produced by the slotted-tip blade is significantly less dense when compared to that of the rectangular blade. Also notice from the top views that the quantity of dust reingested into the rotor is much larger when using the rectangular blade. The presence of a red band close to the ground shows that the cloud density is greater in this small region when using the slotted-tip blade.

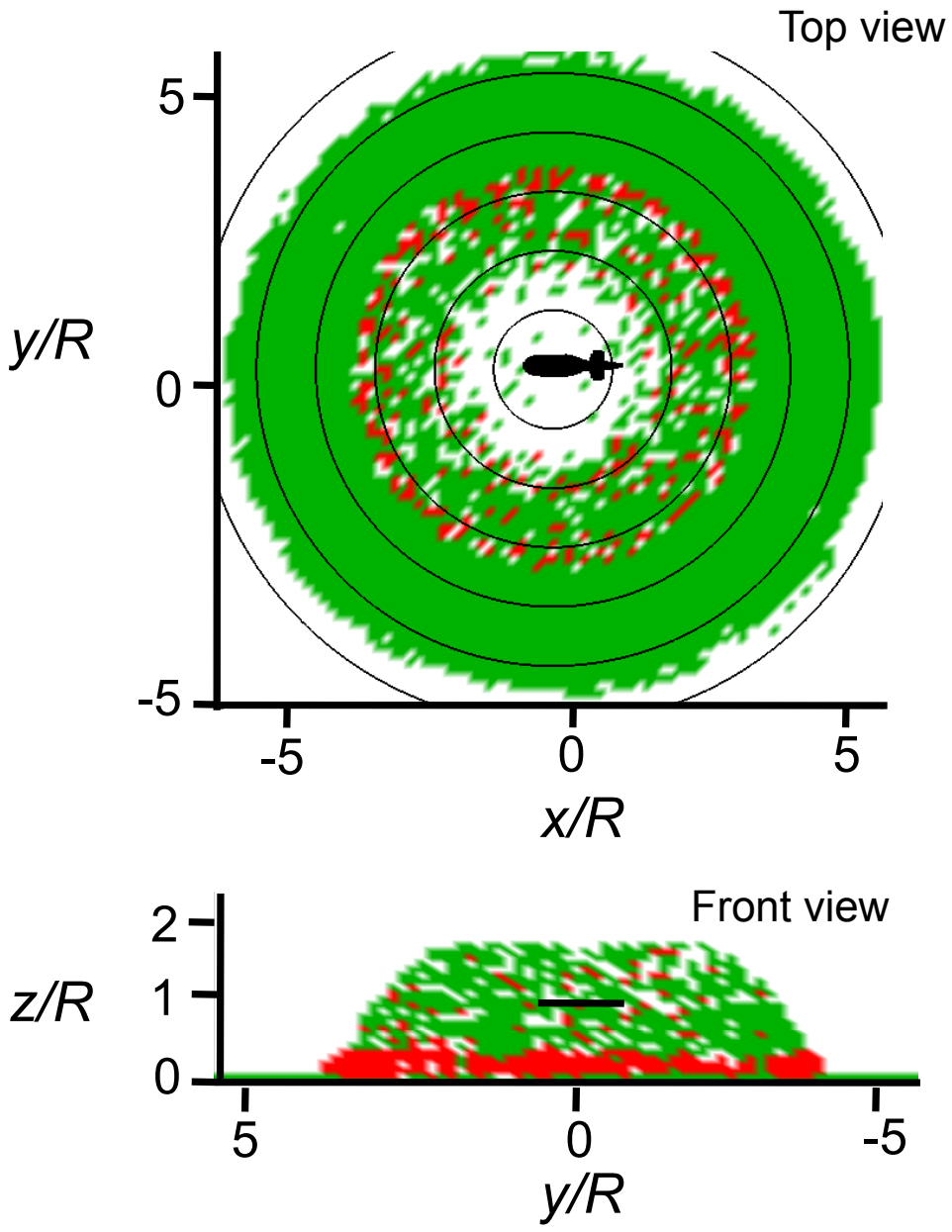

Figure 3.104: Contour maps showing difference in the densities of the dust clouds produced by the rectangular and slotted-tip blades. Red color indicates the regions where the cloud from the slotted-tip blade is more dense, and green color shows the regions where the dust cloud from the rectangular blade is more dense.

Dust Entrainment Mechanisms

Figures 3.105(a) and 3.105(b) show the quantity of dust that was uplifted by the action of direct entrainment and bombardment ejection mechanisms, respectively. The results were normalized by the total quantity of dust that was uplifted by the rotor with the rectangular blades at the end of the simulation, i.e., at 17.5 seconds. As shown in the previous section, the slotted-tip blade produced lower instantaneous flow velocities and less intense pressure fields on the ground, which resulted in a lower quantity of dust being uplifted, as shown in Fig. 3.105.

On average, there was an order of magnitude reduction in the total quantity of dust uplifted when using the slotted-tip blade through shear and pressure mechanisms; see Fig. 3.105(a). The most significant reduction in dust entrainment was via the bombardment ejection mechanism, which was about two orders of magnitude lower when using the slotted-tip, as shown in Fig. 3.105(b). As previously seen in Section 3.3, bombardment ejections take place primarily in the regions where stronger vortices impinge on the sediment bed. Therefore, with the more diffused vortices generated by the slotted-tip, the quantity of particles mobilized by bombardment ejections was significantly reduced.

Notice that although a similar time-averaged flow field was generated by the slotted and rectangular blades (shown previously in Figs. 3.101(a) and 3.101(b)), the quantity of uplifted dust was very different. This outcome suggested that the uplifted particles depend on the fluctuating part of the velocity field, which was significantly less intense for the slotted-tip blade. This outcome was because of the reduced swirl velocities of the tip vortices, the less coherent vortex structures near the ground, and the overall lower induced velocity excursions. All of these effects lead to reduced friction velocities (Section 2.3.3),

bombardment ejections (Section 2.5), and less intense dust clouds.

Brownout Cloud in the Pilot's FOV

With an understanding that brownout is fundamentally a fluid dynamics problem but ultimately a piloting concern, a metric developed by Tritschler et al. (Ref. 87) was adopted to describe the effects of a given brownout cloud on the pilot's visibility of the landing zone. This metric is discussed in Appendix E, and was used in the present study to compare the dust clouds produced by the rectangular and slotted-tip blades in the pilot's field of vision (FOV).

Figure 3.106(a) shows a comparison of the normalized quantity of dust in the pilot's FOV for the rectangular and slotted-tip blades. This metric can be used as a surrogate for the visual obscuration observed by the pilot. Notice that the quantity of dust in the pilot's FOV was significantly lower for the slotted-tip blade. Using the metric defined previously, the slotted-tip resulted in about a 75% reduction in the quantity of particles in the pilot's FOV over the duration of the simulation, indicating that the dust cloud generated by the slotted-tip was significantly less intense and should give the pilot better visibility during landing.

The average quantity of dust in the pilot's FOV is shown in Fig. 3.106(b). Interestingly, the smaller dust particles (i.e., those with $d_p < 20$ μm) are the most predominant when using the rectangular blades. These particles have very small terminal velocities, and once entrained and uplifted they tend to remain in the flow for longer times. Because the slotted-tip blade resulted in a significantly reduced quantity of dust being mobilized by bombardment ejections, the quantity of these smaller-sized particles in the flow was

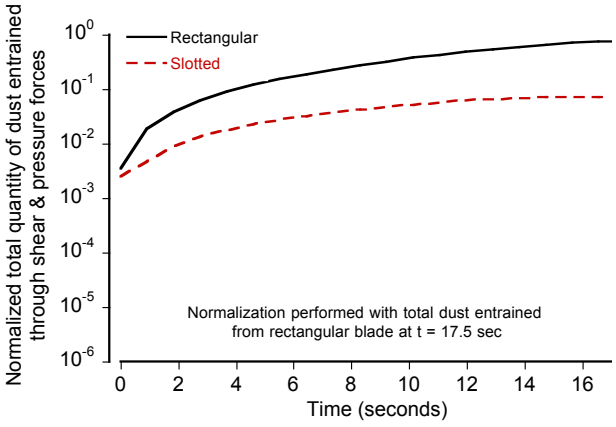

(a) Direct aerodynamic entrainment

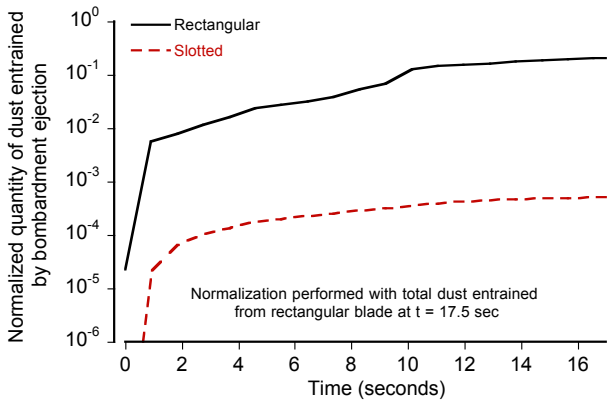

(b) Bombardment ejection

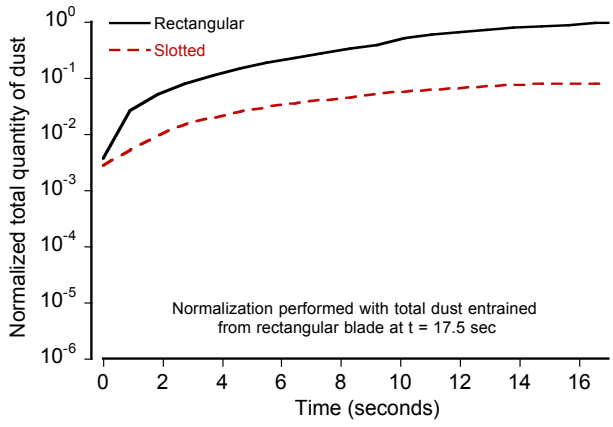

(c) Total entrainment

Figure 3.105: Time-history of normalized quantity of dust entrained for hover in ground effect at $z/R = 1$ from: (a) direct aerodynamic entrainment, (b) bombardment ejection, and (c) the total dust entrained.

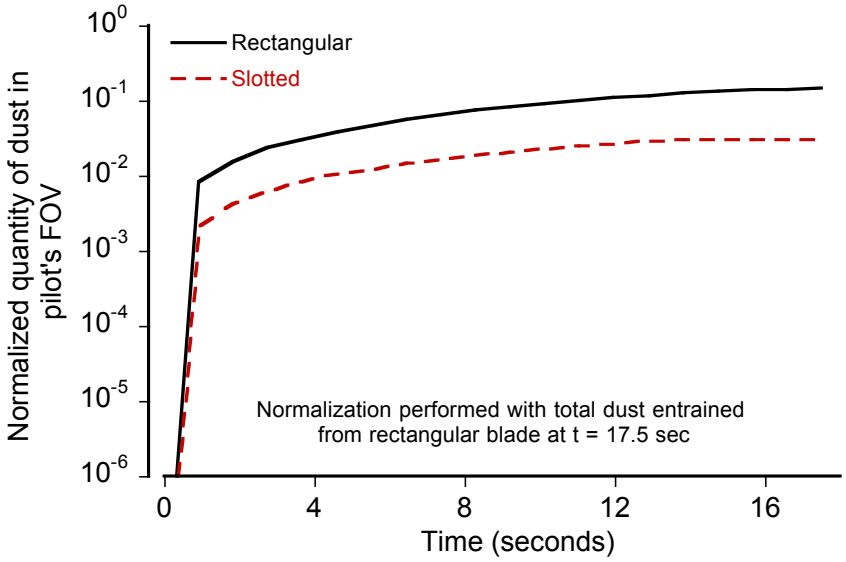

(a) Total quantity of dust in pilot's FOV versus time

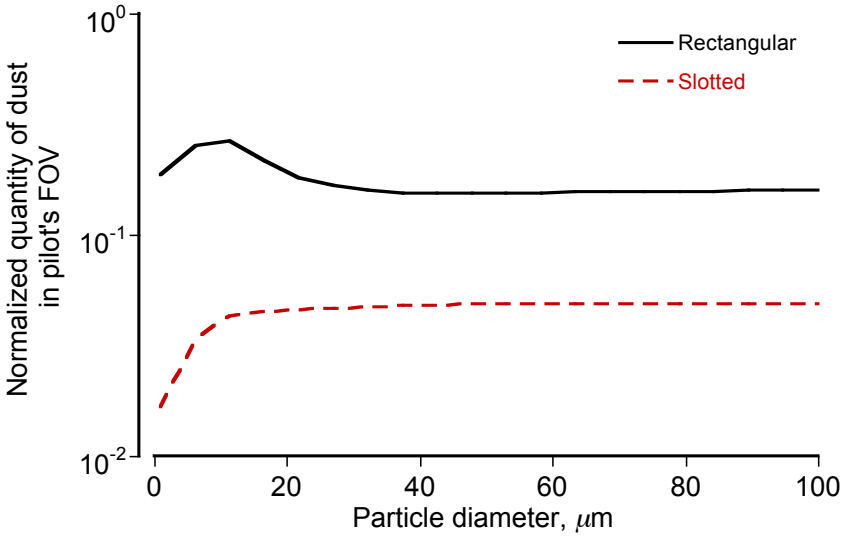

(b) Average quantity of dust in pilot's FOV from different particle sizes

Figure 3.106: Comparison of normalized quantity of dust in pilot's FOV for the rectangular and slotted-tip blades.

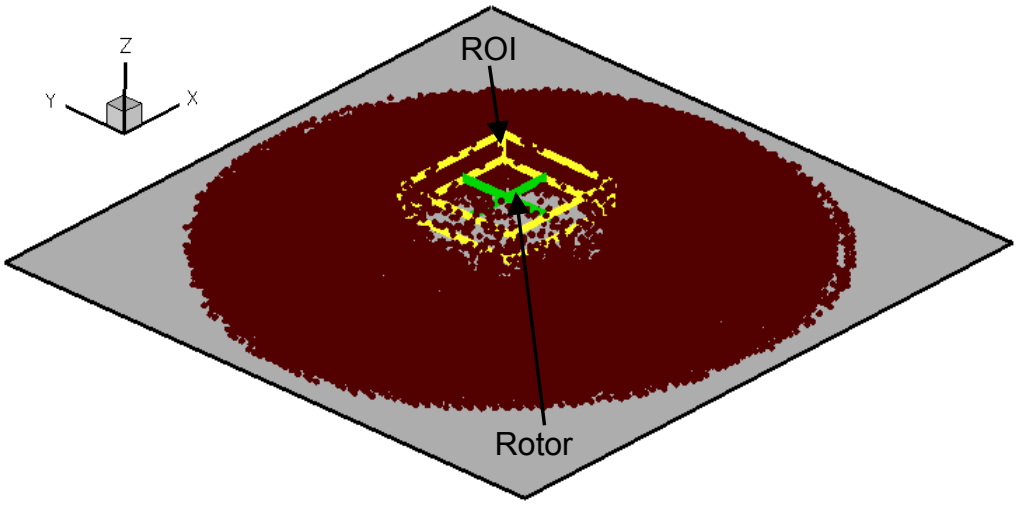

Figure 3.107: An instantaneous realization of the dust cloud showing a region of interest (ROI) used to analyze the dust clouds closer to the rotor disk. The dimensions of this region are: $x/R = -1.25$ to 1.25, $y/R = -1.25$ to 1.25, and $z/R = 0.75$ to 1.25.

also reduced. In general, the use of the slotted-tip blade produced fewer suspended dust particles of all sizes by means of all of the primary mobility and uplift mechanisms. These results, therefore, clearly show the effectiveness of diffusing the tip vortices for brownout mitigation, however it might be obtained.

Dust Clouds Near the Rotor Disk

It was mentioned previously in Section 1.1 that the suspended dust particles in a brownout cloud can also lead to rapid abrasion of the rotor blades, as well as engine wear and tear problems, which can cause expensive maintenance issues. An assessment of the effects of the dust clouds on these problems can be made by analyzing the density of the dust cloud in the region closer to the rotor disk.

To this end, a region marked as ROI in Fig. 3.107, was chosen to analyze the dust

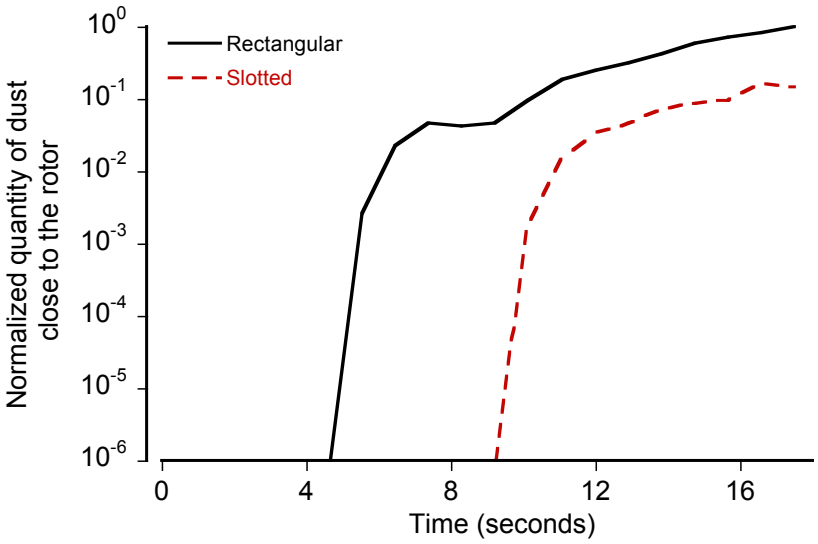

(a) Total quantity of dust in region close to the rotor disk versus time

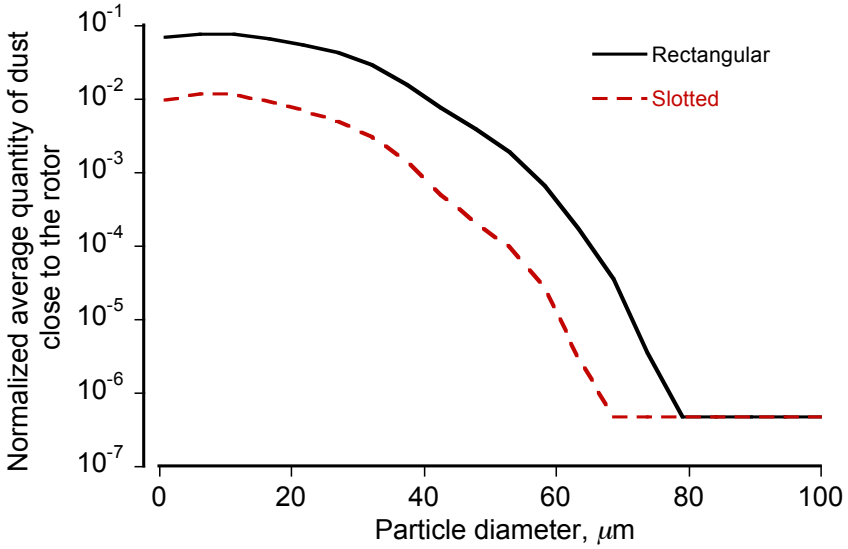

(b) Average quantity of dust in region close to the rotor disk for different particle sizes

Figure 3.108: (a) Normalized particle quantity versus time in the ROI close to the rotor disk, (b) Normalized average particle quantity versus particle diameter in the region closer to the rotor disk. Normalization was performed by the total quantity of dust in this region at t = 17.5 seconds as obtained with the blade with the rectangular tip.

concentration and the rate of cloud development closer to the rotor disk. The dimensions of this region were: $x/R = -1.25$ to 1.25, $y/R = -1.25$ to 1.25, and z/R = 0.75 to 1.25. The time-history of the evolving concentration of dust in this region is shown in Fig. 3.108. Notice that the quantity of dust in the chosen region started to increase at about 4.25 seconds into the simulation when using the rectangular blade, and at about 9.2 seconds with the slotted-tip blade. This outcome confirmed that the rate of vertical development of the dust cloud was much less for the slotted-tip blade. Also, the concentration of dust in this region was found to be an order of magnitude lower for the slotted-tip blade in comparison to using the rectangular blade.

Figure 3.108(b) shows an average concentration of the different particle sizes in this region over the entire simulation of 17.5 seconds. Interestingly, the concentration of sand-sized particles (i.e., $d_p > 70$ μm) close to the rotor disk was found to be the lowest, suggesting that the well-known problems of blade abrasion in brownout conditions may be caused by the smaller dust-sized particles. For these small particles, the slotted-tip blade was found to produce an order of magnitude reduction in the quantity of dust in proximity to the rotor disk, and so should also be expected to reduce abrasion and wear and tear on the rotor system.

3.5 Summary

This chapter has discussed the results obtained using the brownout simulation methodology that was developed during the course of the present research. The chapter was divided into four sections: description and analysis of the numerical methods being used,

comparisons of the predictions with measurements, analysis of the evolution of the dust cloud during simulated landing and takeoff maneuvers, and the effects on the development of the dust clouds produced by more rapidly diffusing the tip vortices.

In Section 3.1, the processes associated with bombardment ejection have been studied in detail, where a suspended particle impacts the bed and dislodges more particles. Two simpler conditions were examined in detail: (a) the effect of particles of various sizes that impact the bed with same velocities, and (b) the effect of different sizes of particles encountering the same flow velocities before impact. The results showed that the process of bombardment can eject a large quantity of small-sized particles from the bed. It was also found that bombardment of a small-sized particle onto the bed can eject a large quantity of the same sized particles, but the bombardment of a large particle on the bed can eject only fewer particles of its own size.

The accuracy and convergence of the time-marching schemes that were developed to solve the particle equations of motion were analyzed in Section 3.1.2. This analysis was performed for: one-dimensional harmonic flow, a two-dimensional vortex flow, and three-dimensional rotor flow in ground effect. Numerical schemes based on a predictor-corrector formulation (i.e., involving the quadratic extrapolation of the particle position in the predictor step) were shown to be the most suitable for solving the equations of motion. It was found that the use of lower-order schemes at the initial time steps can reduce the overall order of accuracy of the solution. The implicit, predictor-corrector scheme that was ultimately selected was based on a two-point backward difference method that was second-order accurate, which also showed grid independence for azimuthal and wake discretization of less than 5°.

Section 3.2 has compared the results obtained from the modeling with available measurements. First, results from the free-vortex method were validated against flow measurements made with laboratory-scale and full-scale rotors operating in ground effect. These results were also compared with flow field predictions made using CFD (RANS), where the predicted rotor wake geometry and tip vortex strengths were found to be in good agreement. The radial velocity profiles on the ground plane below the rotor were also found to be in good agreement with both the CFD results and the measurements, except for the regions very close to the ground. The groundwash velocities predicted using the free-vortex method were also compared to full-scale measurements made for helicopters hovering over the ground, with reasonably good agreement being obtained.

Section 3.2 has also shown predictions of the dynamic evolving dust clouds against photogrammetric measurements made for a helicopter undergoing taxi-pass and approach-to-touchdown maneuvers over a dusty surface. The primary challenge in this study was that not all of the parameters needed to conduct a thorough validation were actually measured. Therefore, the sensitivities of the shapes of the time evolving dust clouds were examined, including the effects of the weight of the helicopter, the wind conditions, and the initial flight profile. The results showed that the evolving dust clouds can be sensitive to all of these parameters, especially as they affect the process of wake bundling in front of the rotor on the ground. In particular, wake bundling was shown to be a primary contributor to the formation of dust clouds.

Section 3.3 has further analyzed the evolution of the dust clouds for three flight conditions: hover at one rotor radius above the ground, a representative landing maneuver, and a maximum performance takeoff maneuver. The different aspects of particle motion

were better exposed in these simulations, namely, creep, saltation, secondary suspension, vortex trapping, saltation bombardment and reingestion bombardment. Bombardment ejection of particles were greatly increased in regions at the ground that were affected by the presence of the blade tip vortices. The processes of vortex bundling and the formation of a super-vortex near the front of the rotor disk was found to be particularly important as it affected the intensity bombardment ejections and the volume of suspended dust. This combined vortex flow not only mobilizes a large quantity of particles from the bed, but also determines the growth of the dust cloud along the vertical and radial directions. It was also found that bombardment ejections resulting from the reingestion of suspended dust through the rotor disk also affected the severity of brownout conditions.

Finally, a study was conducted in Section 3.4 to explore the possibilities of brownout mitigation by diffusing the blade tip vortices, i.e., by enhancing the core growth and diffusing vorticity. This study was also motivated by experiments that had been conducted previously using different blade tip shapes, where one particular blade geometry was shown to produce much more diffused tip vortices. In the present level of modeling, the effects of this blade tip shape was modeled by artificially increasing the rate of core growth based on experimental measurements. The results showed that diffusing the tip vortices produced lower instantaneous velocity and pressure fields near the ground, and significantly lower quantities of particles were also mobilized. This study showed that diffusing the tip vortices, regardless of how this might be obtained in practice, could be very beneficial for the mitigation of brownout.

Chapter 4

Conclusions

A comprehensive numerical methodology has been developed to analyze the processes involved in the formation of brownout dust clouds produced by the rotors of rotorcraft in ground effect operations. The significance of the brownout problem is that its onset can markedly reduce the pilot's visibility of the ground during landings or takeoffs and so can pose a serious safety of flight risk. A high fraction of human-factor related mishaps, particularly with military helicopters, have been caused by pilots encountering brownout conditions.

The overall goal of the present work was to develop a comprehensive dust cloud simulation methodology that is also computationally efficient enough to be practically used to study various brownout scenarios, eventually helping to explore the possibilities of brownout mitigation. The work contributes significantly to the understanding of the brownout problem, and better exposes the fluid dynamic mechanisms that are responsible for the mobilization and uplift of dust by the action of the rotor wake.

This final chapter discusses the key conclusions that have been drawn from the present work, and also suggests directions for future research.

4.1 Summary of Contributions

A detailed literature review and a survey of prior art was covered in Chapter 1. Besides prior work on rotors in ground effect operations, more recent experimental and computational work on the brownout problem has been reviewed. Laboratory measurements of rotors operating above mobile sediment beds have shown that there are important two-phase fluid dynamic mechanisms that particularly contribute to the brownout problem. These mechanisms differ from the more classical mechanisms affecting sediment mobility under the action of uniform flows, and so pose different and more complex challenges from a modeling perspective. Prior literature in the field of sedimentology and the aeolian sciences was also reviewed, which contains many useful experimental results and mathematical models that can be adopted or extended to model sediment mobility under the action of a rotor wake.

A review of the prior art with actual brownout simulations showed that most existing approaches are based on several approximations and assumptions that are more questionable for the two-phase dusty flow environment produced by a rotor. One important aspect of the present work was to better understand the processes involved in sediment mobilization in vortically dominated rotor wake flows, and to develop improved numerical models that can better simulate the key physical processes that contribute to the formation of dust clouds produced by the rotor wake.

Details of the elements of the methodology that was developed during the course of the present work has been thoroughly discussed in Chapter 2. It was shown how the rotor flow in ground effect conditions can be modeled by using a free-vortex method, at least

away from the immediate region near the ground. A semi-empirical model for the vortex core growth was used in terms of the initial core radius and the time rate of diffusion under the action of viscosity and turbulence. The advantages on the free-vortex wake method include good fidelity predictions of the rotor wake flow and the relatively low computational cost. Nevertheless, it is still an inviscid approach and so it cannot predict the boundary layer profile and so does not satisfy the no-slip condition at the ground plane. Nevertheless, the free-vortex approach was shown by means of comparisons with experiments to give excellent predictions of the unsteady wall-jet nature of the flow as it developed over the ground below a rotor.

To model the viscous flow in the immediate vicinity of the ground, a semi-empirical model was developed. Some of the information needed for this approach was taken from the free-vortex method. To this end, the velocities at an interface located at a small distance above the ground (of the order of the boundary layer thickness) were used to define the flow conditions that were necessary to calculate the friction velocities on the sediment bed. The general nature of the velocity profile in the boundary layer region was determined from experiments made with a rotor hovering above a ground plane, and used within this modeling construct to estimate the more general nature of the velocity profiles under the action of the specific external flows.

It was shown that the determination of the friction velocities is necessary but insufficient to determine the onset of particle motion. A sediment mobility model based on the concept of exceeding threshold conditions defined by both the friction velocities and the unsteady pressures was developed in the present work. This model considered the equilibrium of moments acting on a stationary particle on the bed from the action of

boundary layer shear, unsteady pressures, gravitational forces, and inter-particle forces. This new model differed from previous mobility models in that the effects of unsteady pressure forces were explicitly included, the effects of pressure forces being potentially very important in the vorticity laden flows produced by rotor. For example, the passage of vortices trailed from the rotor blades can induce high enough unsteady pressures on the bed that they can produce forces on particles that completely dominate over those produced by boundary layer shear. In the final model, the effects of shear and pressure were considered simultaneously in that they both affected the threshold conditions for the onset of sediment mobility. The efficacy of this model was examined for both simpler two-dimensional flows, as well as for the more three-dimensional brownout conditions generated by a rotor.

Recent measurements with laboratory-scale rotors operating over mobile sediment beds have also suggested that the mechanism of bombardment ejection is an important contributor to the ejection and uplift of small-sized dust particles into rotor wake and, therefore, to the overall formation of brownout dust clouds. In this process, previously suspended particles in the flow can bombard the bed with high velocity (e.g., if entrained into a local vortex flow, or into the recirculating rotor flow in general) and can then forcibly eject many more particles from the bed. In the present work, a method based, in part, on the outcomes from research conducted in the field of aeolian sediment transport was developed to model the mechanism of bombardment ejections. In this model, the volume of the crater produced by bombardment was first estimated, which was then used to calculate the quantity of ejected particles. The locations of the ejected particles were determined by conserving the respective momentum and energy of the impacting particle

and the total number of ejected particles. The efficacy of this model was examined for a variety of two-dimensional and three-dimensional vortically dominated flows.

Once mobilized, the motion of uplifted particles in the flow was tracked by solving their governing equations of motion, which were formulated by considering inertial, aerodynamic, and gravitational forces. A Stokes drag assumption for the particles was used, which was shown to be justified for the brownout problem with only a few exceptions such as immediately near the ground. In the present work, these equations of motion were solved numerically by using a time-marching integration scheme. Because these equations are numerically stiff, a thorough stability and accuracy analysis was conducted. The goal was to determine the best numerical integration scheme such that larger and more computationally practical time step sizes could be used in the brownout simulation, while also maintaining the stability and accuracy of the solution. Ultimately, an implicit, multi-step, second-order accurate method based on a two-point backward difference scheme was shown to be the most suitable scheme to solve the equations describing the motion of these particles. Because of the very large number of particles that must be convected through the flow, the possible application of particle clustering methods was also discussed.

In Chapter 3, the results from the methodology were compared against available measurements, including both flow velocity measurements and measurements of the shapes of brownout dust clouds. First, the predicted groundwash velocities and velocity profiles near the ground were compared to measurements, with good general agreement. Second, the predicted dust clouds were compared to dust clouds measured for a helicopter during taxi-pass and approach-to-touchdown maneuvers over a prepared test range. While only

measurements of the external shape of the dust clouds were available, the comparisons gave good confidence in the capabilities of the model to predict dynamically evolving brownout conditions. Unfortunately, important parameters such as the weight of the helicopter, the wind conditions and exact flight profile were not measured, which increased the uncertainties in the outcomes from the study. Therefore, sensitivities of the predicted dust clouds were also explored. Overall, the outcomes from this study emphasized the importance of making careful measurements of all of the critical parameters affecting the problem if brownout is to be fully understood.

A study was also conducted to analyze the development of brownout dust clouds during a series of hover, landing, and takeoff flight maneuvers. This study helped to expose the resulting flow mechanisms that were responsible for the formation of dust clouds, and why under certain conditions the dust clouds can become more severe than under other conditions. In particular, it was shown that the bundling of the wake vortices and the formation of a ground vortex during the landing maneuver significantly affected the uplift of dust and the formation of the dust clouds. In the field, helicopter pilots have apparently adopted specific flight profiles to avoid this very problem where the rotor wake settles on the ground in front of the helicopter and stirs up dust. Although the effects of the velocity field below and in front of the rotor was shown to be an important contributor to the onset of sediment motion and uplift, the action of unsteady pressure forces and bombardment ejections were shown to be primary contributors to the uplift and suspension of small-sized particles in the developing dust cloud.

Because of the important effects of the blade tip vortices on the mobilization and uplift of sediment particles, the effects obtained by artificially diffusing the vortices were

also examined. Practically, it has been shown that certain blade tip shapes or blade tip modifications can affect the growth and diffusion of the trailed vortices. The present results clearly showed that diffusing the vorticity of the tip vortices (however, this effect might ultimately be obtained) has great potential for mitigating the severity of brownout conditions. In particular, the adoption of a slotted tip blade has been shown to be a particularly effective way of diffusing the vortices and spinning down their strong induced velocities. The practicality of doing this with actual helicopters in the field, however, still needs to be established. Nevertheless, the present work has shown beyond a doubt that the strength and flow structure of the tip vortices are one of the most important fluid dynamic contributors to the rotorcraft brownout problem.

4.2 Detailed Conclusions and Specific Contributions

The key observations and conclusions drawn from the present work are summarized in this section. These conclusions are divided into four subsections: 1. The dust cloud simulation methodology, 2. Comparisons of the developed methodology against measurements, 3. Analysis of the developments of the dust clouds and exposition of the underlying physics, and 4. Analysis of the dust clouds produced by more artificially diffused tip-vortices, such as might be used for brownout mitigation.

4.2.1 Methodology

1. The free-vortex wake model was shown to give good predictions of the flow environment at the ground, except within the boundary layer region. The approach was

also validated against a first-principles based CFD solution, with good agreement being shown. The confidence obtained with the free-vortex method lent confidence in the prediction of the resulting action of the rotor wake flow on the development of the dust clouds, with the assumption that sediment mobility conditions can also be established accurately.

2. Existing sediment mobility models, which generally include surface shear effects alone, were considered to be inadequate for modeling the conditions found on sediment beds below a rotor. Therefore, a new sediment mobility model was developed by considering the balance of effects produced by unsteady pressure, shear, inter-particle, and gravitational forces. The results showed that the presence of the unsteady pressure forces on the bed can also mobilize particles besides those mobilized by the action of shear effects alone. The final model that was developed represented the effects of both shear and pressure forces on sediment mobility.

3. A bombardment ejection model was developed to predict the quantity and the velocity of ejected particles after an impact from a previously suspended particle. This model was developed based on the initial velocity and size of the impacting particle, as well as the properties of the sediment bed. Bombardment ejections have been noted to be an important mechanism for mobilizing particles in experiments that have been conducted with rotors operating over mobile sediment beds. An analysis of the outcomes from the model that was developed showed that the process of bombardment generally produces the ejection and rapid build up of a large number of smaller-sized dust particles in the resulting dust cloud.

4. An efficient, multi-step time-marching scheme has been successfully developed to integrate the governing equations describing particle motion. These equations are numerically stiff and required special treatment to preserve their overall stability and accuracy. A variety of numerical experiments showed that the method that was ultimately adopted is stable, convergent, and exhibits good second-order accuracy. The sensitivity of the results obtained for different step sizes was examined, and was shown to exhibit a grid independent behavior for wake discretizations of less than 5° of blade azimuth.

5. The large number of suspended particles typical of brownout conditions means that high accumulating computational costs are a serious concern in any form of calculation of the problem. The computational time required for the simulations was reduced by a factor of 50 by implementing the velocity field computations on graphical processor units (GPUs.) This GPU implementation was performed in double-precision, and it was shown that no additional errors were incurred in the use of this approach.

4.2.2 Comparisons with Measurements

1. Predictions of the rotor flow field near the ground, as obtained with the free-vortex wake method, showed good agreement with measurements from both laboratory-scale and full-scale rotor tests. Predictions of the wake geometry, the tip vortex strengths, and the groundwash velocities were also compared to CFD simulations based on a RANS approach. The comparisons of the radial velocity profiles close

to the ground compared favorably with the measurements and with the CFD, except in the immediate boundary layer region.

2. Predictions of the overall size and three-dimensional features of brownout dust clouds were compared to photogrammetry measurements made with a helicopter at a test range over a prepared sediment bed. The outcomes from the model showed good agreement for the taxi-pass maneuver where the helicopter flew slowly at a relatively constant speed and altitude above the ground. For the approach-to-touchdown maneuver, however, the agreement was generally good along the longitudinal and lateral directions, but the simulated dust clouds were underpredicted in terms of their vertical developments. Both the measurements and the calculations suggested that dust particles were mobilized and entrained into the flow before the helicopter reached the prepared sediment bed, which may account for some of these differences.

3. The predicted dust clouds were found to be relatively sensitive to the weight of the helicopter. Because weight profoundly affects the wake geometry at low airspeeds (especially the wake skew angle), the wake dynamics at the ground are also affected. Sensitivities were noted especially in regions where the rotor wake and its embedded vortices more closely interacted with the ground, often forming a bundle of vortices or a super-vortex. This super-vortex, when formed, was responsible for the mobilization and uplift of large quantities of sediment. The geometry of the dust clouds and the quantity of uplifted dust was found to be more difficult to predict during the approach-to-touchdown maneuver because of the more complicated

wake structures and more intense vortex wake interactions that occurred with the ground.

4.2.3 Analysis of the Dust Cloud Developments

1. Bombardment ejections from the bed were found to be driven by the close passage or the impingement of blade tip vortices onto the underlying sediment bed. Such ejections were enhanced by the bundling of vortex filaments near the bed, such as was found during the approach and takeoff maneuvers. Under these conditions, bombardment ejections produced a rapid increase in the quantity of suspended particles in the evolving dust clouds. This outcome suggests that all things being equal, rotorcraft with stronger tip vortices and/or with more blades (which have a tendency to more easily promote vortex bundling) may be more susceptible to the development of brownout conditions.

2. The formation of ground vortex was found to play critical role in the development of dust clouds during a landing maneuver. The ground vortex can pair and merge with the blade tip vortices and form a stronger super-vortex upstream of the leading edge of the rotor disk. The super-vortex also forms a merging flow region on the bed, from where many particles can be uplifted and then tend to define the outer boundary of the dust cloud. This super-vortex was found to increase the vertical growth of the dust cloud upstream of the rotor disk, eventually resulting in the reingestion of dust back through the rotor disk. Such reginestion processes were generally always associated with many more bombardment ejections, which then

act to quickly increase the quantity of suspended dust.

3. An analysis of the evolving dust clouds at older times showed that they were comprised primarily of smaller-sized particles, a result also seen in field experiments with helicopters encountering brownout conditions. This outcome is because the smaller particles tend to remain suspended in the flow field to long times because of their low settling velocities. A particle quantity analysis showed that many of the smaller-sized particles had been mobilized and uplifted both by unsteady pressure and bombardment ejection mechanisms. These results help to explain why there is generally a preponderance of smaller particles that become suspended in brownout clouds.

4.2.4 Effects of More Diffused Tip Vortices

1. The effects of artificially diffusing the tip vortices was found to have profound effects on the development of the resulting dust clouds. Experiments have previously shown that rotor blades with special slotted tips produced a much more diffused vorticity field when compared to what was obtained using regular blades with rectangular tips. Lower instantaneous velocities and reduced pressure fields were produced by the slotted-tip blade, both near the rotor and at the ground plane. However, the mean flow fields produced were found to be substantially the same.

2. Overall, the rotor system with the artificially enhanced diffusion of the tip vortices generated much less intense dust clouds, mainly because of the significant reduction in the quantity of dust being uplifted by the normal mechanisms of mobilization and

entrainment. The most notable reduction in the dust was from bombardment ejection mechanism, which occurred because of the lower velocity excursions produced by the more diffused tip vortices as they reached the ground.

3. The dust cloud generated by more rapidly diffusing the tip vortices was also found to be more benign from the pilots perspective. In this regard, the overall density of the dust cloud within the pilot's field of view was significantly lower, resulting in lower levels of visual obscuration. The rate of vertical development of the dust clouds was also found to be significantly slower with the more diffused tip vortices, which is also very desirable from the perspective of brownout mitigation.

4.3 Recommendations for Future Research

1. The comprehensive modeling of brownout dust clouds is clearly a significant computational challenge. The high computational cost involved in the calculation of the induced velocity field from the rotor not only limits the time step size that can be used, but also limits the total number of particles that can be convected in the flow. Both of these issues compromise the overall fidelity of dust cloud simulations. To this end, implementation of Fast Multipole Methods (FMM) could be considered to achieve significant reductions in computational time. Ultimately, the best reductions in time can be obtained by implementing the entire methodology on GPUs, i.e., the needed computational accelerations must be achieved by using both the FMM and GPU techniques.

2. The more thorough modeling of the viscous flow in ground effect could be achieved

in the future by using a RANS-based CFD solution. However, a CFD simulation of the entire flow field for a rotorcraft undergoing flight maneuvers is computationally an enormously expensive problem, and will remain computationally intractable in the near term. However, it is possible that some form of hybrid approach can also be formulated in which the flow field from the FVM can be coupled to a boundary layer solution or to a localized CFD solution near the ground. Such an approach should allow the calculation of the friction velocities without any a priori assumptions of the boundary layer profile.

3. The brownout simulation could be coupled with a full pilot-in-the-loop flight dynamic simulation methodology to better simulate the various flight maneuvers, i.e., moving away from the a priori prescription of the flight profile. The landing maneuvers simulated in the present work were only approximate because of the assumptions made about the rotor trim state. A careful coupling of the rotor solution to a flight dynamics analysis should allow for better simulations of the landing and takeoff maneuvers.

4. The effects of the airframe and tail rotor of the helicopter on the formation of the brownout dust clouds should also be analyzed. The tail rotor can be modeled in a manner similar to that used for the main rotor. However, modeling the aerodynamics of the fuselage requires a panel method or an immersed boundary method approach, which will significantly increase the computational cost of the simulations. Nevertheless, in the future there will be a need to model the elements comprising the complete rotorcraft if accurate quantitative simulations of the brownout clouds

are the ultimate objective.

5. New experiments should be conducted to further understand the processes involved in the mobilization of sediment particles under the action of rotor wake flows. These experiments should be conducted with two main objectives in mind. First, the significance of the shear in the mobilization of sediment must be better understood. Second, the significance of the pressure forces on particle mobilization must be further quantified. These measurements will also help to validate the mobilization and entrainment model that was developed during the course of the present work. Furthermore, experiments should also be conducted to simulate the conditions found during the process of bombardment ejections to help validate the modeling approaches. Although such experiments will require considerable effort, there will be much value to the field if such results can be obtained.

6. Further laboratory-scale experiments and flight tests must also be conducted to measure the overall characteristics of the brownout dust clouds if more thorough validation of the predicted clouds is to be obtained. The measurement of as many parameters as possible must be the objective. While it is understood that not everything that might be desired can be measured, the present results give better insight as to what parameters are more important and those that might be less so. In regard to flight test measurements, parameters such as the actual weight of the helicopter, the instantaneous wind velocities, the actual flight path followed by the helicopter, and the blade control angles should be measured. The characteristics of the dust bed and the various properties of the sediment bed should also be measured if the

more complete validation of modeling approaches is to be obtained.

7. The dust cloud simulation methodology should be advanced further by modeling multidisperse dust clouds, i.e., dust particle simulations should be undertaken with nonuniform particle sizes. To this end, modeling the particle-particle interactions during bombardment ejections and particle collisions may be needed. In regard to bombardment ejections that occur in multidisperse dust clouds, a particle impacting the underlying bed could eject various particles of different sizes. In regard to modeling particle collisions, overcoming high computational costs will remain the main challenge because of the large number of particles present in the dust clouds and the potentially large number of collisions, especially near the ground.

Appendix A

Sediment Layer Activation Delay Time

It has been explained in Section 2.6 how the particles comprising the sediment bed are arranged computationally in the form of layers. Particles that are directly in contact with the external flow are termed as "active" particles, i.e., these particles are eligible to be mobilized if conditions permit. These active particles become mobilized when the mobility criteria of direct entrainment is satisfied, the mathematical conditions being discussed in Section 2.3. Initially, particles in the uppermost sediment layer are active and eligible to be mobilized. Only when the particles from this layer are removed and become entrained into the flow, do the particles in the layer underneath become active.

It is known from videographic results showing the development of actual brownout clouds forming around landing helicopters that the process of mobilization and entrainment of the dust particles is more intermittent rather than continuous, i.e., dust is usually uplifted from the ground in bursts. While the physical mechanisms for this behavior are not yet understood, it is hypothesized to be related to the moisture and compactness characteristics of the sediment particles comprising the bed.

This behavior is computationally modeled in the present work by using the concept of an activation delay time, δt, which is the time period between the activation of two successive particle layers on the sediment bed. While the actual value of δt can only be determined by means of experiments, it was chosen to balance the fidelity of the dust

cloud simulations with the computational expense, which is $O(N^2)$ where N is the total number of particles in the dust cloud; see Section 2.7. Notice that a larger value of δt means that a larger quantity of potentially active particles are present on the sediment bed.

A sensitivity study was conducted to analyze the effects of δt on the dust cloud developments, so as to choose a value of δt that can best represent the physical details of the dust clouds while using the fewest number of particles. For this study, a representative landing maneuver was considered, the details being given in Section 3.3.3. This case was used because most of the results obtained in the present work have been centered around this landing maneuver.

The sediment bed considered in the following example was comprised of a total of 27 layers, with each layer consisting of 10^4 particles. Five different dust cloud simulations were conducted for values of δt, i.e., $\delta t = 0.25$, 0.5, 1.0, 1.5 and 2.0 s. Notice that the number of active particles at a given time, t, in the simulation by using a delay time, δt, will be $[(1 + t/\delta t) \times 10^4]$, i.e., there will be more potentially active particles when using smaller values of δt.

Figure A.1 shows the time-histories of the quantity of particles present in the dust clouds by using different values of δt. Notice that the dust clouds with smaller values of δt contained many more particles, which is a consequence of having more active particles on the sediment bed at a given time, as was explained previously. Furthermore, notice that the number of uplifted particles show convergence as the value of δt is reduced. These convergence characteristics vary with the flight condition, and can be further analyzed by examining the normalized quantity of particles in the dust clouds.

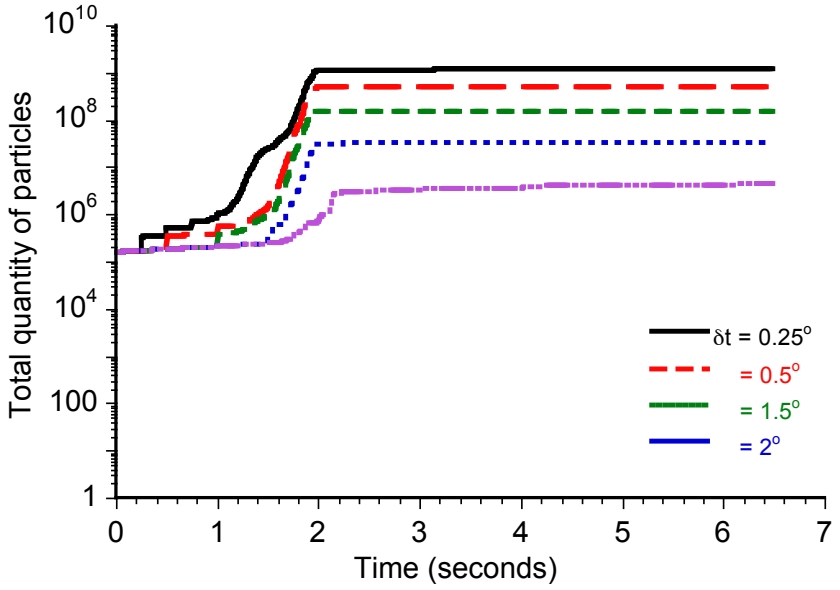

Figure A.1: Time-histories of the total number of particles in the dust clouds obtained using different delay times, i.e., in this case with $\delta t = 0.25$, 0.5, 1.0, 1.5 and 2.0 s.

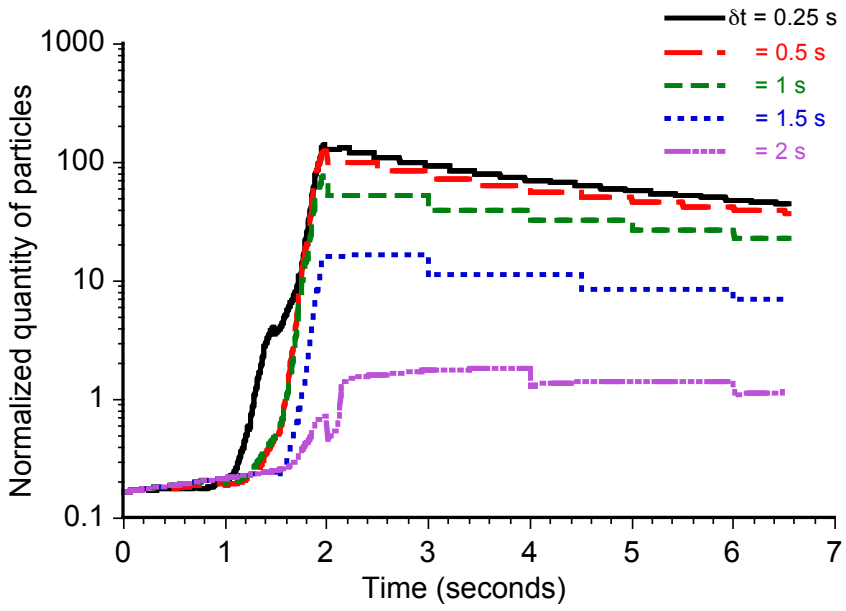

Figure A.2: Time-histories of the normalized number of particles present in the dust clouds obtained with different delay times, i.e., with $\delta t = 0.25$, 0.5, 1.0, 1.5 and 2.0 s. Normalization was performed by using the total number of active particles at a given time.

Normalizationcan be performed by using the total number of active particles on the bed at that time, i.e., by $[(1+t/\delta t)\times 10^4]$ particles. For example, for the simulation made using $\delta t = 1$ s, the normalization at $t = 0$, 1 and 2 s was performed by using 10^4, 2×10^4 and 3×10^4 particles, respectively. Similarly, for the simulation using $\delta t = 0.5$ s, the normalization at $t = 0$, 0.5 and 1 s was performed by using 10^4, 2×10^4 and 3×10^4 particles, respectively.

As shown in Fig. A.2, the normalized quantity of particles also shows variable convergence characteristics, depending upon the flight condition. Transient convergence can be observed when the helicopter was decelerating and approaching the ground, i.e., up to $t = 2.3$ s. The evolutionary characteristics of the wake during these times produced transients in the flow, the effects of which can only be modeled in the dust cloud simulations by using a smaller value of δt. For example, notice in Fig. A.2 that the simulation conducted with $\delta t = 2$ s underpredicts the number of bombardment ejections between $t = 1$ and 2.3 s because the changes in the flow field take place over a shorter time than δt. As the helicopter transitions into hover, a clear asymptotic convergence can be seen in Figs. A.1 and A.2. Details of the wake behavior during this maneuver have been shown in Section 3.3.3.

These results suggest that the choice of δt will be problem dependent. For a steady flight condition, a larger value of δt may be sufficient, however, for a transient or maneuvering flight condition a smaller value of δt may be needed depending, in part, on the time scales of the maneuver relative to the number of rotor revolutions. For the case considered here, a value of δt =1 s provided an acceptable solution, allowing the essential details of the dust clouds to be modeled by using as few particles as possible.

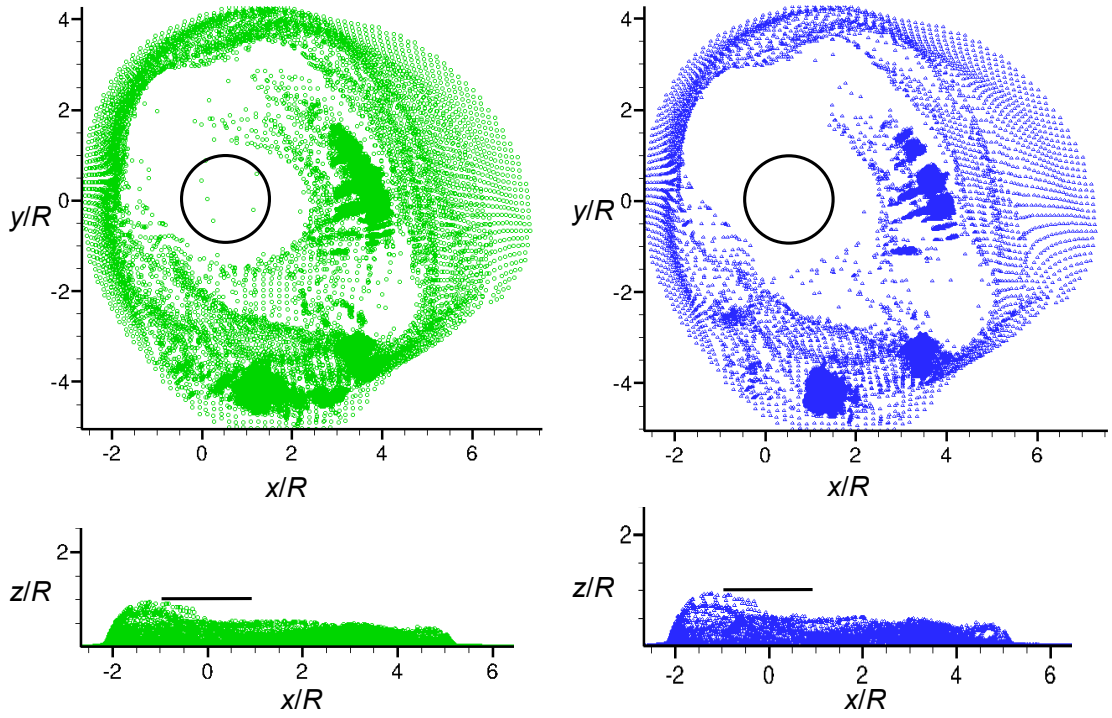

(a) For $\delta t = 0.25$ s

(b) For $\delta t = 1$ s

Figure A.3: Top and side views of the dust clouds obtained using values of δt = 0.25 and 1.0 s, respectively.

Finally, Figs. A.3(a) and A.3(b) show comparisons of the top and side views of the dust clouds that were obtained by using activation delay times of $\delta t = 0.25$ s (green) and $\delta t = 1$ s (blue), respectively; these dust clouds are shown for $t = 3$ s. Notice that the two dust clouds have similar outer envelopes and regions of particle concentrations. The differences are mainly in the number of entrained particles, as was shown previously in Fig. A.1. Therefore, at least for the maneuvers considered in the present study, the dust clouds predicted with $\delta t = 1$ s represents an acceptable trade in terms of modeling fidelity against computational cost. However, it must be recognized that the value of δt is not absolute, and depending on the problem its proper selection will generally require at least some numerical experiments to be performed.

Appendix B

Utilization of Parallel Hardware for High-Performance Computing

The numerical solution for the free-vortex wake and the dust cloud can be accelerated by using the state-of-the-art parallel computing techniques, e.g., openMP, Message Passing Interface (MPI), Graphical Processing Units (GPU) programming, etc. In the present work, hardware parallelism of the multicore architecture of CPUs was utilized using MPI (Ref. 125), and that of the GPUs by using the Compute Unified Device Architecture (CUDA) (Ref. 126).

B.1 Parallelization on Multiple CPU Threads using MPI

In the first attempt to expedite the brownout simulations, the methodology was designed to be executed on multiple processors by using MPI (Ref. 125). In this regard, the initial number of particles on the sediment bed can be equally divided into groups based on their spatial location. The total number of groups depend upon the total number of available "threads" on the processors.

For example, Fig. B.1 shows an example of the vertical component of rotor flow velocity on the sediment bed (which spans from x/R, $y/R = -5$ to 5). The sediment bed in this case was divided into four groups, and the convection of particles in each group is carried out in their respective threads. These threads can be the cores of a multicore processor or nodes of a high-performance cluster. In the present formulation of

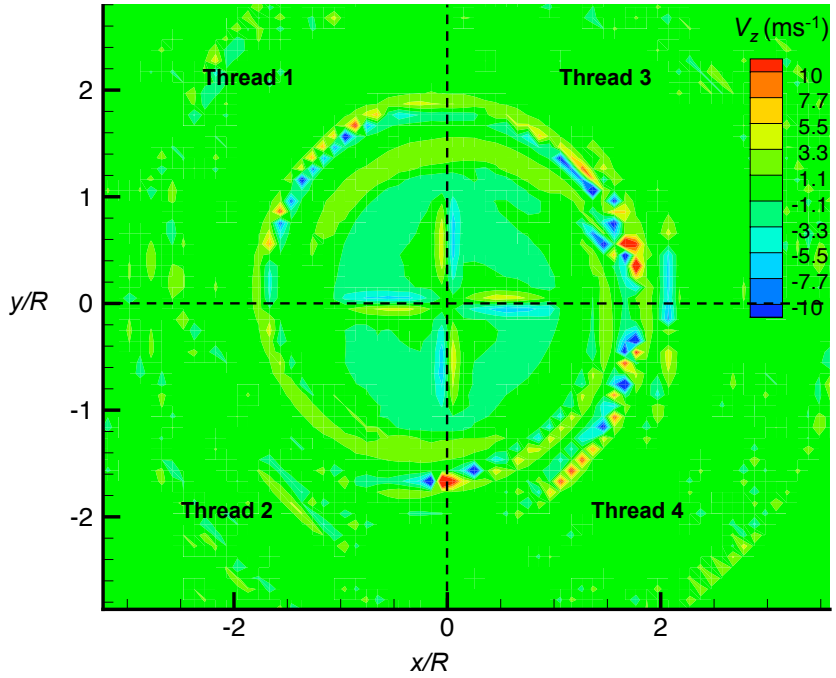

Figure B.1: Grouping of a sediment bed into different regions. The convection of particles in individual regions is carried out in different threads.

the methodology, particles were convected in the flow field independently of the other particles. The parallelization of this problem then becomes a single instruction multiple data (SIMD) problem, in which a single instruction can be computed independently in the different threads.

However, there are several challenges involved in this parallelization process. For the parallelization process to be efficient, the algorithm must be designed such that there is a minimum of interactions between the different threads. Also, the work assigned to different threads must be balanced equally such that the total number of induced velocity computations must be approximately equal in each thread. In the present formulation of the problem, the induced velocity computations take place only for "active" particles; see Section 2.6. Particles stationary on the bed then become active depending upon the

induced velocity field produced on the sediment bed, i.e., particles stationary in regions of high induced velocities will have higher possibility of becoming active.

For example, for the velocity field shown in Fig. B.1, threads 3 and 4 will contain a higher number of active particles when compared to other threads. At other times, this scenario may change depending upon the velocity field, and other threads may contain a higher number of active particles. This makes the parallelization a dynamic process in which the number of active particles must be balanced in all the threads at each time step. Secondly, the particles ejected after bombardments can make the work balance between the threads very uneven. Bombardment ejections usually take place in regions of high flow velocity on the bed. The particles ejected by bombardment ejections are initially assigned to the thread to which the impacting particle belongs. However, bombardment can turn into a local chain reaction and eject a very large number of particles, which can then make the work balance between different threads very uneven. The thread with larger number of particles will take more computational time, and this outcome can become the bottleneck in solving the problem.

It is, therefore, important to dynamically balance the work between different threads by dividing the active particles equally into each thread at the end of each time step. To achieve this goal, the concept of a "master" thread was used, which balances the work between all of the threads at each time step. This master thread, however, does not perform any actual computations. In this respect, the other threads can be called as the "working" threads. All of the working threads send information about the total number of active particles to the master thread at each time step. The master thread then calculates the mean of the total number of active particles in the brownout simulation, and

balances the work between all the working threads. In the present work, the parallelization algorithm was designed such that the working threads interact only with the master thread, and not with each other. This strategy was adopted so as to minimize the communications between the working threads. Notice that a limitation of the present approach, is that except for balancing the work between the working threads, the master thread for the most part remains computationally idle.

The performance of this foregoing implementation was tested on an actual brownout calculation with a rotor hovering at one rotor radius above the ground. The total number of particles in the simulation was only 10,000, which was sufficient to understand the process. The simulations were performed on a MacPro with two Intel Xeon quad-core processors. The total CPU time taken to execute the brownout simulations with a different number of working threads is shown in Fig. B.2. Notice that the computational time reduces by increasing the number of working threads. For example, the time taken reduces by half by using two threads. However, for a larger number of threads the time reduces only marginally. As per the law of diminishing returns, the CPU time becomes almost constant for the simulations if more than five working threads are used. The reason for this outcome is the overheads produced by: (a) the number of communications between the working and master threads, which increase by increasing the number of working threads, and (b) the memory access costs involved by outputting and writing particle data into different files, which becomes more significant than for the induced velocity computations. Therefore, for the most part the performance of the parallelization process is bounded by the costs involved in communicating between the different working threads and the master thread at each time step. This cost can be reduced by using the parallel

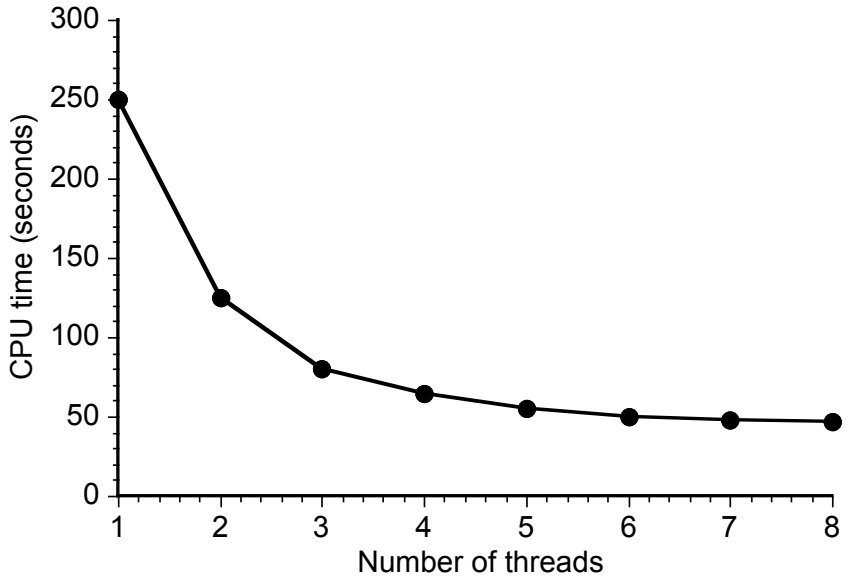

Figure B.2: Performance gain with GPU implementation of the dust cloud simulation.

architecture of GPUs, which is discussed next.

B.2 Parallelization on GPUs

The multicore architecture of graphical processing units (GPUs) was also used to perform parallel computations. A GPU is a highly parallel, multithreaded, many-core processor with high computational power and memory bandwidth. GPUs are designed for efficient single instruction multiple data (SIMD) computations, with more transistors being devoted to data processing rather than to data caching and flow control, as shown in Fig. B.3.

Over the years, GPU architectures have evolved tremendously. Although earlier GPUs were optimized for gaming purposes, current GPUs are capable of both single- and double-precision scientific computations. GPUs employ a threaded parallel computational architecture. High-end GPUs designed for computations are already incorporated

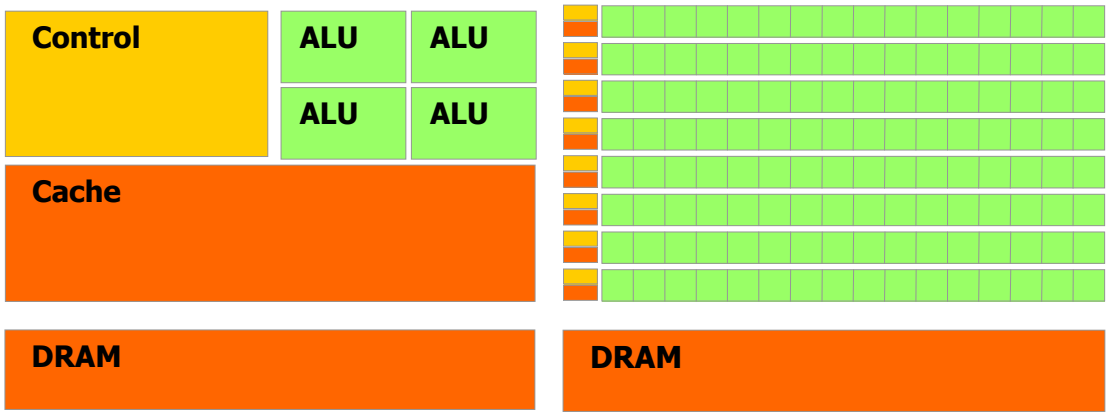

(a) CPU (b) GPU

Figure B.3: Memory architecture on a CPU versus a GPU (Ref. 126).

into many high-end performance clusters to achieve computational speeds in the high Tera-FLOPs range (Ref. 127). A FLOP (floating-point operations per second) is a measure of performance in scientific calculations, where Tera-FLOPs denote that GPUs can execute 10^{12} floating-point operations per second, which is at least an order of magnitude faster than the computational speeds obtained with high-performance CPUs.

In the GPU computations, data from the CPU are transferred to the GPU memory back-and-forth during the entire computational process. However, these CPU-GPU memory communications are expensive to perform when compared to GPU computations. Therefore, the philosophy of GPU programming is to minimize data transfer, while processing as much data on the GPU as possible per data transfer.

One main challenge in GPU programming is to efficiently use the hierarchical memories in the threaded model given the tradeoff between speed and size. Details on the different types of GPU memories is given in Ref. 128. Programming on GPUs can be performed by using a general-purpose parallel computing architecture called CUDA

(Ref. 126), which was developed by NVIDIA. CUDA allows a programmer to easily manipulate the structure of the GPU and use a large number of threads by executing them in parallel to each other. Tremendous performance gains can be obtained by using hundreds of cores of GPUs versus a limited number of cores present on a multiprocessor CPU.

In the present work, only the induced velocity computations were performed on the GPUs. Therefore, at each time step positions of particles were transferred from the CPU to the GPU, and the velocities induced at these particles were transferred back from the GPU to the CPU. The parameters of the rotor wake solution, i.e., the wake geometries, the vortex strengths, and the core radii, are transferred only once from the CPU to the GPU, and are stored in the constant memory of the GPU for use by all of the GPU threads. Because of the very high memory bandwidth of the current state-of-the-art GPUs (i.e., $\sim$200 GB/s), the velocity computations needed for a very large number of particles ($\sim O(10^7)$) can be performed with only one CPU-GPU transfer per time step.

A study was undertaken to compare the computational time required to execute brownout dust cloud simulations on: (a) a parallel platform utilizing multiple cores of the CPU, and (b) a multi-core GPU architecture. If there are N_v number of vortex elements and N is number of particles in the simulations, then the problem becomes $O(N \times N_v)$. In the present study, N_v was considered to be 1500 and N was varied from 100 to 10^7. The current study was performed on a Mac Pro with a dual 2.66 GHz Quad-core; the GPU was NVIDIA GeForce GTX 285 with 220 cores.

Figure B.4 shows gain in computational performance obtained by using 8 threads of a CPU and by using one GPU. In this study, the velocity field computations on GPU were performed in single-precision; however, all the computations in CPU were performed in

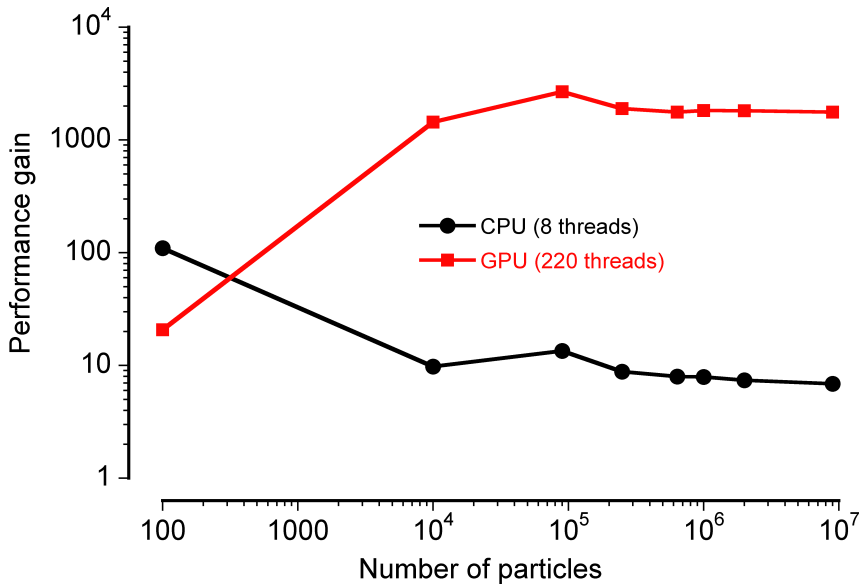

Figure B.4: Comparison of computational performance gains obtained from code parallelization and by using GPUs.

double-precision. The results clearly show that while using 8 threads gives a speedup by about 7 times, the speedup obtained from the GPU compared to the 8 threads on the CPU is approximately three orders of magnitude. This simple analysis shows the massive performance gainsthat can be potentially obtained by GPUs for brownout simulations.

In another study, a more advanced GPU Tesla C2050 was used with Fermi architecture, which is optimized for double-precision computations. Figure B.5 shows the computational performance gains obtained for such brownout simulations as implemented on both the single-precision and double-precision GPU architectures with different particle counts. The performance gain is defined as a ratio of wall-clock times required to run a case by using a GPU architecture versus the full CPU simulation. The results obtained are clearly very impressive: 250 times speed-up with single-precision and 25 times speed-up with double-precision.

The accuracies of both single- and double-precision implementations of the velocity field computations on the GPU were compared to the double-precision CPU results for a brownout simulation of a rotor hovering at $z/R = 1$. The number of particles considered was 5,000. The absolute errors in the calculations of the velocities, $\mathbf{V}$, and positions, $\mathbf{X}_p$, of all of the particles in the simulations that were conducted on the GPU are compared to those of the CPU computations. Table B.1 shows a comparison of the maximum absolute errors in the velocities, $\varepsilon_{\mathbf{V}_{\max}}$, and the positions, $\varepsilon_{\mathbf{X}_{\max}}$, at three different times $t =$ 0.0065, 1.3, 7.8 s. Notice that the errors in the calculations that were conducted in single-precision on the GPU increase with time, while the calculations from the corresponding double-precision GPU implementation remains as accurate as the CPU implementation when performed in double-precision. This outcome suggests that the accumulated errors if single-precision is used can become unacceptable at larger times. Therefore, all of the results obtained in the present work were obtained by using a double-precision GPU implementation.

Table B.1: Comparison of maximum errors in calculating particle velocities and positions in two brownout simulations that were conducted on GPUs in single- and double-precision, respectively.

Precision	Parameter	$t = 0.0065$ s	$t = 1.3$ s	$t = 7.8$ s
Single	$\varepsilon_{\mathbf{V}_{\max}}$ (ms^{-1})	3×10^{-6}	1.967	2.679
Single	$\varepsilon_{\mathbf{X}_{\max}}$ (m)	1×10^{-6}	1.04	1.5
Double	$\varepsilon_{\mathbf{V}_{\max}}$ (ms^{-1})	0	0	0
Double	$\varepsilon_{\mathbf{X}_{\max}}$ (m)	0	0	0

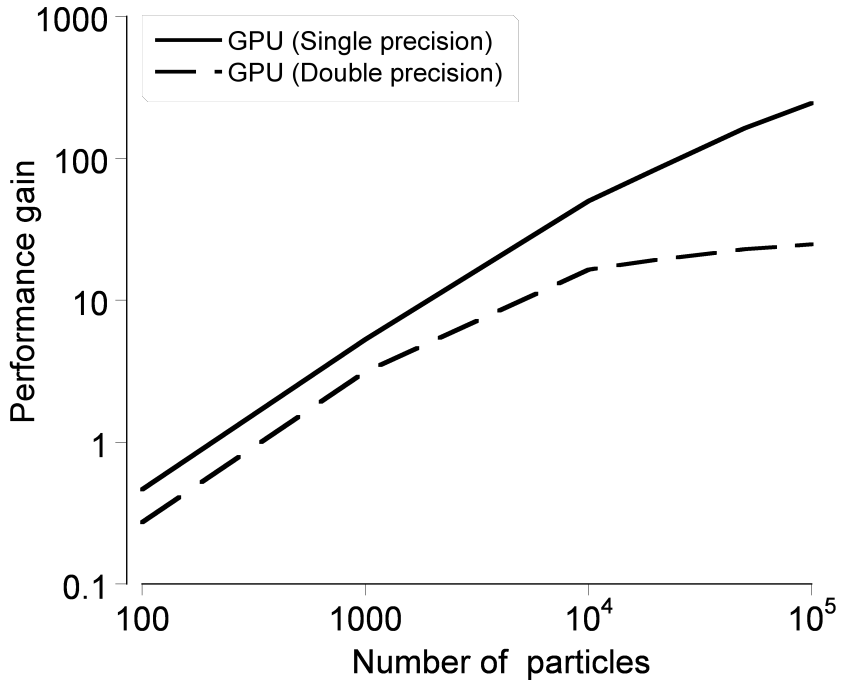

Figure B.5: Performance gain with GPU implementation of the dust cloud simulation.

The maximum size of the calculations that can be performed on a single GPU are limited by the quadratic cost. To consider even larger problems, algorithmic accelerations such as those provided by Fast Multipole Methods (FMM) may be utilized, which can reduce the computational cost to $N \log N$. Hu et al. (Ref. 97) showed that by using the FMM for such problems, and also by implementing the algorithm on GPUs, it can provide speedups of at least two orders of magnitude. This FMM technique, however, was not used in the present work.

Appendix C

Particle Clustering Algorithms

Clustering is a technique that allows for the tracking of groups of particles in a brownout dust cloud instead of tracking them individually. Particles are grouped into clusters, to which the EOMs are then applied, the result being significant savings in computational costs. The particles associated with a cluster are convected to the next time step by using different clustering techniques. The effectiveness of the clustering technique depends on two conditions: (a) the number of clusters should be such that significant computational benefits can be obtained, and (b) the accuracy of the clustered solution must be measurable and within the required solution tolerance. Only if these two conditions are satisfied can clustering techniques be used effectively for predicting the development of the dust clouds.

Wachspress et al. (Ref. 40) employed a Gaussian-based clustering technique for their brownout simulations. However, the accuracy of this technique was not quantified. Govindarajan & Leishman (Ref. 96) have studied the applicability of three particle clustering techniques for brownout simulations: (a) Gaussian-based clustering, (b) the k-means, and (c) Osiptsov's method. The outcomes of this study suggested that each clustering technique has its advantages and disadvantages, and the outcomes from these methods must be analyzed thoroughly to account for any errors that might be incurred during clustering. The Gaussian method, which was designed to preserve the actual com-

puted solution even in regions of high velocity gradients, was shown to provide the most encouraging results when applied to the full brownout problem. Therefore, the Gaussian clustering method is discussed in detail here.

In the Gaussian-based clustering approach, the individual particles in a brownout simulation are treated as clusters; each cluster is associated with a specific number of particles. The clusters are convected at each time step using the EOMs. The positions of individual particles associated with a cluster are calculated by using multi-variate Gaussian distribution.

If there are N particles assumed in the brownout cloud simulation, then each of these particles can be treated as a cluster representing a further N_2 particles, giving a total of $N(N_2+1)$ particles. In the Gaussian method, the N_2 particles around each N particle are distributed in a Gaussian form; they remain with the cluster for the entire simulation even though their positions will change relative to the cluster center.

For these clustered particles to follow the convection of the unclustered particles in the flow at any given time, the mean vector μ_c and covariance matrix Σ_c for each cluster can be defined as

$$\mu_c = \begin{bmatrix} V_{px} & V_{py} & V_{pz} \end{bmatrix} \tag{C.1}$$

and

$$\Sigma_c = \frac{1}{E_c} \begin{bmatrix} k_1|V_{px}|^2 & k_2|V_{px}||V_{py}| & k_2|V_{px}||V_{pz}| \\ k_2|V_{py}||V_{px}| & k_1|V_{py}|^2 & k_2|V_{py}|V_{pz}| \\ k_2|V_{pz}||V_{px}| & k_2|V_{pz}||V_{py}| & k_1|V_{pz}|^2 \end{bmatrix} \tag{C.2}$$

where V_{px}, V_{py} and V_{pz} are the instantaneous velocities of each cluster and E_c is a measure of the kinetic energy. Ideally, the cluster spread should be proportional to E_c. This result,

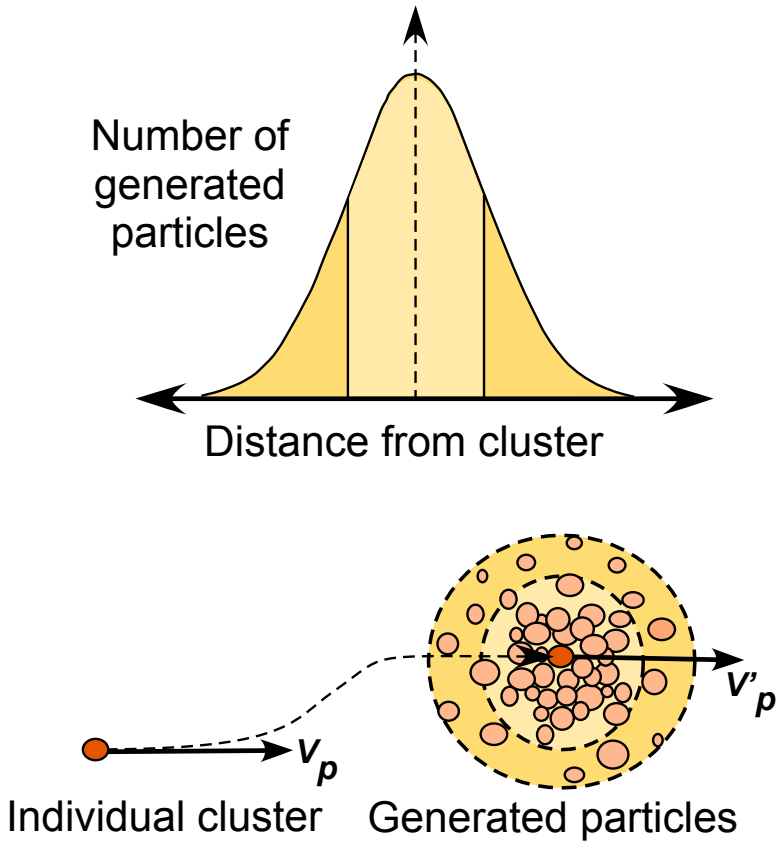

Figure C.1: Schematic showing the Gaussian method of particle clustering. (Source: Ref. 129)

however, would lead to a large non-physical spread of the cluster in regions of high flow velocity. Scaling the covariance matrix by ${E_c}^{-1}$ is, therefore, performed where the local velocities are large, which in a worst case situation would collapse the particles down to the locations of the original particle.

The conditions on the above matrix to be positive definite are

$$k_1 > 0, k_2 > 0, (k_1 - k_2) > 0 \tag{C.3}$$

which is derived from Sylvester's condition for a positive definite matrix (Ref. 130) and

$$\frac{k_2}{k_1} < min\left[\frac{|V_{px}|}{|V_{py}|+|V_{pz}|}, \frac{|V_{py}|}{|V_{px}|+|V_{pz}|}, \frac{|V_{pz}|}{|V_{px}|+|V_{py}|}\right] \tag{C.4}$$

which is derived for a matrix to be diagonally dominant. The parameter k_1 is a scalar that dictates the spread in each of the principal directions, and k_2 can be viewed as a cross-coupling coefficient. The positions of the N_2 particles are then calculated using the velocities obtained from the foregoing distribution matrix.

Estimates of the errors incurred by the clustered solution is important to establish confidence in the clustering technique. Govindarajan (Ref. 129) discussed several error estimation techniques, e.g., the root mean square, or Pearson's coefficient. The limitation of such error estimates is that they are applicable only for simpler problems. Error estimates using Pearson's coefficient showed that if sufficient number of clusters are used in an actual brownout simulation, then the clustered solution can very effectively represent the details of the actual solution.

An example of the application of the Gaussian clustering technique to a simpler flow field is shown in Fig. C.2. The details of this flow is given by Govindarajan (Ref. 129, Chapter 2, pp. 41–45). Figure C.2 shows two solutions: one obtained using the exact computation, and the second one using the Gaussian clustering approach. The exact computation contains 5,625 particles, and in the Gaussian clustering approach 1,125 particle clusters were simulated, each cluster being associated with 5 particles. Figures C.2(a) and C.2(b) compare the positions of particles in the exact simulation and in the clustered solution, respectively. Notice that the two solutions look similar to each other but the cost of obtaining the clustered solution is approximately five times lower than that of the computational cost of the exact simulation. The densities of the particles in the two solutions are compared in Figs. C.2(c) and C.2(d). Notice that these results also look very similar to each other. The errors in the particle density were compared using Pearson's coefficient

with a 90% correlation, the details being given by Govindarajan (Ref. 129).

Govindarajan (Ref. [129]) also found that Pearson's coefficient cannot be used to estimate errors for clustered dust clouds in the three-dimensional case. A very large number of cluster centers must be used to simulate actual brownout clouds before the fidelity of the simulation can be enhanced by using the Gaussian clustering technique. Figure C.3 show a comparison of the solution obtained with 10^6 cluster centers (denoted by the black dots in subfigure Fig. C.3(a)) and one using the distributed particle clusters (Fig. C.3(b)) with a total of 100 particles per cluster, i.e., with 100 million particles. Notice that the clustered solution, as shown by Fig. C.3(b), identifies the actually computed cluster centers as "black" dots, and the particles obtained through the Gaussian clustering technique as "brown" dots. The results clearly show that the clustered solution brings out the finer, structured details of the dust cloud. Figure C.3(c) shows the density of the dust cloud that is derived from the clustered solution, and Fig. C.3(d) shows some details of the dust cloud near the ground, the concentrations of which can be correlated to the positions of the tip vortices in the flow.

Figure C.4 shows the actual simulated and the clustered solutions at a later time step. Again, it can be seen from these results that the clustered solution brings out all the finer details of the actual solution. It has been pointed earlier that the Gaussian clustering technique does not adversely impact the accuracy of the cluster centers, the positions of which are actually computed using the EOMs (i.e., Eqs. 2.86 and 2.87). In fact, in the regions of high velocity gradients where other clustering techniques can cause errors, the Gaussian clustered solution will be the same as the actually computed solution and will not cause any additional errors in the simulation.

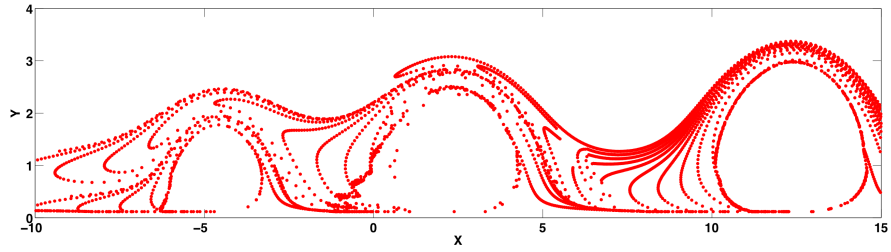

(a) Particle positions - Exact solution

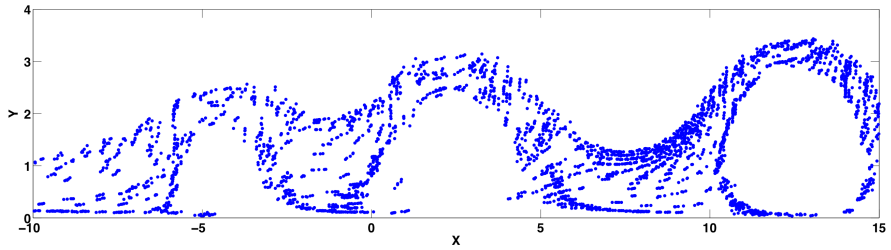

(b) Particle positions - Clustered solution: Gaussian

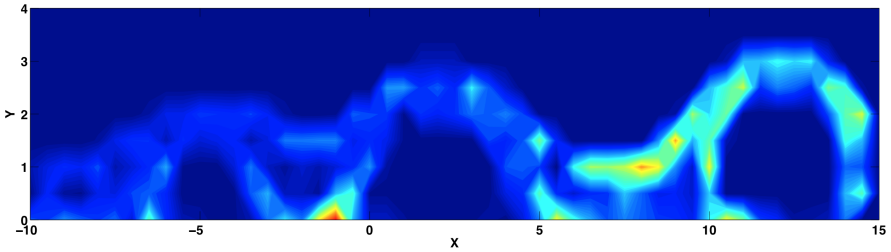

(c) Density contour plot - Exact solution

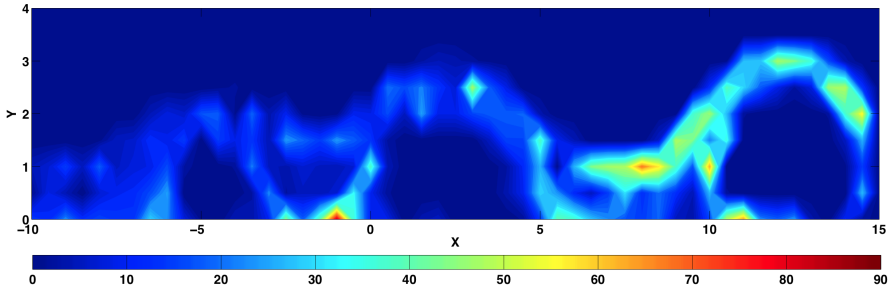

(d) Density contour plot - Clustered solution: Gaussian

Figure C.2: An example of Gaussian solution obtained from Ref. 129: Total number of clusters = 1,125, total number of particles per cluster = 5, i.e., total number of particles in the clustered solution = 5,625.

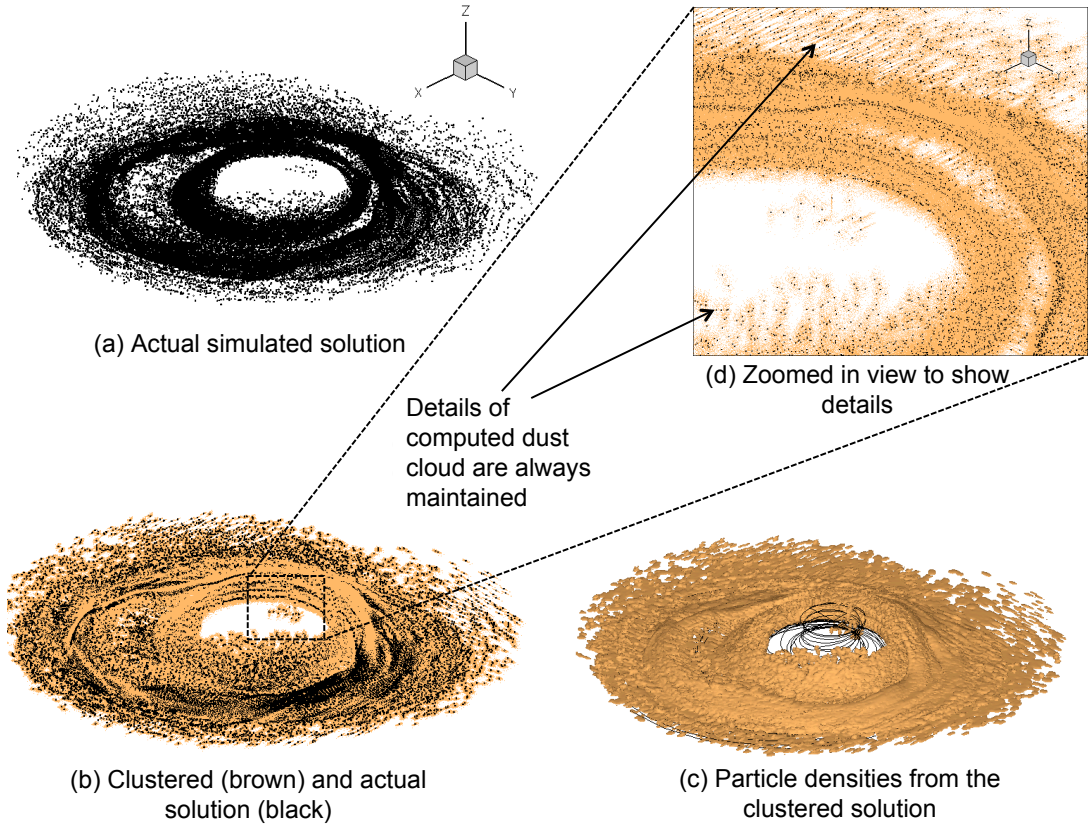

Figure C.3: A solution obtained from brownout dust field computations when using the Gaussian clustering distribution method.

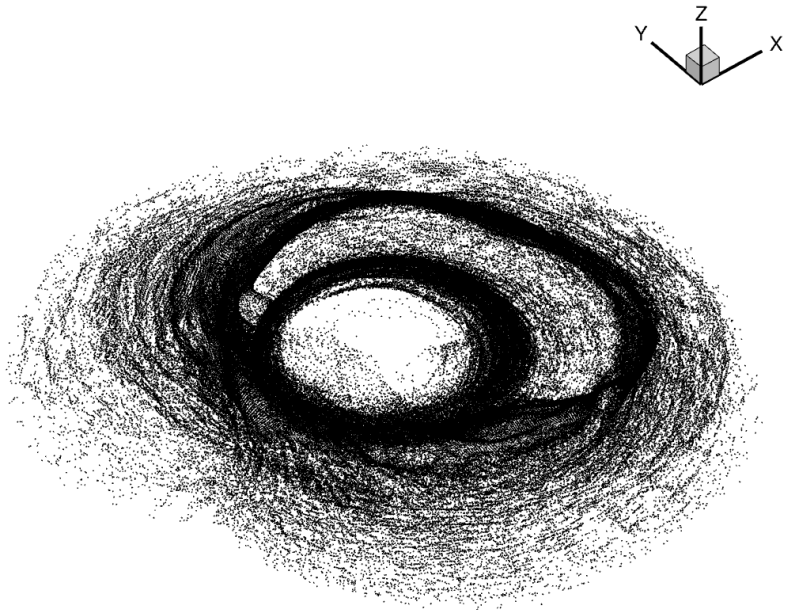

(a) Actual simulated solution

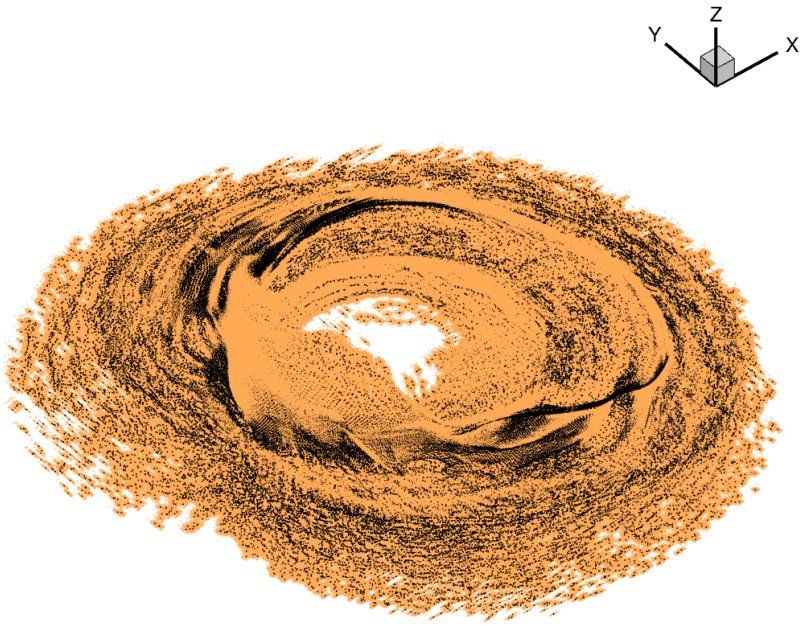

(b) Gaussian clustered solution

Figure C.4: Another example of a brownout dust field computation using the Gaussian clustering distribution method. (Source: Ref. 129)

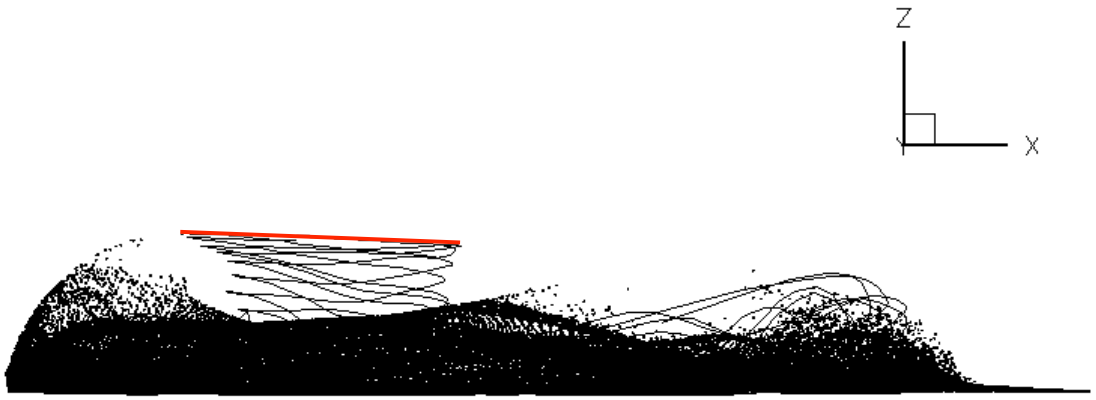

(a) Actual simulated solution

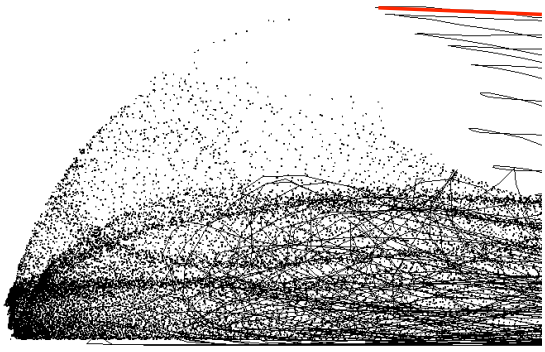

(b) Zoomed in view of the actual solution

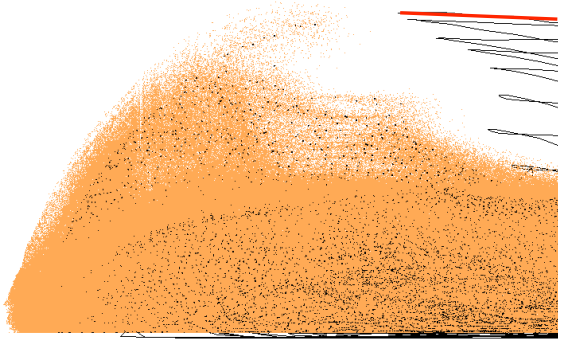

(c) Zoomed in view of the Gaussian clustered solution

Figure C.5: Actual and clustered solution during a landing maneuver using the Gaussian clustering distribution method. (Source: Ref. 129)

A further comparison of the side views of these two dust clouds are shown in Fig. C.5; Fig. C.5(a) shows a complete side view of the actual calculated brownout cloud, and Figs. C.5(b) and C.5(c) show the detailed views of the front of the rotor disk as obtained from the actual simulation as well as the clustered solution. Notice that the dimensions of the brownout dust cloud obtained using the clustering technique are nearly the same as the dimensions from the exact solution. Overall, these results show that the Gaussian clustering method can be reliably used to bring out the finer details of the dust cloud without adding substantially to the computational cost. Therefore, this method was used in the present work to simulate brownout dust clouds.

Appendix D

Helicopter Rotor Specifications

This Appendix provides the specifications of the different helicopter rotors that were used for analysis in the present work. Five different rotor system were used: (a) Laboratory-scale rotor 1, (b) Laboratory-scale rotor 2, and (c) Full-scale exemplar helicopter rotor, (d) CH-54 rotor, and (e) UH-1 rotor.

Table D.1: Specifications of laboratory scale Rotor 1.

Parameter	Value
Number of rotors, N_r	1
Number of blades, N_b	2
Rotor diameter, D	0.408 m
Chord, c	0.0445 m
Twist, θ_{tw}	0°
Angular velocity, Ω	194.78 rad s^{-1}

Table D.2: Specifications of laboratory scale Rotor 2.

Parameter	Value
Number of rotors, N_r	1
Number of blades, N_b	2
Rotor diameter, D	0.086 m
Chord, c	0.019 m
Twist, θ_{tw}	0°
Solidity, σ	0.14
Angular velocity, Ω	314.15 rad s^{-1}
Collective pitch, θ_0	12°

Table D.3: Specifications of a full-scale exemplar helicopter rotor.

Parameter	Value
Number of rotors, N_r	1
Number of blades, N_b	4
Rotor diameter, D	54 ft
Chord, c	1.7 ft
Twist, θ_{tw}	-18°
Solidity, σ	0.083
Angular velocity, Ω	27 rad s^{-1}

Table D.4: Specifications of the CH-54 helicopter rotor.

Parameter	Value
Number of rotors, N_r	1
Number of blades, N_b	6
Rotor diameter, D	11 m
Chord, c	0.66 m
Twist, θ_{tw}	-6°
Solidity, σ	0.115
Angular velocity, Ω	19.37 rad s^{-1}

Table D.5: Specifications of the UH-1 helicopter rotor.

Parameter	Value
Number of rotors, N_r	1
Number of blades, N_b	2
Rotor diameter, D	7.32 m
Chord, c	0.533 m
Twist, θ_{tw}	-10.9°
Solidity, σ	0.138
Angular velocity, Ω	33.5 rad s^{-1}

Appendix E

Projecting the Brownout Cloud in the Pilot's FOV

With an understanding that brownout is fundamentally a fluid dynamics problem but ultimately a piloting concern, a metric developed by Tritschler et al. (Ref. 87), was adopted to describe the effects of a given brownout cloud on the pilot's ability to control the aircraft. From a handling qualities point of view, a brownout cloud that completely deprives the pilot of visual cues is intuitively "bad," while one that allows perfect visibility is intuitively "good." The brownout metric utilized in the present study is one form of measure of the density of the dust cloud, and hence can be used as a surrogate for the visibility through the cloud from the pilot's perspective.

The calculations are obtained by first projecting the position of each particle in the dust cloud onto a sphere that is centered at the pilot's head. This projection is performed through a sequence of coordinate transformations from a ground-based Cartesian coordinate system to a pilot-centered spherical coordinate system, as shown in Fig. E.1. The details of this procedure are given by Tritschler et al. (Ref. 87). This procedure results in a distribution of dust cloud density in the pilot's field of view, which can be used as a surrogate for the visual obscuration that the pilot experiences during the development of the brownout cloud.

It is important to note that there are only certain regions of the brownout cloud that can potentially affect the pilot's ability to maintain control of the aircraft. To account for

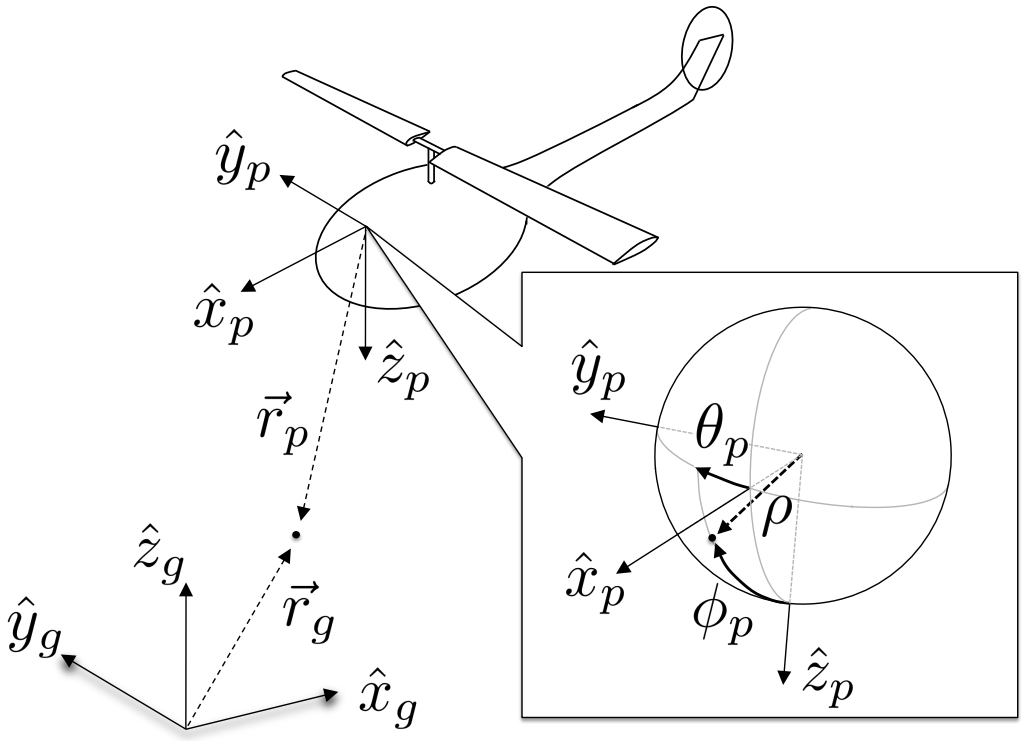

Figure E.1: Diagram depicting the necessary coordinate transformations for projecting the cloud in the pilots FOV. (Source: Ref. 132).

this effect, a 200° by 120° region to the front of the aircraft was chosen as being typical of a pilot's binocular field of view (FOV) (Ref. 131). It should be noted here that the cockpit design of each aircraft (and additional equipment such as night vision goggles) can impose significant constraints on the pilot's FOV; a representative right-seat cockpit FOV is shown in Fig. E.2) though such additional equipment factors are not considered in the present level of analysis.

The metric used in the present study is the sum of the particles within the pilot's FOV over the duration of the simulation. Stated mathematically, the metric, *B*, is defined

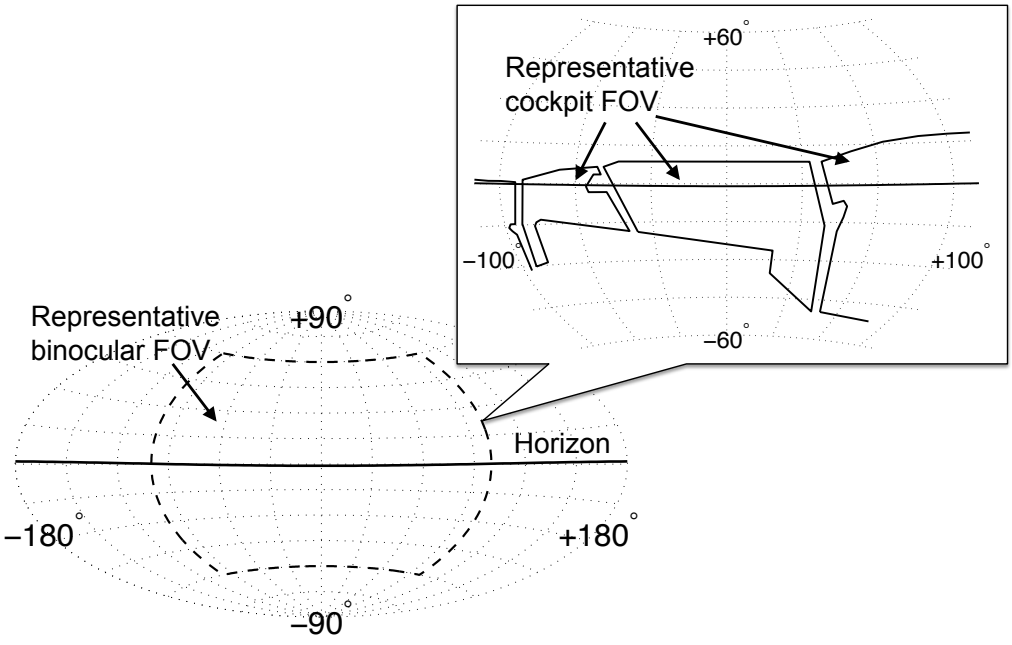

Figure E.2: Representation of the visual scene surrounding a pilot. The FOV is constrained by both human and aircraft cockpit window limitations. (Source: Ref. 132.)

as

$$B = \sum_{t=1}^{N_t} \left[\sum_{\phi_P=-60^\circ}^{60^\circ} \sum_{\theta_P=-100^\circ}^{100^\circ} n_P(\phi_P, \theta_P) \right]$$

where t is the time step index, T is the total number of time steps in the simulation, and $n_P(\phi_P, \theta_P)$ is the number of dust particles in the one-degree solid angle centered at ϕ_P and θ_P. Notice that this metric is simply a first step toward the development of a more thorough optical metric that describes handling qualities degradation during brownout conditions. For example, metrics could be developed to incorporate the Modulation Transfer Function (MTF) (Ref. 133), which can be used as a better quantitative measure of the loss of visibility caused by the brownout cloud (Ref. 88), and to determine when degraded visual conditions are experienced by the pilot.

Bibliography

[1] Mapes, P., Kent, R., and Wood, R., "DOD Helicopter Mishaps FY85- 05: Findings and Recommendations," US Air Force, 2008.

[2] National Transportation Safety Board, NTSB Accident Briefs: LAX01LA283, LAX01LA304, LAX04LA285, SEA05CA173.

[3] Warren, T., Hong, S. C., Yu, C. J., and Rosenzweig, E. L., "Enhanced Erosion Protection for Rotor Blades," 65th Annual Forum Proceedings of the American Helicopter Society, Grapevine, TX, May 27–29, 2009.

[4] Jansen, C., Wennemers, A., and Groen, E., "FlyTact: A Tactile Display Improves a Helicopter Pilots Landing Performance in Degraded Visual Environments," *Haptics: Perception, Devices and Scenarios*, Vol. 502, No. 4, 2008, pp. 867–875.

[5] "Sandblaster 2: Support of See-Through Technologies for Particulate Brownout," Task 1 Technical Report, Sponsored by the Defense Advanced Research Projects Agency (DOD) Strategic Technology Office, Issued by U.S. Army Aviation and Missile Command under Contract No. W31P4Q-07-C-0215, MRI Project No. 110565, October 31, 2007.

[6] "Sandblaster 2: Support of See-Through Technologies for Particulate Brownout," Task 5 Final Technical Report, Sponsored by the Defense Advanced Research Projects Agency (DOD) Strategic Technology Office, Issued by U.S. Army Avia-

tion and Missile Command under Contract No. W31P4Q-07-C-0215, MRI Project No. 110565, October 31, 2007.

[7] Pickford, M., "Operating Helicopters Safely in a Degraded Visual Environment in Support of Military Operations," Proceedings of the Royal Aeronautical Society Rotorcraft Group Conference, Operating Helicopters Safely in a Degraded Visual Environment, London, UK, June 16–17, 2010.

[8] Milluzzo, J., and Leishman, J. G., "Assessment of Rotorcraft Brownout Severity in Terms of Rotor Design Parameters," *Journal of the American Helicopter Society*, Vol. 55, No. 3, DOI: 10.4050/JAHS.55.032000, October 2010.

[9] Cheeseman, I. C., and Bennett, W. E., "The Effect of the Ground on a Helicopter Rotor in Forward Flight," ARC RM 3021, 1955.

[10] Fradenburgh, E. A., "The Helicopter and the Ground Effect Machine," *Journal of the American Helicopter Society*, Vol. 5, No. 4, October 1960, pp. 24–33.

[11] Knight, M., and Hefner, R. A., "Analysis of Ground Effect on the Lifting Airscrew," NACA TN 835, 1941.

[12] Hayden, J. S., "The Effect of the Ground on Helicopter Hovering Power Required," 32nd Annual Forum Proceedings of the American Helicopter Society, Washington D.C., May 10–12, 1976.

[13] Curtiss, H. C., Sun, M., Putman, W. F., and Hanker, E. J., "Rotor Aerodynamics in Ground Effect at Low Advance Ratios," *Journal of the American Helicopter Society*, Vol. 29, No. 1, 1984, pp. 48–55.

[14] Light, J. S., "Tip Vortex Geometry of a Hovering Helicopter Rotor in Ground Effect," *Journal of the American Helicopter Society*, Vol. 38, No. 2, 1993, pp. 34–42.

[15] Prouty, R. W., "Ground Effect and the Helicopter," AIAA Paper 85-4034, AIAA/AHS/ASEE Aircraft Design Systems and Operations Meeting, Colorado Springs, CO, October 14–16, 1985.

[16] Leishman, J. G., *Principles of Helicopter Aerodynamics* 2nd Edition, Cambridge University Press, New York, NY, 2006.

[17] Sydney, A., Baharani, A., and Leishman, J. G., "Understanding Brownout using Near-Wall Dual-Phase Flow Measurements," 67th Annual Forum Proceedings of the American Helicopter Society, Virginia Beach, VA, May 3–5, 2011.

[18] Johnson, B., Leishman, J. G., and Sydney, A., "Investigation of Sediment Entrainment Using Dual-Phase, High-Speed Particle Image Velocimetry," *Journal of the American Helicopter Society*, Vol. 55, 042003, 2010.

[19] Lee, T. E., Leishman, J. G., and Ramasamy, M., "Fluid Dynamics of Interacting Blade Tip Vortices with a Ground Plane," *Journal of the American Helicopter Society*, Vol. 55, 022005, 2010.

[20] Milluzzo, J., Sydney, A., Rauleder, J., and Leishman, J. G., "In-Ground-Effect Aerodynamics of Rotors with Different Blade Tips," 66th Annual Forum Proceedings of the American Helicopter Society, Phoenix, AZ, May 10–13, 2010.

[21] Nathan, N. D., and Green, R. B., "Measurements of a Rotor Flow in Ground Effect and Visualisation of the Brownout Phenomenon," 64th Annual Forum Proceedings of the American Helicopter Society, Montréal, Canada, April 29–May 1, 2008.

[22] Phillips, C., and Brown, R.E., "Eulerian Simulation of the Fluid Dynamics of Helicopter Brownout," *AIAA Journal of Aircraft*, Vol. 46, No. 4, July 2009, pp. 1,416–1,429.

[23] Bagnold, R. A., *The Physics of Blown Sand and Desert Dunes,* Dover Publications, Inc., Mineola, NY, 1941.

[24] Greeley, R., and Iversen, J. D., *Wind as a Geological Process on Earth, Mars, Venus and Titan,* Cambridge University Press, New York, NY, 1985.

[25] Shao, Y., *Physics and Modelling of Wind Erosion,* Springer, 2nd Edition, 2008.

[26] Sutherland, A. J., "Proposed Mechanism for Sediment Entrainment by Turbulent Flows," *Journal of Geophysical Research*, Vol. 72, No. 24, December 1967, pp. 6,183–6,194.

[27] Rauleder, J., and Leishman, J. G., "Measurements of the Turbulent Flow Environment on the Ground Below a Hovering Rotor," Proceedings of the 37th European Rotorcraft Forum, Gallarate (VA), Italy, September 13–15, 2011.

[28] Shao, Y., Raupach, M. R., and Findlater, P. A., "Effect of Saltation Bombardment on the Entrainment of Dust by the Wind," *Journal of Geophysical Research*, Vol. 98, No. D7, February 1993, pp. 12,719–12,726.

[29] Lu, H., and Shao, Y., "A New Model for Dust Emission by Saltation Bombardment," *Journal of Geophysical Research*, Vol. 104, No. D14, July 1999, pp. 16,827–16,842.

[30] Shao Y., "A Model for Mineral Dust Emission," *Journal of Geophysical Research*, Vol. 106, No. D17, September 2001, pp. 20,239–20,254.

[31] Kalra, T. S., Lakshminarayan, V. K., and Baeder, J. D., "CFD Validation of Micro Hovering Rotor in Ground Effect," 66th Annual Forum Proceedings of the American Helicopter Society, Phoenix, AZ, May 10–13, 2010.

[32] Kalra, T. S., Lakshminarayan, V. K., Baeder, J. D., and Thomas, S., "Methodological Improvements for Computational Study of Hovering Micro-Rotor in Ground Effect," AIAA 2011-3552, 20th AIAA Computational Fluid Dynamics Conference, Honolulu, HI, June 27–30, 2011.

[33] Wachspress, D. A., Keller, J. D., Quackenbush, T. R., Whitehouse, G. R., and Yu, K., "High Fidelity Rotor Aerodynamic Module for Real-Time Rotorcraft Flight Simulation," 64th Annual Forum Proceedings of theAmerican Helicopter Society, Montréal, Canada, April 29–May 1, 2008.

[34] Griffiths, D. A., Ananthan, S., and Leishman, J. G., "Predictions of Rotor Performance in Ground Effect Using a Free-Vortex Wake Model," *Journal of the American Helicopter Society*, Vol. 50, No. 4, October 2005, pp. 302–314.

[35] Gillies, J. A., Etyemezian, V., Kuhns, H., McAlpine, J. D., King, J., Uppapalli, S., Nikolich, G., and Engelbrecht, J., "Dust Emissions Created by Low-Level Rotary-

Winged Aircraft Flight Over Desert Surfaces," *Atmospheric Environment*, Vol. 44, No. 8, 2010, pp. 1043–1053.

[36] Ryerson, C. C., Haehnel, R. B., Koenig, G. G., and Moulton, M. A., "Visibility Enhancement in Rotorwash Clouds," Paper AIAA-2005-263, 43rd AIAA Aerospace Sciences Meeting and Exhibit, Reno, NV, January 10–13, 2005.

[37] Wenren, Y., Walter, J., Fan, M., and Steinhoff, J., "Vorticity Confinement and Advanced Rendering to Compute and Visualize Complex Flows," Paper AIAA-2006-945, 44th AIAA Aerospace Sciences Meeting and Exhibit, Reno, NV, January 9–12, 2006.

[38] Haehnel, R. B., Moulton, M. A., Wenren, W., and Steinhoff, J., "A Model to Simulate Rotorcraft-Induced Brownout," 64th Annual Forum Proceedings of the American Helicopter Society, Montréal, Canada, April 29–May 1, 2008.

[39] D'Andrea, A., "Numerical Analysis of Unsteady Vortical Flows Generated by a Rotorcraft Operating on Ground: A First Assessment of Helicopter Brownout," 65th Annual Forum Proceedings of the American Helicopter Society, Grapevine, TX, May 27–29, 2009.

[40] Wachspress, D. A., Whitehouse, G. R., Keller, J. D., Yu, K., Gilmore, P., Dorsett, M., and McClure, K., "A High Fidelity Brownout Model for Real-Time Flight Simulations and Trainers," 65th Annual Forum Proceedings of the American Helicopter Society, Grapevine, TX, May 27–29, 2009.

[41] Rodgers, S. J., "Evaluation of the Dust Cloud Generated by Helicopter Rotor Downwash," USAAVLABS Technical Report, Issued by U.S. Army Aviation Material Laboratories, Fort Eustis, VA, under Contract DA 44-177-AMC-289(T), March 1968.

[42] Wong, O. D., and Tanner, P. E., "Photogrammetric Measurements of an EH-60L Brownout Cloud," 66th Annual Forum Proceedings of the American Helicopter Society, Phoenix, AZ, May 10–13, 2010.

[43] Tanner, P., "Photogrammetric Characterization of a Brownout Cloud," 67th Annual Forum Proceedings of the American Helicopter Society International, Virginia Beach, VA, May 3–5, 2011.

[44] Taylor, M. K., "A Balsa-Dust Technique for Air-Flow Visualization and its Applications to Flow Through Model Helicopter Rotors in Static Thrust," NACA Technical Note 2220, Langley Aeronautical Laboratory, Langley Air Force Base, VA, November 1950.

[45] Haehnel, R. B., and Dade, W. B., "Physics of Particle Entrainment Under the Influence of an Impinging Jet," Proceedings of Army Science Conference, Orlando, FL, December 1–4, 2008.

[46] Mulinti, R., and Kiger, K., "Two-Phase PIV Measurements of Particle Suspension in a Forced Impinging Jet," 63rd Annual Meeting of the APS Division of Fluid Dynamics, Vol. 55, No. 16, November 21–23, 2010.

[47] Geiser, J., and Kiger, K., "A Simplified Analog for a Rotorcraft-in-Ground-Effect Flow Using a Forced Impinging Jet," 63rd Annual Meeting of the APS Division of Fluid Dynamics, Vol. 55, No. 16, November 21–23, 2010.

[48] Betz, A., "The Ground Effect on Lifting Propellers," NACA TM 836, April 1937.

[49] Krishnamurthy, K., *Principles of Ideal-Fluid Aerodynamics* Wiley, New York, NY, 1966.

[50] Lakshminarayan, V. K., and Baeder, J. D., "Computational Investigation of Micro Hovering Rotor Aerodynamics," *Journal of the American Helicopter Society*, Vol. 55, 022001, 2010, pp. 14–29.

[51] Lakshminarayan, V. K., "Computational Investigation of Micro-Scale Coaxial Rotor Aerodynamics in Hover," Ph.D. Dissertation, Department of Aerospace Engineering, University of Maryland, College Park, MD, 2009.

[52] Buelow P. E. O., Schwer D. A., Feng J., and Merkle C. L., "A Preconditioned Dual-Time, Diagonalized ADI scheme for Unsteady Computations," AIAA Paper 1997-2101, 13th AIAA Computational Fluid Dynamics Conference, Snowmass Village, CO, June 29–July 2, 1997.

[53] Pandya, S. A., Venkateswaran, S., and Pulliam, T. H., "Implementation of Preconditioned Dual-Time Procedures in OVERFLOW," AIAA Paper 2003-0072, 41st AIAA Aerospace Sciences Meeting and Exhibit, Reno, NV, January 6–9, 2003.

[54] Spalart, P. R., and Allmaras, S. R., "A One-equation Turbulence Model for Aerodynamic Flows," AIAA 1992-0439, 30th AIAA Aerospace Sciences Meeting and Exhibit, Reno, NV, January 6–9, 1992.

[55] Rajagopalan, R. G., and Fanucci, J. B., "Finite Difference Model for Vertical Axis Wind Turbines," *Journal of Propulsion and Power*, Vol. 1, 1985, pp. 432–436.

[56] Phillips, C., and Brown, R., "Eulerian Simulation of the Fluid Dynamics of Helicopter Brownout," 64th Annual Forum Proceedings of the American Helicopter Society, Montréal, Canada, April 29–May 1, 2008.

[57] Phillips, C., Kim, H. W., and Brown, R.E., "The Flow Physics of Helicopter Brownout," 66th Annual Forum of the American Helicopter Society, Phoenix, AZ, May 10–13, 2010.

[58] Brown, R.E., "Rotor Wake Modeling for Flight Dynamic Simulation of Helicopters," *AIAA Journal*, Vol. 38, No. 1, January 2000, pp. 57–63.

[59] Brown, R.E., and Line, A. J., "Efficient High-Resolution Wake Modeling using the Vorticity Transport Equation," *AIAA Journal*, Vol. 43, No. 7, July 2005, pp. 1,434–1,443.

[60] Toro, E. F., "A Weighted Average Flux Method for Hyperbolic Conservation Laws," *Proceedings of the Royal Society of London, Series A: Mathematical and Physical Sciences*, Vol. 423, No. 1864, 1989, pp. 401–418.

[61] Keller, J. D., Whitehouse, G. R., Wachspress, D. A., Teske, M. E., and Quackenbush, T. R., "A Physics-Based Model of Rotorcraft Brownout for Flight Simulation

Applications," 62nd Annual Forum Proceedings of the American Helicopter Society International, Phoenix, AZ, May 9–11, 2006.

[62] Bagai, A., "Contributions to the Mathematical Modeling of Rotor Flow-Fields using a Pseudo-Implicit Free-Wake Analysis," Ph.D. Dissertation, Department of Aerospace Engineering, University of Maryland, College Park, MD, 1995.

[63] Bagai, A., and Leishman, J. G., "Rotor Free-Wake Modeling using a Relaxation Technique - Including Comparisons with Experimental Data," *Journal of the American Helicopter Society*, Vol. 40, No. 3, July 1995, pp. 29–41.

[64] Bhagwat, M. J., "Mathematical Modeling of the Transient Dynamics of Helicopter Rotor Wakes Using a Time-Accurate Free-Vortex Method," Ph.D. Dissertation, Department of Aerospace Engineering, University of Maryland, College Park, MD, 2001.

[65] Bhagwat, M. J., and Leishman, J. G., "Time-Accurate Modeling of Rotor Wakes Using A Free-Vortex Wake Method," Proceedings of the 18th AIAA Applied Aerodynamics Conference, Denver, CO, August 2000.

[66] Bhagwat, M. J., and Leishman, J. G., "Stability, Consistency and Convergence of Time-Marching Free-Vortex Rotor Wake Algorithms," *Journal of the American Helicopter Society*, Vol. 46, No. 1, January 2001, pp. 59–71.

[67] Bhagwat, M. J., and Leishman, J. G., "Accuracy of Straight-Line Segmentation Applied to Curvilinear Vortex Filaments," *Journal of the American Helicopter Society*, Vol. 46, No. 2, April 2001, pp. 166–169.

[68] Leishman, J. G., Bhagwat, M. J., and Bagai, A., "Free-Vortex Filament Methods for the Analysis of Helicopter Rotor Wakes," *Journal of Aircraft*, Vol. 39, No. 5, 2002, pp. 759–775.

[69] Ananthan, S., and Leishman, J. G., "Role of Filament Strain in the Free-Vortex Modeling of Rotor Wakes," *Journal of the American Helicopter Society*, Vol. 49, No. 2, April 2004, pp. 176–191.

[70] Bhagwat, M. J., and Leishman, J. G., "Generalized Viscous Vortex Core Models for Application to Free-Vortex Wake and Aeroacoustic Calculations," 58th Annual Forum Proceedings of the American Helicopter Society, Montréal, Canada, June 11–13, 2002.

[71] Pomeroy, J. W., and Gray, D. M., "Saltation of Snow," *Water Resources Research*, Vol. 26, No. 7, 1990, pp. 1,583–1,594.

[72] Wenren, Y., Steinhoff, J., and Caradonna, F., "Application of Vorticity Confinement to Rotorcraft Flows," 31st European Rotorcraft Forum, Florence, Italy, September 12–16, 2005.

[73] Steinhoff, J., and Wenren, Y., "An Efficient Vorticity Confinement Based Lifting Surface Method for Rotor Wake Computations," 32nd European Rotorcraft Forum, Maastricht, Netherland, September 12–14, 2006.

[74] White, B. R., "Soil Transport by Winds on Mars," *Journal of Geophysical Research*, Vol. 84, No. B9, August 1979, pp. 4,643–4,651.

[75] Shao Y., and Lu, H., "A Simple Expression for Wind Erosion Threshold Friction Velocity," *Journal of Geophysical Research*, Vol. 105, No. D17, 2000, pp. 22,437–22,443.

[76] D'Andrea, A., "Unsteady Numerical Simulations of Helicopters and Tiltrotors Operating in Sandy-Desert Environments," Proceedings of the American Helicopter Society Specialists Conference on Aeromechanics, San Francisco, CA, January 20–22, 2010.

[77] D'Andrea, A., and Scorcelletti, F., "Enhanced Numerical Simulations of Helicopter Landing Maneuvers in Brownout Conditions," 66th Annual Forum Proceedings of the American Helicopter Society, Phoenix, AZ, May 11–13, 2010.

[78] D'Andrea, A., "Development and Application of a Physics-Based Computational Tool to Simulate Helicopter Brownout," Proceedings of the 37th European Rotorcraft Forum, Gallarate (VA), Italy, September 13–15, 2011.

[79] Morales, F., and Squires, K. D., "Simulation of Rotor Vortex Interactions with a Particle-Laden Turbulent Boundary Layer," Proceedings of the 29th AIAA Applied Aerodynamics Conference, Honolulu, HI, June 27–30, 2011.

[80] Iversen, J. D., and White, B. R., "Saltation Threshold on Earth, Mars and Venus," *Sedimentology*, Vol. 29, No. 1, February 1982, pp. 111–119.

[81] Marticorena, B., and Bergametti, G., "Modeling the Atmospheric Dust Cycle: 1. Design of a Soil-Derived Dust Emission Scheme," *Journal of Geophysical Research*, Vol. 100, No. D8, August 1995, pp. 16,415–16,430.

[82] Greeley, R., "Saltation Impact as a Means for Raising Dust on Mars," *Planetary and Space Sciences*, Vol. 50, No. 2, February 2002, pp. 151–155.

[83] Greeley, R., Balme, M. R., Iversen J. D., Metzger, S., Mickelson, R., Phoreman, J., and White, B., "Martian Dust Devils: Laboratory Simulations of Particle Threshold," *Journal of Geophysical Research*, Vol. 108, No. E5, 2003, pp. 7-1–12.

[84] Balme, M. R., Stephen, M., Towner, M., Ringrose, T., Greeley, R., and Iversen, J., "Dust Devils on Earth and Mars," *Geophysical Research Letters*, Vol. 30, No. 16, August 2003, pp. 1–4.

[85] Balme, M. R., and Greeley, R., "Dust Devils on Earth and Mars," *Reviews of Geophysics*, Vol. 44, No. RG3003, September 2006, pp. 1–22.

[86] Gillette, D. A., "Fine Particulate Emissions Due to Wind Erosion," *Transactions of the ASABE*, Vol. 20, No. 5, 1977, pp. 0890–0897.

[87] Tritschler, J. K., Syal, M., Celi, R., and Leishman, J. G., "A Methodology for Rotorcraft Brownout Mitigation Using Rotor Design Optimization," 66th Annual Forum Proceedings of the American Helicopter Society, Phoenix, AZ, May 11–13, 2010.

[88] Tritschler, J. K., and Celi, R., "The Use of the Modulation Transfer Function for Brownout Cloud Characterization," *Journal of the American Helicopter Society*, Vol. 55, 045001, 2010.

[89] Tritschler, J. K., and Celi, R., "Ground-Level Measurements of the Modulation Transfer Function of a Brownout Cloud," Proceedings of the 37th European Rotorcraft Forum, Gallarate (VA), Italy, September13–15, 2011.

[90] Harrison, R., Stacey, S., and Hansford, B., "BERP IV: The Design, Development and Testing of an Advanced Rotor Blade," 64th Annual Forum Proceedings of the American Helicopter Society, Montréal, Canada, April 29–May 1, 2008.

[91] Han, O. Y., and Leishman, J. G., "Experimental Investigation of Tip Vortex Alleviation Using a Slotted Tip Rotor Blade," *AIAA Journal*, Vol. 42, No. 3, 2004, pp. 523–535.

[92] Whitehouse, G. R., Wachspress, D. A., Quackenbush, T.R., and Keller, J. D., "Exploring Aerodynamic Methods for Mitigating Brownout," 65th Annual Forum Proceedings of the American Helicopter Society, Grapevine, TX, May 27–29, 2009.

[93] Whitehouse, G. R., Wachspress, D. A., and Quackenbush, T.R., "Aerodynamic Design of Helicopter Rotors for Reduced Brownout," Proceedings of the International Powered Lift Conference, Philadelphia, PA, October 5–7, 2010.

[94] Phillips, C. and Kim, H.W., and Brown, R. E., "Helicopter Brownout—Can it be Modelled?," *The Aeronautical Journal*, Vol. 115, No. 1164, February 2011, pp. 123–133.

[95] Brown, R., and Whitehouse, G., "Modelling Rotor Wakes in Ground Effect," *Journal of the American Helicopter Society*, Vol. 49, No. 3, October 2004, pp. 238–249.

[96] Govindarajan, B., and Leishman, J. G., "Evaluation of Particle Clustering Algorithms in the Prediction of Brownout Dust Clouds," 67th Annual Forum Proceedings of the American Helicopter Society, Virginia Beach, VA, May 3–5, 2011.

[97] Hu, Q., Syal, M., Gumerov, N. A., Duraiswami, R., and Leishman, J. G., "Toward Improved Aeromechanics Simulations Using Recent Advancements in Scientific Computing," 67th Annual Forum Proceedings of the American Helicopter Society, Virginia Beach, VA, May 3–5, 2011.

[98] Greengard, L., and Rokhlin, V., "A Fast Algorithm for Particle Simulations," *Journal of Computational Physics*, Vol. 73, No. 2, December 1987, pp. 325–348.

[99] Ananthan, S., "Analysis of Rotor Wake Aerodynamics During Maneuvering Flight Using a Free-Vortex Wake Methodology," Ph.D. Dissertation, Department of Aerospace Engineering, University of Maryland, College Park, MD, 2006.

[100] Batchelor, G. K., *An Introduction to Fluid Dynamics,* Cambridge University Press, Cambridge, UK, 1967.

[101] Gupta, S., and Leishman, J. G., "Accuracy of the Induced Velocity of Wind Turbine Wakes Using Vortex Segmentation," 23rd ASME Wind Energy Symposium and the 42nd AIAA Aerospace Sciences Meeting, Reno, NV, January 5–8, 2004.

[102] Weissinger, J., "The Lift Distribution of Swept-Back Wings," NACA TM 1120, 1947.

[103] Saffman, P. G., *Vortex Dynamics,* Cambridge University Press, Cambridge, UK, 1992.

[104] Leishman, J. G., and Beddoes, T. S., "A Semi-Empirical Model for Dynamic Stall," *Journal of the American Helicopter Society*, Vol. 34, No. 3, July 1989, pp. 3–17.

[105] Beddoes, T.S., "Representation of Airfoil Behavior," *Vertica*, Vol. 7, No. 2, 1983, pp. 183–197.

[106] Crouse, G. L., "An Analytical Study of Unsteady Rotor/Fuselage Interaction in Hover and Forward Flight," Ph.D. Dissertation, Department of Aerospace Engineering, University of Maryland, College Park, MD, 1992.

[107] Vatistas, G. H., Kozel, V., and Mih, W. C., "A Simpler Model for Concentrated Vortices," *Experiments in Fluids*, Vol. 11, 1991, pp. 73–76.

[108] Bagai, A., and Leishman, J. G., "Flow Visualization of Compressible Vortex Structures Using Density Gradient Techniques," *Experiments in Fluids*, Vol. 15, 1993, pp. 431–442.

[109] Squire, H. B., "The Growth of a Vortex In Turbulent Flow," *Aeronautical Quarterly*, Vol. 16, August 1965, pp. 302–306.

[110] Ramasamy, M., and Leishman, J. G., "A Generalized Model for Transitional Blade Tip Vortices," 60th Annual Forum Proceedings of the American Helicopter Society, Baltimore, MD, June 7–11, 2004.

[111] Jaraiz, E., Kimura, S., and Levenspiel, O., "Vibrating Beds of Fine Particles: Estimation of Interparticle Forces from Expansion and Pressure Drop Experiments," *Powder Technology*, Vol. 72, No. 1, 1992, pp. 23–30.

[112] Xu, C., and Zhu, J. X., "Effects of Gas Type and Temperature on Fine Particle Fluidization," *China Particuology*, Vol. 4, No. 3–4, 2006, pp. 114–121.

[113] Lorber, P. F., and Egolf, T. A., "An Unsteady Helicopter Rotor-Fuselage Aerodynamic Interaction Analysis," *Journal of the American Helicopter Society*, Vol. 35, No. 3, July 1990, pp. 32–41.

[114] Bagnold R. A., "The Flow of Cohesionless Grains in Fluids," *Philosophical Transactions Royal Society of London. Series A, Mathematical and Physical Sciences*, Vol. 249, No. 964, December 1956, pp. 239–97.

[115] Iversen, J. D., Pollack, J. B., Greeley, R., and White, B. R., "Saltation Threshold on Mars: The Effect of Inter-Particle Force, Surface Roughness, and Low Atmospheric Density," *Icarus*, Vol. 29, 1976, pp. 318–383.

[116] Chepil, W. S., "Dynamics of Wind Erosion," *Soil Science*, Vol. 60, No. 5, November 1945, pp. 305–320.

[117] Hamakar, H. C., "The London–Van der Waals Attraction Between Spherical Particles," *Physica*, Vol. 4, No. 10, October 1937, pp. 1,058–1,072.

[118] Crowe, C., Sommerfeld, M., and Tsuji, Y., *Multiphase Flows with Particles and Droplets,* CRC Press, Washington DC, 1998.

[119] Lomax, H., Pulliam, T. H., and Zingg, D. W., *Fundamentals of Computational Fluid Dynamics,* Springer, 2001.

[120] Hairer, E., and Warner, G., *Solving Ordinary Differential Equations I and II* Springer-Verlag, New York, NY, 1980.

[121] Poppe T., Blum, J., and Henning, T., "Analogous Experiments on the Stickiness of Micron-sized Preplanetary Dust," *The Astrophysical Journal*, Vol. 533, No. 1, April 2000, pp. 454–471.

[122] Leese, G. W., and Knight, I. T., "Helicopter Downwash Data," AD-780 754, June 1974.

[123] Moen, C. G., DiCarlo, D. J., and Yenni, K. R., "A Parametric Analysis of Visual Approaches for Helicopters," NASA TN D-8275, December 27, 1976.

[124] Carpenter, P. J., and Friedovich, B., "Effect of a Rapid Blade-Pitch Increase on the Thrust and Induced-Velocity Response of a Full-Scale Helicopter Rotor," NACA TN 3044, November 1953.

[125] Aoyama, Y., and Nakano, J., *RS/6000 SP: Practical MPI Programming* IBM Redbooks, August 1999.

[126] "NVIDIA CUDA C Programming Guide," NVIDIA, November 2010.

[127] "China Grabs Supercomputing Leadership Spot in Latest Ranking of World's Top 500 Supercomputers," http://www.top500.org/lists/2010/11/press-release, November 11, 2010.

[128] "NVIDIA's Next Generation CUDA Compute Architecture: Fermi," NVIDIA, 2009.

[129] Govindarajan, M. B., "Evaluation of Particle Clustering Algorithms in the Prediction of Brownout Dust Clouds," M.S. Thesis, Department of Aerospace Engineering, University of Maryland, College Park, MD, 2011.

[130] Wei Li, "Practical Criteria for Positive-Definite Matrix, M-Matrix and Hurwitz Matrix," *Applied Mathematics and Computation*, Vol. 185, 2007, pp. 397–401.

[131] Rash, C. E., McLean, W. E., Mozo, B. T., Licina, J. R., and McEntire, B. J., "Human Factors and Performance Concerns for the Design of Helmet-Mounted Displays," RTO HFM Symposium on "Current Aeromedical Issues in Rotary Wing Operations, San Diego, CA, October 19–21, 1998.

[132] Syal, M., Rauleder, J., Tritschler, J. K., and Leishman, J. G., "On the Possibilities of Brownout Mitigation Using a Slotted-Tip Rotor Blade," AIAA 2011-3183, 29th AIAA Applied Aerodynamics Conference, Honolulu, HI, June 27–30, 2011.

[133] Hoh, R., "Investigation of Outside Visual Cues Required for Low Speed and Hover," Paper No. AIAA 85-1808, 12th AIAA Atmospheric Flight Mechanics Conference, Snowmass, CO, August 1985, pp. 337–349.